On the diurnal and field-scale variability of atmospheric ammonia over Dutch grasslands

Ruben B. Schulte

Propositions

1. Stomatal exchange of ammonia and water vapor are both leakage processes which plants cannot fully control.
   (this thesis)

2. The focus on long-term averaging has hampered understanding ammonia surface-atmosphere exchange.
   (this thesis)

3. Taxing nitrogen emissions would solve the Dutch nitrogen crisis.

4. Ammonia exchange only occurs in the presence of water.

5. The lack of permanent contract postdoc positions is a net loss for universities.

6. Working from home is unhealthy for PhD candidates and should not be encouraged.

Propositions belonging to the thesis, entitled

On the diurnal and field-scale variability of atmospheric ammonia over Dutch grasslands

Ruben B. Schulte
Wageningen, 24 March 2023

On the diurnal and field-scale variability of atmospheric ammonia over Dutch grasslands

Ruben B. Schulte

On the diurnal and field-scale variability of atmospheric ammonia over Dutch grasslands

Ruben B. Schulte

Summary

Excess nitrogen deposition not only leads to environmental damage, but there are also serious political and societal consequences when reduction measures fail, as demonstrated by the Dutch nitrogen crisis. Deposition of atmospheric ammonia (NH_3) plays a key role, as it accounts for three-quarters of all nitrogen deposition in the Netherlands. Atmospheric NH_3 is governed by a wide range of processes and scales, spanning multiple disciplines, such as meteorology, biology and chemistry. The scales involved range from long-range transport driven by meteorological processes at the synoptic scale (1000 km) or the day and night cycle of the atmospheric boundary layer (1 - 2 km), down to dry deposition at field scale (100 - 1000 m) or the formation of aerosols ($\approx 10\ \mu$m).

Taking measurements of NH_3 deposition is a notoriously difficult endeavor, as the gas tends to "stick" to inlet surfaces. This reactive nature of NH_3 also leads to fast removal of atmospheric ammonia through (dry) deposition and aerosol formation. The short atmospheric lifetime (1 - 2 days), combined with heterogeneously distributed emission (point) sources with a wide range of emission rates, results in high spatial variability in both the NH_3 concentration and flux. While current measurement and modeling frameworks are well suited to monitor NH_3 at long time scales (months to years) and at regional scales (10 - 100 km), there still are significant challenges in both high-frequency (time) observations and high-resolution modeling (sub-kilometer) of NH_3 concentrations and dry deposition.

In this thesis, we aim to investigate the relationships of these processes and scales which govern the diurnal variability of ammonia. We introduce and apply a new comprehensive approach, including representations of the processes governing the NH_3 budget, to advance the interpretation of NH_3 observations and to improve modeling of ammonia surface-atmosphere exchange. We introduce and apply a new comprehensive approach, including representations of the processes governing the NH_3 budget, to advance the interpretation of NH_3 observations and to improve modeling of ammonia surface-atmosphere exchange. To this end, we combine advanced instruments, measuring both the NH_3 concentration and flux, with conceptual models and explicitly resolved turbulent simulations at field-scale. With our focus on interpretation of observations, it is our goal to translate the theoretical

concepts from fields like high-resolution atmospheric modeling or plume dispersion, to practical applications for the measurement and decision-making community.

Chapter 2 aims to identify and quantify the individual contributions of key processes to the diurnal variability of atmospheric NH_3, including chemical aerosol formations and the observed surface deposition. To this end, we combine high-resolution optical measurements of the Differential Optical Absorption Spectroscopy (DOAS) flux measurement setup at the Veenkampen meteorological site (NL) with a conceptual boundary-layer model, focusing on clear-sky convective conditions. By prescribing the observed NH_3 flux to the conceptual model, characterized by strong deposition in the late afternoon, we are able to reproduce the observed NH_3 variability and identify the processes driving the NH_3 budget. We find that the variability of atmospheric NH_3 in the morning is mainly governed by entrainment of ammonia-low air from the free troposphere, while the afternoon is driven by both the surface-atmosphere exchange and regional NH_3 advection. Special emphasis is placed on the surface-atmosphere exchange in this Chapter. We identify a mismatch between the observed and parameterized NH_3 flux at subdaily scales, particularly in the regulation by plants throughout stomatal exchange.

Chapter 3 continues the study of the NH_3 surface-atmosphere exchange, with special emphasis on stomatal exchange. We aim to relate the NH_3 flux to the observed stomatal exchange of CO_2 and water vapor. The study is centered around high-resolution measurements of the newly developed miniDOAS NH_3 flux measurement setup, the successor of the DOAS setup of Chapter 2, taken at the Ruisdael Observatory at Cabauw (NL). We are able to link observed NH_3 fluxes, characterized by daytime NH_3 emission, to stomatal exchange. However, the analysis is hampered by the complex conditions at the Ruisdael Observatory, located only 50 km west of Veenkampen. The (NH_3) characteristics at the site strongly differ from semi-natural grassland at Veenkampen, characterized by intensely managed and grazed agricultural grassland and several emission sources in close proximity to the site. These highly heterogeneous NH_3 surface characteristics result in at least one nearby emission event being identified in the observations. Despite the challenging conditions, we do find high correlation between the observed NH_3 flux and the observed latent heat flux, as well as to solar radiation. The comprehensive approach presented in this Chapter shows the potential of combining high-quality NH_3 observations with auxiliary flux measurements of CO_2, water vapor and other meteorological variables.

Chapter 4 investigates how nearby NH_3 emission sources affect measurements of NH_3 concentration and flux. To this end, we develop a high-resolution (20 x 20 x 5 m^3) turbulent resolved simulation framework based on the Dutch Atmospheric Large-Eddy Simulation (DALES) model, including realistic representations of each of the processes governing the NH_3 budget. Using the simulation framework, we are not only able to simulate the turbulent dispersion of emitted NH_3, but we also distinguishing between the emitted NH_3 and the background concentration. A new concept is introduced, the blending distance,

describing the distance at which the emission plume is considered well-mixed with respect to the background NH_3 concentration. By performing a suite of numerical experiments, we quantify the blending distance for a wide range of meteorological and NH_3 conditions. Here, we find that an emission plume impacts observations at distances of $0.5 - 3.0$ km for NH_3 concentration measurements, and $1 - 4.5$ km for flux measurements.

Chapter 5 expands upon the concept of blending distance, as we study the sensitivity of the blending distance to changes in the turbulent dynamics of the atmospheric boundary layer. First, we simulate the arrival of a mesoscale sea-breeze front, represented by large-scale forcing terms of cold and humid air. Next, the diurnal variability of the blending distance is studied. Finally, we perform two numerical experiments in which more than one meteorological and/or NH_3 processes is varied, studying potential non-linear interactions. Based on these new numerical experiments, we find the blending distance to be highly sensitive to NH_3 fluctuations and boundary layer stability. The transition from an unstable to a stable boundary layer leads to a strong reduction in the blending distance, but changes in turbulent characteristics of an already unstable boundary layer has little impact. The blending distance is most sensitive to changes in the NH_3 fluctuations through turbulent mixing of air masses with different NH_3 characteristics. Through entrainment, pockets of ammonia-low free-tropospheric air can reach the surface, enhancing fluctuations in the background NH_3 and reducing the blending distance for concentration measurement, or increasing the blending distance for flux measurements.

The wide range of processes, scales and disciplines affecting atmospheric ammonia requires an integrated approach at high spatio-temporal resolutions, as presented in this thesis. With the recent advances in both high-resolution measurements of the NH_3 concentration and flux, as well as the use of turbulent resolved models, this level of detail can now be achieved. Moving forward, we suggest to expand the simulation framework presented in this thesis with dynamic representation of the surface-atmosphere exchange and gas-aerosol transformations. These efforts should be incorporated into the Ruisdael TestBed, which almost continuously combines observations and simulations of the meteorological conditions in the Netherlands at 100 m resolution. Furthermore, the results presented in this thesis indicate that stomatal exchange of NH_3 is not yet fully understood and that the parameterization of the stomatal compensation point needs to be revisited to improve the performance at subdaily scales. Recent developments in advanced instrumental techniques for NH_3 flux measurements, like the miniDOAS NH_3 flux setup, allow for such in-dept parameterization studies in the near future. We believe that such a measurement approach should include representation of all processes governing the NH_3 diurnal variability, supported by atmospheric models and a wide range of observations of meteorological variables and trace gasses (e.g. CO_2). With the lessons learned in this thesis and the recent developments in both the use of advanced instrumental techniques and high spatio-temporal simulations, we are taking research on atmospheric ammonia to a higher level of quantification and detail.

Contents

Chapter 1

Introduction

1.1 The challenge in context

Sustainable food production becomes increasingly important as the human population increases. With the increased demand, it is important to maintain balance between efficiency and the environmental impact of agricultural activity. The environmental impact ranges from the use of pesticides, to the emission of greenhouse gasses and reactive nitrogen (Duxbury, 1994; Erisman et al., 2003; McAllister et al., 2011; Stavi and Lal, 2013). While nitrogen is an essential nutrient for the growth of plants, acting as a fertilizer, excess deposition of reactive nitrogen leads to significant environmental damage through ecosystem acidification and eutrophication, leading to a loss of biodiversity (Erisman and Schaap, 2004; Sutton and Bleeker, 2013; Sutton et al., 2008). Deposition can occur through direct exchange between the atmosphere and surface (vegetation), i.e. dry deposition, or reactive nitrogen species can be captured by rain droplets, i.e. wet deposition (Asman, 1995; Behera et al., 2013; van Zanten et al., 2017).

In the atmosphere, reactive nitrogen mainly consists of nitrogen oxides (NO_x), originating mainly from combustion processes, and ammonia (NH_3), primarily originating from agricultural activity like livestock husbandry and manure application (Erisman et al., 2011; Erisman et al., 2003; van der Hoek, 1998; Wichink Kruit et al., 2017). Additionally, gaseous NH_3 can form fine particles through chemical reactions, ammonium (NH_4^+) aerosols, which can directly affect human health (Brunekreef and Holgate, 2002; Erisman et al., 2013; Seaton et al., 1995; Smit and Heederik, 2017). As a result, policies are implemented aiming to mitigate the harmful effects of excesses of atmospheric nitrogen, especially in densely populated and highly agricultural areas like the Netherlands, as well as regions all across the world with intensive livestock farming, e.g. North-West Germany, the province of Lerida in Spain, the state of North-Carolina in the USA or the Hai River Basin in China.

The current situation in the Netherlands shows that there are serious societal consequences when these mitigation attempts are ineffective. The country is currently in the midst of a so called nitrogen crisis (Stokstad, 2019). In May 2019, the highest administrative court of the Netherlands ruled that the policies meant to mitigate the harmful effects of nitrogen deposition were insufficient, as nitrogen deposition in 118 out of 162 Dutch protected natural areas (Natura 2000 areas) exceeds ecological risk thresholds. With this ruling, the court struck down the system for receiving a permit for projects which includes any form of nitrogen pollution, blocking plans for farm expansions, as well as the construction of homes, roads and airport runways. Additionally, a significant reduction in nitrogen emissions is required to allow these natural areas to recover. The high court decision led to significant economic damage, as well as serious political and social unrest.

Ammonia plays a key role in this crisis. The Netherlands is one of the hot spots for high NH_3 concentrations in Europe (Wichink Kruit et al., 2012). Ammonia deposition
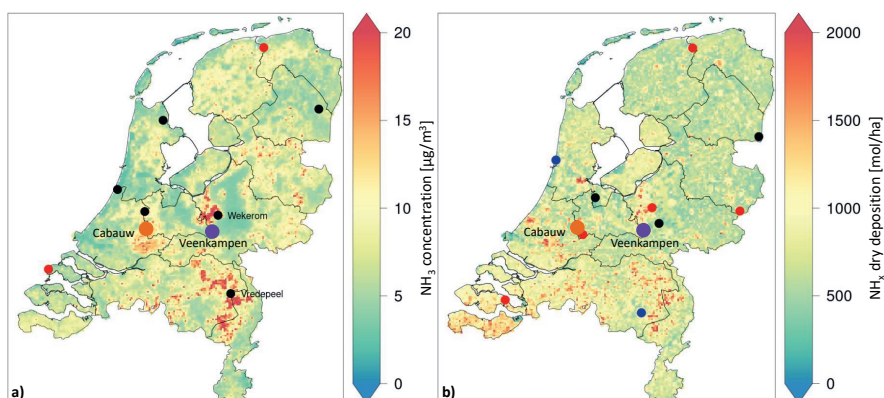
Figure 1.1: The modeled 2020 yearly average NH$_3$ concentration (a) and NH$_x$ dry deposition (b) in the Netherlands. The dots represent the locations of the existing measurement sites (black), proposed sites (red), and the sites currently in development (blue), as well as the measurement sites which are the focus of this thesis; Veenkampen (purple) and the Ruisdael Observatory at Cabauw (orange). (Wichink Kruit et al. (2021), modified)

accounts for about three-quarters of all nitrogen deposition in the country (RIVM et al., 2019; Wichink Kruit and van Pul, 2018). As ammonia mainly originates from agricultural activity, Dutch agricultural sector is the largest contributor to the total nitrogen deposition at about 44%, followed by deposition of nitrogen originating from outside the Netherlands at about 36%, "other" sources at 6.9% and road traffic at 6.7% (Hoogerbrugge et al., 2021; van der Maas et al., 2021).

Starting in the early 1990, the Dutch National Institute for Public Health and the Environment has been operating an automated network of hourly NH$_3$ concentration measurements to monitor the effect of Dutch policies meant to reduce emissions, which is run alongside the Dutch National Air Quality Monitoring Network (LML) (Buijsman et al., 1998; van Zanten et al., 2017). Figure 1.1 shows the locations of NH$_3$ measurement sites of the network in 2021, from here referred to as the LML. The locations of the sites are shown on top of a map showing the modeled yearly average NH$_3$ concentration (Fig. 1.1a) and dry deposition (Fig. 1.1b) of ammonia and ammonium (NH$_x$) for 2020. Additionally, Fig. 1.1 shows the locations of the two meteorological measurement sites which are the focus of this thesis; Veenkampen, operated by Wageningen University (`https://www.wur.nl/en/show/Weather-Station-De-Veenkampen.htm`), and the Ruisdael Observatory at Cabauw, operated by the Royal Netherlands Meteorological Institute (KNMI) (`https://ruisdael-observatory.nl/cabauw/`).

Concentration measurements are taken at six stations, shown black in Fig. 1.1a, with two new upcoming stations shown in red. Each station is equipped with a state-of-the-art optical miniDOAS instrument (Differential Optical Absorption Spectroscopy), measuring

30 minute average NH_3 concentrations (Berkhout et al., 2017; Wichink Kruit et al., 2021). Measurements of NH_3 dry deposition are taken at the locations shown in Fig. 1.1b. Here, the COnditional Time-Averaged Gradient (COTAG) system is used to measure the monthly average NH_3 dry deposition (Famulari et al., 2010; Stolk et al., 2014). Currently, there are only three operational measurement sites (black), but the network is being expanded with two more sites that are currently in development (blue) and preparations are being made for five additional measurement sites (red) (Wichink Kruit et al., 2021).

Furthermore, ammonia wet deposition is measured at 10 sites (not shown), with two new measurement locations being currently in development (van Zanten et al., 2017; Wichink Kruit et al., 2021). In addition to the ammonia network at the LML stations, the Measuring Ammonia in Nature (MAN) network began operation in 2005 (Lolkema et al., 2015; Noordijk et al., 2020). The MAN network uses commercial passive samplers providing monthly average NH_3 concentrations at 255 locations in 86 Natura 2000 nature reserves and will be expanded with 10 new locations in rural areas and 9 new locations in urban areas (Wichink Kruit et al., 2021).

All these measurements together form one of the densest networks for observations of atmospheric NH_3 and NH_3 deposition in the world, especially with the additions of the new measurement locations. The networks provide sufficient spatial coverage of the Netherlands, ranging from coastal areas, to rural areas, to natural reserves, as well as locations with varying levels of NH_3 concentration and deposition, as shown in Fig. 1.1 for the LML stations.

This high level of coverage is essential for the two main purposes of the NH_3 measurement networks: monitoring and model validation (van Pul et al., 2004; Wichink Kruit et al., 2020). In the Netherlands, NH_3 concentrations and deposition are modeled using the Operational Priority Substances (OPS) model (Sauter et al., 2018; van Jaarsveld and de Leeuw, 1993). OPS models emission, dispersion, transport, chemical conversion and deposition of atmospheric pollutants over the Netherlands at a chosen spatial resolution, e.g. 1 x 1 km^2. Ammonia dry deposition is estimated in the OPS model using the state-of-the-art DEPosition of Acidifying Compounds (DEPAC) module (Schrader et al., 2016; van Zanten et al., 2010; Wichink Kruit et al., 2010b).

The modeled concentration and deposition values of Fig. 1.1a and 1.1b highlight one of the major challenges of atmospheric NH_3. Both maps show high spatial variability, with localized hot spots of high concentration or deposition, e.g. in the east. This spatial variability in the NH_3 deposition is exemplified in Fig. 1.2, which shows the observed NH_3 exchange at both Veenkampen and Cabauw sites. Despite being located only 50 km apart, as shown in Fig. 1.1, the observations at Cabauw are dominated by daytime emission, while strong afternoon deposition is observed at Veenkampen.

This high variability is the result of several interacting processes, spanning multiple disciplines and acting on different spatio-temporal scales. Strong local emission sources
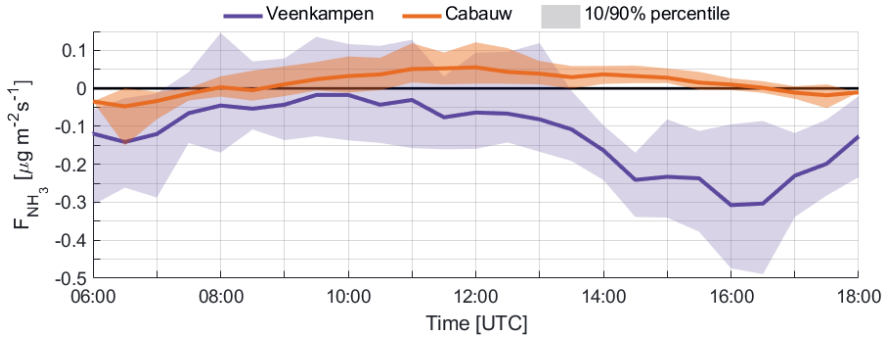
Figure 1.2: The observed NH_3 fluxes at Veenkampen (purple) for clear-sky convective conditions, taken from May to August 2013, and Cabauw (orange), taken in September 2021. The shaded area represents the 10 and 90 percentile of all the filtered observations for each location.

as a result of agricultural activity leads to a high level of (surface) heterogeneity. Once emitted, atmospheric NH_3 is affected by meteorological processes, e.g. changes in wind direction and turbulent dispersion. The highly reactive gaseous NH_3 has a short lifetime of about a single day, much shorter than that of nitrogen oxides (Adams et al., 1999; Erisman et al., 2007; Galloway et al., 2003).

Ammonia is removed from the atmosphere through multiple processes. The main removal mechanism of atmospheric NH_3 is dry deposition. Here the gas directly interacts with the (vegetated) surface. It is an ecophysiological process acting at field scale in which (vertical) turbulent mixing plays a key role. A second mechanism is wet deposition, where gaseous NH_3 is captured by water droplets, like rain or fog. Finally, there is the chemical transformation to form fine aerosols, a few micrometers in size. This mechanism can go in both directions, as some aerosols can evaporate again, depending on temperature and relative humidity.

All these processes affecting gaseous NH_3 at subdaily timescales make studying atmospheric ammonia and dry deposition a multi-scale and multi-process problem. Taking high-frequency NH_3 observations is particularly challenging, as gaseous NH_3 has a tendency to stick to inlet surfaces or tubing of measurement instruments, causing a delay in the concentration measurements (Parrish and Fehsenfeld, 2000). Additionally, observations of the NH_3 concentration can be contaminated by gaseous NH_3 from evaporating aerosols (Mozurkewich, 1993; Stelson and Seinfeld, 1982). These problems pose a significant challenge for high-frequency measurements (e.g. 30 minute) of ammonia dry deposition, where high precision is particularly important (Nemitz et al., 2004a; von Bobrutzki et al., 2010; Whitehead et al., 2008).

While the current measurement and and modeling frameworks are well suited to monitor NH_3 at long time scales (months to years) and at regional scales (10 - 100 km), there is still are significant challenges in both high-frequency (time) observations and high-resolution modeling (sub-kilometer) of NH_3 concentrations and dry deposition to better understanding the processes governing the atmospheric NH_3 budget and its diurnal variability. In this thesis, we aim to investigate the relationships of these processes and scales which govern the diurnal variability of ammonia. We introduce and apply a new comprehensive approach to advance the interpretation of NH_3 observations and to improve modeling of ammonia surface-atmosphere exchange. To this end, we combine advanced instruments, measuring both the NH_3 concentration and exchange flux, with conceptual models and explicitly resolved turbulent models. With our focus on interpretation of observations, it is our goal to translate the theoretical concepts, from fields like high-resolution atmospheric modeling or plume dispersion, to practical applications for the measurement and decision-making community.

Following this approach, we aim to answer the overarching research question of this thesis: *What processes and scales control the ammonia diurnal variability over Dutch grassland? Why are Cabauw and Veenkampen so different?*

1.2   Processes and scales

1.2.1   The role of atmospheric processes

Once emitted, NH_3 enters the atmosphere and is transported and mixed with the background NH_3, influenced by the changing conditions of the atmosphere, i.e. the weather at all scales. Wind speed and direction determine area affected by the emission plume, as these variables govern the main mechanism for transport of atmospheric pollutants. Other meteorological variables influence the (wet) deposition and chemical conversion rates of atmospheric NH_3, like temperature, humidity or clouds, which affect the available energy from (solar) radiation and can lead to rain. These (local) meteorological conditions are driven by meteorological processes acting on a wide range of scales.

At the largest scale, the synoptic scale (order of 1000 km), there is the formation of high and low pressure systems. As the wind swirls from high pressure systems towards low pressure systems, these synoptic-scale processes are driving the wind speed and direction at the surface. Furthermore, these pressure systems lead to changes in weather conditions, as high pressure systems are commonly associate with light winds and clear skies, while low pressure systems are characterized as windy and cloudy, with possible rain or even storms. These large-scale processes are driving weather phenomena in the so-called free troposphere layer, occurring at a smaller scale, i.e. the mesoscale (5 - 1000 km). Such mesoscale processes include phenomena like (rain) fronts (100 - 1000 km), sea breeze (10 - 100 km) and large thunderstorms (5 - 10 km).

In modeling all these scales, there is always a trade-off between cost efficiency and the level of detail at which processes are represented. The large-scale meteorological processes are typically well represented by operational (chemical) transport models. More specifically for NH_3, three representative examples are the aforementioned OPS model (Sauter et al., 2018), the LOng Term Ozone Simulation EURopean Operational Smog (LOTOS-EUROS) model (Manders et al., 2017; Schaap et al., 2008) or the European Monitoring and Evaluation Programme (EMEP) model that deals with acid deposition, tropospheric ozone and particles in Europe (Simpson et al., 2012). These models operate at spatial resolutions ranging from 1 to 50 km and temporal resolutions of days to months. Smaller scale processes, acting on scales similar or smaller as the model resolution, need to be represented by mathematical descriptions that require parameters. Such descriptions are called parameterizations.

1.2.2   The role of day-by-day turbulence

The free troposphere is connected to the surface through the atmospheric boundary layer (ABL), also known as the mixed layer. From here on, the large-scale processes described above function as boundary conditions for the evolution of the ABL, as we focus on surface-atmosphere interactions at field level (10 m - 10 km). The ABL is defined as the layer that is directly influenced by the surface. This layer therefore experiences a clear diurnal cycle, as the surface responds to changes in (solar) radiation (Moene and Van Dam, 2014; Vilà-Guerau de Arellano et al., 2015).

The surface-atmosphere exchange is governed by the available energy from (solar) radiation and heat stored in the ground. During the day, this energy heats up the surface and is released into the atmosphere, partitioned between the transfer of heat (sensible heat flux) and the evaporation of water (latent heat flux). The increase in temperature and humidity reduces the density of near-surface air, causing it to rise, creating instability. The rising plumes of warm and humid air are accompanied by downdrafts, dictated by the conservation of mass, transporting cold and dry air from aloft towards the surface, after which the process is repeated. The rising air form turbulent eddies (10 - 100 m) that can group together to form thermal plumes (i.e. large-eddies), which can reach sizes similar to the height of the boundary layer (1 - 2 km). This process is called convection, or buoyancy induced turbulence, and it plays a key role in both the vertical mixing of thermodynamic characteristics of the ABL and the dispersion of trace gasses, e.g. NH_3.

In absence of dominant synoptic situations, it is through convection that the ABL experiences a clear diurnal cycle, shown in Fig. 1.3. Just before sunrise, the available energy from radiation and the heat stored in the soil is insufficient so start convection. As a result, the ABL is shallow, i.e. only a couple hundred meters high. Little to no mixing occurs and the ABL is stably stratified. As the sun rises, the available energy increases and the turbulent mixing through convection starts. Now, in what is called an unstable,
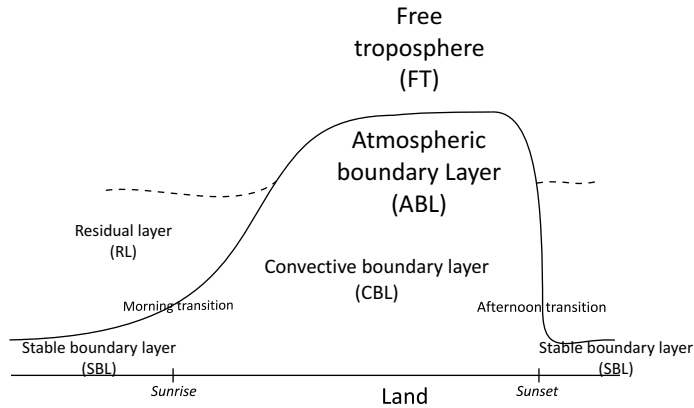
Figure 1.3: A schematic representation of the temporal evolution of the atmospheric boundary layer (Source: Vilà-Guerau de Arellano et al. (2015))

or convective boundary layer, the ABL will rapidly grow until the air at the top is in equilibrium with the free troposphere, reaching heights of 1 - 2 km, or even up to 4 km in the tropics. At the top of the ABL, the up and downdrafts lead to exchange of air between the ABL and free troposphere, a process called entrainment.

During the rapid morning growth of the ABL, two processes can affect the NH_3 concentration. Firstly, the rapid ABL growth increases the entrainment rate of low-ammonia air from the free troposphere into the ABL, diluting the NH_3 concentration. Secondly, as the ABL height increases, the mixing volume for atmospheric NH_3 also increases. As a result, the NH_3 concentration is often observed to decrease as the boundary layer height increases (Ferrara et al., 2021; Schulte et al., 2021; von Bobrutzki et al., 2010; Wichink Kruit et al., 2007). At the end of the day, around sunset, the available energy is no longer sufficient to sustain convective turbulence and the boundary layer collapses. After the collapse of the ABL, a residual layer can form for multiple hours, as shown in Fig. 1.3, characterized by weak sporadic turbulence.

Convection is not the only driver of turbulent mixing. There is also shear-induced turbulence resulting from friction acting on the air flow. This can occur when atmospheric layers with different wind speeds and direction interact high in the atmosphere, or at the surface when the airflow passes buildings, trees or even grass. It is possible for a mixed layer to be maintained by only shear induced turbulence, when driven by sufficiently high wind speeds. For shear induced turbulence, horizontal mixing is dominant over vertical mixing, resulting in the ABL being classified as a neutral boundary layer.

Turbulent flows are inherently chaotic and non-linear, making it impossible to be reproduced in detail. Turbulent eddies are driven by momentum and/or density variations and vary strongly in size and lifetime. As mentioned before, the largest eddies can reach the size of

the ABL height (1 - 2 km) and last for over 30 minutes. Over time, these large eddies break up into smaller eddies, with the smallest spanning only a few centimeters and last for a couple of seconds.

Due to the chaotic nature, turbulent flows are generally treated in a statistical sense, based on averages, standard deviations and exchange fluxes. The main method to observe turbulent exchange fluxes, the eddy-covariance (EC) method, follows such a statistical approach. The EC method is based on averaging high-resolution measurements of turbulent fluctuations of the vertical wind speed and a physical quantities like temperature, wind, water vapor, CO_2 or NH_3. This is the most direct and most common method to determine the (vertical) flux of trace gasses, but it does require high-frequency analyzers (>10 Hz). An alternative to these high-frequency measurements is the flux-gradient method (FG), where the flux is inferred from observed vertical concentration differences, combined with a measure of vertical transport (Nemitz et al., 2004a; Swart et al., 2023; Wyers et al., 1993). The latter method is most common for observing turbulent NH_3 exchange, although EC systems are currently being developed as well, as will be discussed later.

The knowledge on the dynamics of the ABL was gained through a long history of combining observations with modeling. By reproducing the meteorological observations with models, we increase our understanding of the processes and interactions between processes in the ABL. This generally starts with the lowest complexity models, conceptual mixed-layer or one-dimensional ABL models (Stull, 1988; Tennekes and Driedonks, 1981; Vilà-Guerau de Arellano et al., 2015). These models are based on simplified, yet physically sound and well-proven assumptions of the processes governing the evolution of the ABL, like turbulent mixing. The main advantages of conceptual models are the low operational cost and their simplicity, making them easy to understand. As a result, these conceptual models are ideal for developing a conceptual understanding of complex problems or interactions in the ABL and test the sensitivity to a wide range of meteorological conditions.

The relations developed with conceptual models can be tested, refined and expanded upon using three-dimensional turbulent resolved simulations (Barbaro et al., 2014; Vilà-Guerau de Arellano et al., 2011). Here, we make the distinction between modeling techniques, which still require parameterization, and simulation techniques, where turbulence is explicitly resolved. These more complex simulation techniques do have a higher computational cost, at the advantage of a realistic representation of the ABL and turbulent mixing. The most common types of turbulent resolved simulation techniques are the Large-Eddy Simulation (LES) technique and the Direct Numerical Simulation (DNS) technique.

Models utilizing LES to resolve turbulent mixing are much more common, as these models find a balance between operational cost and the level of detail. Nearly all (80 - 95%) turbulent energy is explicitly resolved in LES models, while eddies smaller than the model grid are parameterized. As a result, LES models can operate at high spatio-temporal resolutions (10 - 100 m and 1 - 30 minutes) and domains of similar order of magnitude

as the resolutions of operational weather or chemical transport models (10 - 100 km). This makes these simulation technique well suited to focus on the sub-diurnal variability and study processes and interactions at the subgrid-scale of the large-scale operational (transport) models. For example, turbulent dispersion of an emission plume is explicitly resolved using LES models, but this process requires parameterization in large-scale chemical transport models, e.g. the OPS model uses a Gaussian plume model (Sauter et al., 2018). In analyzing the data from turbulent resolved simulations, often combined with in-field observations, we can improve the parameterizations of large-scale (transport) models.

When comparing model results to meteorological and atmospheric composition measurements, a comprehensive set of (turbulent) meteorological measurements is required. So-called meteorological supersites, like the Ruisdael Observatory, can provide a long-term continuous datasets (50 years) of a wide range of meteorological measurements, including measurements of radiation, surface fluxes, clouds, trace gasses and measurements of thermodynamic variables along the 213 m mast (Bosveld et al., 2020).

An alternative for meteorological supersites are temporary measurement campaigns (Holtslag et al., 2012; Mangan et al., 2023; Vilà-Guerau de Arellano et al., 2020). Campaigns encompass a wide range of (labor intensive) measurements tailored towards a specific goal and offer a unique opportunity for international collaboration. The CloudRoots campaign is an example of an international collaboration, combining meteorological observations with detailed measurements at leaf level to study the interactions between vegetation, atmospheric turbulence and cloud formation (Vilà-Guerau de Arellano et al., 2020).

A new approach of combining observations with models is introduced by the Ruisdael Observatory project. This national initiative sets out to model the entire Dutch atmosphere with a high resolution of only 100 meters (Russchenberg et al., 2022). The modeling effort is supported by a very dense nationwide network of fixed and mobile measurements spanning multiple ecosystems, like forests, coastal areas and the cities of Rotterdam and Amsterdam. The wide range of local lessons about weather and climate that can be learned from such an integrated approach will lead to improvements of operational weather and air quality models.

1.2.3 Ammonia dispersion above a heterogeneous surface

The Ruisdael project touches upon one of the major challenges in studying the atmospheric boundary layer: surface heterogeneity. Local differences in the properties of soil and vegetation characteristics play a key in the evolution and characteristics of the ABL (Marth, 2000; Van Heerwaarden and Vilà-Guerau de Arellano, 2008). Due to differences in surface conditions, characterized by variations in the soil and plant characteristics, the surface-atmosphere exchange can locally lead to very different atmospheric conditions. For example, there is a noticeable difference in temperature on a warm summer day between

an urban area and the grassland only hundred meters away (Arnfield, 2003; Heusinkveld et al., 2014; Oke, 1982; Steeneveld et al., 2011), or between an irrigated crop field and the bare soil next to it (Boone et al., 2021; Mangan et al., 2023; Vilà-Guerau de Arellano et al., 2020).

Through turbulent mixing, the different characteristics are mixed within the boundary layer and the influence of this surface heterogeneity will decrease after a certain height, called the blending height (Garratt, 1991; Grant, 1991; Marth, 1996). Above this blending height, it is the combined characteristics of the heterogeneous surface that make up the well-mixed ABL. Distinguishing between these local and non-local processes with a single or a few point measurements still remains a challenge for observational studies (Bou-Zeid et al., 2020; Butterworth et al., 2021; Cuxart et al., 2016; Vilà-Guerau de Arellano et al., 2020).

With atmospheric ammonia, human activity adds an additional level of complexity to the challenge of surface heterogeneity. The NH_3 surface-atmosphere exchange is typically governed by the surface characteristics and type of land use, resulting in differences in the NH_3 surface-atmosphere exchange at field scale. Additionally, human activity like livestock husbandry and manure application, leads to local NH_3 emission sources which are orders of magnitudes larger than natural emission sources, resulting in locally very large concentration differences (Fowler et al., 1998; Shen et al., 2016; Sommer et al., 2009; van Pul et al., 2004).

The effects of heterogeneity-induced circulation are difficult to represent well in large-scale models, because these flows are mostly in the subgrid scale of the models(van Heerwaarden et al., 2014). High-resolution models are able to explicitly simulate these processes, but are often limited to an idealized representation of a heterogeneous surface because of the otherwise very high operational costs (Ouwersloot et al., 2011; Van Heerwaarden and Vilà-Guerau de Arellano, 2008). Recent efforts to incorporate realistic heterogeneous surface representations in LES modeling studies show promising results (Heinze et al., 2017; Schalkwijk et al., 2015) and it is one of the main themes in the aforementioned Ruisdael Project (van Stratum, 2022). Additionally, describing emission plumes based on field observations remains a challenge to this day (Mylne and Mason, 1991; Ražnjević et al., 2022), but developments in the field of turbulent plume dispersion have resulted in statistical descriptions of the mixing of emission plumes, e.g. Gaussian plume models, which are commonly used in chemical transport models (Cassiani et al., 2020; Gailis et al., 2007; Sauter et al., 2018; Sommer et al., 2009; van der Swaluw et al., 2017).

1.2.4 Removal processes of atmospheric ammonia

The three removal mechanisms of atmospheric ammonia are chemical reactions forming aerosols, dry deposition and wet deposition, i.e. gaseous ammonia being captured by rain droplets. Ammonia reacts with a few acid gasses to transform the gasses into ammonium

aerosol particles. The most common ammonium aerosols are ammonium sulphate and ammonium nitrate. The latter reaction is reversible, meaning that the solid aerosols can evaporate, depending on atmospheric temperature and humidity (Behera et al., 2013; Nemitz et al., 2004a; Tang, 1996). As temperature and humidity changes with height, the formation and evaporation of ammonium aerosols leads to vertical heterogeneity in the ABL (aan de Brugh et al., 2012; aan de Brugh et al., 2013; Barbaro et al., 2015).

Concentration measurements of aerosols, including ammonium aerosols, are part of the LML network, as atmospheric aerosols pose a serious risk to human health (Erisman and Schaap, 2004; Pöschl, 2005; Smit and Heederik, 2017). However, these are measurements of the total aerosol concentration and do not distinguish between the different types of aerosols. Taking measurements of aerosol composition is typically done on a campaign basis, as these instruments are expensive and labor intensive to operate (Meng et al., 2018; Rumsey et al., 2014; ten Brink et al., 2009; Thomas et al., 2009).

In models, the chemical gas-aerosol transformations are represented with different levels of detail. The Dutch OPS model for example, uses a percentage loss per hour to represent the transformation from gaseous NH_3 to ammonium aerosols. A more complex representation is used in LOTOS-EUROS model, which uses thermodynamic equilibrium chemistry module to represent both the formation and evaporation of aerosols. However, the model lacks the level of detail to accurately represent the local heterogeneous effects of the chemical reactions, due to its large grid size (Manders et al., 2017; Schaap et al., 2008). This level of detail can be achieved when coupling these thermodynamic chemistry modules to LES models, as was done by aan de Brugh et al. (2013) and Barbaro et al. (2015).

While aerosol formation plays an important role in the atmospheric NH_3 budget, the main removal process is dry deposition through surface-atmosphere exchange, also known as the turbulent NH_3 flux. The NH_3 flux follows three parallel pathways; the stomatal, external leaf and the soil pathway. The dry deposition process can be simplified as NH_3 dissolving in water on different surfaces, with the main difference between each pathway being the location of the water (Flechard et al., 1999; Fowler et al., 2009). For the stomatal pathway, water is located inside the plant, called the apoplast fluid (Farquhar et al., 1980). For the external leaf and soil pathways, the water is found as a thin film of water and leaf surface waxes, or as moisture in between grains of soil (Van Hove et al., 1989).

For dense vegetation like grassland, which is the focus of this thesis, the soil is completely covered by vegetation and exchange through the soil pathway is assumed to be negligible (van Zanten et al., 2010). Grassland is the dominant land-use type in the Netherlands (30%) and covers approximately half of all agricultural land in the country, where rotational grazing is the most common land use (Jacobs et al., 2007; van Jaarsveld et al., 2000). As a result, most of the NH_3 emitted from agricultural activity, the dominant emission source, is deposited on grassland.

To estimate the surface-atmosphere exchange of ammonia, a representation of an internal NH_3 concentration is used, i.e. the compensation point. The compensation point can be estimated for the stomatal and external leaf pathway individually. When the compensation point is lower/higher than the atmospheric concentration, NH_3 deposition/emission takes place. When there is a concentration difference between the surface and atmosphere, exchange of NH_3 requires turbulent mixing, i.e. transporting the atmospheric ammonia towards the surface in case of deposition. Without one of these two ingredients, there will be no exchange of ammonia between the surface and atmosphere.

The efficiency of the NH_3 exchange is governed by local meteorological and surface conditions, as well as the state of the vegetation. For the external leaf path, the most important variable is thickness of the water film, governed by dew formation, rain and relative humidity (Flechard et al., 1999; Van Hove and Adema, 1996). The NH_3 exchange through the stomatal pathway is governed by the dynamic response of vegetation to meteorological conditions.

Vegetation regulates the opening and closing of the stomata (literally 'mouths') for CO_2 uptake (photosynthesis) and to regulate evaporation of water. During the day, the stomata are open, using part of the solar radiation for photosynthesis. Water evaporates (plant transpiration) while the stomata are open, depending on the leaf temperature and the water vapor pressure deficit, i.e. the difference between the moisture the air can hold and the actual moisture in the air. The plant can regulate the stomatal aperture, closing the stomata to reduce the loss of water or opening them further to use enhanced evaporation to lower the leaf temperature. During the night, there is no radiation for photosynthesis and the stomata close. This allows for a distinction between the stomatal and the external leaf pathway when performing NH_3 flux measurements. While the stomata are only a couple of micrometers in size, the stomatal response of the vegetation affects the atmospheric conditions at field scale.

The knowledge of the ammonia exchange through the different pathways is gained through high-resolution observations of the NH_3 surface-atmosphere exchange. The aforementioned eddy-covariance method is the most direct way to measure surface fluxes and is the golden standard for (trace) gasses like CO_2. However, the EC method requires high frequency ($>$ 10 Hz) and precise concentration measurements, which is particularly challenging for NH_3 (Baldocchi et al., 2001; Mauder et al., 2021). Recent developments in using this method for NH_3 measurements are promising, but these instruments are very labor intensive and often require tubing, making them sensitive to the aforementioned 'stickiness' of NH_3 (Famulari et al., 2005; Moravek et al., 2019; Sintermann et al., 2011; Swart et al., 2023; Wang et al., 2021; Whitehead et al., 2008).

Historically, the flux-gradient method (FG) has been used to observe the NH_3 flux (Erisman and Wyers, 1993; Nemitz et al., 2004a; Sutton et al., 2009; Wichink Kruit et al., 2007; Wyers et al., 1993). With this method, there is no need for high-frequency measurements,

allowing for slower chemical denuder systems to be used (Sutton et al., 2009; Wichink Kruit et al., 2007; Wyers et al., 1993). Currently, optical systems are more common in both NH_3 concentration and flux measurements, e.g. instruments using the Differential Optical Absorption Spectroscopy (DOAS) technique (Berkhout et al., 2017; Volten et al., 2012a). The FG method is limited by the assumptions of the theory describing the relations between the vertical gradient and turbulent transport, i.e. Monin-Obukhov Similarity Theory (MOST). By applying MOST, one assumes that the mean turbulent quantities doe not change in time, do not change in space horizontally (horizontal homogeneity) and are only affected by processes in the lowest part (10%) of the ABL (Businger et al., 1971; Moene and Van Dam, 2014; Monin and Obuhhov, 1954). As both the FG and the EC method operate following different principles, the two methods are complementary. Using both methods alongside each other can help to validate both systems and advance our understanding of both methods and the NH_3 surface-atmosphere exchange (Swart et al., 2023).

With these high-resolution observational studies, one can develop parameterizations for the surface-atmosphere exchange of ammonia. The most common method to parameterize the process is by using the single-layer or 'big-leaf' approach (Massad et al., 2010; Wichink Kruit et al., 2010b; Zhang et al., 2010). Multi-layer models for NH_3 exchange have also been developed (Nemitz et al., 2000), but these are used for more complex canopy types like crop fields or forests, which are outside the scope of this thesis. Single-layer models, like the aforementioned DEPAC module (van Zanten et al., 2010), have separate parameterizations for the NH_3 compensation point and the exchange efficiency of each individual pathway.

The efficiency of stomatal exchange is well studied for CO_2 and water vapor, and is based on meteorological variables (temperature, humidity and radiation), as well as vegetation type. Common parameterizations are the A-g_s (Ronda et al., 2001) or the Jarvis-Steward approach (Jarvis et al., 1976; Stewart, 1988). Such parameterizations are applied to describe the efficiency of the stomatal exchange of ammonia. The exchange efficiency of the external leaf pathway is based on several laboratory and field campaigns, and is related to the relative humidity (Benner et al., 1992; Sutton and Fowler, 1993; Van Hove et al., 1989). Validation of large-scale models using the observational networks measuring atmospheric ammonia do indicate that these parameterizations of the NH_3 compensation points and the exchange efficiencies are sufficiently accurate. However, studies targeting the accuracy of these parameterizations at the subdaily scale are rare Schrader et al. (2016). Recent developments in high-frequency NH_3 flux measurements for long-term hands-off monitoring, e.g. the mniniDOAS flux setup, open up new possibilities to evaluate these parameterizations at both short an long time scales. These new developments which will certainly lead to advancements in our understanding of the NH_3 surface-atmosphere exchange and improvements to parameterizations.

1.3   A new approach

In this thesis, we apply and consolidate an integrated approach to study atmospheric ammonia and the surface-atmosphere exchange, coupling the surface flux to both surface and atmospheric boundary-layer conditions. We take full advantage of the latest developments in high-resolution optical ammonia measurements, which circumvent the typical challenges which come with measuring ammonia (Berkhout et al., 2017; Swart et al., 2023; Volten et al., 2012a). Combining these state-of-the-art observations with both conceptual (Ouwersloot et al., 2012; Vilà-Guerau de Arellano et al., 2015) and explicit turbulence models (Heus et al., 2010; Ouwersloot et al., 2017a), allows us to perform a comprehensive analysis, incorporating all processes and scales relevant to the diurnal variability of atmospheric ammonia.

The scope of this thesis is visualized in Fig. 1.4. The pictures of the two measurement sites at Cabauw (Fig . 1.4a) and Veenkampen (Fig. 1.4b), appear to show two very similar and typical grassland sites. However, both sites are a sharp contrast with regards to NH_3 characteristics. The measurements at Veenkampen are taken over semi-natural grassland, while the Cabauw site is characterized as actively managed agricultural grassland, resulting in the contrast in the observed flux shown in Fig. 1.2. The two pictures also include representations of the models employed at both sites. Here, the dashed line showing the ABL growth in Fig. 1.4b represents a conceptual mixed-layer model applied in combination with the Veenkampen observations and the 3D grid in Fig. 1.4a representing a high-resolution LES model centered around Cabauw. The level of detail at which turbulent mixing can be resolved using the LES model is shown in Fig. 1.4c. This vertical cross-section shows the entrainment of ammonia-low air from the free troposphere at the time the ABL just reached its maximum height. The Figure shows downward plumes with ammonia-low air (purple) from aloft entering the ABL and even reaching the surface. This entrainment process, and other processes governing the atmospheric ammonia budget, are shown in a simple schematic in Fig. 1.4d.

We start in Chapter 2 by investigating the diurnal variability of atmospheric ammonia, placing special emphasis on the surface-atmosphere exchange. The study is centered around high-resolution optical measurements of the NH_3 flux and concentration at Veenkampen, shown as yellow beams in Fig. 1.4b. The observed NH_3 flux over the semi-natural grassland at Veenkampen is characterized by strong deposition in the late afternoon (purple in Fig. 1.2). Focusing on clear-sky convective conditions, we combine the observed NH_3 flux with a conceptual ABL model to reproduce the observed NH_3 concentration. We aim to identify and quantify the individual contributions of key processes to the diurnal variability of the NH_3 concentration, including chemical aerosol formations and the observed surface deposition. Additionally, the combination of NH_3 flux observations with modeling also allows us to evaluate the performance of the DEPAC parameterization at the subdaily scale.
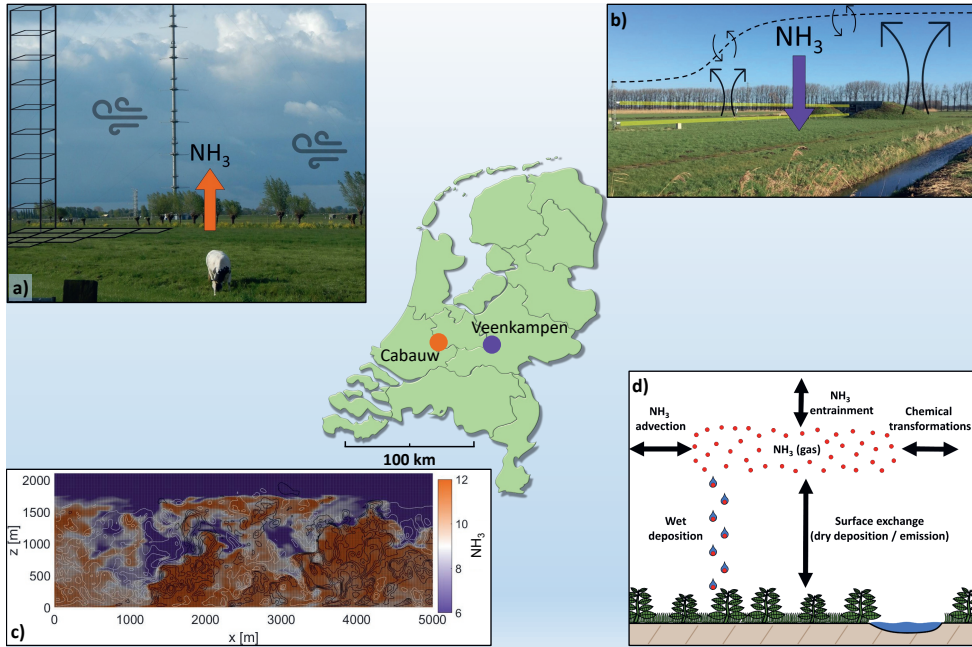
Figure 1.4: An overview of the scope of this thesis. (a) Shows the Ruisdael Observatory supersite at Cabauw, characterized by NH_3 emissions, including representations of varying weather conditions, agricultural activity and the 3D model applied at Cabauw. (b) Shows the Veenkampen site, characterized by deposition, with the optical NH_3 flux setup (yellow) and representations of convective conditions and the mixed-layer model (dashed line) applied at Veenkampen. (c) Shows a vertical cross-section of the NH_3 concentration in the ABL at noon, simulated at 20 x 20 x 5 m^3 resolution. The four main processes governing the gaseous atmospheric NH_3 budget are shown in (d).

With this combination of high-resolution observations and modeling we aim to answer the sub-question to our main research question: *How do the individual processes governing the ammonia budget contribute to the diurnal variability of atmospheric ammonia?*

Closely connecting with the topic of the diurnal variability and the surface-atmosphere exchange, we analyze NH_3 measurements at the Ruisdael Observatory at Cabauw (Fig. 1.4a) in Chapter 3. Despite being located only 50 km west of Veenkampen, the conditions at Cabauw are a sharp contrast compared to Veenkampen. The area at the Cabauw site is characterized by intensely managed and grazed agricultural grassland, leading to highly heterogeneous NH_3 surface characteristics. Furthermore, the observations were taken under varying meteorological conditions, governed by frontal passages, adding an additional layer of complexity. At Cabauw, the observed NH_3 flux is dominated by emissions as shown in Fig. 1.4d. The observed diurnal cycle of the NH_3 flux strongly resembles that of the CO_2

flux. This would indicate towards stomatal exchange for the daytime NH_3 emissions, which is governed by the opening and closing of the stomata for CO_2 uptake and evaporation of water for photosynthesis.

We therefore aim to link the NH_3 flux to photosynthesis in Chapter 3 with the following two sub-questions. *What are the relationships between the observed NH_3 flux and the CO_2 uptake and transpiration by vegetation? Can this understanding help us to improve the NH_3 stomatal exchange parameterization?*

The close proximity of NH_3 emission sources during the observations in Chapter 3 sparked questions on the impact of an emission plume on ammonia concentration and flux measurements. There is currently no consensus on a recommended minimum distance between concentration or flux measurements and NH_3 emission sources (EMEP/CCC, 2001; Schaug, 1988; Wichink Kruit et al., 2021). Literature on turbulent plume dispersion also cannot provide answers, as these studies rarely include chemical and deposition processes, or study the role of the emission plume relative to a background concentration.

We therefore study the impact of NH_3 emissions in proximity of flux and concentration measurements in Chapter 4. To this end, we develop a high-resolution (20 x 20 x 5 m^3) simulation framework centered around the Cabauw supersite (Fig. 1.4a). Using the simulation framework, we are not only able to simulate the turbulent dispersion of emitted NH_3, but also to isolate the role of the emission plume by distinguishing between the emitted NH_3 and the background concentration. Unique to this simulation framework is the inclusion of realistic representations of each of the processes governing the NH_3 budget shown in Fig. 1.4d. We introduce a new concept, the blending distance, describing the distance at which the emission plume is considered well-mixed with respect to the background ammonia. By performing a suite of numerical experiments, we quantify the blending distance for a wide range of meteorological and NH_3 conditions and provide a first-order estimate of the minimum distance between NH_3 observation and strong local emission sources.

Focusing on the role of local surface heterogeneity in Chapter 4, we set-up the following sub-question: *What is the impact of ammonia surface heterogeneity (e.g. a local emission source) on ammonia concentration and flux measurements?*

In Chapter 5, we address the interplay between boundary-layer dynamics and the ammonia heterogeneity. Here, we expand upon the previous Chapter by studying the sensitivity of the blending distance to changes in the turbulent dynamics of the ABL. We start with studying the response of the blending distance to large-scale meteorological forcing, by simulating the arrival of a sea-breeze front. Acting at the mesoscale (Section 1.2.1), a sea-breeze front advects (transports) cooler air with increased humidity, which in turn changes the turbulent characteristics of the ABL. We follow up by testing the sensitivity of the blending distance to the diurnal variability, where both atmospheric stability and boundary-layer growth affect the mixing of NH_3 in the ABL. As shown in Fig. 1.4c, the

strong entrainment resulting from rapid boundary-layer growth can have a significant impact on the NH_3 spatial variability and the blending distance can vary throughout the day as a result. Furthermore, we study possible non-linear relationships of the blending distance to scenarios where multiple variables are changed with respect to the reference experiment presented in Chapter 4.

With the new numerical experiments presented in Chapter 5, we expand our knowledge and the applicability of the concept of the blending distance. This leads to the final sub-question: *How do changes in the turbulent characteristics, driven by external factors, affect the impact of an emission plume on ammonia measurements?*

Finally, we connect each of the chapters in Chapter 6. In Section 6.1, we first address each of the sub-questions individually. We then connect the Chapters, as we answer the overarching research question at the end of Section 1.1. We end this thesis with Section 6.2, where we present our vision for the future of atmospheric ammonia research, utilizing both high-resolution ammonia observations and turbulent resolved simulation techniques.

Chapter 2

Unraveling the diurnal atmospheric ammonia budget of a prototypical convective boundary layer

Abstract

We investigate diurnal variability of the atmospheric ammonia (NH_3) budget over un-fertilized grassland by combining observations with a conceptual atmospheric boundary layer model. Our combined approach of diurnal observations and modeling enables us to identify the contribution of the four governing processes to the NH_3 diurnal cycle: surface-atmosphere exchange, entrainment, advection and chemical gas-aerosol transformations. The observations contain new NH_3 flux and molar fraction measurements obtained using the Differential Optical Absorption Spectroscopy (DOAS) remote sensing technique, elimi-nating problems related to inlet tubing. Using strict filter criteria, 22 days with clear-sky summer conditions are selected. From this selection, we analyze a single representative day characterized by prototypical convective boundary layer conditions, using the boundary layer model constrained by meteorological observations.

We design two numerical experiments to study the NH_3 diurnal variability and the individual contributions of the processes governing the ammonia budget. These experiments only differ in their representation of the NH_3 surface exchange. First, a fitted function through the observed NH_3 flux is prescribed to the model. In the second numerical experiment, the surface flux is solved following the DEPosition of Acidifying Compounds (DEPAC) parameterization. With a prescribed surface flux, the modeled NH_3 molar fraction closely fits the observations. Two regimes are identified in the NH_3 diurnal cycle: the morning, where boundary layer dynamics dominate the budget through entrainment, and the afternoon, where multiple processes are of importance. A similarly close fit to the observed molar fraction is achieved in the second experiment, but we identify a mismatch between the observed and parameterized NH_3 surface flux. As a result, the model requires an unrealistic budget representation to achieve this close fit, e.g. high free tropospheric NH_3. Our findings on the NH_3 budget, based on integrating modeling and observations, paves the way for future research on the NH_3 surface-atmosphere exchange at the subdaily scales.

2.1   Introduction

It is well established that excess nitrogen deposition leads to acidification and eutrophication of soils; threatening biodiversity (Bobbink et al., 2003; Erisman et al., 2007; Erisman et al., 2013). The European Union has made the conservation of natural habitats, i.e. Natura 2000 areas, an essential objective through the EU Habitats Directive (92/43/EEC) and EU Birds Directive (79/409/EEC). This includes mitigation of the harmful effects of nitrogen deposition. Currently, nitrogen deposition in most Dutch Natura 2000 areas exceed critical loads, leading to the highest administrative court of the Netherlands scrapping the permit system for all projects which include any nitrogen pollution, blocking plans for farm expansions and construction of new homes, roads and airport runways. The high court decision led to economic damage and political and social unrest, known as the Dutch nitrogen crisis. Ammonia (NH_3) plays a key role in this crisis as it accounts for two-thirds of all nitrogen deposition in the Netherlands between 2005 and 2016 (Wichink Kruit and van Pul, 2018). Policies to mitigate the adverse effects of ammonia are supported by several decades of scientific studies on atmospheric ammonia, leading to observational networks, deposition parameterizations and air quality forecasting models (Sutton et al., 2008). However, these studies are mainly focusing on low spatio-temporal resolutions, e.g. monthly to yearly averages with grids ranging from 1 x 1 km to 50 x 50 km (Manders et al., 2017; Matthias et al., 2018; Sauter et al., 2018; Schaap et al., 2008; Schrader et al., 2016; Schrader et al., 2018; Simpson et al., 2012). As a result, surface, dynamic and chemistry processes governing the diurnal evolution of the atmospheric ammonia budget are often simplified or not well captured. This study aims to disentangle the atmospheric ammonia budget by combining observations with a convective boundary layer model at subdaily and local scales.

The atmospheric ammonia budget is studied as a mass balance between the atmospheric molar fraction ("Storage"), sources and sinks. Figure 2.1 shows a schematic representation of this budget in an evolving convective boundary layer (CBL), with the four main processes governing the budget: (bi-directional) surface exchange, entrainment of free tropospheric (FT) air, advection and chemical gas-particle transformations. These processes combine multiple disciplines, such as biology and chemistry, and interact on multiple spatio-temporal scales, ranging from stomatal responses of vegetation to NH_3 advection over several kilometers (Farquhar et al., 1980; Fowler et al., 1998; Shen et al., 2016; Sommer et al., 2009; Sutton et al., 1995). Integration of these disciplines and scales is essential for any study concerning atmospheric ammonia, making it a highly complex exercise. It is the novelty of this study that we integrate these four processes via modeling and the maximum use of observations. Observations of ammonia add an additional layer of complexity as the gas tends to "stick" to inlet walls of conventional instruments, causing slow response times, hysteresis and a sensitivity to changes in relative humidity. Additionally, evaporation of ammonium aerosols from filters and the instrument interior leads to further inaccuracies
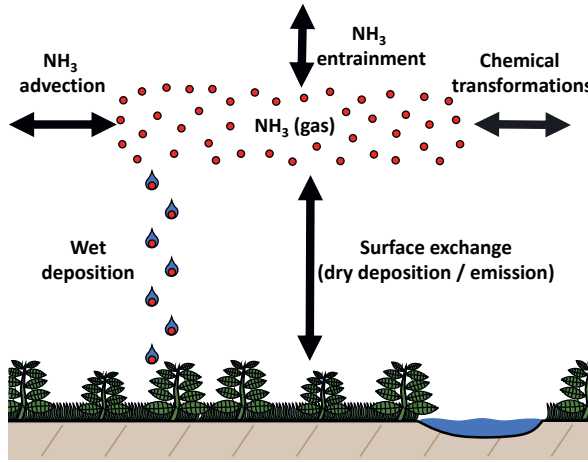
Figure 2.1: Schematic representation of the atmospheric ammonia budget.

with conventional NH_3 observations (von Bobrutzki et al., 2010; Whitehead et al., 2008). As a result, ammonia concentration and flux measurements at high temporal resolution are scarce.

By analyzing observations over more than 100 days, collected over an unfertilized grass field in the Netherlands, we design a case study to identify the contributions of each process to the diurnal variability of the NH_3 budget. The numerical experiments are constrained by observations of a representative single-day Case, characterized by convective boundary-layer conditions. The observations include ammonia concentration and flux measurements by a state-of-the-art optical instrument, eliminating the inlet issues typical for conventional NH_3 observations. We set up a two-experiment approach where we first disentangle the ammonia budget based on observations and follow up by evaluating the standard parameterization against the observations at subdaily scales. To this end, we prescribe the observed NH_3 flux to the model in the first numerical experiment. Next, we change the representation of the NH_3 surface exchange in the second experiment by parameterizing the NH_3 flux following the parameterization standard in the Netherlands: DEPosition of Acidifying Compounds (DEPAC) v.3.11 (van Zanten et al., 2010).

2.2   Methodology

2.2.1   Meteorological site description

This study focuses on the Veenkampen meteorological site in the Netherlands, located west of Wageningen (51.98º N, 5.62º E) at 4 m above sea level. The site is maintained by Wageningen University & Research and has been in operation since 2011, succeeding the

former Haarweg meteorological site which operated from 2001 to the end of 2011 (Calders et al., 2015). The automated weather station provides half-hourly measurements of several meteorological variables, radiation and soil temperature and moisture. An overview of the available measurements can be found at `https://met.wur.nl/veenkampen/graphs/cur/` and the data is freely available at `https://met.wur.nl/veenkampen/data`. The soil at the 17-ha Veenkampen site consists of a clay layer of approximately one meter over peat. In 2011, the site was sown in with reyegrass and species composition has not been monitored or managed since. The grass has an approximated height of 10 cm and is cut regularly during the growing season (April to September). Fertilization of the site stopped in 1979. Yearly average deposition of NH_x, modeled by the Dutch National Institute of Public Health and the Environment at 1 x 1 km resolution (Velders et al., 2014), is about 1000 mol ha^{-1}year^{-1} at the site.

At the northern border of the Veenkampen site, about 50 meters from the centerline, reeds up to 1.5 m high are found. The nearest trees are 350 m east of the site. Both the reeds and the trees could impact the turbulent flow at the site for medium to high wind speeds. Neighboring fields are similar in composition, but could differ in nitrogen content as intensive management only stopped some time before 2011. Farms, mostly livestock, are found in all directions, with the closest located about 1.75 km north, 1.20 km east, 1.50 km south and 0.65 km west of the Veenkampen. These nearby farms are likely to contribute significantly to the atmospheric NH_3 concentrations and high deposition at Veenkampen.

To complement the observations at Veenkampen, we support our study with boundary layer height observations from the Ruisdael Observatory at Cabauw (`www.ruisdael-observatory.nl`). These measurements are taken using a LD40 ceilometer (Vaisala, Bonn, Germany). Additionally, radiosonde measurements from the De Bilt weather station of the Royal Netherlands Meteorological Institute (KNMI) were used. These two locations are located 50 km and 35 km west of Veenkampen.

2.2.2   Ammonia observations

Ammonia concentration and flux measurements are taken at the Veenkampen by two Differential Optical Absorption Spectroscopy (DOAS) instruments (Volten et al., 2012a). These instruments measure the average NH_3 mass density (ρ_{NH_3}) over a 50 m open path between the instrument and its retroreflector. Two parallel paths are set up above one another at heights of 0.65 m and 2.36 m respectively, referred to as $NH_{3,\ 0.65\ m}$ and $NH_{3,\ 2.36\ m}$. The mass density is calculated from 30-minute averaged spectra with a typical standard deviation of 0.15 µg m^{-3} (Volten et al., 2012a). Both DOAS instruments are intercalibrated regularly in the field with special measurements. The instruments are placed in a small building, covered by a smooth man-made hill to minimize flow disturbance, about 30 m in diameter and 3 m high. The setup includes 20 Hz turbulent measurements at

3.2 m from a CSAT3 sonic anemometer (Campbell Scientific Inc., Logan, UT, USA). The anemometer is located in the middle of the path to get the 30-minute average turbulent properties representative for the path. This state-of-the-art NH_3 measurement setup is unique in the world and has so far been used in two studies: NH_3 exchange measurements over a corn field (Volten et al., 2012b; Wichink Kruit et al., 2010a) and as part of a surface exchange parameterization validation study over grassland (Schrader et al., 2016).

The ammonia flux (F_{NH_3}) is inferred from DOAS concentration observations by applying the flux-gradient method, following Eq. 2.1.

$$F_{NH_3} = -K_{NH_3} \frac{\partial NH_3}{\partial z} \approx -K_{NH_3} \frac{\Delta NH_{3\ obs}}{\Delta z_{obs}} \tag{2.1}$$

Here $\frac{\Delta NH_{3\ obs}}{\Delta z}$ is the observed concentration gradient and K_{NH_3} is the eddy diffusion coefficient for NH_3. We parameterize K_{NH_3} similar to the diffusion coefficient of heat, using Monin-Obukhov similarity theory including the stability effects, which depends on the intensity of turbulent mixing resulting from the sonic anemometer observations. K_{NH_3} is determined using Eq. 2.2,

$$K_{NH_3} = \frac{ku_*z}{\phi_{NH_3}(z/L)} \tag{2.2}$$

where k is the von Karman's constant (assumed $k = 0.4$), u_* is the observed friction velocity, z is the height above the displacement height d, defined by 2/3 of the canopy height. The atmospheric stability effects are taken into account by $\phi_{NH_3}(z/L)$, the dimensionless flux-gradient relationship as a function of z/L, where L is the Obukhov length. For the flux-gradient relationships, we use the commonly used Businger-Dyer relationships (Dyer and Hicks, 1970).

To derive F_{NH_3}, we vertically integrate the gradients of Eq. 2.1 to obtain Eq. 2.3.

$$F_{NH_3} = \frac{-u_*k\ (NH_{3,\ 2.36\ m} - NH_{3,\ 0.65\ m})}{ln(\frac{z_{2.36\ m}-d}{z_{0.65\ m}-d}) - \Psi_{NH_3}(\frac{z_{2.36\ m}-d}{L}) + \Psi_{NH_3}(\frac{z_{0.65\ m}-d}{L})} \tag{2.3}$$

We use $z_{0.65\ m}$ and $z_{2.36\ m}$ to represent the height of the NH_3 concentration measurements, with a displacement height d of 0.07 m, and Ψ_{NH_3} represents the integrated flux-gradient relationship for ammonia. For the latter, we assume the relation for ammonia to be equal to those of water vapor and heat, following Ψ_h derived by Paulson (1970), based on the Businger-Dyer flux-gradient relationships for unstable conditions ($z/L < 0$). For stable conditions, Ψ_h is derived by Beljaars and Holtslag (1991).

Note that DOAS observes the mass density of ammonia (ρ_{NH_3}), in µg m^{-3}. We convert the DOAS observations following Eq. 2.4 as the model solves chemical species as molar fraction.

Table 2.1: Filter criteria for clear-sky summer conditions, applied to meteorological and DOAS NH$_3$ observations for the months May up to and including August of 2013.

Filter	Criterion	Acceptance [%]	[hours]
Unfiltered observations	-	100%	2952
DOAS intercalibration	*Exclude*	74%	2172.5
DOAS signal intensity (Xe)	$Xe > 15{,}000$ counts	47%	1402
NH$_3$ $_{obs}$ error: $\begin{array}{l} \text{NH}_3\,_{obs} < 20 \text{ µg m}^{-3} \\ \text{NH}_3\,_{obs} \geq 20 \text{ µg m}^{-3} \end{array}$	$\begin{array}{l} \sigma_{NH_3} < 0.3 \text{ µg m}^{-3} \\ \sigma_{NH_3} < 0.015\, NH_3\,_{obs} \end{array}$	47%	1384
Net radiation (Q_n)	$Q_n > 0$	30%	888
Atmospheric stability	$z/L < 0$	21%	606.5
Sunshine duration $t_{sunshine}$	$t_{sunshine} > 1350\ s/1800\ s$	9%	267

$$NH_{3,v} = \frac{V_{STP}}{M_{NH_3}}\ \frac{T}{T_{STP}}\ \frac{p_{STP}}{p}\ \rho_{NH_3} \qquad (2.4)$$

Here NH_3 $_v$ is the NH$_3$ molar fraction in ppb, T is the observed temperature and p is the observed pressure. The other variables are constants for the molar mass of NH$_3$ (M_{NH_3} = 17.03 kg kmol^{-1}), volume of air at Standard Temperature and Pressure (V_{STP} = 22.4 m^3), standard temperature (T_{STP} = 273.15 K) and standard pressure (p_{STP} = 101.325 10^3 Pa). In this Chapter, we show the NH$_3$ flux in µg m^{-2}s^{-1} for the sake of interpretation and consistency with literature.

2.2.3   Data filtering

We apply several filter criteria to the observations, shown in Table 2.1. As we are interested in the interaction between processes spanning various spatio-temporal scales, we aim to study the budget under meteorological conditions in which the local land-atmospheric conditions are dominant. Therefore, we focus in this study on the ammonia budget under typical clear-sky summer conditions, i.e. the months of May to August.

We first filter the DOAS observations to ensure high quality measurements. To this end, we only consider observations from 2013, because of the high data availability and quality compared to other years. Intercalibration measurements are excluded as well, as no NH$_3$ flux can be inferred from these observations. A minimum DOAS signal intensity is required to assure high quality concentration measurements. Note that these optical measurements are sensitive to meteorological conditions which can obstruct the open path and lead to a significant reduction of signal intensity, e.g. rain or (shallow) fog events which are particularly common in the Netherlands (Izett et al., 2018). Furthermore, we filter out NH$_3$
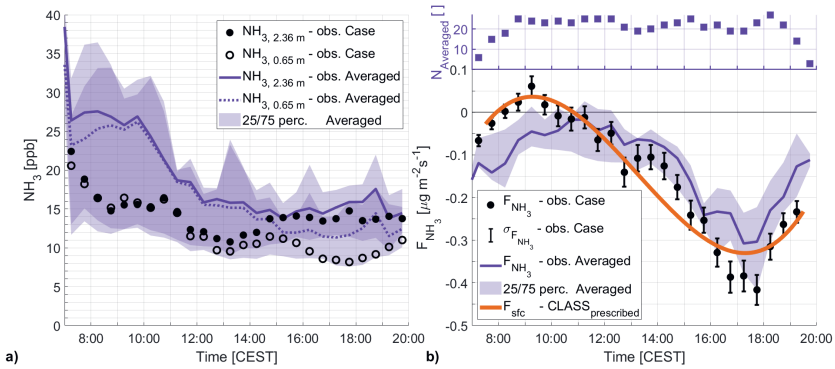
Figure 2.2: The diurnal variability of the ammonia molar fraction observations (a) and ammonia surface flux (b). Uncertainties for the molar fraction observations are smaller than the symbols. Case observations of 8 July 2013 are shown in black and the multi-day Averaged Summer Day observations are shown as a purple line, with their respective 25/75 percentile shown as purple shading. Atop the NH$_3$ flux, we display the N number of observations over which the average is taken to construct the Averaged Summer Day. A third degree polynomial fit to the Case NH$_3$ flux, used in the CLASS$_{prescribed}$ experiment, is shown in orange.

concentration measurements with a standard deviation over 0.3 µg m^{-3} for concentrations below 20 µg m^{-3}, or over 1.5% of concentrations over 20 µg m^{-3}. After these DOAS quality filters, 47% of all observations from May to August remain.

Secondly, we filter the observations for the meteorological conditions required to perform this case-study. We characterize typical summer conditions by a convective boundary layer and clear skies. Three criteria are set up to find observations under these conditions. We first filter the data for convective conditions with two criteria: positive net radiation ($Q_n > 0$) and a negative Monin-Obukhov stability parameter ($\frac{z}{L} < 0$). The remaining 21% of the data is filtered for clear-sky conditions, using the sunshine duration observations of a CSD3 Sunshine Duration Sensor (Kipp & Zonen, Delft, Netherlands) at Veenkampen. Here, we apply a minimum sunshine duration of 22.5 minutes per 30 minutes. After filtering, 9% of the available observations remain, i.e. 267 hours. When one considers a 12 period hours per day for which these criteria are met, this translates to about 22 days of observations.

2.2.4 Representing a prototypical convective boundary layer

The selection of the single day for the case-study, representative of typical summer day conditions, requires one additional criterion: full data coverage from sunrise to sunset ($Q_n > 0$). Out of the remaining four complete days (not shown), 8 July 2013 is selected as our Case, because of the low variability in wind direction (not shown) and because the main surface and boundary-layer characteristics follow a representative situation of convective

summer conditions. Case observations of boundary layer height (h), potential temperature (θ) and specific humidity (q) are discussed in Section 2.3.1. The observed NH_3 molar fraction and surface flux are shown in black in Fig. 2.2. The observed diurnal variability of the molar fraction of our Case is characterized by high values in the early morning, followed by a rapid decrease. The molar fraction temporarily levels with a possible local maximum between 8:00 and 11:00 CEST, after which the molar fraction rapidly decreases again. Between 13:00 and 19:00 CEST, the molar fraction stabilizes at approximately 12 ppb. Note that the vertical NH_3 molar fraction gradient significantly increases between 12:00 and 19:00 CEST.

The Case observed NH_3 flux in Fig. 2.2b, where a negative flux represents deposition, also shows a clear distinction between the morning and afternoon. From 7:00 to 12:00 CEST, both low deposition and low emission are observed. As a result of the increasing NH_3 gradient, a large negative flux is found between 12:00 and 19:00 CEST, peaking around 17:30 CEST.

In addition to our single day Case, we find this observed diurnal variability in multiple convective conditions. In short, we analyze 267 hours of filtered data to calculate the average diurnal variability for clear-sky summer days. The NH_3 molar fraction and surface flux of this representative "Averaged Summer Day" (purple lines) are shown in Fig. 2.2. Here we find that the Case observed molar fraction (black) is within the 25 and 75 percentile of the Averaged Summer Day (purple shading). Note that, while the Case observations are in the lower end of the spread, both the Case and the Averaged Summer Day follow a similar diurnal pattern. In Fig. 2.2a, a strong decrease in the NH_3 molar fraction in the morning, as well as a clear vertical gradient between 12:00 and 19:00 CEST, are found for both sets of observations. Considering the NH_3 surface flux in Fig. 2.2b, the Case observed flux is shown to be partly outside the rather small 25/75 percentile spread of the Averaged Summer Day. Again, the same subdaily pattern of low deposition/emission in the morning and high deposition in the afternoon is found for both the sets of observations. We therefore conclude that the results presented in this study can be generalized to cloudless convective conditions, characterized by weak large-scale forcing.

2.2.5 Model description

The Chemistry Land-surface Atmosphere Soil Slab (CLASS) model (Vilà-Guerau de Arellano et al., 2015) is a convective boundary layer model used to support the interpretation of the observations. With CLASS, we aim to integrate the processes that drive the diurnal variability of NH_3 concentration and flux. We represent and connect all relevant processes to the boundary layer ammonia budget of Fig. 2.1 in order to identify their respective influences.

CLASS solves the surface-atmosphere exchange using five interacting layers: the mixed-layer, the atmospheric surface layer, the surface, the top soil layer and the deep soil. It is in the well-mixed layer that the model describes the state conserved boundary layer variables, which include meteorological variables and chemically active species (Ouwersloot et al., 2012). The surface layer, the bottom 10% of the CBL, connects the mixed-layer to the surface. Parameterization of surface characteristics is done at the infinitesimally thin surface. Using moisture exchange (latent heat) as an example, three parallel paths are parameterized: soil evaporation, liquid water (dew) evaporation and vegetation evapotranspiration. The latter follows the A-g_s approach (Ronda et al., 2001), where the A represents the photosynthesis process and g_s represents the stomatal conductance of carbon dioxide/water at canopy level. While the top soil layer also directly interacts with the atmosphere, the deep soil layer mainly acts as reservoirs of heat and moisture, only interacting with the top soil layer. These layers are coupled, i.e. actively solved by the model and only require initial values.

CLASS assumes the boundary layer to be well-mixed, requiring the same well-mixed conditions for which we filter the observations in Section 2.2.3. It allows us to describe atmospheric and chemical variables as a bulk model in which quantities are approximately constant with height without losing representativeness.

In order to describe any quantity $\psi(t,x,y,z)$ as a bulk variable, several assumptions are required. First, we assume the CBL flow to have horizontally homogeneous properties for all variables: $\psi(t,x,y,z) \approx \psi(t,z)$. Secondly, the mean vertical velocity within the CBL is assumed to be zero: $\overline{w} \approx 0$, i.e. we only account for the vertical turbulent flux $(\overline{w'\psi'})$. Finally, there is the assumption that thermodynamic variables are well mixed in convective conditions and are therefore approximately constant with height. It allows us to represent any variable in the whole vertical domain with a single value, the bulk value, by integrating with height: $\psi(t,z) \approx \langle\psi(t)\rangle$. With these assumptions, we can describe the temporal evolution of $\langle\psi\rangle$ with Eq. 2.5.

$$\underbrace{\frac{\partial\langle\psi\rangle}{\partial t}}_{Storage} = \underbrace{\frac{1}{h}\left(\overline{w'\psi'}\right)_s}_{SFC} - \underbrace{\frac{1}{h}\left(\overline{w'\psi'}\right)_e}_{ENT} + \underbrace{\langle adv\rangle}_{ADV} + \underbrace{\langle chem\rangle}_{CHEM} \tag{2.5}$$

Here, $(\overline{w'\psi'})_s$ and $(\overline{w'\psi'})_e$ describe the turbulent fluxes at the surface and entrainment at the top of the CBL. Additional changes to $\langle\psi\rangle$ can result from advection (ADV) and chemical transformations (CHEM). Other sources and sinks can be added to Eq. 2.5 similar to these last two terms. In order to resolve the evolution equation, we require parameterization of the turbulent entrainment flux $(\overline{w'\psi'})_e$ (Eq. 2.6 and 2.7).

$$\left(\overline{w'\psi'}\right)_e = -w_e\Delta\psi = \left(\frac{\partial h}{\partial t} - w_s\right)\Delta\psi \tag{2.6}$$

$$\frac{\partial \Delta \psi}{\partial t} = \gamma_\psi \left(\frac{\partial h}{\partial t} - w_s \right) - \frac{\partial \langle \psi \rangle}{\partial t} \tag{2.7}$$

In Eq. 2.6 and 2.7, w_e represents the entrainment velocity, i.e. the exchange velocity between the CBL and the free troposphere (FT), w_s represents the subsidence velocity resulting from large scale synoptic weather, Δ_ψ represents the infinitely small inversion layer at the top of the CBL: $\Delta_\psi = \psi_{FT} - \psi_{CBL}$. Finally γ_ψ represents the lapse rate of ψ. The entrainment velocity is related to the growth/decline of the CBL ($\frac{\partial h}{\partial t}$), which specifically depends on the virtual potential temperature (θ_v). This is shown in Eq. 2.8, where β is the ratio of the entrainment to the surface buoyancy flux, for which we use $\beta = 0.2$ as closure assumption (Stull, 1988).

$$\frac{\partial h}{\partial t} = \frac{\beta \left(\overline{w'\theta'_v} \right)_s}{\Delta \theta_v} + w_s \tag{2.8}$$

With these four equations, the CLASS model is used to integrate the evolution with time of atmospheric ammonia ($\psi = NH_3$), or any meteorological, chemical or tracer variable.

2.2.6   Research design

The combination of the CLASS model and the DOAS NH_3 observations allows us to design a two-experiment approach to study the diurnal variability of the ammonia budget and the individual contributions of the four governing processes of Eq. 2.5. These numerical experiments only differ in their representation of the surface exchange process (SFC). In the first experiment, named CLASS$_{prescribed}$, we fully control the surface exchange by prescribing the NH_3 surface flux to the model (F_{sfc}) following a third order polynomial fit to the DOAS observed surface flux (F_{NH_3}), shown in orange in Fig. 2.2b. Here the flux is decoupled from the surface conditions. This experiment allows us to quantify the contributions of each process to the temporal evolution of $\langle NH_3 \rangle$, i.e. changes in the NH_3 storage term of Eq. 2.5.

In the second numerical experiment, we release our control on the NH_3 surface exchange and couple the surface flux to the diurnal variability of the state variables. For this purpose, the model uses the DEPosition of Acidifying Compounds (DEPAC) v.3.11 parameterization (van Zanten et al., 2010; Wichink Kruit et al., 2010b). With this second experiment, named CLASS$_{DEPAC}$, we aim to evaluate the performance of the parameterization against the DOAS observations.

The representations of the remaining three budget processes are the same for both experiments. Entrainment (ENT) depends on boundary layer growth ($\frac{dh}{dt}$) and the free tropospheric ammonia molar fraction ($NH_{3,\ FT}$). While $\frac{dh}{dt}$ is constrained by ceilometer observations at Cabauw, $NH_{3,\ FT}$ requires estimation as observations are lacking. Similarly,
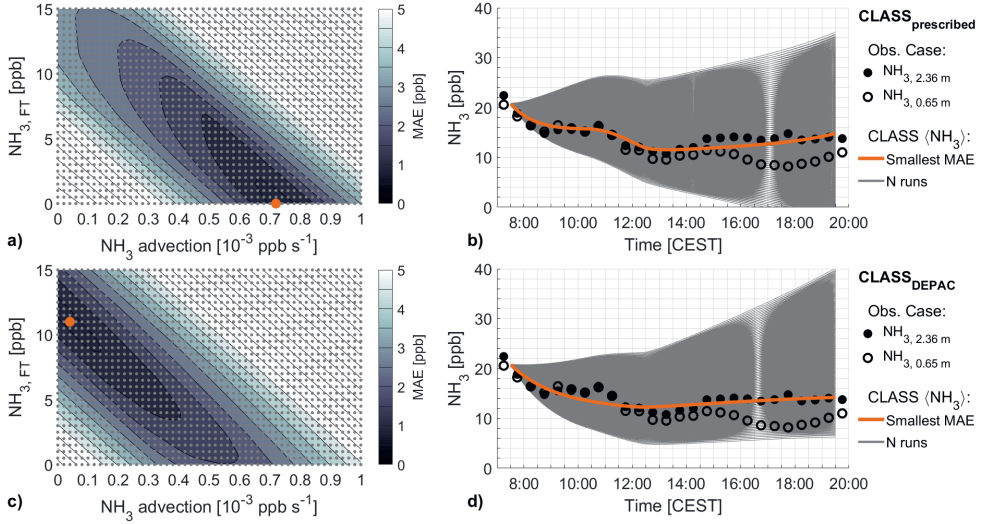
Figure 2.3: The results of the systematic estimation of the initialization of $NH_{3,\ FT}$ and advection for the $CLASS_{prescribed}$ experiment (a and b) and $CLASS_{DEPAC}$ experiment (c and d). The sensitivity of $\langle NH_3 \rangle$ to these variables by ways of the MAE with respect to the observed $NH_{3,\ 2.36\ m}$ is shown left (a and c). The modeled $\langle NH_3 \rangle$ of each individual combination is shown shown right (b and d). Results of the individual runs are shown in grey, with the smallest MAE combination shown in orange. The experiments are initialized with the $NH_{3,\ FT}$ and advection resulting in the smallest MAE.

advection (ADV) requires estimation due to a lack of observations. In this study we prescribe advection to CLASS as a constant forcing term, as a first order estimate. Finally, chemical transformations (CHEM) are solved by implementing the ISORROPIA version 2 thermodynamic equilibrium model (Fountoukis and Nenes, 2007). ISORROPIA2 provides the equilibrium molar fractions in the ammonium-nitrate-sulfate system, which are sensitive to the atmospheric temperature and relative humidity. We account for the equilibrium time by calculating the new molar fraction following Eq. 2.9.

$$\frac{\partial \langle NH_3 \rangle}{\partial t} = \frac{NH_{3,\ eq} - \langle NH_3 \rangle}{\tau_p} \tag{2.9}$$

Here, $NH_{3,\ eq}$ is the equilibrium molar fraction from ISORROPIA2 in ppb and τ_p is the partitioning time scale, set to 1800 seconds (30 minutes) (aan de Brugh et al., 2013; Barbaro et al., 2015; Guo et al., 2018). We initialize our model with a total amount of ammonia/ammonium, nitrate and sulfate in the boundary layer by only initializing these species in the gas phase following aan de Brugh et al. (2013), shown in Table 2.B1 of Appendix Appendix 2.B. At the very first time step (not shown), the model finds the

gas-aerosol equilibrium. For the remaining simulation time, both gaseous NH_3 and NH_4^+ aerosols are simulated and the partitioning time is applied.

We perform a systematic estimation of the initial conditions of $NH_{3, \text{ FT}}$ and advection, by studying the sensitivity of the modeled mixed layer molar fraction ($\langle NH_3 \rangle$) to these two variables. We vary $NH_{3, \text{ FT}}$ and advection and compare the modeled $\langle NH_3 \rangle$ to the observed molar fraction at 2.36 m ($NH_{3, \text{ 2.36 m}}$) by calculating the Mean Absolute Error (MAE) between the two. The combination of $NH_{3, \text{ FT}}$ and advection with the smallest MAE will be used to initialize the CLASS model. In doing so, we aim to find the best initial conditions in absence of measurements. The process is repeated for both the CLASS$_{\text{prescribed}}$ and CLASS$_{\text{DEPAC}}$ experiment, as any change in the representation of the surface exchange could potentially lead to a different result. Figure 2.3 shows both the resulting MAE (left) and each resulting $\langle NH_3 \rangle$ (right) for both the CLASS$_{\text{prescribed}}$ (a and b) and the CLASS$_{\text{DEPAC}}$ (c and d) experiment. These results are interpreted in Sections 2.3.2 and 2.3.3. The initialization of both CLASS$_{\text{prescribed}}$ and CLASS$_{\text{DEPAC}}$ can be found in Table 2.B1 of Appendix Appendix 2.B.

2.3 Results

2.3.1 Model performance

Figure 2.4 shows the observed and modeled boundary layer height (h), specific humidity (q), potential temperature (θ) and modeled entrainment velocity (w_e) between 9:30 CEST and 19:30 CEST, i.e. convective conditions ($Q_n > 0$). It shows that CLASS represents these main characteristics of the boundary-layer dynamics well, as the model output closely resembles the observations.

We take a closer look at the boundary layer height in Fig. 2.4a. To achieve a good representation of the boundary layer growth, the model is initialized with three atmospheric regimes based on both radiosonde and ceilometer observations: the initial inversion layer, the residual layer and the free troposphere. The transitions between each regime is highlighted with A at 400 m and with B at 700 m. Each regime is characterized by its own lapse rate for heat (γ_θ) and moisture (γ_q), which can be found in Table 2.B1. As a result, each regime is characterized by a different rate of boundary layer growth. This is best visualized by the entrainment velocity (w_e) from Eq. 2.6, shown in Fig. 2.4c. Here we find a rapid velocity increase from the moment h reaches the residual layer at 400 m (A). Boundary layer growth, and entrainment velocity with it, slows down when h reaches the free troposphere at 700 m (B). These different regimes allow us to make a distinction between the morning with an actively developing boundary layer until 12:21 CEST (B) and the afternoon where boundary layer growth slows down.
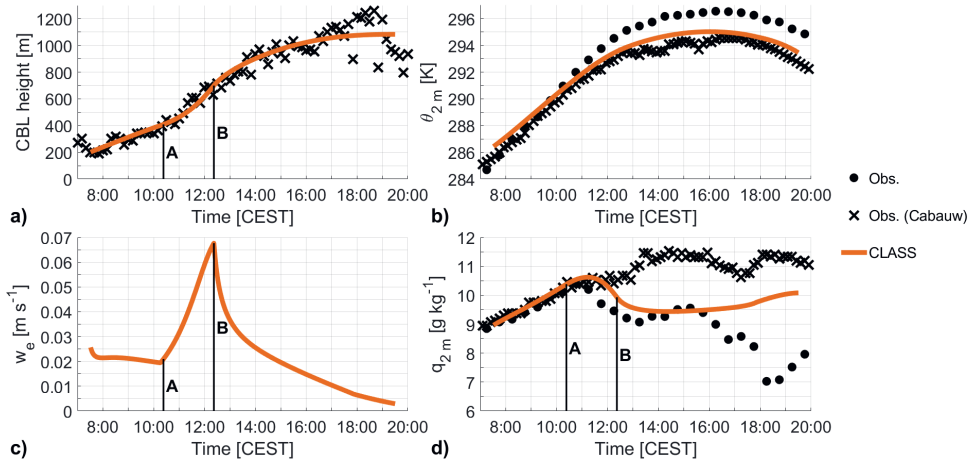
Figure 2.4: The Case observed (black) and modeled (orange) diurnal cycle of the CBL height (a), potential temperature (b), entrainment velocity (c) and specific humidity (d). Highlighted are the moments the boundary layer height reaches the top of the transitional layer (A) and residual layer (B).

When inspecting the modeled 2 m potential temperature in Fig. 2.4b, we see that it follows the observations quite well. The model underestimates the maximum 2 m θ by 2 K when compared to Veenkampen observations and overestimates the more western Cabauw observations by 1 K. A temperature difference between the two locations is expected, as the west of the Netherlands is generally cooler in summer due to the influence of the North Sea. Overall, θ is well represented by the model, considering that h is constrained by observations at Cabauw and De Bilt, west of Veenkampen.

Moisture acts on a more local scale than temperature, as it highly depends on the local vegetation and soil conditions. This is clearly shown by the observed specific humidity at Veenkampen and Cabauw in Fig. 2.4d. While the pattern of the temperature is similar for both locations, the humidity observations only agree until 11:00 CEST, after which the specific humidity decreases at Veenkampen. Note that our boundary conditions lead to a drying of the CBL driven by entrainment. A sharp decrease of over 1 g kg^{-1} in q is observed at 18:00 CEST, as well as a collapse of the CBL at 18:30 CEST. These features are not well reproduced by the model as they are a likely a result of changes in synoptic weather, e.g. a sea breeze effect or a weak cold front as seen on the synoptic weather map for 8 July 2013 (https://www.knmi.nl/nederland-nu/klimatologie/daggegevens/weerkaarten). The disagreement between the modeled and the observed specific humidity can have a small impact on the chemical gas-aerosol equilibrium, as it is sensitive to changes in relative humidity. The disagreement can also have a minor impact on the magnitude of the parameterized NH$_3$ flux, as DEPAC follows

a resistance based modeling approach with surface resistances being sensitive to changes in humidity (Appendix Appendix 2.A).

2.3.2   Experiment 1: The diurnal variability of atmospheric NH$_3$

The satisfactory agreement between meteorological observations and modeling enables us to move on and model the ammonia budget following Eq. 2.5. Figure 2.5 shows the modeled and observed ammonia molar fraction(a), the modeled and observed NH$_3$ flux (b) and the changes in the modeled molar fraction with time of the CLASS$_{prescribed}$ experiment (c) and the CLASS$_{DEPAC}$ experiment (d). Figure 2.5a shows that the modeled molar fraction ($\langle NH_3 \rangle$) closely follows the observations for the CLASS$_{prescribed}$ experiment (solid orange), where the surface flux is prescribed as shown in solid orange in Fig. 2.5b. We place special emphasis on the temporarily leveling of the molar fraction in the observations between 9:00 CEST and 11:00 CEST, as it is a distinct feature of the diurnal ammonia cycle that is well captured by CLASS$_{prescribed}$ and will be discussed later.

CLASS$_{prescribed}$ is initialized with low NH$_{3, FT}$ and high advection, as shown in Fig. 2.3a. The best fit to the top DOAS observations ($NH_{3, 2.36\,m}$), with an MAE of 0.87 ppb, is achieved with NH$_{3, FT}$ = 0.00 ppb and ADV = 0.72 10^{-3} ppb s^{-1}. Such low free tropospheric molar fraction is in line with the findings of Tevlin et al. (2017), who observed that ammonia molar fractions rapidly decreases with height just above the boundary layer in both tower and aircraft observations. While no observations are available on advection, a large positive contribution is in line with our expectations for unfertilized grass-land surrounded by agricultural activities. Large horizontal molar fraction gradients have been observed over only one kilometer from sources (Fowler et al., 1998; Shen et al., 2016; Sommer et al., 2009). However, the horizontal gradient corresponding to the modeled advection, estimated by dividing ADV by the average 10 m wind speed (3.8 m s^{-1}, not shown), is low at 0.19 ppb km^{-1}. This indicates that, even though advection appears to play a significant role in the NH$_3$ budget, the modeled advection most likely represents a background concentration.

With CLASS$_{prescribed}$, we are able to identify the contribution of the four processes governing the NH$_3$ budget at the diurnal scale (Fig. 2.1 and Eq. 2.5). For the CLASS$_{prescribed}$ experiment, these contributions are visualized in Fig. 2.5c, which shows changes in ammonia with time, where negative/positive values represent a decrease/increase in atmospheric ammonia, i.e. a sink/source. When analyzing the overall change in the modeled ammonia molar fraction, i.e. "Storage" in Eq. 2.5, a distinction between the morning and the afternoon can be made, based on boundary layer dynamics. We use the moment that boundary layer growth begins to stabilize as the start of the afternoon, marked by the decrease of w_e at 12:21 CEST (B). In the morning, the negative values for the Storage term in Fig. 2.5c indicate decreasing $\langle NH_3 \rangle$, as shown in Fig. 2.5a. In the afternoon, the positive values indicate an increasing $\langle NH_3 \rangle$. Note that values close to
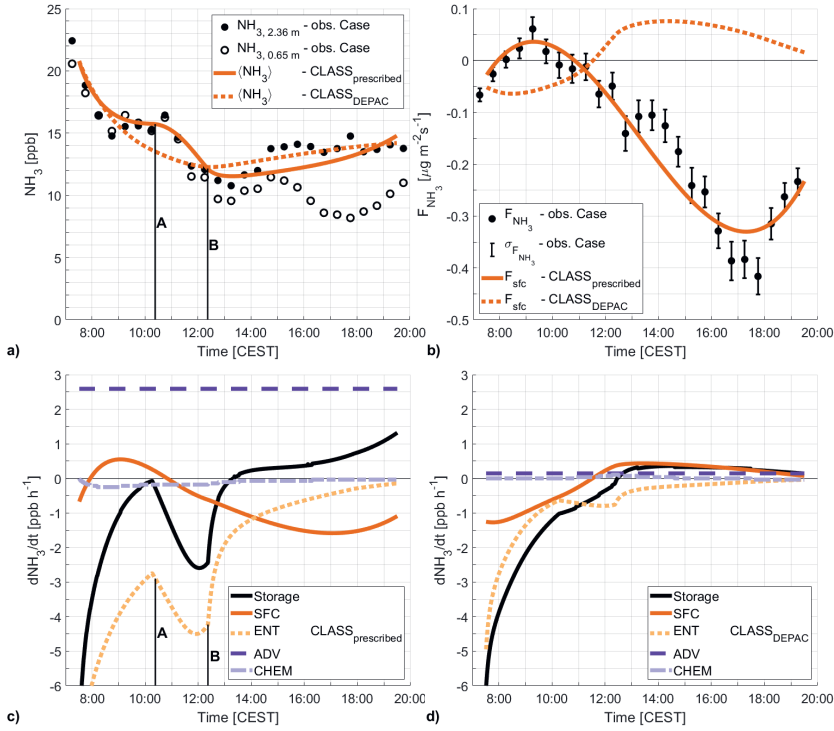
Figure 2.5: The diurnal variability of the observed (black) and modeled (orange) NH_3 molar fraction (a), the observed (black) and modeled (orange) NH_3 surface flux (b) and the contributions of each of the four governing processes to the change in modeled NH_3 molar fraction (Storage) for the $CLASS_{prescribed}$ (c) and $CLASS_{DEPAC}$ experiment (d). The results of the $CLASS_{prescribed}$ experiment are shown as a solid orange line in (a) and (b), with the $CLASS_{DEPAC}$ results shown as a dotted orange line. Highlighted in (a) and (c) are the moments the boundary layer height reaches the top of the transitional layer (A) and residual layer (B).

zero are found in Fig. 2.5c, which coincide with the distinct leveling of the morning molar fraction.

In the morning, until 12:21 CEST, entrainment (ENT) has the largest contribution the ammonia budget. The same can be found in Fig. 2.6a, which shows the averaged contribution of each process in the morning (from 7:30 CEST to 12:21 CEST) in ppb h^{-1}. Here, ENT is the largest sink of NH_3, with -4.28 ppb h^{-1}, being the main cause of the Storage reduction of -1.80 ppb h^{-1}. Advection (ADV) is the largest source of NH_3 in the morning, adding 2.60 ppb h^{-1} to the budget. Both the surface exchange (SFC) and chemical transformations (CHEM) are shown to only play a small role in the morning budget. Note that entrainment is distinctly shaped as a result of its relation to the entrainment velocity, w_e (Equation 2.6). The local absolute minimum and maximum of ENT coincide with the
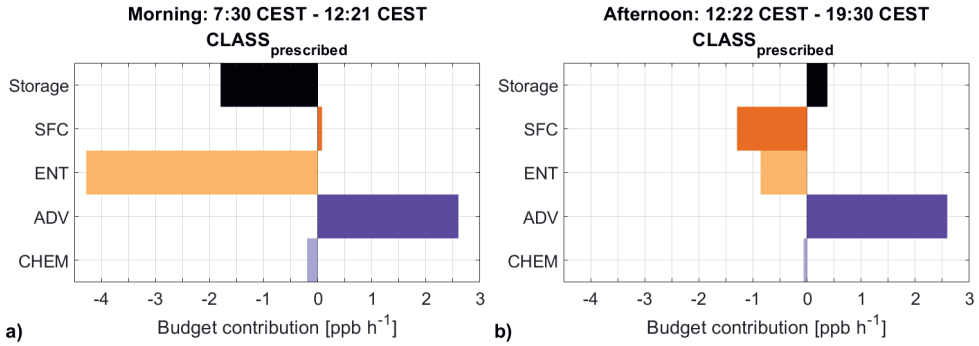
Figure 2.6: The individual contributions of each governing process (Equation 2.5) to the changing NH_3 molar fraction (Storage) of the $CLASS_{prescribed}$ experiment, averaged over the morning (7:30 - 12:21 CEST) and afternoon (12:22 - 19:30 CEST) regimes.

local minimum and maximum of w_e in Fig. 2.4c, highlighted by A and B in both Fig. 2.4 and 2.5. Both the magnitude of ENT and strong visual similarities with the Storage term indicate that entrainment dominates the morning budget.

By analyzing Fig. 2.5c, we can explain the distinct leveling of the NH_3 molar fraction around 10:00 CEST. This distinct feature is a result of changes in the surface exchange and entrainment. While SFC mainly acts as a sink of ammonia by means of deposition, emission is observed in the morning between 8:00 and 11:00 CEST, making the surface exchange a temporary source of NH_3. Additionally, entrainment temporarily weakens around this time, with a local absolute minimum around 10:20 CEST highlighted by A. This weakening of ENT is a result of a slowdown of the boundary layer growth and the rapid decrease of ΔNH_3 (not shown) with decreasing $\langle NH_3 \rangle$ in the early morning. The combination of these two processes are temporarily in balance with the constant advection, resulting in the leveling of the NH_3 molar fraction.

In the afternoon, from 12:22 CEST to 19:30 CEST, several processes play an important role in the variability of the NH_3 molar fraction. Figure 2.5c shows that the contribution of ENT decreases, caused by the slowdown of the boundary layer growth. From 14:00 CEST, SFC becomes the largest sink as the observed deposition peaks in the afternoon. Advection remains the largest, and now only, source of ammonia, as shown in both Fig. 2.5c and 2.6b, with a contribution of 2.60 ppb h^{-1} to the budget. Advection is only partly compensated by the surface exchange and entrainment, which contribute -1.29 and -0.86 ppb h^{-1}, respectively. This results in a small increase in $\langle NH_3 \rangle$ (Storage) of 0.38 ppb h^{-1} on average. Similar to the morning, chemical transformations have a negligible contribution, due to the abundance of ammonia and the high temperature, hampering significant transfer of gaseous NH_3 to aerosols.

2.3.3   Experiment 2: The impact of the NH$_3$ surface exchange on the diurnal variability.

Next, we repeat the previous numerical experiment, but we now release our control on surface exchange. Here, the ammonia surface flux is coupled to the atmospheric diurnal variability, similar to heat and moisture, following the DEPAC parameterization. In short, DEPAC solves the NH$_3$ surface flux following resistance modeling, where resistances are placed between the atmospheric molar fraction and a canopy compensation point (χ_c), i.e. the canopy internal NH$_3$ molar fraction (van Zanten et al., 2010; Wichink Kruit et al., 2010b). Two paths are defined for exchange over grassland: the stomatal and external leaf path. Their path-specific resistances and compensation points are parameterized by DEPAC. A full description of the parameterization for grassland is found in Appendix Appendix 2.A.

Figure 2.5a shows that $\langle NH_3 \rangle$ of the CLASS$_{DEPAC}$ experiment closely follows the observed molar fraction. Here, the model fits the observations more closely in the afternoon, but it is unable to capture the distinct leveling off in the morning. Despite the differences, the performance of the two experiments appears to be similar, with an MAE of 0.91 ppb for CLASS$_{DEPAC}$ compared to 0.87 ppb for CLASS$_{prescribed}$.

Figure 2.5b shows that the parameterized surface flux (F$_{sfc}$) of the CLASS$_{DEPAC}$ experiment does not match the observed F$_{NH_3}$, with F$_{sfc}$ differing in both magnitude and sign. This change in the surface exchange leads to different representations of the other processes, as we tune advection and NH$_{3, FT}$ following our systematic estimation of the initial conditions for the model. CLASS$_{DEPAC}$ is initialized with a high free tropospheric molar fraction, NH$_{3, FT}$ = 11.0 ppb, and low advection, ADV = 0.04 10^{-3} ppb s^{-1} (Fig. 2.3c). The impact of the new SFC on the other processes of the CLASS$_{DEPAC}$ experiment is shown in Fig. 2.5d, showing the strongly reduced advection and weaker entrainment compared to the first numerical experiment. An NH$_{3, FT}$ that is similar in magnitude as the observed afternoon molar fraction does not match the observations by Tevlin et al. (2017) and seems unrealistic, since there are no sources of NH$_3$ outside the boundary layer. Even though the low advection also does not match our expectations, we cannot rule this out as a realistic possibility due to the lack of observations on the process. Based on the mismatch between the observed F$_{NH_3}$ and parameterized F$_{sfc}$, the unrealistic NH$_{3, FT}$ and the unexpected low advection, we conclude that the CLASS$_{DEPAC}$ experiment does not realistically reproduce the atmospheric ammonia budget at the temporal resolution of this study.

Our main explanation for the disagreement on the parameterized F$_{sfc}$ and the observed F$_{NH_3}$ concerns the parameterization of the stomatal compensation point (χ_{stom}) in DEPAC. The contribution of the stomatal path increases in the afternoon as the resistance of the external leaf path increases with decreasing relative humidity (Equation 2.A6 of Appendix Appendix 2.A). Additionally, the stomatal compensation point is related to (leaf) surface temperature, increasing χ_{stom} with the increasing temperatures. In the afternoon, this

leads to an increasing canopy compensation point (χ_c) as well, with temperatures being high and relative humidity being low. Note that F$_{sfc}$ is proportional to the difference between $\langle NH_3 \rangle$ and χ_c. As a result, the parameterized surface flux will always give weak deposition or emission in the afternoon and a deposition peak in the morning, under clear sky convective conditions.

2.4 General discussion

2.4.1 Derivation of the NH$_3$ surface flux from observations

The DOAS setup shows high potential as an optical system to observe the ammonia concentration and flux, therefore eliminating the inlet issues typical of conventional NH$_3$ observations. However, further developments are recommended to improve the quality of the DOAS gradient measurement. The main challenge with this setup is the need for intercalibration of the two sensitive DOAS instruments in the field. The aim of this intercalibration is to match the zero-level and the span of both instruments to an accuracy that the small concentration differences from dry deposition can be observed. The current process requires manual realignment of the two DOAS instruments with respect to their retroreflectors. When manually switching back to flux measurement mode, there still appear to be unresolved issues that could prevent maintaining the zero-offset between the instruments that was just obtained. As a result, there may currently still be an unknown fixed offset between the two instruments. It is therefore possible that the fluxes presented in this study are a minor overestimation or underestimation of the actual NH$_3$ surface exchange.

Inferring fluxes using the flux-gradient method requires several assumption with respect to the surface layer, chemical reactions and horizontal homogeneity. Vilà-Guerau de Arellano et al. (1993) showed for the NO-O$_3$-NO$_2$ system that the flux-gradient relationships become more complex when phase transitions and chemical reactions occur at time scales comparable to that of turbulence, which are typically around 15 - 30 minutes under diurnal conditions (aan de Brugh et al., 2013; Vilà-Guerau de Arellano et al., 2015). The gas-particle interactions of ammonia, particularly with ammonium nitrate, can indeed lead to a divergence of the turbulent diffusion flux. These interactions are related to the temperature and relative humidity, which do have near-surface vertical gradient. During the day, these gradients could potentially lead to outgassing of NH$_3$ from volatile aerosols close to the surface (aan de Brugh et al., 2013; Nemitz et al., 2004a). Nemitz et al. (2004a) concluded that a flux underestimation of 0.02 µg m^{-2}s^{-1} could be representative for Dutch grassland during daytime. We expect this underestimation for our case study to be small, as nearly all ammonium nitrate aerosols are expected to have evaporated due to the high temperatures. When inferring fluxes using the flux-gradient method, one could estimate, and possibly correct for, this effect by observing temperature and humidity

at the individual measurement heights. These new observations can be combined with a thermodynamic equilibrium model, e.g. ISORROPIA2, to calculate a potential molar fraction gradient resulting from NH_3 gas-aerosol interactions.

Additionally, nearby obstacles could disrupt the turbulent flow of air and, depending on wind speed and direction, affect the horizontal homogeneity of the observed gradient as a result, e.g. reeds (Section 2.2.1). Such disruptions are especially relevant for the DOAS measurement setup, as the ammonia molar fractions are measured as the average molar fraction over the 100 m path average NH_3, i.e. twice the 50 m distance to the retroreflectors. In doing so, we additionally assume the vertical NH_3 gradient to be horizontally homogeneous along the path. The potential impact of flow disruptions on the observed flux is difficult to quantify. However, we minimize the impact on the observations presented in this study, as we strictly filter for clear-sky summer condition where wind speeds are low. With less strict filter conditions however, these factors will likely influence the derived surface fluxes.

While these measurement uncertainties and proposed improvements could affect the inferred ammonia flux, the general observed pattern is still expected to remain. This pattern, where a large NH_3 gradient in the late afternoon results in high deposition, is not unique to our single-day Case, but is also found in the Averaged Summer Day observations.

2.4.2   The CLASS model

The CLASS mixed-layer model has proven an effective and inexpensive method to represent key CBL processes. The model was previously used to study the role of boundary-layer dynamics on atmospheric chemistry by Vilà-Guerau de Arellano et al. (2011) and Ouwersloot et al. (2012). Vilà-Guerau de Arellano et al. (2011) additionally compared the model performance to the CBL-averaged values of the Dutch Atmospheric Large Eddy Simulation (DALES) model and concluded that the CLASS performance was reasonably similar to DALES. In this study, the CLASS model proved to be both powerful and flexible in its representation of processes involving (chemical) scalars, e.g. surface-atmosphere exchange, which can be either prescribed or parameterized.

This flexibility comes at the cost of simplifications. The main simplification is the description of atmospheric/tracer variables as a single value for the well-mixed CBL. As a result, the vertical gradient resulting from the gas-aerosol equilibrium of NH_3, which depends on temperature and relative humidity, is not captured by CLASS. These changes in equilibrium mixing ratios were shown to be important for ammonium nitrate mixing ratios (aan de Brugh et al., 2013). However, we again expect the impact on gaseous ammonia to be small due to the high temperatures. Furthermore, CLASS assumes horizontal homogeneity, which possibly does not hold true for ammonia, due to the nearby agricultural activity where very high NH_3 molar fractions are expected. The final major simplification of the model, the infinitely small inversion layer, is expected to only have a minor impact as

well. This simplification mainly affects entrainment, which plays an important role in the morning growth of the CBL and is well represented by CLASS, as shown in Fig. 2.4a. The comparison by Vilà-Guerau de Arellano et al. (2011) also shows that CLASS performs well regarding entrainment and boundary layer growth when compared to the DALES model.

2.4.3 Representation of the NH₃ surface exchange

The process of surface-atmosphere exchange is represented following two different approaches: a prescribed NH₃ flux based on observations (Section 2.3.2) and a parameterized flux following DEPAC (Section 2.3.3). The ability to compare the performance of both approaches is a major advantage of the current strategy. It allows us to evaluate both the DOAS observed flux and the representation of the diurnal variability of the ammonia surface exchange by DEPAC.

DEPAC is well-established as a parameterization and is currently applied in Dutch operational air quality models OPS (Sauter et al., 2018) and LOTOS-EUROS (Manders et al., 2017; Schaap et al., 2008). These models are used in air quality predictions and policy making by the Dutch government, where the long term impact of ammonia on nitrogen deposition is the main focus. Therefore, these models are evaluated as such in literature and focus on yearly averages rather than subdaily scales as studied here. Despite the lack of emphasis on the subdaily time scales, which is the focus of this study, these validation studies still give us some indication of the performance of DEPAC under these prototypical convective conditions.

One of the few validation studies of DEPAC outside operational models is presented by Schrader et al. (2016). Here, the non-stomatal ammonia deposition path of DEPAC is compared to that of Massad et al. (2010), using observations from 5 locations in Europe, including the DOAS setup at Veenkampen. They showed that the performance of both parameterizations strongly differs per measurement site and an overall tendency for DEPAC to overestimate the non-stomatal ammonia deposition. However, only nighttime observations are used in this study as it is assumed that non-stomatal exchange is dominant during the night (Schrader et al., 2016). Furthermore, the observations used by Schrader et al. (2016) are taken over long time periods, e.g. 22 months at Veenkampen, and presented as daily averages. As a result, they mainly focused on the long term representation of NH₃ deposition, even though half-hourly observations are used.

Our study enables us to analyze how diurnal variations of meteorological variables influence the DEPAC model performance. In Section 2.3.3, we explain the mismatch between the DOAS observations and DEPAC, focusing on the parameterization of the stomatal compensation point, χ_{stom}. This stomatal compensation point is related to the emission potential (Γ_{stom}) following $\chi_{stom} = f(T)\Gamma_{stom}$, where $f(T)$ only depends on temperature as shown in Eq. 2.A7 of Appendix Appendix 2.A. Wichink Kruit et al. (2010b) discuss

that Γ_{stom} can be estimated from both bioassay measurements and micrometeorological observations. However, the latter method generally results in Γ_{stom} being a factor 3 higher compared to bioassay estimates in more polluted areas like Veenkampen (see Figure 9 from Wichink Kruit et al. (2010b)). This is supported by Loubet et al. (2002), who found stomatal compensation points for grass (*Lolium perenne*) up to 10 µg m^{-3} right after fertilization, based on bioassay measurements. DEPAC is based on micrometeorological measurements over unfertilized grass (*Lolium perenne*), but the CLASS$_{DEPAC}$ experiment estimates the daily average χ_{stom} to be 24 ppb, or 17 µg m^{-3}, shown in Fig. 2.C3 of the Appendix Appendix 2.C. As a result of this high stomatal compensation point, emission is found in the afternoon of the CLASS$_{DEPAC}$ experiment (2.5b). Such high values for χ_{stom} seem unrealistic, since the Veenkampen grassland site is unfertilized since 1979.

We do recognize that the DOAS observed fluxes are uncharacteristic over grassland in the Netherlands. High deposition up to -0.4 µg m^{-2}s^{-1} has been observed before, but only in the early morning in relation to deposition onto dew droplets (Wichink Kruit et al., 2007). Focusing on the diurnal variability and these convective conditions, large afternoon NH$_3$ gradients, and the resulting deposition fluxes as presented in this study, have not been reported before over grassland and cannot be reproduced by the DEPAC parameterization. Loubet et al. (2012) did observe afternoon deposition of similar magnitude over tritical crop, where emission was expected. Their measurements could only partly be explained by high concentrations of certain acid gases (HNO$_3$ and SO$_2$) leading to high surface acidity. The large afternoon gradient presented here could not be explained by enhanced NH$_3$ deposition due to higher surface acidity (Appendix Appendix 2.A), nor by observational uncertainties or gas-aerosol interactions (Section 2.4.1).

The results presented in this study on the diurnal variability of NH$_3$, as well as differences in χ_{stom} estimations based on micrometeorological or bioassay measurements (Wichink Kruit et al., 2010b), indicate that the mechanisms behind the surface-atmosphere exchange of ammonia are not yet fully understood. This could have significant implications for approaches that incorporate the DEPAC module. It is relevant to note however, that these results on the diurnal variability cannot necessarily be applied directly to longer time scales, e.g. the seasonal variability which is reported on by Wichink Kruit et al. (2010b). We therefore recommend several follow-up studies, including validation of the DEPAC parameterization on longer time scales similar to Schrader et al. (2016), but now taking both the stomatal and the non-stomatal pathway into account. It would also be worthwhile to systematically study the performance of alternative parameterizations on the subdaily variability of the NH$_3$ flux. Finally, we believe systematic observations of the NH$_3$ vegetation-atmosphere exchange, focusing on the diurnal variability and covering different land use types, are required to allow for the development of more accurate parameterizations.
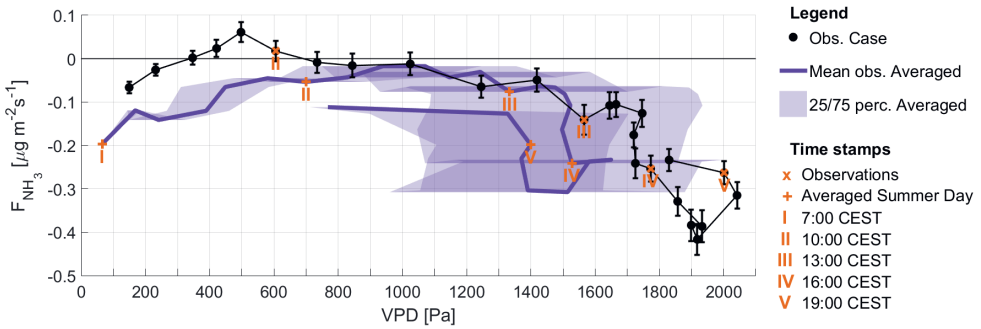
Figure 2.7: The observed NH$_3$ flux against the water vapor pressure deficit plotted for the single-day Case (black) and the multi-day Averaged Summer Day (purple) with corresponding time stamps. Also shown are the uncertainty of NH$_3$ flux observations for the Case (error bars) and the 25 and 75 percentile spread of the Averaged Summer Day observations for the VPD (purple shading).

Related to the strong variability of temperature and therefore on vapor pressure deficit (VPD), new insights on the ammonia surface-atmosphere exchange could be gained by studying its relation to these meteorological variables. Figure 2.7 shows observations of the NH$_3$ flux against the observed VPD. It seems that high deposition is related to the VPD increase in the afternoon. These observations show some similarities to the well-reported diurnal hysteresis between evapotranspiration and the VPD (de Groot et al., 2019; Zhang et al., 2014). Unfortunately, eddy-covariance measurements of the water vapor and CO$_2$ fluxes are not available for this study. Therefore, we are unable to further study the response of vegetation to the meteorological conditions and the potential relation to the ammonia surface exchange. However, these observations indicate that the ammonia surface-atmosphere exchange might be strongly regulated by the response of vegetation to diurnal meteorological conditions.

2.4.4   Representation of NH$_3$ entrainment

Observation and modeling studies showed that entrainment is as important as the surface exchange process in estimating the diurnal budget for moisture and CO$_2$ (Casso-Torralba et al., 2008; Davis et al., 1994; Martin et al., 1988; van Heerwaarden et al., 2009; Vilà-Guerau de Arellano et al., 2004b). Furthermore, scientific studies on ammonium aerosols in the convective boundary layer have been conducted using large eddy simulations (LES), with entrainment being explicitly resolved (Barbaro et al., 2015). However, the role of this process on the diurnal variability of atmospheric ammonia has not yet been studied.

We describe the entrainment flux following Eq. 2.6, based on the modeled boundary layer dynamics (w_e) and the free tropospheric NH$_3$ molar fraction. Observations of free tropospheric ammonia are limited to tower observations and a handful of airborne

campaigns, e.g. Nowak et al. (2010) and Tevlin et al. (2017). In the Netherlands, there have only been campaigns with ammonia measurements at the Cabauw meteorological tower up to 200 m, e.g. Erisman et al. (1988) and Dammers et al. (2017). While valuable, such tower observations are still within the convective boundary layer.

As observations are lacking, we perform a systematic estimation to find the best initial values for $NH_{3,\,FT}$ and the advection, as described in Section 2.2.6. This approach provides us with a robust method for a first estimate of the tropospheric NH_3 molar fraction, while testing the sensitivity of the ammonia budget to this variable. In doing so, $NH_{3,\,FT}$ is assumed to be constant with time and with height. This means that no NH_3 residual layer is simulated, even though radiosonde observations indicate the presence of a residual layer of potential temperature and specific humidity. However, as entrainment is dominant during the morning boundary layer growth, the estimated $NH_{3,\,FT}$ would effectively represent the NH_3 residual layer molar fraction. Therefore, the assumption of constant $NH_{3,\,FT}$ with height could lead to an overestimation of $NH_{3,\,FT}$ in the afternoon.

In order to better understand the role of entrainment on the budget, it would be convenient to observe NH_3 continuously at higher levels (> 100 m), similar to for example CO_2 and methane (CH_4) (Vermeulen et al., 2011). Our understanding of the role of entrainment in the diurnal variability of atmospheric ammonia could be further expanded by modeling studies where turbulent entrainment is explicitly resolved.

2.4.5   Representation of NH_3 advection

In boundary layer studies of atmospheric compounds, advection is generally considered a large-scale forcing term, e.g. for heat and moisture (Ouwersloot et al., 2012; Vilà-Guerau de Arellano et al., 2015) or CO_2 (Vilà-Guerau de Arellano et al., 2004b). For ammonia, it acts on smaller scales (100 m to several kilometers) as the high molar fraction over source areas decreases rapidly with distance (Fowler et al., 1998; Shen et al., 2016; Sommer et al., 2009). Depending on wind direction and source proximity, advection is shown to strongly increase NH_3 molar fractions (Loubet et al., 2012). Operational models do represent long-range advection, but are unable to capture this at sub-kilometer scales, as their typical spatial resolution ranges from 1 x 1 km to 50 x 50 km (Sauter et al., 2018; Schaap et al., 2008; Simpson et al., 2012). Attempts to capture and quantify short-range advection with observations has proven to be very challenging (Aubinet et al., 2010; Mauder et al., 2010). As a result, the representation of advection strongly differs in modeling studies (aan de Brugh et al., 2012; Barbaro et al., 2015; Vilà-Guerau de Arellano et al., 2004b; Vilà-Guerau de Arellano et al., 2011).

In this study, advection is the only term that is not based on observations. Ammonia advection is mainly driven by wind speed and direction, as well as the emission strength of nearby sources. The emission strength of a source is only rarely constant with time, e.g. emissions from organic wastes are related to changes in temperature (Pagans et al., 2006).

We expect such changes to have a negligible impact on the advection at Veenkampen, as the small horizontal NH_3 gradient estimated from the prescribed advection indicates that the NH_3 emitted from nearby sources is already largely diluted when it reaches our site. Additionally, the wind direction during our Case is approximately constant and wind speeds are low. We therefore expect the assumption of constant advection to be valid as a first order estimate.

2.4.6 Representation of NH_3 chemical transformations

Chemical transformations of ammonia between the gas and aerosol phase only play a very small role in this budget study. We represent this process by coupling the ISORROPIA2 thermodynamic model to the CLASS model with a partitioning time (τ_p) of 30 minutes. ISORROPIA2 is used in the operational LOTOS-EUROS model and was used by aan de Brugh et al. (2013), Barbaro et al. (2015) and Guo et al. (2018). The partitioning time is very difficult to derive from in-situ measurements, but the impact on ammonium nitrate formation was studied by aan de Brugh et al. (2013). They presented $\tau_p = 30$ minutes in their main results and the same time scale was later on used by Barbaro et al. (2015) and Guo et al. (2018).

The main source of uncertainty to our representation of the chemical transformation is a lack of observations on both the molar fraction of the relevant gaseous species and on particulate matter molar fractions and its composition. Such measurements, e.g. similar to Meng et al. (2018), could significantly improve our representation of this process. As it stands, we initialize CLASS based on the observations used by aan de Brugh et al. (2013), which were taken under similar fair-weather conditions and with ammonia molar fractions comparable to our Case. Due to the high temperatures and abundance of ammonia in our single-day Case, we expect this uncertainty to only have a minor impact on the modeled ammonia budget.

Further sources of uncertainty come from the bulk model approach of the CLASS model as discussed in Section 2.4.2. The NH_3 gas-aerosol equilibrium moves towards gaseous NH_3 near the surface (high T and low RH) and towards aerosols near the top of the mixed-layer (low T and high RH). We expect that the aerosol molar fraction is slightly overestimated by using a bulk model approach, as the largest vertical gradient of the equilibrium molar fraction is found in the bottom half of the mixed-layer (aan de Brugh et al., 2013).

2.5 Conclusions

To analyze the diurnal variability of atmospheric ammonia (NH_3) over non-fertilized grassland, we perform a case study where we combine multiple observations with the CLASS conceptual boundary layer model. With the model, we disentangle and quantify the

contributions of the four main processes governing the ammonia budget: surface-atmosphere exchange, entrainment, advection and chemical gas-aerosol transformations.

Our approach allows us to specifically addresses the role of the NH_3 surface-atmosphere exchange, by performing two numerical experiments where we vary the representation of this process. We first prescribe the surface flux based on observations and follow up by parameterizing the surface exchange. While both experiments perform similarly in reproducing the observed NH_3 molar fraction, we identify a mismatch between the DEPAC parameterized surface exchange and the observed flux. This leads to an unrealistic representation of the NH_3 budget for the second experiment, e.g. unrealistic high free tropospheric NH_3. The mismatch in the surface flux cannot be explained by the uncertainty of the NH_3 flux observations. This indicates a need for further research in the NH_3 surface-atmosphere exchange. Advancements such as improving the quantification of the stomatal compensation point through both micrometeorological and bioassay observations are recommended.

Based on the combination of the model and observations, our findings are summarized as follows:

- The mixed-layer model accurately reproduces the diurnal variability in the observed NH_3 molar fractions, when prescribing the observed surface flux.

- In the morning, boundary layer dynamics dominate the atmospheric NH_3 variability through entrainment.

- In the afternoon, the atmospheric NH_3 variability is controlled by processes acting on both non-local (advection) and local scales (surface-atmosphere exchange).

- Combining observations with the conceptual CLASS model has proven a powerful tool to both interpret observations and to analyze the performance of parameterizations to the diurnal variability of ammonia.
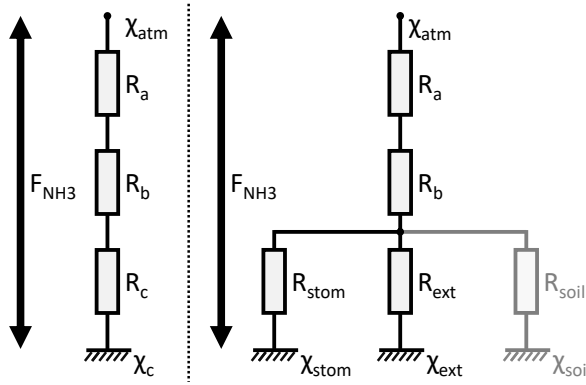
Figure 2.A1: A schematic representation of the DEPAC parameterization resistance model. A simplified representation with a combined canopy resistance and canopy compensation point is shown left. The complete resistance model with the separate deposition/emission paths is shown on the right. The soil path is shown grey as this path is assumed to be negligible for grassland, which is the focus of this study.

Appendix 2.A   DEPAC parameterization for grassland

The DEPAC parameterization module is used in the Dutch OPS model and LOTOS-Euros to calculate the dry deposition of ammonia and other acidifying acids. The module allows for 9 land use types, ranging from grass to coniferous forest and urban areas. Here, we describe the DEPAC modeling approach and the parameterization for grassland.

DEPAC describes multiple deposition pathways following the resistance modeling approach (van Zanten et al., 2010). Here, the deposition/emission flux results from a molar fraction difference ($\Delta\chi$) between the atmosphere ($\chi_{atm.}$) and the canopy at the surface (χ_c) and the resistance between them, i.e. $F = \Delta\chi/R$ equivalent to $I = V/R$ for electric circuits.

The atmosphere is connected to the surface by three resistances in series: two atmospheric resistances (R_a and R_b) and one canopy resistance (R_c), as shown on the left in Fig. 2.A1. The ammonia surface flux (F_{sfc}) is calculated following Eq. 2.A1.

$$F_{sfc} = \frac{\chi_c - \chi_{atm}}{R_a + R_b + R_c} \tag{2.A1}$$

Here, χ_{atm} is the atmospheric ammonia molar fraction, R represents the resistances and χ_c is the canopy compensation point, which represents the internal molar fraction of the canopy surface. Within the canopy, three deposition paths are described by the parameterization, as shown right in Fig. 2.A1. The stomatal path (subscript *stom*) and

the external leaf path (subscript *ext*) describe the atmosphere-vegetation exchange. The third pathway is to soils (subscript *soil*) and describes the atmosphere-soil exchange. The total canopy resistance R_c is calculated as three parallel resistances, following Eq. 2.A2.

$$\frac{1}{R_c} = \frac{1}{R_{stom}} + \frac{1}{R_{ext}} + \frac{1}{R_{soil}} \tag{2.A2}$$

The canopy compensation point is the weighted average of the individual path compensation points, as shown in Eq. 2.A3.

$$\chi_c = \frac{R_c}{R_{stom}}\chi_{stom} + \frac{R_c}{R_{ext}}\chi_{ext} + \frac{R_c}{R_{soil}}\chi_{soil} \tag{2.A3}$$

The first of the atmospheric resistances, the aerodynamic resistance (R_a), describes transport by turbulence and follows Eq. 2.A4.

$$R_a = \frac{1}{k\ u_*} \left[ln\left(\frac{z-d}{z_0}\right) - \Psi_H\left(\frac{z-d}{L}\right) + \Psi_H\left(\frac{z_0}{L}\right) \right] \tag{2.A4}$$

Here, k is the Von Karman constant, u_* is the friction velocity, z is the height above the surface, d is the displacement height, z_0 is the roughness length, L is the Obukhov length and Ψ_H is the integrated stability function for heat of Paulson (1970) and Dyer (1974). The second atmospheric resistance is the quasi-laminar boundary layer resistance (R_b). Turbulent eddies do not penetrate this thin quasi-laminar boundary layer, which is in direct contact with the (canopy) surface. R_b is parameterized following to Eq. 2.A5.

$$R_b = \frac{2}{k\ u_*} \left(\frac{Sc}{Pr}\right)^{2/3} \tag{2.A5}$$

Here, k is the Von Karman constant, u_* is the friction velocity, Sc is the Schmidt number and Pr is the Prandtl's number.

These three deposition pathways are shown left in Fig. 2.A1. The stomatal path and the external leaf path describe the atmosphere-vegetation exchange. The soil pathway describes the atmosphere-soil exchange. For short and dense vegetation, like the grassland canopy used in this study, the single-layer or 'big-leaf' approach is applied and the soil pathway is assumed to be negligible.

Stomatal resistance (R_{stom}) is calculated following the A-g$_s$ approach, as described in Section 2.2.5. The external leaf resistance (R_{ext}) in Eq. 2.A6 is based on the minimum external leaf surface resistance by Sutton and Fowler (1993) and observations at the Haarweg meteorological site by Wichink Kruit et al. (2010b).

$$R_{ext} = \frac{SAI_{Haarweg}}{SAI} \alpha \; exp \left(\frac{100 - RH}{\beta} \right) \tag{2.A6}$$

Here, $SAI_{Haarweg}$ and SAI are the surface area index at the Haarweg and at the to be calculated location, RH is the relative humidity in % and α and β are parameterization constants with $\alpha = 2$ s m^{-1} and $\beta = 12\%$.

The compensation points of both paths are parameterized following Eq. 2.A7, based on the formulation of Nemitz et al. (2001) and Wichink Kruit et al. (2007).

$$\chi_{path} = \frac{2.75 \; 10^{15}}{T_s + 273.15} exp \left(\frac{-1.04 \; 10^4}{T_s + 273.15} \right) \Gamma_{path} \tag{2.A7}$$

Here, T_s is the leaf surface temperature in °C and Γ is the dimensionless molar ratio between NH_4^+ and H^+, or emission potential. Subscript "$path$" indicates the deposition pathway, i.e. the stomatal or external leaf path. The two pathways differ only in their respective Γ parameterizations. For the stomatal deposition path, Γ_{stom} is solved following Eq. 2.A8, as described by Wichink Kruit et al. (2010b).

$$\Gamma_{stom} = 362\chi_{atm, \; 4m, \; long-term} \; 4.7exp \left(-0.071T_s \right) \tag{2.A8}$$

Here, T_s is the leaf surface temperature in °C and $\chi_{atm, \; 4m, \; long-term}$ is the 'long-term' NH_3 molar fraction at four meters height, for which we take the monthly average molar fraction. The external leaf deposition path is parameterized following Eq. 2.A9. The original formulation as described by van Zanten et al. (2010) is expanded with the codeposition factor for enhanced NH_3 deposition in the presence of SO_2, as described in Wichink Kruit et al. (2017).

$$\Gamma_{ext} = F \left(\alpha_{SN} \right) \left[1.84 \; 10^3 \chi_{atm, \; 4m} \; exp \left(-0.11T_s \right) - 850 \right]$$
$$F \left(\alpha_{SN} < 0.83 \right) = 1.10 - 1.32\alpha_{SN} \tag{2.A9}$$
$$F \left(\alpha_{SN} \geq 0.83 \right) = 0$$

Here, T_S is the leaf surface temperature in °C, $\chi_{atm, \; 4m}$ is the atmospheric molar fraction at four meters height and α_{SN} is the molar ratio between annual average SO_2 and NH_3.

Appendix 2.B   Experiment initialization

The CLASS$_{prescribed}$ and CLASS$_{DEPAC}$ numerical experiments are initialized following Table 2.B1.

Table 2.B1: Initialization of the CLASS$_{prescribed}$ and CLASS$_{DEPAC}$ numerical experiments.

Parameter	Symbol	Initial value	
		General	
Start time	t_0		05:30 UTC
End time	t_{end}		17:30 UTC
Step size	Δt		1 s
		Meteorological variables	
CBL height at t_0	$\boldsymbol{z_{0,\,1}}$		**200 m**
Transitional layer height at t_0	$\boldsymbol{z_{0,\,2}}$		**410 m**
Residual layer height at t_0	$\boldsymbol{z_{0,\,3}}$		**700 m**
Wind speed at t_0	u_0		2.0 m s^{-1}
Geostrophic wind speed at t_0	$u_{geo,\,0}$		10.0 m s^{-1}
Flow divergence factor (subsidence)	$wsls$		3 10^{-6} s^{-1}
		Heat ($X = \theta$)	Moisture ($X = q$)
Initialization CBL at t_0	X_0	286 K	8.8 g kg^{-1}
Initialization inversion at t_0	ΔX	0.5 K	0.0 g kg^{-1}
Transition layer lapse rate	$\gamma_{X,\,1}$	0.030 K m^{-1}	-0.005 g kg^{-1}m^{-1}
Residual layer lapse rate	$\gamma_{X,\,2}$	0.005 K m^{-1}	-0.018 g kg^{-1}m^{-1}
Free troposphere lapse rate	$\gamma_{X,\,3}$	0.010 K m^{-1}	-0.005 g kg^{-1}m^{-1}
		Surface properties	
Albedo	A		0.28
Leaf area index	LAI		3.0 (van Tiggelen et al., 2018)
Surface temperature at t_0	$T_{s,\,0}$		289.5 K
Soil temperature top layer at t_0	$T_{soil,\,0}$		292.0 K
Soil temperature deeper soil layer	T_2		282.0 K
Volumetric water content top soil layer at t_0	$w_{g,\,0}$		0.40 m^3 m^{-3}
Volumetric water content deeper soil layer	w_2		0.72 m^3 m^{-3}
Volumetric water content field capacity	w_{fc}		0.75 m^3 m^{-3}
Saturated volumetric water content	w_{sat}		0.80 m^3 m^{-3}
Wilting point	w_{wilt}		0.35 m^3 m^{-3}

<div align="center">**Table 2.B1:** (Continued)</div>

Parameter	Symbol	Initial value	
		Chemical species	
Chemical equilibrium time	τ		1800 s
Long term NH_3 molar fraction	$\chi_{atm,\ long-term}$		15 ppb
		$CLASS_{prescribed}$	$CLASS_{DEPAC}$
NH_3 CBL at t_0	$NH_{3,\ 0}$	27 ppb	27 ppb
NH_3 FT	$\boldsymbol{NH_{3,\ FT}}$	**0.00 ppb**	**11.0 ppb**
NH_3 advection	**ADV**	**0.72 10^{-3} ppb s^{-1}**	**0.04 10^{-3} ppb s^{-1}**
HNO_3 CLB at t_0	$HNO_{3,\ 0}$	3.5 ppb	3.5 ppb
HNO_3 FT	$HNO_{3,\ FT}$	1.0 ppb	1.0 ppb
H_2SO_4 at t_0	$H_2SO_{4,\ 0}$	1.3 ppb	1.3 ppb
H_2SO_4 FT	$H_2SO_{4,\ FT}$	0.0 ppb	0.0 ppb

Appendix 2.C   Supplementary Figures

2.C.1   An alternative initialization of the $CLASS_{DEPAC}$ experiment

The $CLASS_{DEPAC}$ experiment of Section 2.3.3 is now initialized following the initialization for advection (ADV) and the free tropospheric NH_3 molar fraction ($NH_{3,\ FT}$) of the $CLASS_{prescribed}$ experiment of Section 2.3.2 (Table 2.B1). This increases ADV from 0.04 10^{-3} ppb s^{-1} to 0.72 10^{-3} ppb s^{-1} and decreases $NH_{3,\ FT}$ from 11 ppb to 0 ppb. Figure 2.C1 shows the observed and modeled NH_3 molar fraction (a) and flux (b) for this alternative initialization ($CLASS_{DEPAC\ alternative\ init.}$) and the original initialization ($CLASS_{DEPAC}$).

2.C.2   The diurnal variability of the observed NH_3 flux from 2012 to 2015

Figure 2.C2 shows, similar to Fig. 2.2b, the average mean diurnal variability of the observed ammonia flux in the months May up to and including August of 2013 (orange) and 2012 to 2015 (purple). The filter criteria of Table 2.1 were applied to these observations. Solid lines represent the mean diurnal variability, averaged over N number of observations shown above. Note that 2013 contains about half the number of observations (N) of the 2012 - 2015 period. Similar to Fig. 2.2b, the coloured shadings show the 25/75 percentile of each set of observations.
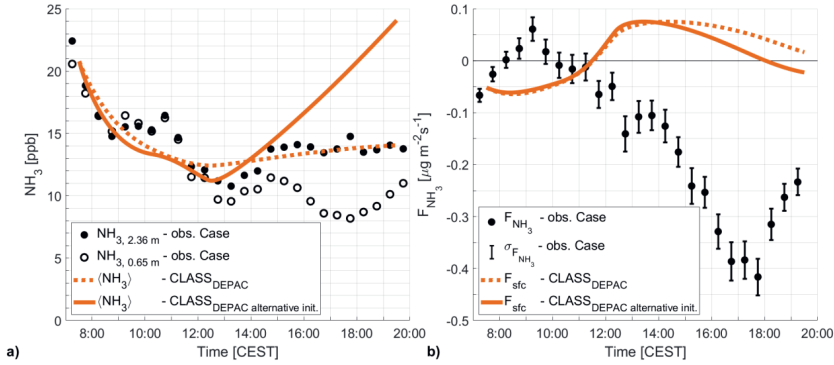
Figure 2.C1: The observed (black) and modeled (orange) NH_3 molar fraction (a) and flux (b). An alternative initialization of the $CLASS_{DEPAC}$ experiment (ADV = 0.72 10^{-3} ppb s^{-1}, $NH_{3, FT}$ = 0 ppb) is shown in solid orange, with the original initialization (ADV = 0.04 10^{-3} ppb s^{-1}, $NH_{3, FT}$ = 11 ppb) is shown in dotted orange as a reference. Note that this alternative initialization is the same as used in the $CLASS_{prescribed}$ experiment.

Note: Figure 2.C2 is based on a dataset which was provided in an earlier stage of the research. Since then, improvements have been made in the processing of the DOAS measurements, which can lead to minor changes in the NH_3 flux.

2.C.3   The DEPAC parameterized canopy compensation points

In Fig. 2.C3a, the observed (black) and modeled (orange) NH_3 molar fraction is compared to the modeled compensation points (purple). The modeled NH_3 flux is proportional to the difference between the modeled molar fraction ($\langle NH_3 \rangle$, orange) and the canopy compensation point (χ_c, solid purple), following Eq. 2.A1, and compared to the observed flux (black) in Fig. 2.C3b. This canopy compensation point is calculated as the average of the stomatal compensation point (χ_{stom}, dotted purple) and the external leaf compensation point (χ_{ext}, dashed purple), weighted by the path specific resistances (not shown), following Eq. 2.A3.
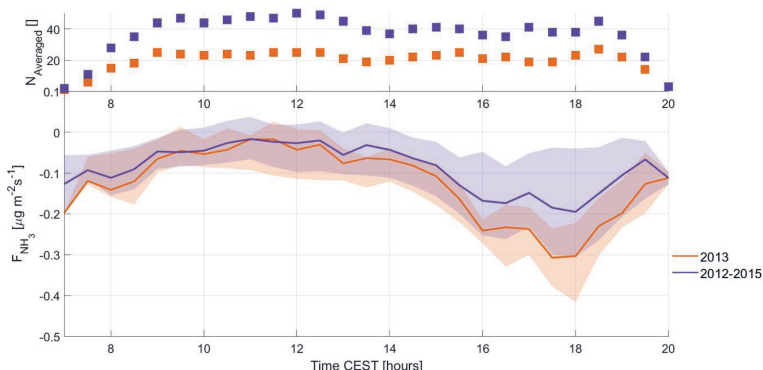
Figure 2.C2: The mean diurnal variability (solid line), with the 25/75 percentile (shading), of the observed NH_3 flux for the months May to August of 2013 (orange) and 2012 to 2015 (purple). The observations for these aggregated diurnal cycles are filtered for high quality DOAS observations and cloudless convective conditions, characterized by weak large-scale forcing (Table 2.1). Atop the NH_3 flux, the N number of observations over which the averages is taken is shown.
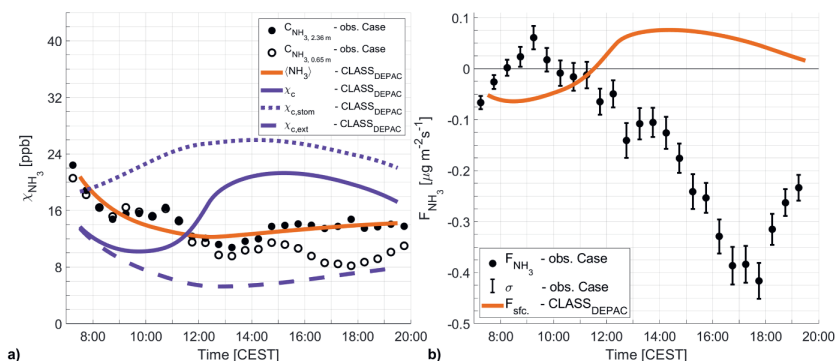
Figure 2.C3: The observed (black) and modeled (orange) NH_3 molar fractions, with the modeled compensation points (purple), (a) and the observed and modeled NH_3 flux (b). The canopy compensation point (χ_c, solid purple) is calculated as the average of the stomatal compensation point (χ_{stom}, dotted purple) and the external leaf compensation point (χ_{ext}, dashed purple), weighted by the path specific resistances (not shown) following Eq. 2.A3.

Chapter 3

Observational relationships between ammonia, carbon dioxide and water vapor under a wide range of meteorological and turbulent conditions: RITA-2021 campaign

Abstract

In this study, we present a comprehensive observational approach, aiming to establish relations between the surface-atmosphere exchange of ammonia (NH_3) and the CO_2 uptake and transpiration by vegetation. These processes are well understood and can lead to new insights in the NH_3 stomatal exchange. The NH_3 concentration and flux are measured using a novel open-path miniDOAS measurement setup, taken during the RITA-2021 campaign at the Ruisdael Observatory at Cabauw, the Netherlands. After filtering for unobstructed flow, sufficient turbulent mixing and CO_2 uptake, we find the diurnal variability of the NH_3 flux to be characterized daytime emissions (0.05 μg m^{-2}s^{-1} on average) and deposition at sunrise and sunset (-0.05 μg m^{-2}s^{-1} on average). We first compare the NH_3 flux to the observed gross primary production (GPP), representing CO_2 uptake, and latent heat flux (L_vE), representing to evapotranspiration. Next we organize the observations following the main drivers of the dynamic vegetation response, based on temperature (T), photosynthetically active radiation (PAR) and the water vapor pressure deficit (VPD). We find strong indications towards stomatal emission of NH_3, with high correlation between the observed emissions and both L_vE (0.70) and PAR (0.72), as well as clear similarities in the diurnal variability of the NH_3 flux and GPP. However, the efforts to establish relationships are hampered due to the amount of diversity of NH_3 sources of the active agricultural region and low data availability after filtering. Still, the results of this study do demonstrate that there is room to find patterns between the high-quality NH_3 observations and fluxes of CO_2 and water vapor.

3.1   Introduction

While nitrogen is an essential nutrient for the growth of plants, acting as a fertilizer, excess nitrogen deposition causes environmental damage and leads to an increased public health risk through the formation of particulate matter (Behera et al., 2013; Bobbink et al., 2003; Erisman et al., 2013; Erisman and Schaap, 2004; Smit and Heederik, 2017). When nitrogen critical loads are exceeded, excess nitrogen deposition threatens biodiversity through acidification and eutrophication of soils. When mitigation of the harmful effects of nitrogen fails, there can be serious political, economic and societal consequences, as demonstrated by the current Dutch nitrogen crisis (Stokstad, 2019). Atmospheric ammonia (NH_3) plays a key role in the deposition of nitrogen, mainly originating from agricultural activity. This is especially true in the Netherlands where NH_3 deposition accounts for about three-quarters of all nitrogen deposition (RIVM et al., 2019; Wichink Kruit and van Pul, 2018).

Efforts to mitigate the harmful effects of nitrogen deposition heavily rely on models representing the concentration and deposition of nitrogen compounds, supported by a network of concentration and surface-atmosphere exchange measurements. The surface-atmosphere exchange in such models is represented by parameterizations, which are developed, validated and improved based on advanced high-resolution observations. In the case of atmospheric ammonia, taking accurate high-resolution measurements is notoriously difficult, due to the reactive nature of gaseous NH_3 causing the gas to "stick" to inlet walls of conventional instruments (Parrish and Fehsenfeld, 2000; von Bobrutzki et al., 2010). These challenges are amplified when measuring the NH_3 surface-atmosphere exchange flux (deposition or emission), where high precision is particularly important (Nemitz et al., 2004a; Whitehead et al., 2008).

Recent developments in advanced instrumental techniques resolve these inlet issues by using optical open-path analyzers. Swart et al. (2023) presents an intercomparison of two novel open-path measurement setups, aimed at measuring the NH_3 flux at half-hourly resolution: the RIVM-miniDOAS 2.2D and the commercial Healthy Photon HT8700E. The two setups showed very similar results, despite being widely different in their measurement principle and approach to derive the flux from concentrations, as the Healthy Photon uses the eddy covariance technique while the miniDOAS applies the flux-gradient method to line average concentration measurements over a 22 m open-path at two heights. In this study, we continue the analysis of the observations of the miniDOAS system presented by (Swart et al., 2023), as the system provides reliable measurements of both the concentration and flux with a high operational uptime.

In a previous study, based on measurements from the predecessor of the miniDOAS system at the Veenkampen meteorological site in the Netherlands, we identified that the mechanisms behind stomatal exchange of NH_3 are not yet fully understood (Schulte et al.,

2021). Here, we continue to study this stomatal exchange pathway by linking the observed NH_3 flux (F_{NH_3}) to photosynthesis, i.e. the stomatal exchange of CO_2 and water vapor (plant transpiration). The similarities between the stomatal exchange of NH_3 and CO_2 have long been recognized (San José et al., 1991; Schrader et al., 2020). However, there are very few parallel measurements of NH_3 and CO_2 fluxes, and research into the two gases is generally conducted by separate scientific communities (Milford et al., 2001). Milford et al. (2001) performed one of the few attempts to develop a simple parameterization for both the CO_2 and NH_3 flux, but was unsuccessful to find such relations for NH_3 as the observed NH_3 flux over Scottish Heathland was dominated by non-stomatal exchange.

In this Chapter, we re-ignite the efforts in linking NH_3 and CO_2 fluxes to further our understanding of NH_3 stomatal exchange. Utilizing the recent developments in NH_3 measurement techniques, we combine the high-quality miniDOAS F_{NH_3} observations with measurements of both CO_2 and water vapor fluxes, as well as other meteorological variables. We first describe the observations, after which we link the observed F_{NH_3} to stomatal exchange, with the intention to establish relationships between the stomatal exchange of ammonia and the processes of CO_2 uptake and transpiration by vegetation. As these processes of photosynthesis are well understood, we explore how this understanding can lead to further improving the parameterization of the NH_3 stomatal exchange.

3.2   Characterizing the RITA-2021 campaign observations

3.2.1   Site description and measurement strategy

In September 2021, the Ruisdael Land-Atmosphere Interactions Intensive Trace-gas and Aerosol measurement campaign, known as RITA-2021, took place at the Cabauw Observatory (`https://ruisdael-observatory.nl/cabauw/`). The Cabauw Observatory, one of the 6 sites within the Ruisdael Observatory, is located on flat grassland in the Netherlands (51.971^oN, 4.927^oE), with an average grass height of 0.1 m. The site provides a unique set of surface and upper air observations, matched by only a very few station world-wide. This includes measurements of thermodynamic variables along the 213 m mast, radiation, surface fluxes, clouds and trace gasses. Surface elevation changes are at most a few meters over 20 km and the nearby region is agricultural. An overview of the Cabauw site, the instruments stationed at the site and its 50-years of observations is given in Bosveld et al. (2020).

During the campaign, 48 days of ammonia measurements are taken using the miniDOAS (Differential Optical Absorption Spectroscopy) flux measurement setup (Berkhout et al., 2017), starting on 25 August until 12 October. The measurement setup and more details on the measurement campaign are described in Swart et al. (2023). In short, the miniDOAS
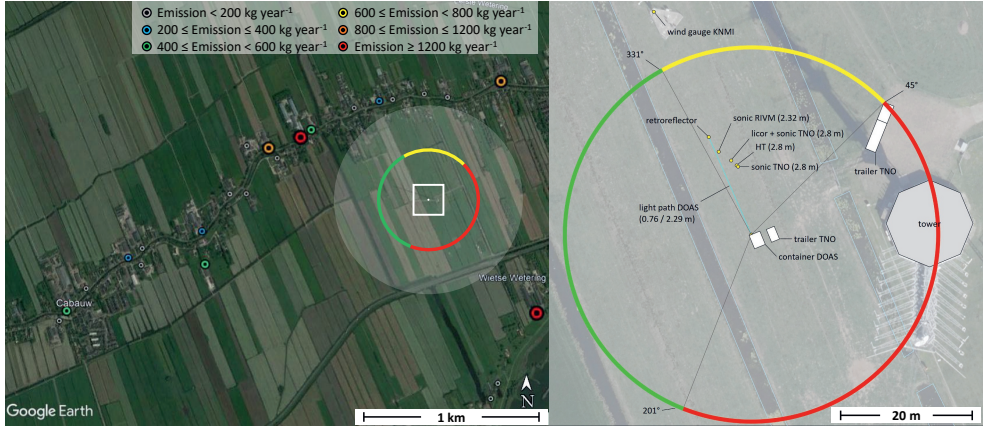
Figure 3.1: The area surrounding the Cabauw Observatory (left) and the setup of the instruments at the measurement site (right). The transparent white circle represents a distance of 500 m from the NH$_3$ measurements and the color coded dots represent the locations of nearby farms, i.e. emission sources of NH$_3$ (Source: Emissieregistratie, www.emissieregistratie.nl, last access 21 January 2022). The colored circle in both panels indicates the wind directions where the airflow towards the miniDOAS light-path is obstructed by either other instruments (yellow) or larger structures (red). (Source left panel: "Cabauw Observatory", 51.971^{o}N, 4.927^{o}E. GOOGLE EARTH, 27 January 2022, Image by Landsat / Copernicus. Source right panel: Swart et al. (2023), modified)

is an optical instrument, measuring the line average concentration (mass density) over a 22 m open path from instrument to its retroreflector. The 30 minute average NH$_3$ concentrations have an accuracy of 0.01 μg m^{-3}. The flux measurement setup uses two miniDOAS instruments, which measure the concentration over parallel paths at different heights, i.e. 0.76 m and 2.29 m respectively. F$_{NH_3}$ is then inferred using the flux-gradient method, based on the Monin–Obukhov similarity theory (Moene and Van Dam, 2014). The flux-gradient method combines the observed vertical NH$_3$ gradient with turbulent measurements of a sonic anemometer (model Gill WindMasterPro^{TM} Gill Instruments, Lymington, UK) (Nemitz et al., 2004a; Schulte et al., 2021; Wichink Kruit et al., 2007; Wyers et al., 1993).

The measurement field and its surroundings are shown in Fig. 3.1. The miniDOAS light paths are aimed in north-northwestern direction (right panel) to ensure unobstructed flow for wind coming from the west, which is the dominant wind direction in the Netherlands. North of the light path, shown in yellow in Fig 3.1, the flow of air is obstructed by several instruments, including the aforementioned sonic anemometer. To the east and south, the airflow is obstructed by a trailer, the 213 m high meteorological tower and the container which houses the miniDOAS instruments. The unobstructed region west of the

Table 3.1: Filter criteria with the filter acceptance rates (in percentages and hours).

#	Filter	Criterion	Acceptance [%]	[hours]
-	Unfiltered observations	-	100%	1152
Discard 1:	miniDOAS intercalibration	-	65%	746
Discard 2:	Fertilization events 11 - 12 September	-	61%	698
Filter 1:	Wind direction	$331^o \geq U_d \geq 201^o$	16%	188
Filter 2:	Rain duration	$t_{rain} \leq 5\ min$	16%	179.5
Filter 3:	Turbulent mixing	$u_* > 0.1\ ms^{-1}$	13%	151
Filter 4:	Gross primary production	$GPP > 0\ mgCm^{-2}s^{-1}$	11%	123.5
Filter 5:	Incoming short-wave radiation	$SW_{in} > 10\ Wm^{-2}$	9%	102

measurement field, is mainly characterized by actively managed agricultural grassland and the small town of Cabauw (about 750 inhabitants), as shown left in Fig. 3.1. Several farms can be seen northwest and west of the measurement field, with varying emission strengths up to over 1200 kg NH$_3$ year^{-1}. Sheep and cattle graze on these agricultural fields, which are actively maintained and fertilized. These activities were not documented and sporadic fertilization events do affect the NH$_3$ measurements, as will be discussed later.

3.2.2   Data filtering

We apply several filter criteria to the RITA-2021 observations, which are shown in Table 3.1 with acceptance rates for each individual filter criterion. The miniDOAS flux setup requires several days of intercalibration measurements, as described in Swart et al. (2023). No ammonia flux can be inferred from these intercalibration measurements, leaving 65% of the campaign observations suitable for flux measurements. We furthermore discard observations from 11 - 12 September, as these NH$_3$ emission fluxes are outliers with respect to the average observed NH$_3$ flux, indicating towards a fertilization event in close proximity to the measurement site.

The remaining measurements are processed by applying 5 filters in total. The use of the flux-gradient method requires unobstructed upwind air flow with sufficient turbulent mixing. Figure 3.1 shows that the instruments were positioned anticipating winds from the south-west (green), with the obstacles located east (red) and north (yellow) of the miniDOAS optical path. We therefore apply a criterion filtering for wind directions between 201° and 331°. This filter leads to a large reduction data available for analysis, decreasing the available data from 61% to 16% as the prevalent wind direction during the campaign was from the north-east. As a secondary effect of this filter, the available observations are

taken under synoptic weather conditions characterized frontal passages with some rain events. The second filter excludes rain events lasting more than 5 min, as rain droplets can obstruct the light path of the miniDOAS. Finally, sufficient turbulent mixing is one of the main requirements for flux measurement using the flux-gradient method. The third filter therefore requires the friction velocity to have a value of at least 0.1 m s^{-1} (u$_*$ $\geq$ 0.1 m s^{-1}). With these three filters, we ensure the quality of the ammonia measurements, observing the NH$_3$ flux with an accuracy of 0.01 μg m^{-2}s^{-1}.

The fourth and fifth filter criteria focus on the ammonia surface-atmosphere exchange pathways. The NH$_3$ flux follows three pathways: the stomatal pathway, external leaf surface pathway and the soil pathway (Massad et al., 2010; Nemitz et al., 2001; van Zanten et al., 2010). The latter is generally assumed to be negligible for the F$_{NH_3}$ over grass, as the dense vegetation completely covers the soil. The external leaf pathways, represents exchange of ammonia with a thin film of water and leaf surface waxes on the leaf surface, depending on the relative humidity (RH) (Van Hove et al., 1989). Finally, the stomatal pathway represents exchange of NH$_3$ through the plant stomata with ammonium dissolved in the apoplast fluids of the plant (Farquhar et al., 1980; Wichink Kruit et al., 2010b). While these processes happen at very small scales, at micrometer or milometer level, they can be represented at the canopy level, i.e. at field scale (Vilà-Guerau de Arellano et al., 2020).

The NH$_3$ exchange through the stomatal pathway is governed by the dynamic response of vegetation to meteorological conditions and is closely related to photosynthesis. The stomata open during the day in response to solar radiation, as the vegetation uses energy for photosynthesis, particularly the photosynthetically active radiation (PAR) (Cowan and Farquhar, 1977; Hsiao, 1973; Papaioannou et al., 1996; Ronda et al., 2001). Plants ingest CO$_2$ through the stomata, but water from inside the plant can evaporate as the stomata are opened. The plant can reduce this loss of water by (partly) closing the stomata in case of high water vapor pressure deficit (VPD), or increase the evaporation rate by actively opening the stomata. Increasing the evaporation rate provides cooling, lowering the leaf temperature to reach optimal conditions to perform photosynthesis (de Groot et al., 2019; Jacobs and de Bruin, 1997; Takagi et al., 1998; Vilà-Guerau de Arellano et al., 2020). As the temperature and VPD are often highest in the late afternoon, the stomata often partly close to manage the loss of water. During the night, there is no PAR for photosynthesis, so the stomata are closed. As a result, the characteristics of ammonia surface-atmosphere exchange of NH$_3$ differ between day and night, with the stomatal pathway being dominant during the day and the external leaf pathway being the dominant pathway during the night and in the early morning.

The uptake of CO$_2$ is represented by the Gross Primary Production (GPP), in mgC m^{-2}s^{-1}. The GPP and the (soil) CO$_2$ respiration (RESP) combined define the Net Ecosystem Exchange (NEE) of CO$_2$, following $NEE = GPP + RESP$, which is measured as the CO$_2$

flux. The CO_2 respiration is estimated by taking the average campaign nighttime ($Q_{net} <$ 0) CO_2 flux, which is approximately 2.2 mgCO_2 m^{-2} s^{-1}. The GPP is then estimated by subtracting this respiration estimate from the observed CO_2 flux, or $GPP = NEE - RESP$. Note that a positive GPP (carbon uptake) corresponds to a observed negative CO_2 flux (CO_2 deposition).

To capture observations whit active stomatal exchange, Filter 4 is set to only accept GPP > 0 mgCO_2 m^{-2} s^{-1}. Due to the uncertainty of our GPP estimate, there are still some night-time observations which pass the filter. We therefore add an additional 5th filter using incoming shortwave radiation (SW_{in}). Only measurements with $SW_{in} > 10$ W m^{-2} will pass, in order to filter out these last remaining night-time observations.

After filtering, 102 hours (9%) of all RITA-2021 observations, or 18% of all daytime RITA-2021 observations, are available for analysis. These observations are taken over 17 unique days, spanning 29 August to 30 September, with an average of 6 hours and a maximum of 12 hours of accepted measurement per day.

3.2.3   Characterization of the campaign meteorology

The summer months (June, July and August) leading up to the RITA-2021 campaign are characterized as an average Dutch summer, with average temperatures (17.7 ^{o}C), above average precipitation (244 mm accumulated) and below average hours of sunshine (618 hours). Additionally the ground and surface water levels are actively managed for the agricultural activity in the area (Brauer et al., 2014). It is therefore expected that the role of long-term vegetation stress on stomatal exchange is negligible during the RITA-2021 campaign.

As discussed in Section 3.2.2, high temperatures or VPD can induce vegetation stress during the campaign. We therefore characterize the meteorological conditions of the 17 unique days in which the 102 hours of filtered measurements were taken. The meteorological conditions of these days are summarized in Table 3.2, which shows the 17 day average and the observed range of the diurnal minimum/maximum of several variables. The 17-day average values provide a characterization of mild meteorological conditions with no indication that the vegetation is under stress. Additionally, Table 3.2 includes an estimate of the maximum daytime footprint of the sonic anemometer, as a first-order approximation of the footprint of the NH$_3$ flux measurements. The footprint shown in Table 3.2 is the 70% footprint of the sonic anemometer at a height of 2.8 m, following the method from Kljun et al. (2015).

As the filtered campaign measurements are characterized by frontal passages, the weather conditions range from clear sky summer conditions with moderately high temperatures, to colder cloudy days with short precipitation events (not shown). Furthermore, the atmospheric stability for the 102 hours of filtered measurements is classified using the

Table 3.2: A characterization of the meteorology of the 17 unique days at which any number of observations passes the filters, with the 17 day average and the range of the diurnal minimum/maximum of several (meteorological) variables. A requirement of non-zero net radiation is set for the GPP and footprint anemometer, due to the measurement uncertainty of these variables during stable nights.

Variable	Symbol	Diurnal minimum/maximum			
		17-day average		17-day range	
Daily minimum temperature	T_{min}	11.5	°C	5.6 - 16.7	°C
Daily maximum temperature	T_{max}	19.7	°C	13.6 - 25.5	°C
Daily maximum wind speed	u	4.5	m s^{-1}	2.2 - 7.2	m s^{-1}
Daily maximum net radiation	Q_{net}	295	W m^{-2}	137 - 400	W m^{-2}
Daily maximum sensible heat flux	H	99	W m^{-2}	27 - 173	W m^{-2}
Daily maximum latent heat flux	L_vE	145	W m^{-2}	83 - 230	W m^{-2}
Daily maximum gross primary production	GPP	0.78	mgC m^{-2} s^{-1}	0.57 - 1.4	mgC m^{-2} s^{-1}
Daily maximum water vapor pressure deficit	VPD	966	Pa	365 - 1420	Pa
Daytime maximum sonic anemometer footprint (70%)	$fp_{70\%}$	148	m	88 - 255	m

measured Obukhov length (L) and the height of the sonic anemometer (z = 2.8 m). In total, 4.5 hours (4%) can be classified as stable (z/L > 0.05), 61 hours (60%) as neutral (-0.05 $\leq$ z/L $\leq$ 0.05) and 36.5 hours (36%) as unstable conditions (z/L < -0.05). This variation leads to a large spread in all variables shown in Table 3.2, as indicated by the column showing the 17-day range.

3.2.4   Characterization of the NH$_3$ observations

The variety in meteorological conditions could be an explanation of the large day-to-day difference in the observed NH$_3$ concentrations, shown in Fig. 3.2b. The histogram shows that most observed NH$_3$ concentrations are below 7 μg m^{-3}, with a long tail leading to a maximum concentration of 24.7 μg m^{-3}. Still, the mean (solid line) and median (dotted line) concentrations do indicate that the concentration decreases during the day, until the late afternoon. This would be in line with observations at several other sites, both in the Netherlands (Schulte et al., 2021; Wichink Kruit et al., 2007) and in other countries, e.g. Scotland (von Bobrutzki et al., 2010) or Italy (Ferrara et al., 2021). The large day-to-day differences in the NH$_3$ measurements could be a result of the changing meteorological conditions, the nearby agricultural activity, or a combination of both.

Despite the high variability in the NH$_3$ concentration measurements, a consistent diurnal variability is observed in the NH$_3$ gradient (ΔNH$_3$) and corresponding flux in Fig. 3.2c and 3.2d. Both Fig. 3.2b and 3.2c indicate that the observed ΔNH$_3$ is independent of the absolute NH$_3$ concentration, i.e. high absolute concentrations do not lead to a large concentration difference between the two miniDOAS instruments. The average diurnal variability is characterized by negative ΔNH$_3$ (deposition) in the early morning and late afternoon and positive (emission) ΔNH$_3$ during the afternoon, with a typical range of about 0.5 μg m^{-3} in both directions. In total 79% of the filtered observations have a positive ΔNH$_3$, corresponding to NH$_3$ emissions.

As F$_{NH_3}$ is directly inferred from ΔNH$_3$, the diurnal variability in Fig. 3.2d is very similar. The NH$_3$ flux typically reaches its maximum around noon at little over 0.05 μg m^{-2}s^{-1} on average, with individual noon observations ranging from -0.01 μg m^{-2}s^{-1} to 0.14 μg m^{-2}s^{-1}. Note that the measurements taken on 11 - 12 September, the aforementioned fertilization event, are approximately a factor 4 larger than the mean campaign values. Despite the large observed F$_{NH_3}$ on these days, the observed concentrations are only slightly larger than the campaign averages. These two days will not be included in the analysis presented in this study, but they are shown as an illustration of how fertilization events can impact our analysis.

3.2.5   Characterization of the ammonia flux

The main drivers of ammonia surface-atmosphere exchange are turbulent mixing, as well as the difference between the atmospheric NH$_3$ concentration and the so called canopy
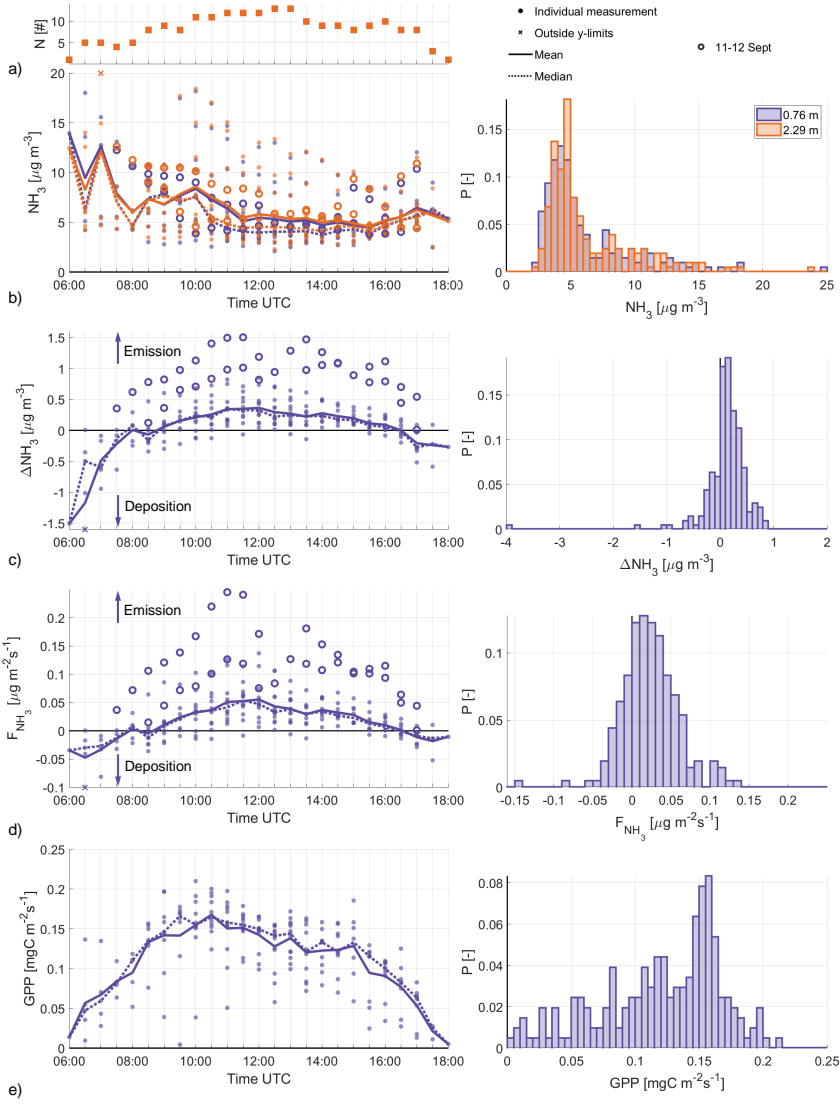
Figure 3.2: The diurnal variability from sunrise (6:00 UTC) to sunset (18:00 UTC) of the filtered NH_3 concentration (b), NH_3 gradient (c), F_{NH_3} (d) and the GPP with the corresponding histogram to the right. At each moment in time, the multi-day mean (solid line) and median (dotted line) are calculated. Highlighted are observations from the fertilization event at 11 - 12 September (open circles). The N number of observations over which these averages are calculated are displayed at the top (a). ΔNH_3 is defined so the sign matches that of F_{NH_3}

Figure 3.3: The 2.8 m temperature plotted against F$_{NH_3}$ (a) and observed NH$_{3,\ 2.29\ m}$ (b). The color coding in (a) represents the NH$_3$ concentration, observed at 2.29 m. In (b), the dotted line re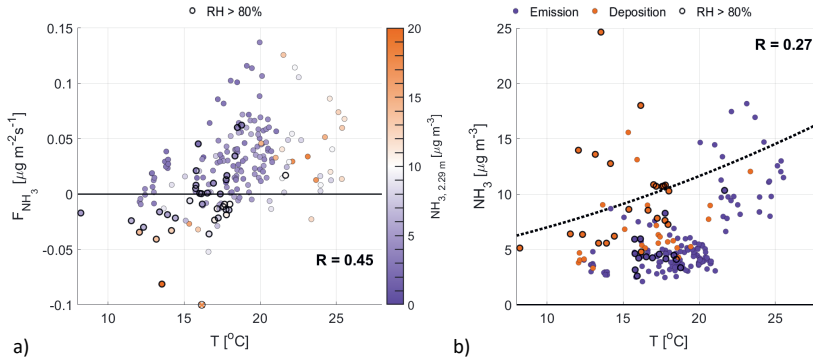presents the theoretical stomatal compensation point (χ_s) for a long-term NH$_3$ concentration of 7.7 μg m^{-3}. Highlighted with black circles are observations with RH > 80%, taken before noon, where NH$_3$ exchange through the external leaf pathway can play a significant role.

compensation point, i.e. an internal NH$_3$ concentration (Farquhar et al., 1980; Nemitz et al., 2001; Wichink Kruit et al., 2007). A compensation point lower than the atmospheric concentration leads to deposition of ammonia and vice-versa. The canopy compensation point consists of individual compensation points for each of the individual flux pathways. Following parameterizations of the stomatal compensation point, we find it related to the (leaf) temperature and some form of nitrogen input parameter (actual or long-term NH$_3$ concentration). The stomatal compensation point increases non-linearly with increasing temperature or nitrogen input (Massad et al., 2010; Nemitz et al., 2001; van Zanten et al., 2010). As the stomatal compensation point increases and becomes larger than the atmospheric NH$_3$ concentration, or as the atmospheric concentration drops below this compensation point, emission will be observed from the stomatal exchange pathway.

In Fig. 3.3a, we show the observed ammonia flux against the observed temperature of the sonic anemometer, with the colors indicating the atmospheric NH$_3$ concentration at 2.29 m. Despite our efforts to filter for observations where the stomatal pathway is dominant, it is possible that the external leaf pathway still plays an important role in the morning, through deposition onto morning dew at canopy level (van Zanten et al., 2010; Wentworth et al., 2016). We therefore use black circles to mark observations taken before 12:00 UTC with RH > 80% in Fig. 3.3. These highlighted observations indeed generally correspond with measurements of deposition or weak emission, indicating that NH$_3$ exchange through the external leaf pathway is still significant for these observations. While the inclusion complicate our analysis of stomatal NH$_3$ exchange, they are still included in the analysis as it also offers an opportunity to test if the relations found in the filtered dataset differ

for the marked- and unmarked observations. If that is the case, it shows we are indeed able to attribute the unmarked observations to stomatal exchange.

Figure 3.3a shows that the observed F_{NH_3} increases with temperature for low atmospheric concentration ($2\ \mu g\ m^{-3} \leq NH_{3,\ 2.29m} \leq 7\ \mu g\ m^{-3}$). We attribute this increase in NH_3 emissions to the change in ΔNH_3 for increasing temperature, i.e. the difference between the approximately constant atmospheric NH_3 concentration and stomatal compensation point. This is indeed shown in Fig. 3.3b, where the theoretical stomatal compensation point (dotted line) increases with temperature. Here, the compensation point is calculated following the DEPosition of Acidifying Compounds (DEPAC) parameterization (van Zanten et al., 2010), using the sonic anemometer temperature and campaign median $NH_{3,\ 2.29\ m}$ ($7.7\ \mu g\ m^{-3}$).

This relation is scattered for measurements taken at high temperatures (> 21 ºC). While there were only small variations in the NH_3 concentration for temperatures below 21 ºC, NH_3 concentration for these warmer temperatures are higher than the campaign average ($> 7\ \mu g\ m^{-3}$) and highly variable. As the NH_3 flux is directly related to the difference between the atmospheric NH_3 and the stomatal compensation point, the variability in the atmospheric concentration leads to the scatter shown in Fig. 3.3a, where higher NH_3 observations correspond to weaker emission fluxes.

3.3 Ammonia flux relationships to dynamic vegetation responses

The diurnal pattern of F_{NH_3} in Fig. 3.2d shows similarities with the diurnal variability of the GPP in Fig. 3.2e. To further study the role of stomatal exchange during the campaign, we link the observed F_{NH_3} to the dynamic vegetation responses. First, we relate the ammonia flux to the GPP, the latent heat flux (L_vE) and the sensible heat flux (H). The GPP and L_vE are directly governed by the opening and closing of the stomata and represent stomatal exchange. Given the low data availability (9%), we are aware that the analysis could be dominated by variations resulting from the diurnal variability of the fluxes. We therefore also include H in our analysis. The sensible heat flux is only indirectly related to the dynamic vegetation response through the surface energy balance, as the available energy from (solar) radiation and the soil heat flux is split between L_vE and H. If the observed fluxes are indeed regulated through the opening and closing of stomata, the analysis for F_{NH_3} to L_vE and GPP should differ from the comparison with H.

Next, we organize the observations following current dynamic vegetation models, based on temperature, radiation and moisture (Jarvis et al., 1976; Ronda et al., 2001; Stewart, 1988). Here, we compare the responses of the four individual fluxes to temperature (T), PAR and VPD. As these three variables control the stomatal response at canopy level, we will use the responses of the fluxes to these variables as a guidance to better understand
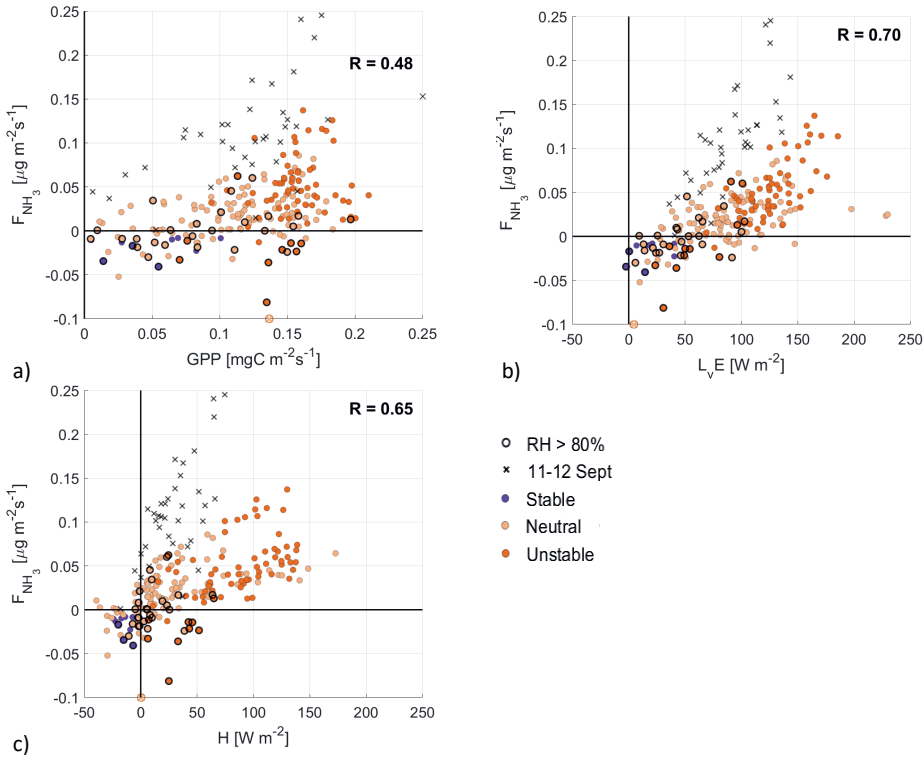
Figure 3.4: Scatter plots of F$_{NH_3}$ against the GPP (a), L$_v$E (b) and H (c), with the colors indicating the ABL stability. Highlighted by black circles are observations with a RH >80%, where deposition through the external leaf path can still play an important role. The black crosses are observations from the fertilization event observed on 11 - 12 September.

the diurnal variability of the ammonia flux. Note that measurements taken on 11 - 12 September are not used to calculate correlation coefficients, but are shown in the figures and included in the visual analysis.

3.3.1   Relating the ammonia flux to photosynthesis

Plotting F$_{NH_3}$ against the GPP in Fig. 3.4a shows a low positive correlation between the two fluxes, with a correlation coefficient of 0.48. There is a large spread in the data, particularly for GPP values larger than 0.125 mgC m^{-2}s^{-1}. Part of this spread is attributed to the high relative humidity (black circles), where F$_{NH_3}$ is not yet dominated by stomatal exchange and exchange through the external leaf pathway is still expected to be significant. Note that the atmospheric stability (color coded) plays an important role for the GPP as unstable conditions are typically characterized by clear skies and high PAR values, which

favors photosynthesis (discussed in Section 3.3.2). This relation is not found in the observed F_{NH_3}, as there is a large spread in F_{NH_3} for both neutral and unstable conditions.

A moderate positive correlation is found in Fig. 3.4b between F_{NH_3} and L_vE. Our interpretation of this moderate correlation is that both evaporation and stomatal NH_3 emissions follow a similar process. The opening of the stomata for photosynthesis allows for the exchange of several gasses, including water vapor and ammonia, depending on VPD or the difference between atmosphere NH_3 and the stomatal compensation point (Cowan and Farquhar, 1977; Farquhar et al., 1980; Hsiao, 1973; Wichink Kruit et al., 2010b). Note that the observations with high relative humidity generally correspond to low L_vE and that again unstable conditions correspond with high L_vE values, related to the VPD between the leaf and stomata, and the atmosphere.

When plotting F_{NH_3} against H, two branches are found in the spread of the data, with a third branch being formed by the filtered out fertilization event on 11 - 12 September (black crosses). The smaller branch, with $F_{NH_3} > 0.1$ μg m^{-2}s^{-1}, could point towards another (weaker) fertilization event. Still, the second highest positive correlation is found at 0.65, indicating that the natural diurnal variability indeed plays and important role. Note that most of the measurements with high relative humidity are clustered around H = 0 W m^{-2}, i.e. there is little transfer of heat between the surface and atmosphere.

Based on the three scatter plots we find the highest correlation between F_{NH_3} and L_vE. Together with the diurnal variability of F_{NH_3}, transitioning from nighttime deposition to daytime emission from 8:30 to 16:30 UTC, this is the second indication towards stomatal emission of NH_3, opposed to emission from fertilization or animal droppings. However, the moderate correlation between F_{NH_3} and H indicates that the diurnal variability of the fluxes influences the correlation coefficient. Finally, we want to mention the observations on 11 - 12 September, which support the interpretation of the scatter plots in showing how fertilization events affect our analysis.

3.3.2 The dynamic vegetation response to varying meteorological conditions

The dynamic response to temperature

We further investigate the stomatal exchange of NH_3 by analyzing the response of F_{NH_3} to varying meteorological conditions. The optimal conditions (PAR, T, VPD) for photosynthesis are different for different vegetation types (Gates, 1980; Jacobs, 1994; Vilà-Guerau de Arellano et al., 2015). Starting with the 2.8 meter temperature (T) in Fig. 3.5, we find a large spread for all four surface fluxes, resulting in low positive correlations (0.33 - 0.51). The lowest correlation coefficients are found for GPP and L_vE, indicating that temperature has little impact on the opening and closing of the stomata. Slightly higher correlation is found for F_{NH_3}, which we attribute to the relation between the stomatal compensation
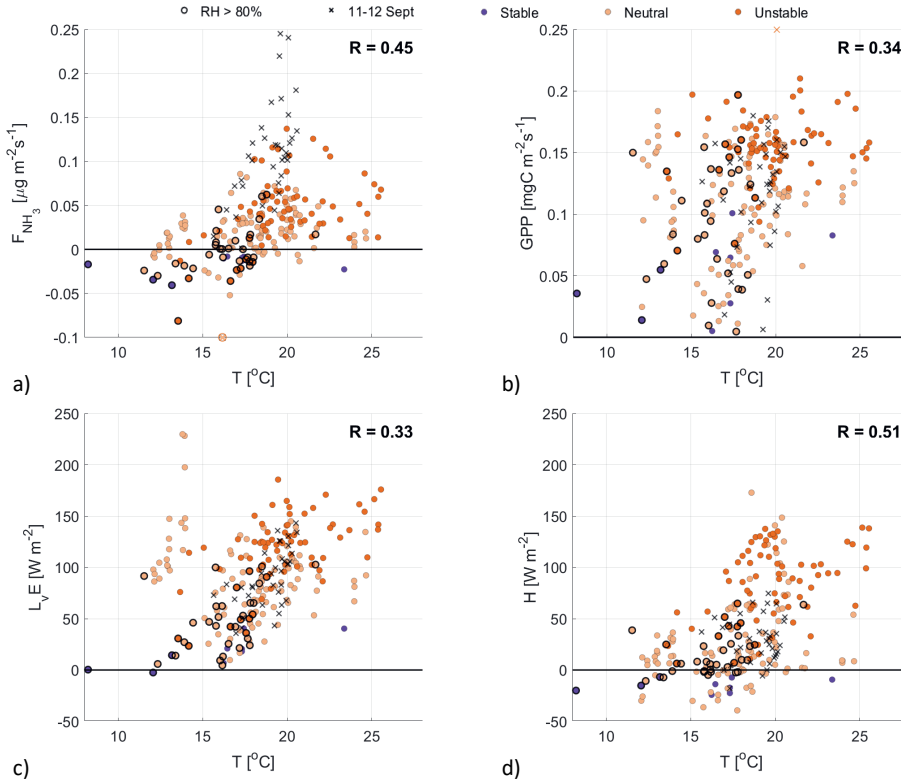
Figure 3.5: Scatter plots of the temperature against F_{NH_3} (a), GPP (b), L_vE (c) and H (d), with the colors indicating the ABL stability. Highlighted by black circles are observations with a RH > 80%. The black crosses are observations from the fertilization event on 11 - 12 September.

point and the NH₃ flux, discussed in Section 3.2.5. Note that the NH₃ emissions on 11 - 12 September stand out as outliers in Fig. 3.5a, while being average for the other three subplots.

The dynamic response to VPD

Moving on to analyzing the response of the four fluxes to the VPD, we find moderate correlation coefficients (0.42 - 0.53) in Fig. 3.6. The latent heat flux shows in Fig. 3.6c a non-linear relationship with the VPD, called the evaporation hysteresis (de Groot et al., 2019; Zhang et al., 2014). This hysteresis is driven by both the vegetation regulating the loss of water through evaporation, described in Section 3.2.2, and the time difference when the maximum values for L_vE (12:00 UTC) and VPD (15:00 UTC) are reached. The same

Figure 3.6: Scatter plots of the VPD against F_{NH_3} (a), GPP (b), L_vE (c) and H (d), with the colors indicating the ABL stability. Highlighted by black circles are observations with a RH > 80%. The black crosses are observations from the fertilization event on 11 - 12 September.

holds true for the other three fluxes (F_{NH_3}, GPP and H), as all three reach their maximum around noon.

Note that the observations of 11 - 12 September again are clear outliers in Fig. 3.6a, forming two branches in the scatter plot. Also standing out are several observations with $F_{NH_3} > 0.1$ μg m^{-2}s^{-1}. These are the observations that appear as the small upper branch in the H - F_{NH_3} scatter plot in Fig. 3.4c and, again, form their separate branch here in Fig. 3.6a. This further indicates that there is a second (weak) fertilization event in the filtered dataset of the RITA-2021 campaign.

The dynamic response to PAR

When relating F_{NH_3} to PAR, we find high positive correlation coefficients for all four surface fluxes (0.72 - 0.93) in Fig. 3.7. The highest value is found for H (Fig. 3.7d), as the
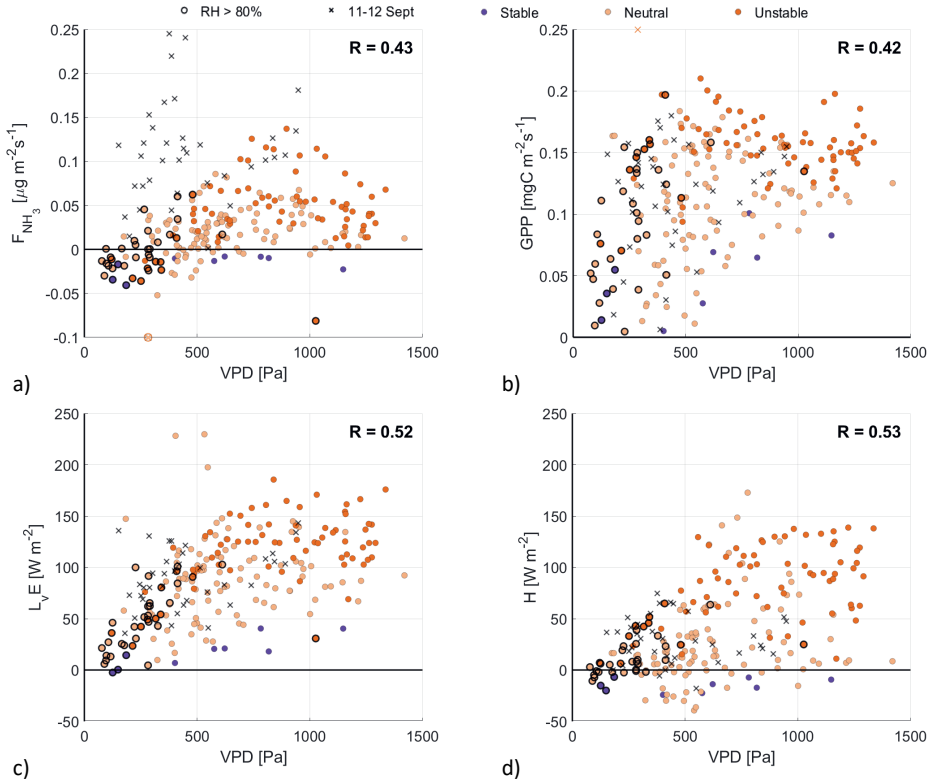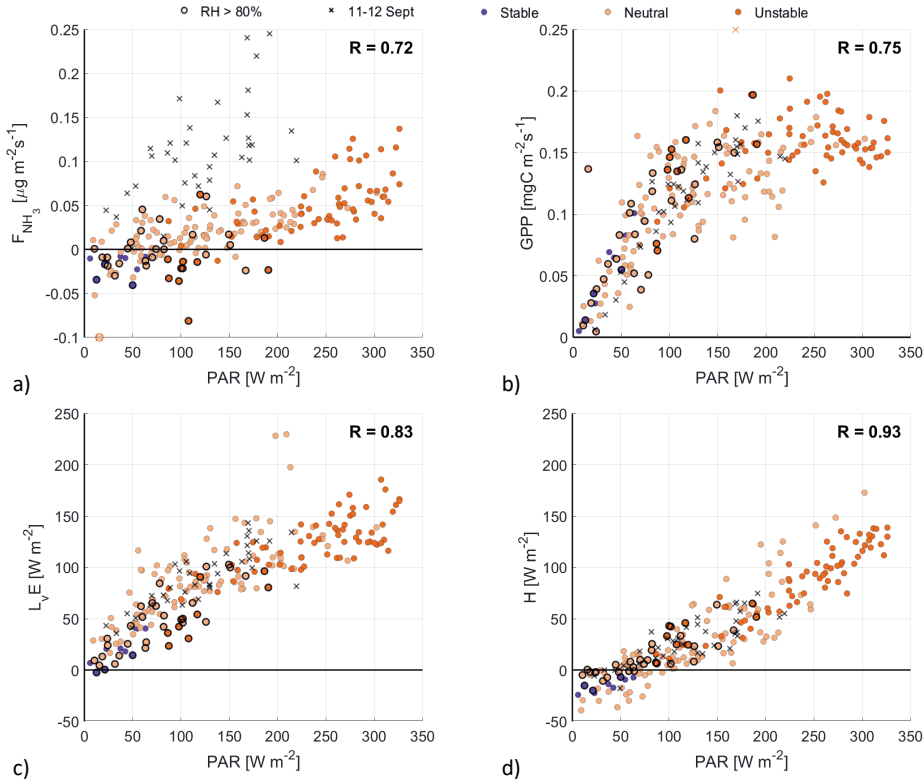
Figure 3.7: Scatter plots of PAR against F$_{NH_3}$ (a), GPP (b), L$_v$E (c) and H (d), with the colors indicating the ABL stability. Highlighted by black circles are observations with a RH > 80%. The black crosses are observations from the fertilization event on 11 - 12 September.

solar radiation is the main source of energy for the surface-atmosphere exchange of heat. Where H exhibits a linear relation to PAR, non-linear effects are observed in the response of the two photosynthesis fluxes GPP and L$_v$E. This difference, together with the high correlation coefficients, indicates that PAR is the main driver of the dynamic vegetation response.

The GPP has a strongly non-linear response to PAR, as the GPP appears to reach a plateau for PAR > 150 W m^{-2}. There are several reasons for this GPP maximum. At constant temperature and PAR, the stomatal uptake of CO$_2$ will increase the concentration within the plant to the point that the CO$_2$ supply is no longer the limiting factor. The GPP then reaches a plateau of maximum photosynthesis rate (see Figure 6.13a Moene and Van Dam (2014)), similar to the observations in Fig. 3.7b. Additionally, the photosynthesis system can become light saturated for high PAR values, at constant temperature. Following this

latter process, the GPP is expected to level off more gradually, compared to the plateau that is reached by CO_2 saturation (see Figure 6.13b Moene and Van Dam (2014)). Finally, the (partly) closing of the stomata in response to high VPD could also reduce the GPP. However, as the VPD typically reaches its maximum around 15:00 UTC (not shown), it is unlikely that this is a limiting factor for GPP at high PAR values, which peaks around noon. All these processes depend on the temperature, VPD and PAR, and can explain the vertical spread in Fig. 3.7b.

When taking a close look at the response of the L_vE to PAR, is it possible to distinguish two phases in Fig. 3.7c. First, for PAR values up to about 100 W m^{-2}, the L_vE increases linearly to roughly 75 W m^{-2}, related to the opening/closing of the stomata around sunrise/sunset. The second phase shows a more gradual linear increase of L_vE to PAR. From the linear response and the small spread in Fig. 3.7c, we conclude that opening and closing of the stomata during the RITA-2021 campaign is governed by PAR and that the role of the VPD or temperature is small.

Similar to the L_vE, the NH_3 flux generally shows a linear response; transitioning from weak deposition to emission as the stomata open in response to increasing PAR. The spread in the F_{NH_3} response is larger compared to the L_vE response, which results in the lowest correlation coefficient at 0.72. We attribute this spread to three factors: the relation between temperature and the stomatal compensation point, the variations in the NH_3 concentration and the measurements where RH > 80% (black circles). Furthermore, observations where $F_{NH_3} > 0.1$ μg m^{-2}s^{-1}, i.e. the possible (weak) fertilization event, again appear to form a second branch in the scatter plot. Based on the strong similarities between F_{NH_3} and L_vE in their response to PAR, we conclude that the observed NH_3 emission is indeed stomatal (re)emission from vegetation.

3.4   Discussion

Observations of the NH_3 flux after filtering, taken over 17 individual days during the RITA-2021 campaign, are characterized by day-time emissions. The measurement site at Cabauw is located on flat grassland in an agricultural area, with the nearby fields being actively managed and/or grazed upon. It is therefore possible that the observed NH_3 emissions originate from sources like fertilization events (e.g. manure application) or animal droppings. We therefore first aim to link the NH_3 emissions to stomatal exchange and follow up by attempting to find relations between F_{NH_3} and observations of the CO_2 and water vapor flux.

The first indication towards stomatal emission is found in the diurnal variability of F_{NH_3}. The flux transitions from deposition to emission in the early morning around 8:00 UTC, reaches maximum emission around 12:00 UTC and transitions to deposition again just before sunset, around 16:30 UTC, as shown in Fig. 3.2c. Our interpretation of this diurnal

cycle is the flux transitions from (nighttime) NH$_3$ deposition, through the external leaf path, towards emission through the stomatal path during the day. This diurnal variability of F$_{NH_3}$ shares similarities to the diurnal variability of the CO$_2$ flux. As the stomata open for photosynthesis in response to PAR, the CO$_2$ flux transitions from CO$_2$ respiration to stomatal uptake of CO$_2$. High correlation coefficients between F$_{NH_3}$ and L$_v$E (0.7) and between F$_{NH_3}$ and PAR (0.72), further point towards stomatal NH$_3$ emission and a possible relation between F$_{NH_3}$ and the photosynthesis fluxes.

3.4.1   Critical analysis of RITA-2021 dataset

The conditions during the RITA-2021 campaign present a challenge for the analysis conducted in this study. The site is located in an active agricultural region, with several potential emission sources within only a few hundred meters to a couple of kilometers distance upwind of the measurement site. The fields next to the site are actively managed and nitrogen contents of the soil and vegetation can differ on a field-to-field basis. This high level of surface heterogeneity within the estimated footprint of the flux measurements (up to about 250 m, Table 3.2) adds an additional level of complexity to the analysis (Swart et al., 2023). Furthermore, there are several farms located within two kilometers of the site, some of which with yearly NH$_3$ emissions up to 12000 kg year^{-1}. Studies on the blending distance indicate that emission plumes from such strong local NH$_3$ sources can affect flux measurements over distances of a couple of kilometers (Schulte et al., 2022a). In this study, at least one instance of strong local emissions has been identified as the fertilization event on 11 - 12 September. Other potential weaker events have been shown and discussed as well in Fig. 3.4a, 3.4c and 3.6a.

The analysis is further complicated by the complex meteorological conditions, characterized by frontal passages. As the miniDOAS setup was positioned anticipating winds from the south-west, the meteorology of the filtered data is characterized by frontal passages. As a result, most observations are taken under neutral stability conditions (60%), with clouds and some rain showers. While rain events are filtered out, wet deposition by rain does lead to a sudden change in the NH$_3$ concentration and can lead to re-emission of NH$_3$ as the rainwater evaporates.

Finally, the south-western orientation of the instruments leads to a significant loss in the availability of data suitable for analysis. Historically, southwestern winds tend to be most common in September, but the wind direction during the campaign was highly variable. Filtering for unobstructed wind directions reduces the availability of viable data by 510 hours, i.e. 44% of all measurement data. As a result, the observed range in the measurements presented in the Figures is strongly influenced by the natural diurnal variability of the variables. While we do address the role of the natural diurnal variability by including the sensible heat flux in our analysis, it does make the observed relations between F$_{NH_3}$ and the other variables somewhat speculative.

The high level of heterogeneity, the low data availability after filtering and the complex weather conditions make the RITA-2021 dataset unfavorable for establishing relationships between F_{NH_3} and the CO_2 or water vapor flux. It highlights the importance of homogeneity of the NH_3 surface characteristics and that proximity of NH_3 emission sources should be considered as well when selecting a measurement site, in addition to the availability of high quality meteorological observations. Despite the challenges, the NH_3 measurements are of unprecedented high quality (Swart et al., 2023) and analyzing the unique dataset following our approach is still worthwhile. While we do not manage to develop new relationships, we are able to link the observed F_{NH_3} emission to stomatal exchange, following an approach where we organize the observations following current dynamic vegetation models.

3.4.2 Recommendations

Following the results presented in this study, we recommend a comprehensive approach to future NH_3 flux measurements, including observations of the CO_2 and water vapor flux as auxiliary measurements. The opening of the stomata for CO_2 uptake through photosynthesis allows for the exchange of several other gasses, including water vapor and ammonia. The process of photosynthesis is well understood and such auxiliary observations can be used to further our understanding of NH_3 exchange through the individual exchange pathways, as was done for ozone deposition by Visser et al. (2021).

Furthermore, we recommend to analyze and compare observations of the NH_3 flux at different measurement (grassland) sites, similar to the intercomparison of CO_2 exchange measurements by Jacobs et al. (2007). For example, the F_{NH_3} diurnal variability presented in this study significantly differs from measurements in 2013 at the Veenkampen meteorological site near the city of Wageningen (`https://www.wur.nl/en/show/Weather-Station-De-Veenkampen.htm`). Located only 50 km east, the diurnal variability of F_{NH_3} at Veenkampen is characterized by weak morning deposition and strong afternoon deposition, up to about -0.3 μg m^{-2}s^{-1}, for clear sky conditions over unfertilized grassland (Schulte et al., 2021). At the Haarweg meteorological site, the predecessor to the Veenkampen, chemical wet denuder measurements of F_{NH_3} in 2004 were characterized by strong deposition in the early morning, attributed to morning dew, and weak stomatal emissions in the afternoon (Wichink Kruit et al., 2007). The differences between observed diurnal variability in these three studies stress the high variability at the local and regional scales and highlight the need for long term high-resolution F_{NH_3} observations at multiple locations.

Efforts to further our understanding of the NH_3 exchange and its diurnal variability are already being made. The miniDOAS setup used in the RITA-2021 campaign will be taking long-term (> 1 year) observations of the NH_3 flux at the Veenkampen meteorological site, starting in the summer of 2022. This year-long record of high-resolution F_{NH_3} observations will be analyzed, alongside a wide range of meteorological and turbulent measurements, including the CO_2 and water vapor flux, aiming to improve the parameterization of the

NH$_3$ surface-atmosphere exchange. The analysis can be taken one step further in the context of the Ruisdael Project, following a process analysis combining the observations with both conceptual and high-resolution turbulent resolved models (Schulte et al., 2021; Schulte et al., 2022a).

3.5 Conclusions

We analyze over a month of ammonia flux measurements (F$_{NH_3}$), taken during the RITA-2021 campaign at the Ruisdael Observatory at Cabauw. The analysis is centered around observations from the miniDOAS flux measurement setup, which applies the flux-gradient method to line average concentration measurements over a 22 m open-path at two heights. We aim to link the observed NH$_3$ flux to stomatal exchange and establish relations to photosynthesis, i.e. the stomatal exchange of CO$_2$ and water vapor (plant transpiration). The process of photosynthesis is well understood and such auxiliary observations can be used to advance our understanding of NH$_3$ surface-atmosphere exchange through the individual exchange pathways, e.g. stomatal exchange.

After filtering, the observed F$_{NH_3}$ is characterized by daytime emissions, averaging at about 0.05 μg m^{-2}s^{-1}, and nighttime deposition of about -0.05 μg m^{-2}s^{-1}. We compare the NH$_3$ flux to the CO$_2$ uptake by vegetation and the exchange of water vapor, represented by the gross primary production (GPP) and latent heat flux (L$_v$E), as well as the sensible heat flux (H) which is only indirectly related to the dynamic vegetation response. Here, we find high correlation between the observed daytime NH$_3$ emissions and L$_v$E (0.70) and the photosynthetically active radiation (0.72). These results indicate towards stomatal emission of NH$_3$ and show that auxiliary flux measurements of CO$_2$ and water vapor are appropriate variables to distinguish stomatal NH$_3$ exchange from non-stomatal exchange.

The analysis presented in this study is hampered by the challenging conditions during the RITA-2021 campaign. The measurement site is located in a highly agricultural region, with actively managed (i.e. fertilized) grassland and emission sources in close proximity ($<$ 2 km) of the NH$_3$ measurements. These heterogeneous NH$_3$ surface characteristics lead to outlier observations caused by at least one fertilization event and there are indications of other (weaker) fertilization events. Additional layers of complexity are added by the varying meteorological conditions, characterized by frontal passages, and the small subset of the campaign measurements being suitable for analysis after filtering (9% or 102 hours). The latter is largely the outcome of filtering out unfavorable wind directions, where the airflow is obstructed. As a result, the observed range in the measurements is largely governed by the natural diurnal variability, hampering the efforts to establish clear relationships.

Despite the challenging conditions, the comprehensive approach presented in this study does show the potential of combining high-quality NH$_3$ observations with auxiliary flux measurements of CO$_2$, water vapor and other meteorological variables. By organizing the

observations following current dynamic vegetation models, we managed to attribute the observed NH_3 emission to stomatal exchange and identify outliers. In order to establish relations between the NH_3 and the photosynthesis fluxes, the approach should be applied to measurements that are still representative of the sources and sinks, but at the same time are well mixed and outside the blending distance of individual or a group of emission sources. The results presented in this study already indicate that there is room to find such patterns.

Chapter 4

Assessing representativity of NH$_3$ measurements influenced by boundary-layer dynamics and turbulent dispersion of a nearby emission source

Abstract

This study presents a fine-scale simulation approach to assess the representativity of ammonia (NH_3) measurements in proximity to an emission source. Close proximity to emission sources (< 5 km) can introduce a bias in regionally representative measurements of the NH_3 molar fraction and flux. Measurement sites should therefore be located a significant distance away from emission sources, but these requirements are poorly defined and can be difficult to meet in densely agricultural regions. This study presents a consistent criterion to assess the regional representativity of NH_3 measurements in proximity to an emission source, calculating variables that quantify the NH_3 plume dispersion using a series of numerical experiments at a fine resolution (20 m). Our fine-scale simulation framework with explicitly resolved turbulence enables us to distinguish between the background NH_3 and the emission plume, including realistic representations of NH_3 deposition and chemical gas-aerosol transformations. We introduce the concept of blending distance, based on the calculation of turbulent fluctuations, to systematically analyze the impact of the emission plume on simulated measurements, relative to this background NH_3. We perform a suite of systematic numerical experiments for flat homogeneous grasslands, centered around the Ruisdael Observatory at Cabauw, to analyze the sensitivity of the blending distance, varying meteorological factors, emission/deposition and NH_3 dependences. Considering these sensitivities, we find that NH_3 measurements at this measurement site should be located at a minimum distance of 0.5 - 3.0 km and 0.75 - 4.5 km from an emission source for NH_3 molar fraction and flux measurements, respectively. The simulation framework presented here can easily be adapted to local conditions and paves the way for future ammonia research to integrate simulations at high spatio-temporal resolutions with observations of NH_3 concentrations and fluxes.

4.1   Introduction

Excess atmospheric nitrogen leads to an increased public health risk through the formation of particulate matter and causes environmental damage: nitrogen deposition leads to eutrophication, ecosystem acidification and shifts in climate change (Behera et al., 2013; Erisman et al., 2013; Erisman and Schaap, 2004; Smit and Heederik, 2017; Sutton et al., 2008). There can be serious societal consequences when nitrogen deposition critical loads are exceeded, as is the case in the Netherlands where the nitrogen crisis threatens the Dutch environment and economy (Stokstad, 2019). Atmospheric ammonia (NH_3) plays a key role in this process, mainly originating from agricultural activities and accounting for two-thirds of all nitrogen deposition in the Netherlands between 2005 and 2016 (Wichink Kruit and van Pul, 2018).

It is therefore important to have a network of NH_3 concentration and deposition measurements used for model validation and (trend) monitoring (Wichink Kruit et al., 2021). For these purposes, the measurement sites in such a network must be representative of a larger region. One requirement for these regional measurement sites is that they are located a sufficient distance away from local NH_3 sources, as local emissions introduce a bias in the observations (EMEP/CCC, 2001; Wichink Kruit et al., 2021). Positioning measurement sites a sufficient distance away from local sources is a challenge in densely agricultural areas like the Netherlands and regions all across the world with intensive livestock farming, e.g., North-West Germany, the province of Lleida in Spain, the state of North Carolina in the USA or the Hai River basin in China.

The emitted NH_3 is transported and mixed within the convective boundary layer (CBL) through turbulent dispersion. The field of turbulent plume dispersion is extensively researched using both observations and turbulent-resolved models. However, these studies typically focus on concentration peaks of highly toxic/flammable gases (Ardeshiri et al., 2021; Cassiani et al., 2020; Mylne and Mason, 1991), quantification of the emission strength and position (Ražnjević et al., 2022; Shah et al., 2020) or on statistical descriptions of the emission plume (Barad, 1958; Dosio and Vilà-Guerau de Arellano, 2006; Dosio et al., 2003; Vrieling and Nieuwstadt, 2003), typically used in chemistry transport models, e.g., OPS (Sauter et al., 2018), LOTOS-EUROS (Schaap et al., 2008) or EMEP MSC-W (Simpson et al., 2012). These transport models typically operate with resolutions at a kilometer scale (1 - 50 km) and parameterized turbulence, making them unsuitable to study the impact of local NH_3 sources on nearby measurement sites at the subkilometer scale.

Furthermore, plume dispersion studies generally focus on chemically inert gases, e.g., methane (Ražnjević et al., 2022; Shah et al., 2020). Ammonia is highly reactive; surface–atmosphere exchanges and chemical transformations play an important role in the NH_3 budget (aan de Brugh et al., 2013; Behera et al., 2013; Fowler et al., 1998; Nemitz et al., 2004b; Schulte et al., 2021; Shen et al., 2016; Van Oss et al., 1998). Additionally,

ammonia emissions in densely agricultural areas are released and mixed into a background concentration, a result of long range transport of NH_3 (10-100 km). Yearly averaged background concentrations can vary from 1-2 μg m⁻³ (e.g in coastal regions) up to up to tens of μg m⁻³ in regions with intensive agricultural activity, which is the focus on this study (van Zanten et al., 2017).

In this study, we investigate the impact of a typical ammonia emission source on the regional representativeness of NH_3 concentration and flux measurements. The novelty of our approach is twofold:

- We use a fine-scale large-eddy simulation (LES) model with explicitly resolved turbulence at a very high spatio-temporal resolutions (10-100 m and 10 s - 1 min).

- We include realistic representations of the surface-atmosphere exchange, chemical gas-aerosol transformations and a background ammonia concentration.

Following this approach, we combine fine-scale simulations, where turbulence is explicitly resolved, with theoretical concepts on turbulent emission plume dispersion. We then translate this knowledge to practical applications for the measurement community. The aim is to carry out a systematic analysis of how meteorological factors, including boundary-layer dynamics, deposition, chemical transformation and model resolution influence the relationships between emission and receptor. To this end, we introduce and analyze the concept of a blending distance (BD), i.e., the horizontal distance at which the emission plume can be considered well-mixed with respect to the background NH_3. With the concept of blending distance, we aim to provide an estimate of the minimum required distance from a typical NH_3 emission source for regionally representative measurements.

4.2   Methodology

4.2.1   NH₃ turbulent dispersion in DALES

To understand the variations of the NH_3 budget due to turbulence and heterogeneous sources and sinks of ammonia, our approach is twofold: (a) an explicit simulation of processes that govern turbulent dispersion and mixing of NH_3 and (b) identifying their individual contributions to the NH_3 molar fraction and surface–atmosphere exchange. For the former, we use the large-eddy simulation technique with a high resolution to solve explicitly turbulence. To this end, we conduct our numerical experiments using a modified version of the Dutch Atmospheric large-eddy simulation (DALES) version 4.2 (Heus et al., 2010; Ouwersloot et al., 2017b), with the original v4.2 freely available online (`http://doi.org/10.5281/zenodo.3759193`, last access: 23 June 2022). DALES explicitly resolves processes at scales ranging from 100 meters to kilometers, using filtered Navier-Stokes equations with the Boussinesq approximation. The filter size is generally equal to the grid size of the simulations, with subfilter-scale processes being parameterized using

one-and-a-half-order closure. The numerical experiments presented here are performed using a 20 m x 20 m x 5 m grid for a 10 km x 4.8 km x 3 km domain (500 x 240 x 600 grid points). Atmospheric NH_3 is added to DALES as a passive scalar in ppb, of which the spatial evolution is solved simultaneously with the thermodynamic variables. The boundary conditions for scalars and meteorological variables are periodic, unless stated otherwise.

The atmospheric ammonia budget is further governed by surface-atmosphere exchange and chemical gas-particle transformations (Schulte et al., 2021). We use a simplified, yet realistic, approach in our representation of these processes. The NH_3 surface-atmosphere exchange is modeled by a constant homogeneous deposition of 0.045 ppb m s^{-1} (about 0.032 μg $m^{-2}s^{-1}$), representative of the observed yearly average NH_3 dry deposition in the Netherlands (`https://www.rivm.nl/stikstof/meten/drogedepositieNH3`; Stolk et al., 2014, last access: 23 June 2022).

The representation of the chemical gas-aerosol transformations follows the approach of the OPS model, applying a percentage per hour change in the molar fraction of gaseous NH_3 to the whole domain (van Jaarsveld, 2004). This simplified, yet realistic, representation of chemistry as a net removal process will reduce the reach of the emission plume. However, the model is unable to resolve potential nonlinear effects of turbulent mixing on the chemical reaction rate within the plume. Turbulent dispersion of the emission plume is characterized by macromixing (meandering) and micromixing (in-plume mixing) (Galmarini et al., 1995; Vilà-Guerau de Arellano et al., 1990). The former is mainly carried out by large-scale turbulent eddies and is related to the average dispersion of the plume. Micromixing is carried out by turbulent eddies smaller than the plume and is related to the fluctuations of NH_3 and its chemical reactants. The reaction rate can slow down close to the emission source, as macromixing is the dominant dispersion process here and little micromixing occurs to supply chemical reactants from outside the plume. The extend to which turbulent mixing can limit the chemical reactions within the plume depends on the ratio of the turbulent timescales and the timescale of chemistry (Damköhler number) (Galmarini et al., 1995; Meeder and Nieuwstadt, 2000). When the timescales of chemistry are similar to the turbulent timescales, as is the case for ammonia (aan de Brugh et al., 2013), the reduction in the chemical reaction rate close to the source can be significant (Vilà-Guerau de Arellano et al., 2004a).

Special attention is placed on the representation of one NH_3 emission source in our domain, a dairy barn. Agricultural activity accounts for over 90% of the NH_3 emissions in the Netherlands and the European Union (Anys et al., 2020; van Bruggen et al., 2021; Vonk et al., 2020). Dairy farms account for approximately 50% of these agricultural NH_3 emissions, with approximately 15.000 farms with about 100 cows each on average in the Netherlands (Research, 2021; van der Peet et al., 2018). A typical cubicle stable for 80 cows has a yearly emission of about 800 kg NH_3 year^{-1} and requires 10 m^2 per cow (800

m^2 in total) (Remmelink et al., 2020, Table 10.19; RIVM, 2021, type A1). Contrary to the closed off and air filtered housing for pigs and chickens, a dairy barn is open and the ammonia-rich air can freely escape. Therefore, we can represent a typical 80-dairy-cow barn as a surface emission source (Theobald et al., 2012), with an emission flux of 45 ppb m s^{-1} (about 32 μg m^{-2}s^{-1}) over an area of 800 m^2.

We identify the individual contributions of ammonia sources to the NH$_3$ molar fraction and surface-atmosphere exchange, with each source of NH$_3$ represented by a unique scalar. In this study, these sources are identified as a background molar fraction (NH$_{3,bg}$) and the NH$_3$ emission plume (NH$_{3,plume}$) from a surface emission source. The sum of these two unique scalars represents the total atmospheric ammonia (NH$_{3,total}$), as would be observed by in-field observations. Here, we modify DALES v4.2 to force the NH$_{3,plume}$ molar fraction to zero at both x edges of the domain (west and east), preventing circulation of the emission plume in x direction.

Further modifications to DALES v4.2 are made to include the remaining processes governing the variability of the atmospheric ammonia budget. The scalar surface flux (F$_{total}$), representing surface atmosphere exchange, is divided between a flux acting on the background scalar (F$_{bg}$) and another flux acting on the emission plume scalar (F$_{plume}$). The magnitude of these two fluxes is weighted by their respective molar fractions (NH$_{3,bg}$ and NH$_{3,plume}$), relative to the total NH$_3$ molar fraction, e.g., $F_{bg} = \frac{NH_{3,bg}}{NH_{3,total}}F_{total}$ for NH$_{3,bg}$.

The final modification adds an additional term to the change in the scalar molar fraction ($\frac{S}{dt}$). This modified change in the scalar molar fraction reads $\frac{dS}{dt} + \frac{R_{chem}}{3600}S$, with R$_{chem}$ representing the gain/loss rate in % hour^{-1} and subscript S representing the scalar molar fraction, which can be substituted by either NH$_{3,plume}$ or NH$_{3,bg}$. The modified DALES v4.2 code used in this study is also freely available online (`http://doi.org/10.4121/19869478`).

4.2.2   Numerical experiments

We simulate the meteorological conditions observed on 8 May 2008 at the Ruisdael Observatory (`https://ruisdael-observatory.nl/cesar/`) at Cabauw in the Netherlands (51.971ºN, 4.927ºE), as described by aan de Brugh et al. (2013) and Barbaro et al. (2015) and Barbaro et al. (2014). The supersite, with a 213 m high mast, is located on flat (agricultural) grassland with an average height of 0.1 m and the surface elevation changes are, at most, a few meters over 20 km. 8 May 2008 is selected as it is widely studied and includes measurements of the NH$_3$ molar fraction. In May 2008, the intensive observational campaign IMPACT/EUCAARI was held, which included ammonia concentration measurements by a MARGA system (aan de Brugh et al., 2012; Mensah et al., 2012) and several additional meteorological variables, including vertical profiles and radiosondes (Kulmala et al., 2011). The meteorology of this day is described in detail by Barbaro et al. (2014), where the experiment is called CESAR2008. Figures 2 and 3 by Barbaro

et al. (2014) show vertical profiles and time series of, among other variables, potential temperature, specific humidity, surface fluxes and boundary-layer heigtt. The case can be characterized as typical clear-sky, fair-weather conditions with an absence of large-scale heat advection. The model is initialized following the conditions as described by Barbaro et al. (2014), and the initial and prescribed meteorological values of the experiment can be found in Barbaro et al. (2014) Table 1.

In the morning, a 1500 m residual layer leads to an overshooting of the boundary layer height around 10:30 CEST, up to roughly 1800 m. In the afternoon (12:30 – 17:00 CEST), CBL growth is weak and the thermodynamic conditions remain relatively constant (Barbaro et al., 2014). Therefore, we only study the turbulent dispersion in the afternoon, when the impact of boundary layer dynamics on the NH_3 budget is minimal. The wind speed is moderate at 5.5 to 7 m s^{-1} in the afternoon, resulting in strong shear production near the surface and a strong momentum entrainment at the CBL top. The convective timescale (τ) in the afternoon is typical for convective fair-weather conditions, increasing from 18 to 27 minutes between 12:30 and 17:00 CEST. The Monin-Obukhov length fluctuates around approximately -50 m.

The numerical experiments are split into three phases: the meteorological spin-up phase, the buffer phase and the analysis phase. During the meteorological spin-up, 8:00 – 12:30 CEST, the ammonia surface-atmosphere exchange and chemical transformations are not active. These processes are activated at the start of the buffer phase, from 12:30 – 14:00 CEST. Entrainment is still an important factor until around 13:00 CEST, causing large fluctuations of the NH_3 molar fraction (> 4 ppb) as will be discussed in Section 4.3.1. The CBL is considered well-mixed around 13:00 CEST, but we extend the buffer phase with one more hour. We do so to minimize the impact of earlier entrainment on the one-hour moving average used to calculate statistics during the analysis phase. The analysis phase therefore starts at 14:00 CEST until the collapse of the CBL around 17:00 CEST. The analysis phase is the focus of this study and it is when we analyze the impact of the emission plume on (simulated) point measurements of the NH_3 concentration and flux.

4.2.3   Quantifying the emission plume impact on NH_3 measurements

Inspired by the plume observation study by Mylne and Mason (1991), we introduce three variables to assess the presence of the emitted NH_3 plume and relevance of the plume fluctuations to nearby observations. These variables - intermittency factor (I), fluctuation intensity (fI) and NH_3 flux (F) - are all defined by fluctuations in the NH_3 molar fraction. Fluctuations in the NH_3 molar fraction result from the turbulent mixing of differences in NH_3, caused by local sinks and sources. NH_3 fluctuations are therefore found in the background molar fraction as a result of ammonia-poor air near the surface (deposition) and the top of the CBL (entrainment). NH_3 fluctuations are further enhanced in proximity to heterogeneous surfaces. A strong local emission source (e.g., a dairy barn), as presented
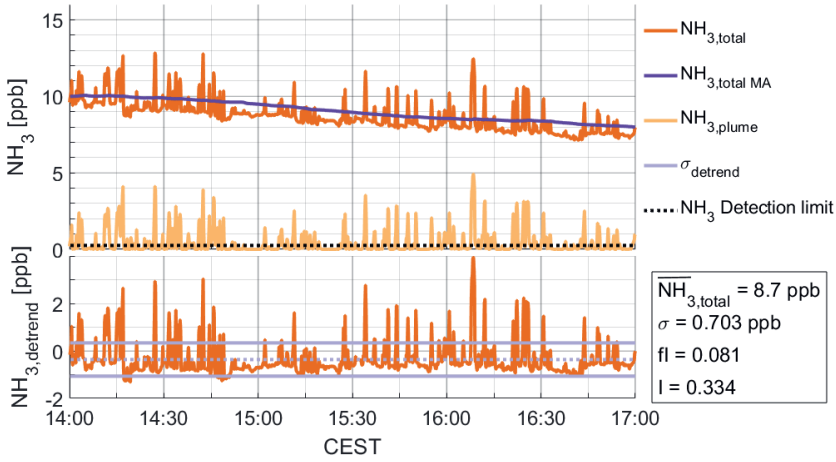
Figure 4.1: Top panel shows 10 s time series of $NH_{3,total}$ (orange) and $NH_{3,plume}$ (yellow) during the analysis phase, at 250 m from the emission source. The detrended $NH_{3,total}$ (orange) is shown in the bottom panel. Fluctuation intensity and intermittency are calculated following Eq. 4.4 and 4.1, respectively, based on the mean $NH_{3,total}$, standard deviation (light purple) and NH_3 detection limit (dotted black).

in this study, will cause an emission plume as the enhanced NH_3 molar fraction is mixed with the background molar fraction through turbulent mixing. Turbulent models like DALES explicitly resolve this turbulent mixing at a high spatial-temporal resolution and can provide valuable information in the interpretation of in-field observations where surface heterogeneity plays an important role.

We first introduce the intermittency factor (I) to quantify the detectability of the emission plume. Intermittency is defined as the proportion of time during which the plume molar fraction is above the detection limit of instruments typically used to measure atmospheric ammonia, as seen in Fig. 4.1 and Eq. 4.1, where N is the number of time steps.

$$I = \frac{1}{N} \sum_{i=1}^{N} \begin{cases} 1, & \text{if } NH_{3,plume}(i) \geq 0.25 ppb \\ 0, & \text{if } NH_{3,plume}(i) < 0.25 ppb \end{cases} \tag{4.1}$$

Note that the intermittency is calculated for each individual grid point during the analysis window (14:00 - 17:00 CEST) at 10 s temporal resolution. We set the NH_3 detection limit at 0.25 ppb, similar to the detection limit of the miniDOAS instrument used in the Dutch ammonia monitoring network (Berkhout et al., 2017). The concept of intermittency cannot be applied to $NH_{3,bg}$ or $NH_{3,total}$, as the background molar fraction always exceeds 0.25 ppb in our numerical experiments, which would result in an intermittency of 1. We therefore only calculate the intermittency for $NH_{3,plume}$ to analyze the detectability of the emission plume.

The second variable, fluctuation intensity (fI), determines the magnitude of the NH_3 fluctuations, i.e., NH_3 standard deviation (σ_{NH_3}), relative to the mean NH_3 molar fraction ($\overline{NH_3}$). Fluctuation intensity is defined following Eq. 4.2:

$$fI = \frac{\sigma_{NH_3}}{\overline{NH_3}}$$
(4.2)

The fluctuation intensity quantifies the level of turbulent mixing. High fI indicates that there are large fluctuations in the measured NH_3, which can introduce a positive bias in measurements. In the field of plume dispersion, high fI is found close to the source where plume meandering dominates the mixing process (Dosio and Vilà-Guerau de Arellano, 2006), or at the edge of the emission plume as a result of lateral entrainment of air from outside the plume (Gailis et al., 2007; Mylne and Mason, 1991; Ražnjević et al., 2022). When analyzing the fluctuation intensity of $NH_{3,\text{total}}$, we have a consistent reference for the fluctuation intensity in $NH_{3,\text{bg}}$. Comparing the fI for the total ammonia (fI_{total}) to the fI for the background ammonia (fI_{bg}) enables us to quantify the relative impact of the emitted NH_3 plume to a simulated measurement. When fI_{total} is of the same order of magnitude as fI_{bg}, we consider the emission plume indistinguishable from the background NH_3, i.e., the plume is well mixed. Note that for $NH_{3,\text{ plume}}$, the average NH_3 concentration is (very close to) zero outside the emission plume, which could lead to an infinitely large fluctuation intensity following Eq. 4.2. Therefore, fI is only calculated inside the plume using an arbitrary requirement of $\overline{NH}_{3,\text{plume}} > 10^{-5}$ ppb.

Fig. 4.1 shows a downward trend in $NH_{3,\text{bg}}$ and $NH_{3,\text{total}}$, resulting from surface deposition and the loss by chemical gas-aerosol transformations. To minimize the impact of this downward trend on σ_{NH_3}, we detrend the simulated molar fraction by subtracting a 1 hour leading moving average ($NH_{3,\text{MA}}$), following Eq. 4.3 and shown in Fig. 4.1. The detrended molar fraction ($NH_{3,\text{detrend}}$) is assumed to only represent turbulent fluctuations and is used to calculate the standard deviation to derive fluctuation intensity. By using $NH_{3,\text{detrend}}$ to calculate σ_{NH_3}, the fluctuation intensity follows from Eq. 4.4.

$$NH_{3,detrend} = NH_3 - NH_{3,MA}$$
(4.3)

$$\begin{aligned} fI &= \frac{\sigma_{NH_3}}{\overline{NH_3}} \\ &= \frac{\sqrt{\frac{1}{N-1}\sum_{i=1}^{N}|NH_{3,detrend} - (\overline{NH_{3,detrend}})|^2}}{\overline{NH_3}} \end{aligned}$$
(4.4)

Finally, we introduce the 30 minute NH_3 flux, studied to mimic the in-field ammonia eddy covariance flux measurements and calculated following Eq. 4.5. The flux presented in this

study is the average 30 minute flux for each individual grid point over the analysis phase between 14:00 and 17:00 CEST.

$$F_{NH_3} = \overline{NH_3' w'} \tag{4.5}$$

4.2.4 The concept of blending distance

We use the fluctuation intensity and flux to quantify the impact of the emission plume on the simulated NH_3 molar fraction and flux measurements, by introducing the concept of blending distance. The blending distance is based on the percentage change (PC_X) in the simulated NH_3 measurements resulting from the emission plume, i.e., the percentage change between $NH_{3,total}$ and $NH_{3,bg}$. PC_X is calculated following Eq. 4.6, where X can be substituted by either fI or F.

$$PC_X = |\frac{X_{total} - X_{bg}}{X_{bg}}| * 100\% \tag{4.6}$$

Based on this percentage change, we define a threshold for which we assume that the impact of the emission plume is negligible. The blending distance (BD_X) is defined as the maximum distance at which PC_X drops below the threshold level (e.g., $PC_X < 25\%$), following Eq. 4.7.

$$BD_X = max(\ dist(\ PC_X < threshold \ ) \ ) \tag{4.7}$$

In this study, we present blending distances based on an arbitrary set of threshold levels, ranging from 5% to 50%.

The concept of blending distance is applied to the fluctuation intensity (BD_{fI}) and the NH_3 flux (BD_F) to quantify the impact on the simulated NH_3 measurements of NH_3 molar fraction and flux, respectively. For context, we also present the intermittency in Section 4.3.2 to quantify the detectability of the plume.

4.2.5 blending distance sensitivity

A key aspect of the study is to determine the sensitivity of the concept of the blending distance to variations in meteorological and NH_3 pollution factors. This is in order study the impact of each process on the blending distance and to identify the driving variables. We study the sensitivity of the blending distance for fluctuation intensity and NH_3 flux by varying the geostrophic wind speed (u_g), initial background molar fraction (C_{bg}) at the start of the analysis phase, emission strength (E), deposition strength (D), chemical conversion rate (R), simulation height (H) and model grid resolution (Δ). Table 4.1 presents the suite of numerical experiments in this study. A single numerical experiment was performed for the sensitivity studies of the NH_3 background, emission, deposition and chemistry, each with separate scalars for $NH_{3,bg}$ and $NH_{3,plume}$. This single experiment,

Table 4.1: Parameter names, symbols, reference values and their respective variations for the sensitivity study of the blending distance, with the reference settings highlighted in bold.

Parameter	Symbol	Reference experiment	Variations				
Geostrophic wind speed	u_g	8 m s^{-1}	2	4	6	**8**	10
Initial NH$_{3\ bg}$	C_{bg}	10 ppb	5	**10**	15	25	
NH$_3$ emission strength	E	45 ppb m s^{-1}	**45**	100	150	200	
NH$_3$ deposition strength	D	-0.045 ppb m s^{-1}	0	-0.025	**-0.045**	-0.075	-0.0100
NH$_3$ chemical conversion rate	R	5% hour^{-1}	0	**5**	15	25	
Simulated measurement height	H	37.5 m	7.5	12.5	...	112.5	117.5
Model resolution	Δ	20 m x 20 m x 5 m	10 x 10 x 2.5	**20 x 20 x 5**	50 x 50 x 15		

which does not include the variations in the geostrophic wind speed nor the high-resolution experiment, generates just under 1 TB of model output with a computational cost of about 64.000 SBU (System Billing Unit, i.e., the usage of one processor of the Cartesius supercomputer system for one hour).

The sensitivity study is structured from large-scale processes to small-scale processes and modeling numerics. Starting with mesoscale processes, we vary the geostrophic wind speed to study the impact of the atmospheric stability on blending distance, i.e., a shear or convection-dominated CBL. Atmospheric stability plays a key role in the turbulent mixing of local sources (emission) and sinks (entrainment and deposition), affecting both the fluctuations in the background molar fraction and the mixing of the emission plume (Dosio et al., 2003). Next, we study the sensitivity of BD to different levels of the background NH$_3$ at the start of the analysis window, representing different levels of regional NH$_3$ pollution. Additionally, varying the background levels of ammonia changes the NH$_3$ inversion at the top of the CBL, affecting the impact of entrainment. Next, the emission strength is varied, in order to study the local effect of different emission strengths.

Furthermore, we study the sensitivity of both BD$_{fl}$ and BD$_F$ to NH$_3$ deposition and the chemical gas-aerosol transformation. These are dynamic processes, i.e., experiencing clear diurnal and seasonal variability, mainly related to temperature, humidity and pollution levels (aan de Brugh et al., 2013; van Zanten et al., 2010; Wichink Kruit et al., 2010b). Our simulation approach, with a simplified representation of deposition and chemistry, allows us to distinctly study the role of these two processes.

Finally, we study the sensitivity of BD to choices made in the numerical setup of the experiments. We vary the height of the simulated measurements. The numerical experiments are generally taken at a simulated height of 37.5 m. This is a trade-off between simulating measurements close to the surface to mimic in-field observations and the resolved turbulent kinetic energy (TKE$_{res}$) of the model. The TKE$_{res}$ at the lowest level of DALES (at 2.5 m) is zero due to the no-slip boundary at the surface (Heus et al., 2010). When we aim for a TKE$_{res}$ of 75% at all three (vertical) resolutions, we find TKE$_{res}$ of 76%, 95% and 96% for the low, middle and high resolution at 37.5 m (36.25 m for high resolution). Additionally, it is also expected that varying the measurement height will allow practical insight for in-field observations. Finally, the sensitivity of the blending distance to changes in resolution is studied with two new numerical experiments with higher and lower resolutions of 10 m x 10 m x 2.5 m (1000 x 480 x 1200 grid points) and 50 m x 50 m x 15 m (200 x 96 x 200 grid points), respectively.
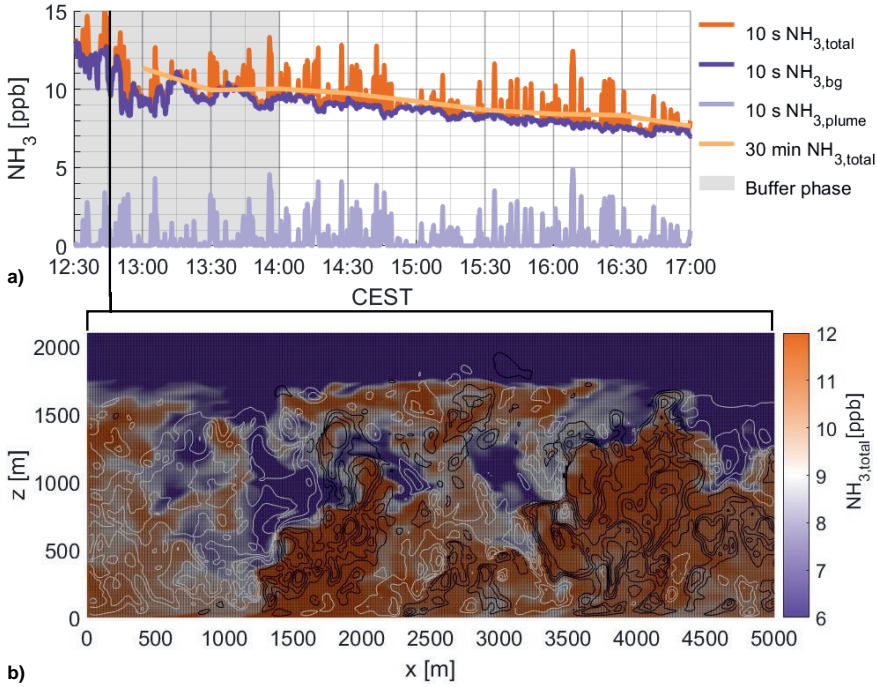
Figure 4.2: 10 s time series (a) of $NH_{3,total}$ (orange), $NH_{3,bg}$ (purple) and $NH_{3,plume}$ (light purple) during the buffer phase (gray area) and the analysis phase, taken at 250 m distance from the emission source. The large high-frequency fluctuations shown (> 4 ppb) are not captured by the 30 minute average of $NH_{3,total}$ (light orange). The vertical xz cross-section at 12:46 CEST (b), displays high spatial variability during the buffer phase in $NH_{3,total}$ (> 4 ppb) over short distances (hundreds of meters). The black/white contour lines represent upward/downward wind speeds in steps of 0.5 m s^{-1}.

4.3   Results

4.3.1   Qualitative analysis of the NH₃ emission plume impact

The concept of blending distance is based on fluctuations in the NH_3 molar fraction. To better understand the sources of these fluctuations, we first study the time series of a "virtual" point measurement at 250 m horizontal distance from the emission source, shown in Fig. 4.2a. Our simulation framework allows us to distinguish the individual contributions of $NH_{3,bg}$ (purple) and $NH_{3,plume}$ (light purple) to $NH_{3,total}$ (orange). Here we find that the large $NH_{3,total}$ fluctuations are mainly ascribed to $NH_{3,plume}$.

As discussed in Section 4.2.3, fluctuations are also found in the background molar fraction ($NH_{3,bg}$), leading to non-zero fl$_{bg}$. Fluctuations $NH_{3,bg}$ are a result of heterogeneous

turbulent mixing. In this study, the fluctuations are caused by vertical gradients only, as we use a homogeneous surface in the simulation of NH$_{3,\,bg}$. These vertical gradients are found near the surface and at the top of the CBL. At the surface, the surface-atmosphere exchange (deposition) decreases the NH$_3$ molar fraction, which results in a vertical gradient in NH$_{3,bg}$. At the top of the CBL, the vertical gradient is a result of the turbulent exchange with the free troposphere (entrainment). Fig. 4.2b shows that the intrusion of NH$_3$-low air masses from the free troposphere are transported by the downdraft subsidence motions, resulting in large fluctuations in NH$_{3,bg}$ in the boundary layer. As shown in Fig. 4.2a, the amplitude of these fluctuations can reach 4 ppb and can last for over 5 minutes. When averaging over 30 minutes, even the large fluctuations between 12:30 and 13:15 are filtered out, but these high-frequency turbulent fluctuations could still be present in raw measurement data of high-resolution in-field observations.

Now that we understand the source of the NH$_3$ fluctuations, we take a closer look at the emission plume without any background NH$_3$. The xy plot in Fig. 4.3a shows low fI in the plume center (≈ 2) and a strong increase near the plume edges, up to fI ≈ 30. This is echoed by the plume transects, as they show the typical "U-shape" found for Gaussian plumes (Gailis et al., 2007; Mylne and Mason, 1991; Ražnjević et al., 2022). These high fI values at the edges of the plume are a result of very low average molar fractions combined with low intermittency. This leads to a high standard deviation, relative to the very low averaged molar fraction, at the plume edges. Without background NH$_3$, it is at the edges of the plume that in-plume lateral entrainment of ammonia-free air happens, diluting the emission plume by turbulent mixing.

The intermittency cross-section in Fig. 4.3b shows that maximum I is only a little over 0.3, resulting from the meandering of the plume. Figure 4.3b also shows that with an NH$_3$ detection limit of 0.25 ppb, the plume can be detected up to a distance of about 2.0 km from the source.

The cross-section of fI changes dramatically when analyzing NH$_{3,total}$, the sum of NH$_{3,bg}$ and NH$_{3,plume}$. With the addition of a non-zero background molar fraction, fI can be calculated over the whole domain, as shown in Fig. 4.3c. Now, we find a much lower fluctuation intensity, with a maximum of 0.08 for NH$_{3,total}$ compared to 30 for NH$_{3,plume}$. The U-shape shown in the transect of Fig. 4.3a is replaced by an approximately Gaussian shape, with the highest fluctuation intensities at the centerline of the plume. This centerline fI decreases with distance from the source and becomes indistinguishable from the out-of-plume fI after approximately 1 km distance, i.e., a rough estimate for BD$_{fI}$.

Finally, Fig. 4.3d shows that the emission plume leads to a positive flux (emission) for NH$_{3,total}$ in proximity to the emission source, while the flux is negative (deposition) outside the plume. Note that significant fluctuations are found in the flux over the full domain, with $\sigma_{F,bg} = 0.0065$ ppb m s^{-1} (prescribed $F_{sfc.} = -0.045$ ppb m s^{-1}) for NH$_{3,bg}$. Similar to fI$_{total}$ in Fig. 4.3c, the transects for the NH$_3$ flux are approximately Gaussian in shape,
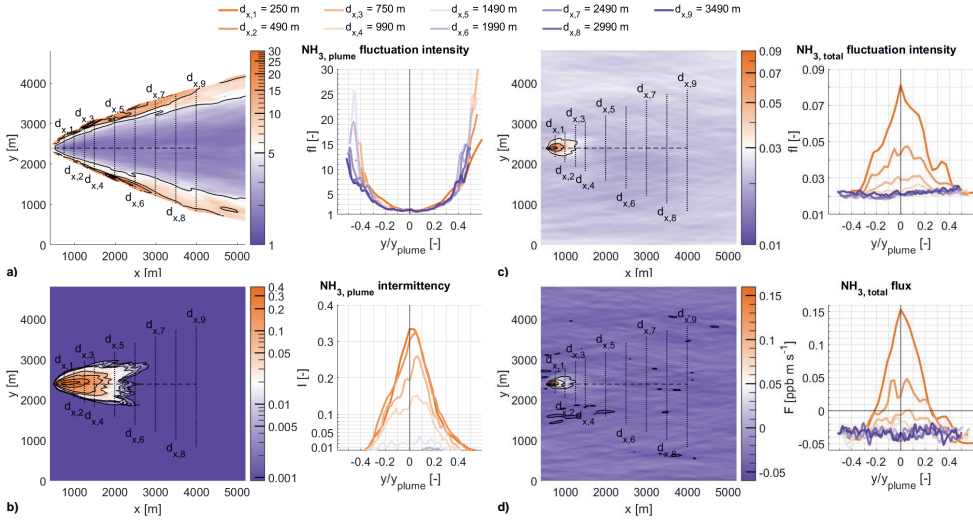
Figure 4.3: The xy cross-sections at 37.5 m with y transects through the NH$_3$ emission plume for the NH$_{3,\text{plume}}$ fluctuation intensity (a), intermittency (b), NH$_{3,\text{total}}$ fluctuation intensity (c) and NH$_{3,\text{total}}$ flux (d). The plume transects are labeled d$_{x,1}$ to d$_{x,9}$ for increasing x distance from the NH$_3$ emission source and normalized by plume width for NH$_{3,\text{plume}}$ > 10^{-5} ppb. The data presented are calculated during the analysis phase (14:00 and 17:00 CEST) at 37.5 m

.

with peak values close to the plume centerline at $y/y_{plume} = 0$. After approximately 1 km at the approximate plume centerline, the in-plume flux becomes visually indistinguishable from the background, i.e., a rough estimate for BD$_F$. This positive anomaly is the result of the emission source being within the footprint of these receptors.

4.3.2 Quantitative analysis of the NH$_3$ emission plume impact

We apply the concept of blending distance in Fig. 4.4 to the fluctuation intensity (a), flux (b) and intermittency (c). The markers represent the value at each individual grid point on the 37.5 m horizontal plane, the continuous orange line represents the grid point with the highest value within a 50 m moving window (maximum), the orange dotted line represents the plume centerline and the purple dashed and continuous lines represent the blending distances for their respective threshold.

We interpret the calculation of the blending distance based on four arbitrary threshold levels (5%, 10%, 25% and 50%) for fI and F, shown in Fig. 4.4a and b. The distance at which the maximum value of PC$_X$ drops below the threshold level is the blending distance. The sensitivity of BD to these thresholds will be discussed in detail in Section 4.4.1, using Fig. 4.6 and 4.7. Additionally, the intermittency in Fig. 4.4c shows that the emission plume is quantifiable up to over 2.4 km distance.
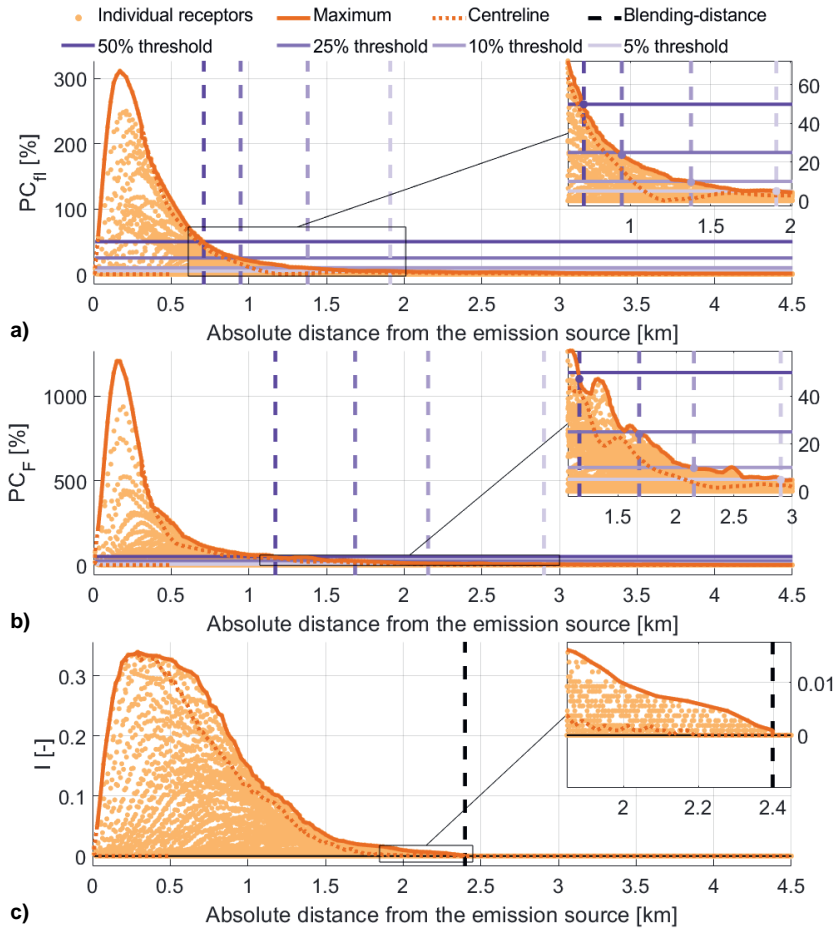
Figure 4.4: The percentage change of NH$_{3,total}$ relative to NH$_{3,bg}$ against absolute distance from the NH$_3$ emission source. The panels show fluctuation intensity (a), NH$_3$ flux (b) and intermittency (c). The maximum value within a 50 m moving window (orange) and the plume centerline (dotted orange) are highlighted. blending distances (purple dashed) are calculated based on four thresholds at 5%, 10%, 25% and 50% (purple continuous).

Starting with the fluctuation intensity (Fig. 4.4a), PC$_{fl}$ peaks at a relative change of about 300%, caused by the NH$_3$ emission plume. BD$_{fl}$ decreases nonlinearly from 0.7 km to 1.9 km with the thresholds decreasing from 50% to 5%. Figure 4.4b shows that the emission plume has a larger impact on NH$_3$ flux measurements than on the fluctuation intensity of the NH$_3$ molar fraction. The large difference between the emission strength (45 ppb m s^{-1}) and the deposition (-0.045 ppb m s^{-1}) results in a maximum PC$_F$ of about 1200% in close proximity to the emission source. The long tail of PC$_F$ indicates that the turbulent
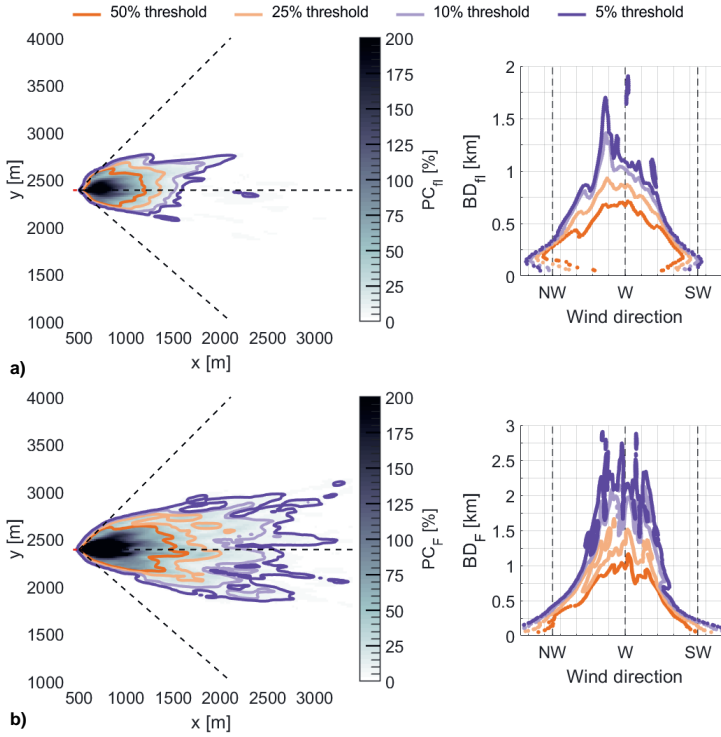
Figure 4.5: The left panels show the spatial structure of the percentage change in grayscale for the fluctuation intensity (PC_{fl}) in (a) and the ammonia flux (PC_F) in (b). The colored contour lines show the locations where the 50% (orange), 25% (light orange), 10% (light purple) and 5% (purple) thresholds are met, representing the blending distance (BD). The right panels show these blending distances as a function of different angles from the plume centerline (W), with these angles representing the wind direction.

fluctuations in the emission plume affect flux measurements over several kilometers. As a result, BD_F increases from 1.2 km to 2.9 km for decreasing thresholds, significantly longer distances than our 1 km qualitative estimate based on Fig. 4.3d. Note that Fig. 4.3d shows that the flux changes signs in proximity to the emission source and that this sign change is not reflected in Fig. 4.4b.

Figure 4.4 shows that the centerline and the maximum statistics give similar results, indicating that the highest values of PC are found at the plume centerline, however with some variability. These variabilities are visualized in Fig. 4.5, which shows the spatial structure of the percentage change in grayscale for the fluctuation intensity (PC_{fl}) in (a) and the ammonia flux (PC_F) in (b). The colored lines in these panels represent the blending distances for different thresholds. The right panels show these same blending
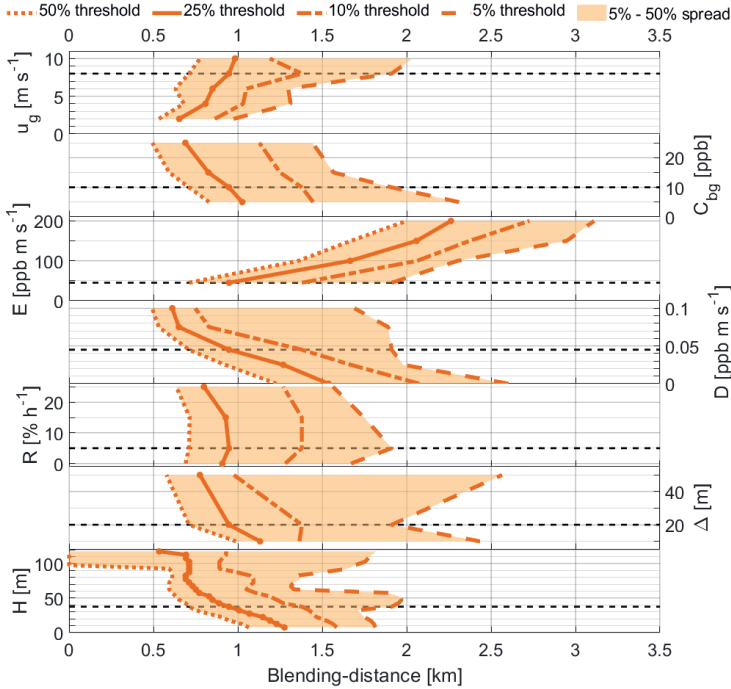
Figure 4.6: The sensitivity of BD_{fI} to the geostrophic wind speed (u_g), initial background molar fraction (C_{bg}), emission strength (E), deposition strength (D), chemical reaction rate (R), model resolution (Δ) and simulated measurement height (H). BD_{fI} is determined for threshold levels ranging from 5% (orange dashed) to 50% (orange dotted).

distances for different angles from the plume centerline (W), representing different wind directions. Fig. 4.5 shows large variability in the blending distance, especially for the 5% and 10% threshold levels, as a result of the chaotic nature of turbulence.

4.4   Discussion

4.4.1   Sensitivity of blending distance to meteorological and NH₃ pollution variables

We study the sensitivities of BD_{fI} and BD_F to a range of meteorological, NH₃ pollution parameters and model resolution and simulated measurement height (Table 4.1). The results of the sensitivity study are shown in Fig. 4.6 and 4.7 for an arbitrary set of thresholds ranging from 5% (orange dashed) to 50% (orange dotted), representing the maximum acceptable difference in fI and F caused by the emission plume in %.

Starting with BD_{fl}, Fig. 4.6 shows that BD_{fl} ranges roughly between 0.5 and 3.0 km, a first-order estimate of the minimum distance for NH_3 molar fraction measurements. There is a negative correlation between BD_{fl} and the choice in threshold, i.e., increasing the threshold level decreases BD_{fl}. We generally find that BD_{fl} decreases nonlinearly by approximately 1.0 km when increasing the threshold level from 10% to 50%, halving BD_{fl}, highlighted by the large difference between the 10% (dashed-dotted) and 5% (dashed) threshold levels for both BD_{fl} and BD_F. We discuss the individual variables of Fig. 4.6 from top to bottom, starting at the mesoscale (u_g), down to the micrometer scale (R) and finishing with the model resolution and simulated measurement height.

The geostrophic wind speed (u_g) is one of the main drivers of turbulent mixing and transport of the plume (Dosio and Vilà-Guerau de Arellano, 2006; Dosio et al., 2003; Vrieling and Nieuwstadt, 2003). Figure 4.6 shows a positive correlation between BD_{fl} and u_g. By varying u_g we move from a convection-driven boundary layer ($u_g = 2$ m s^{-1}) to more shear-driven meteorological conditions ($u_g = 10$ m s^{-1}). In a convection-driven boundary layer, turbulent mixing is rather weak and the NH_3 emission plume rises from the surface as convection plumes are the main drivers of turbulent mixing. Under these conditions, in-plume molar fractions are very high, but horizontal transport of the emission plume is weak, resulting in a low BD_{fl}. For shear-driven conditions, the NH_3 emission plume tends to stick to the surface as the increased horizontal wind speed enhances horizontal transport and turbulent mixing. The enhanced horizontal transport and emission plume sticking to the surface should significantly increase BD_{fl}, but the enhanced turbulent mixing counteracts these processes by reducing the $NH_{3,plume}$ molar fraction and fluctuations. This is shown in Fig. 4.6 and explains why the sensitivity of BD_{fl} increases for lower threshold levels (5%), as smaller plume fluctuations will reach long distances in shear-driven conditions.

One panel below, Fig. 4.6 shows a negative correlation between BD_{fl} and the initial background molar fraction (C_{bg}), i.e., the regional level of NH_3 pollution. The first cause of the negative correlation is the higher average molar fraction, which lowers the relative weight of the $NH_{3,plume}$ fluctuations (σ_{plume}) when fI_{total} is calculated following Eq. 4.2. Additionally, increasing $NH_{3,bg}$ leads to a large difference in the NH_3 air mass characteristics at the top of the boundary layer. The exchange between the boundary layer and free tropospheric air masses through entrainment increases σ_{bg} at 37.5 m from 0.13 ppb ($C_{bg} = 5$ ppb) to 0.38 ppb ($C_{bg} = 25$ ppb), resulting in an increased fI_{bg}. Both processes reduce the magnitude of PC_{fl} with increasing C_{bg} and reducing BD_{fl}.

At the local scale, Fig. 4.6 shows a clear positive and negative correlation when varying emission strength (E) and deposition strength (D), respectively. Both variables directly affect one of the main drivers of turblent mixing - heterogeneity. Increasing the NH_3 emission strength of the local (heterogeneous) source directly increases fI_{plume}, increasing BD_{fl}. Varying the deposition on the other hand, directly affects the vertical gradient of

the NH$_3$ molar fraction near the surface, increasing fI$_{bg}$ for increasing D and therefore reducing BD$_{fI}$.

We only briefly touch upon the chemical conversion rate (R), as Fig. 4.6 shows that varying R does not significantly affect BD$_{fI}$. R is applied uniformly to the 3D domain and has little effect on turbulent mixing. Note that our simplified representation of chemistry could lead to a potential underestimation of the impact of chemistry on BD$_{fI}$, as our approach is unable to resolve potential nonlinear effects of turbulent mixing on the in-plume chemical reaction rate near the emission source (see discussion in Section 4.4.2).

Next, we vary the model resolution (Δ) in Fig. 4.6 and find that BD$_{fI}$ is weakly sensitive to the model resolution. The results indicate that the calculation of the blending distance does benefit by increasing the simulation resolution. However, there is a trade-off between the computational costs of the simulation and the resolution.

Finally, Fig. 4.6 shows two regimes in the sensitivity of BD$_{fI}$ to the simulated measurement height (H). For the 50% threshold, BD decreases by about 500 m with height up to 90 m. Above 90 m, there is a transition where BD$_{fI}$ rapidly goes to zero. In this second regime, the simulated measurements are located above the plume centerline. Thereon, fI$_{plume}$ rapidly decreases with height until PC$_{fI}$ does not reach the 50% threshold and BD$_{fI}$ becomes zero. This rapid decrease is a result of the simulated measurements being located above the emission plume, as the height of the plume does not reach above 150 m for the first 1.5 km horizontal distance. The height of this transition increases with decreasing threshold levels as the thresholds become more sensitive to smaller NH$_{3,plume}$ fluctuations.

Figure 4.7 shows the results of the sensitivity study for BD$_F$ (Table 4.1). Both the blending distance for molar fraction measurements (BD$_{fI}$) and for flux measurements (BD$_F$) can be interpreted as an inverse footprint analysis, as we estimate the area affected by the emission source. The results of the sensitivity study of BD$_F$, however, are different from the BD$_{fI}$ results, as the footprints for flux and molar fraction measurements are not the same. The footprint for flux measurements is smaller than those of molar fraction measurements (Kljun et al., 2003; Rannik et al., 2000; Vesala et al., 2008). However, comparing BD$_{fI}$ to the footprint of NH$_3$ molar fraction measurements is not straightforward, as BD$_{fI}$ is based on the NH$_3$ fluctuation intensity, not the molar fraction. It is therefore interesting to determine whether the results of the sensitivity study of BD$_F$ will differ compared to the results of BD$_{fI}$.

When analyzing Fig. 4.7, we find that there are indeed differences between BD$_F$ and BD$_{fI}$. BD$_F$ is significantly longer, ranging from 0.75 to roughly 5 km, indicating that NH$_3$ flux measurements are more sensitive to the emission plume. Note that we removed the results for D = 0 ppb m s^{-1}. Here, F$_{bg}$ approaches zero, resulting in infinitely large PC$_F$ and unrealistic BD$_F$ values, following Eq. 4.6.
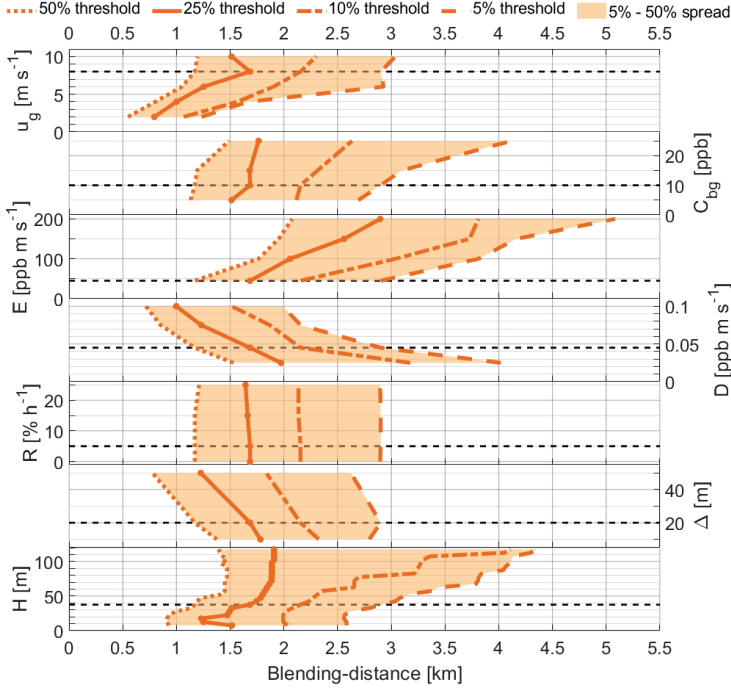
Figure 4.7: The sensitivity of BD_F to the geostrophic wind speed (u_g), initial background molar fraction (C_{bg}), emission strength (E), deposition strength (D), chemical reaction rate (R), model resolution (Δ) and simulated measurement height (H). BD_F is determined for threshold levels ranging from 5% (orange dashed) to 50% (orange dotted).

One of main differences between BD_F and BD_{fl} is found in the sensitivity to the threshold levels (5% to 50%). BD_F is more sensitive to the different threshold levels compared to BD_{fl}. This is in agreement with the results shown in Fig. 4.4b, where we discussed that PC_F is significantly larger than PC_{fl}, with a longer tail. As a result, the nonlinear effect of the aforementioned long tail in PC_F (Fig. 4.4b) increases BD_F for low threshold levels. Despite these differences, the same arbitrary set of thresholds is used for both BD_{fl} and BD_F.

Significant differences between BD_F and BD_{fl} are also found in the sensitivity to the geostrophic wind speed (u_g) and the simulated measurement height (H). Both variables directly affect the footprint of the simulated flux measurements. In shear-driven turbulent conditions (high u_g), the footprint of the measurement is elongated compared to convective conditions. This reduces the width of the footprint and lengthens the up-wind distance at which the emission source can be measurement, thus, increasing BD_F. Increasing H also increases the footprint of the measurements, but there is no elongation of the footprint.

As a result, BD$_F$ has a strong positive correlation to u$_g$, but is only weakly correlated to H, except for the lower threshold levels.

Figure 4.7 appears to show that BD$_F$ has a weak positive correlation with increasing C$_{bg}$. This is mainly attributed to an increase in the spatial variations of the background NH$_3$ flux, which increases from $\sigma_{F,bg}$ = 0.0065 ppb m s^{-1} for C$_{bg}$ = 10 ppb (Fig. 4.3d) to $\sigma_{F,bg}$ = 0.015 for C$_{bg}$ = 25 ppb. As a result, the fluctuations in PC$_F$ shown in Fig. 4.4b increase in amplitude and frequency, which particularly affects the low threshold levels of 5% and 10% .

There are also strong similarities between the sensitivity of BD$_F$ and BD$_{fl}$. Both Fig. 4.6 and 4.7 show that the blending distance is only weakly sensitive to the chemical reaction rate (R) and the model resolution (Δ). For both molar fraction and flux measurements, the emission strength (E), deposition (D) and, to a lesser extent, the geostrophic wind speed (u$_g$) are the driving variables of the blending distance.

4.4.2   Uncertainty of the blending distance estimation

The turbulent dispersion of the emission plume is chaotic by nature and driven by a wide range of factors. We therefore carry out a systematic analysis on how these factors and resolution, influence the relationships between emissions and the simulated in-field measurements. The chaotic nature of turbulence results in random variations in both the emitted NH$_3$ (Fig. 4.3a and b) and the background NH$_3$ (Fig. 4.3c and d). These random fluctuations lead to variability in the calculation of the blending distances, leading to uncertainty in the blending distances presented in this study. The variability increases when using the lower threshold levels (e.g., 5% and 10%), as is visualized and discussed in Section 4.3.1 and 4.3.2. The variability could be reduced by increasing the length of the analysis window, i.e., increasing the averaging time to filter out the small and short spatio-temporal turbulence variability.

Increasing the length analysis window, however, means that the blending distance is calculated using a wider range of boundary layer dynamics and variations in the thermodynamic variables. Boundary layer dynamics are especially relevant in the morning and early afternoon when the boundary-layer grows and air from the residual layer and free troposphere is entrained, or in the afternoon when turbulence decays (Pino et al., 2006). It leads to entrainment being one of the dominant processes driving the NH$_3$ diurnal variability (Schulte et al., 2021; Wichink Kruit et al., 2007). In Fig. 4.2 we show that it leads to large fluctuations in NH$_{3,\ bg}$, significantly increasing fl$_{bg}$. We therefore filter out the impact of boundary layer dynamics and variations in the thermodynamic variables with our choice of analysis window from 14:00 and 17:00 CEST, in order to find a first-order estimate of the blending distance. We do recommend a follow-up study on the role of boundary dynamics.

Finally, there is a downside to our simplified representation of chemical transformations in that it is applied uniformly to the 3D domain. In reality, the equilibrium molar fractions for these chemical transformations are related to temperature and humidity and results in a near-surface NH_3 gradient of the NH_3 molar fraction (aan de Brugh et al., 2013). Therefore, we are likely to underestimate the role of chemical transformations and overestimate BD_{fl}, as turbulent mixing of this near-surface gradient increases fI_{bg}.

The blending distance cannot be captured by a single number. This is partly due to the uncertainty involved in calculating the blending distance, but the blending distances is, most of all, an integrated variable. Several processes are captured by the blending distance in one single variable, including the chaotic nature of turbulent plume dispersion, convective and shear-induced turbulence, atmospheric pollution levels and surface heterogeneity. As shown in Section 4.4.1, each of these processes impacts the blending distance differently. Despite its complexity, the blending distance is a useful variable since it is an integrated variable; all the aforementioned processes are represented in this distance at which the impact of an emission plume is negligible with respect to the background.

The applicability of the results presented here depends not only on the meteorological and NH_3 pollution factors, but also on the physical context of the measurement site. This study is based on the Ruisdael Observatory at Cabauw, which is located on flat agricultural grassland with surface elevation changing only by a few meters over 20 km. A different physical context, like a heterogeneous surface which changes the turbulent properties (Ouwersloot et al., 2011), is likely to significantly affect the resulting blending distances. With the simulation framework presented here, the blending distance can be calculated for specific weather conditions and for the physical context of the measurement site, providing a more accurate assessment of the impact of nearby emissions on NH_3 observations at a specific measurement site. The results presented in this study provide a valuable first estimate of and discussion on a typical blending distance and its driving variables.

4.4.3   blending distance literature for passive tracers

Evaluating the blending distance results against typical literature on plume dispersion is a difficult exercise. The topic is generally not mentioned as these studies focus on the release of passive scalars in an unpolluted environment, and only few studies even research (near) surface releases (Cassiani et al., 2020). Normalization of both distance from the source and the in-plume molar fraction further complicates the interpretation of literature results.

We therefore try to estimate the order of magnitude of the blending distance based on the in-plume molar fraction and fluctuation intensity of plume dispersion modeling studies. Following figures by Dosio et al. (2003) and Dosio and Vilà-Guerau de Arellano (2006), we find that the in-plume molar fraction rapidly decreases for a convection-driven boundary layer ($-z/L \geq 40$ and $u_*/w_* \leq 0.2$) at the surface up to roughly 6 km distance, after

which, it starts to level off. Similar results are found for the fluctuation intensity; however, the results are less pronounced for the near-surface release experiments. The 6 km distance approximately doubles for shear-driven boundary layers ($-z/L \sim 40$ and $u_*/w_* \sim 0.46$). The observations shown in Figure 10 by Mylne and Mason (1991) show that the observed fluctuation intensity also decreases with distance, but levels after roughly 15 km distance from the emission source. We use these distances at which the plume statistics start to level off as an estimate of the order of magnitude of the blending distance, indicating that the blending distance could be in the order of several kilometers (6 to 15 km), based on plume dispersion literature.

These rough estimates of the 6 to 15 km distance are significantly larger than the blending distances presented in this study. Such long distances between source and measurement site would not make feasible requirements in densely agricultural regions, but are likely an overestimation of the blending distance. These estimates are based on the molar fraction and fI of the emission plume, with no representation of background ammonia levels. The latter is especially important, as we show in Section 4.3.1 and 4.3.2 that the impact of the emission plume rapidly decreases relative to the turbulent background ammonia, while the emission plume itself can be detected for several kilometers as indicated by the intermittency.

4.4.4   blending distance literature for ammonia measurements

Articles on ammonia measurements in close proximity to an emission source implicitly include all relevant processes. These studies could also provide a qualitative, perhaps more realistic, evaluation of the NH$_3$ blending distance results presented here. In-field measurements show that the NH$_3$ molar fraction exponentially decreases with distance from the source, with measurements close to the background molar fraction after 300 to 500 m (Fowler et al., 1998; Shen et al., 2016; Sommer et al., 2009). Similar results were obtained in an intercomparison study of short-range atmospheric dispersion models by Theobald et al. (2012), at horizontal resolutions of 25 - 50 m and receptors at 100 m intervals along four radial directions (N, E, S and W). However, these measurements are typically arranged a few lines downwind of the source, with only a handful of measurements over a distance of 300 to 1000 m. At these short distances, plume dispersion is dominated by meandering of the plume (Nieuwstadt, 1992) and the in-plume molar fraction measurements are underestimated as a result, especially given the averaging times of these measurements ranging from several hours up to multiple weeks.

Finally, we can evaluate our findings against measurement site requirements of air quality networks. The Dutch air quality network and the EMEP (European Monitoring and Evaluation Programme) network do set requirements for the minimum distance from emission sources and no references to scientific studies are provided. Back in 1990, the Dutch network required a minimum distance for NH$_3$ sites of 300 - 500 m from NH$_3$ point

or area sources, depending on source strength (Boermans and Erisman, 1990). This is in line with the literature on measurements in proximity to emission sources discussed earlier, but closer than the blending distances presented here. Currently, no hard requirements are in place in the Netherlands, although the potential impact of NH_3 sources is still recognized (Wichink Kruit et al., 2021). At a European level, EMEP measurement sites require a 2 km minimum distance for measurements nearby the stabling of animals and manure application, depending on the number of animals and field size (EMEP/CCC, 2001; Schaug, 1988). This 2 km distance is in line with our recommendations, although the results in this study indicate that distances below 2 km could also be sufficient.

4.4.5   Towards an NH_3 virtual test bed: integrating fine-scale simulations with advanced observations

This study is the first that specifically addresses the regional representativity of ammonia measurements in proximity to an emission source. The systematic analysis presented in Fig. 4.6 and 4.7 can be used as a reference when interpreting in-field NH_3 measurements. Additionally, the simulation framework can be applied to individual locations to study the representativity of (potential new) measurement sites under local conditions by using the concept of blending distance. One can expand the simulation framework to include multiple sources, area sources - each with an unique passive scalar - and heterogeneous surface conditions (Ouwersloot et al., 2011), to simulate local NH_3 conditions.

The DALES model proved to be flexible, allowing for simulations of a convective, sheared convective, stable and cloud-topped boundary layer (Heus et al., 2010; Verzijlbergh et al., 2009). The fine-scale simulation framework will be included in the Ruisdael Observatory at Cabauw (`https://ruisdael-observatory.nl`), a nationwide observatory for measurements and modeling of the atmosphere and air quality. It can be a powerful tool in future ammonia research, e.g., in preparation of (emission) measurement campaigns or to improve interpretation of NH_3 (flux) measurements. Furthermore, we want to stress that the methods presented here are not limited to ammonia, but can be used for any gas for which relevant processes occur at high spatio-temporal resolutions.

We recommend expanding the simulation framework to create a test bed to study NH_3 at high spatio-temporal resolutions, including all processes relevant to the NH_3 diurnal variability. The main additions should be a dynamic parameterization of the surface-atmosphere exchange, e.g., DEPAC (van Zanten et al., 2010), and a thermodynamic chemistry module, e.g., ISORROPIA version 2 (Fountoukis and Nenes, 2007). With these additions, on top of the existing possibility to distinguish between background and emitted NH_3, the fine-scale simulation framework with explicitly resolved turbulence will be well suited to study short-range dispersion of ammonia, e.g., deposition in close proximity to emission sources and the impact of turbulent micromixing on the chemical reaction rate. These studies are typically performed using models where turbulence is parameterized or

Gaussian plume models are used (Loubet et al., 2006; Sommer et al., 2009; van der Swaluw et al., 2017). Furthermore, the addition of a thermodynamic chemistry module can lead to new insights on NH$_3$ flux measurements. The equilibrium molar fractions of the NH$_3$ gas-aerosol transformations depend on atmospheric temperature and humidity, resulting in a near-surface molar fraction gradient. This gradient leads to an underestimation of the NH$_3$ deposition flux of about 0.02 μg m^{-2}s^{-1}, when using the flux-gradient method (Nemitz et al., 2004b). With these additions to the simulation framework, the virtual NH$_3$ test bed can be used improve the interpretation of NH$_3$ flux measurements.

4.5 Conclusions

This study presents a fine-scale simulation framework with which we assess the regional representativity of the NH$_3$ molar fraction and flux measurements in proximity to a typical NH$_3$ emission source. We aim to translate concepts from the fields of plume dispersion and fine-scale simulations to support the analysis of NH$_3$ observations in areas characterized by NH$_3$ (point) source emissions. This includes realistic representations of NH$_3$ surface-atmosphere exchange and chemical gas-aerosol transformations. The concept of a blending distance is introduced to systematically analyze the impact of the emitted NH$_3$ on simulated measurements, relative to a background concentration. Following this approach, we define a first-order estimate of a minimum distance requirement between regional representative measurements and a typical NH$_3$ emission source.

By means of fine-scale simulation of atmospheric NH$_3$, we investigate the representativity of NH$_3$ measurements from kilometer to meter scales in proximity to a typical emission source. The fine-scale simulation framework presented has proven to be a powerful and flexible tool for future research on ammonia, or any gas for which the relevant processes occur at high spatio-temporal resolutions. The simulation framework, with explicitly resolved turbulence not only enables us to quantify the variability in NH$_3$ measurements, but also to analyze and quantify the individual contribution of the NH$_3$ emission plume. The concept of blending distance presents a consistent criterion, based on second-order statistics, for the minimum distance at which the impact of the emitted NH$_3$ is estimated to be indistinguishable from the variability of the background NH$_3$. Following this approach, we perform several numerical experiments to analyze the sensitivity of the blending distance to a variety of meteorological and NH$_3$ pollution variables, centered around the flat grassland at Ruisdael Observatory at Cabauw. This systematic analysis shows a strong sensitivity to the emission strength, deposition and threshold level used in the calculation, and to the stability of the (convective or shear dominated) boundary layer. Furthermore, we find that the blending distances differ for NH$_3$ molar fraction and flux measurements, with flux measurements being more sensitive to the NH$_3$ emission plume. Following this sensitivity analysis, we conclude that NH$_3$ measurements at the Ruisdael Observatory should be

taken at a minimum distance of 0.5 - 3.0 km or 0.75 - 4.5 km from an emission source for measurements of the NH_3 molar fraction or flux, respectively.

Chapter 5

Sensitivity analysis on how the NH$_3$ blending distance is influenced by meteorological large-scale forcing, diurnal variability and the simultaneous interaction of processes

This Chapter expands on the concept of blending distance based on the thorough review of Chapter 4, by investigating new aspects on how the blending distance responds to changes in the turbulent dynamics of the atmospheric boundary layer

Abstract

The blending distance is an integrated variable that quantifies the impact of an emission plume on near-surface concentration and flux measurements, relative to background pollution levels. The concept was introduced analyzing the dynamics and evolution of turbulent fluctuations in the afternoon, when boundary layer growth is weak and almost in steady state. Here, we expand on the concept of blending distance, performing multiple numerical experiments using a large-eddy simulation technique with high resolution (20 x 20 x 5 m^3, 10 seconds) to study three relevant aspects on the blending distance. First, we perform two experiments simulating the arrival of a sea breeze to study how large-scale forcing might vary turbulent conditions governing the dispersion of the NH$_3$ emission plume. We follow up with an experiment to analyze the diurnal variability of the blending distance. These experiments show that changes in the turbulent and stability characteristics of the boundary layer affect the blending distance, increasing the blending distance with decreasing turbulent kinetic energy, especially for the morning transition from a stable to an unstable boundary layer. In an unstable boundary layer, it is the mixing of air masses with different ammonia characteristics, e.g. entrainment of free tropospheric air, that affects the blending distance. Finally, we expend on the original sensitivity study of blending distance, where individual meteorological and ammonia pollution variables are varied. We perform two new experiments in which multiple processes occurring at different scales are varied and interacting. These combined scenarios indicate towards non-linear interactions between the individual driving variables of the blending distance.

5.1 Introduction

Ammonia (NH_3) is a chemically reactive species with a large spatial- and temporal variability. This high variability stems from the interaction of local sources with different emission rates, deposition processes depending on vegetation and thermodynamic turbulent characteristics, chemical reactivity and the influence of local and regional meteorology. In the previous chapter (Chapter 5) we developed a high-resolution simulation framework (20 x 20 x 5 m^3, 10 seconds), freely available for use online (Schulte et al., 2022b), to advance our understanding on how NH_3 varies at short ranges and define improved measurement strategies. To integrate and quantify the results, the concept of blending distance (BD) was introduced for measurements of the NH_3 molar fraction and NH_3 flux in Chapter 4.

The blending distance is defined as the horizontal distance at which the emission plume can be considered well-mixed with respect to the background NH_3. Therefore we identify the individual contributions of the background ammonia ($NH_{3,bg}$) and ammonia emitted from local sources ($NH_{3,plume}$) to the total ammonia molar fraction ($NH_{3,total} = NH_{3,bg}$ + $NH_{3,plume}$), using the high-resolution simulation framework with explicitly resolved turbulent mixing, introduced in Chapter 4. Based on the relative difference between $NH_{3,\ total}$ and $NH_{3,\ bg}$, the blending distance is calculated for near-surface ammonia molar fraction and flux measurements, using the fluctuation intensity (fI) of the NH_3 molar fraction and the 30 minute NH_3 flux respectively.

The introduction of the concept of blending distance provides a first-order estimate of the minimum distance between NH_3 measurements and a local emission source. Based on a sensitivity study, where several individual meteorological and ammonia pollution variables are varied, the blending distance is estimated to range between 0.5 - 3.0 km and 0.75 - 4.5 km for NH_3 molar fraction and flux measurements, respectively. However, these results are limited in their applicability, as the blending distance is calculated only in the analysis phase of the numerical experiment, between 14:00 and 17:00 CEST. As a result, the role of the diurnal variability of boundary-layer dynamics was actively filtered out. Furthermore, the study is build around the well studied meteorological measurements taken on 8 May 2008 at the Ruisdael Observatory at Cabauw (`https://ruisdael-observatory.nl/cabauw/`) in the Netherlands (51.971ºN, 4.927ºE) (aan de Brugh et al., 2013; Barbaro et al., 2015; Barbaro et al., 2014). This day is characterized by clear-sky convective conditions and the surface elevation changes are at most a few meters over 20 km.

In this study, we expand on the original work by performing several new numerical experiments to analyze three relevant aspects on the blending distance. In Section 5.2, we first study the sensitivity of the blending distance to changes in the turbulent and stability conditions of the atmospheric boundary layer (ABL), under the influence of mesoscale or synoptic situations, or as a result of orography or land use contrast of a region. To

this end, we perform two new experiments simulating the arrival of a sea-breeze front. Secondly, the diurnal variability of the blending distance is analyzed in Section 5.3. Finally, we expand on the original sensitivity study in Section 5.4, by performing a multi-variable sensitivity analysis of the blending distance, based on two new experiments. With these new experiments, we aim to expand our understanding of the blending distance as an integrated variable.

5.2   Dependence of blending distance to large-scale forcing

Two new numerical experiments representing the arrival of a sea-breeze front, which is well documented at the Ruisdael Observatory site in Cabauw (the Netherlands) (Arrillaga et al., 2018), are adaptations of the reference experiment described in Chapter 4. The front is represented by the addition of large-scale forcing terms to the simulation for both the potential temperature (θ) and specific humidity (q), adding an additional source or sink of heat and moisture to the simulation without changing the wind direction. The forcing terms are applied from the surface up to just below the boundary-layer height at 1700 m.

We first perform a realistic sea breeze experiment (SB), followed by an enhanced sea-breeze experiment ($SB_{enhanced}$), shown in Table 5.1. The blending distance for each of the two experiments are compared to the results of the reference experiment. The SB experiment is designed based on over 100 days of sea breeze observations at the Ruisdael Observatory at Cabauw, as shown in Figure 8 by Arrillaga et al. (2018). In this numerical experiment, the sea breeze arrives at 15:00 CEST, one hour after the start of the analysis phase at 14:00 CEST, when there are convective conditions (z/L < 0). The forcing terms for θ and q_t are based on Figure 8 by Arrillaga et al. (2018). With the second experiment, $SB_{enhanced}$, we double the strength of the forcing of potential temperature and initialize the forcing earlier, at 13:00 CEST.

Fig. 5.1 shows the changes in the potential temperature and specific humidity as the sea breeze arrives at 15:00 and 13:00 CEST for SB and $SB_{enhanced}$ respectively. For the SB experiment, the cooling by the sea breeze is rather small, reducing the potential temperature by about 1.5 K at 17:00 CEST. The specific humidity increases by over 1 g/kg at 17:00 CEST compared to the reference experiment and a weakening of the inversion is also visible in the humidity vertical profiles. These effects are amplified for $SB_{enhanced}$, reducing the potential temperature by more than 5 K and specific humidity by over 1.5 g/kg at 17:00 CEST in the well-mixed boundary layer.

These changes in the mixed-layer potential temperature and specific humidity lead to changes in the inversion layer at the top of the well-mixed ABL, as shown in the vertical profiles of Fig. 5.1. While the inversion strength increases for the potential temperature,
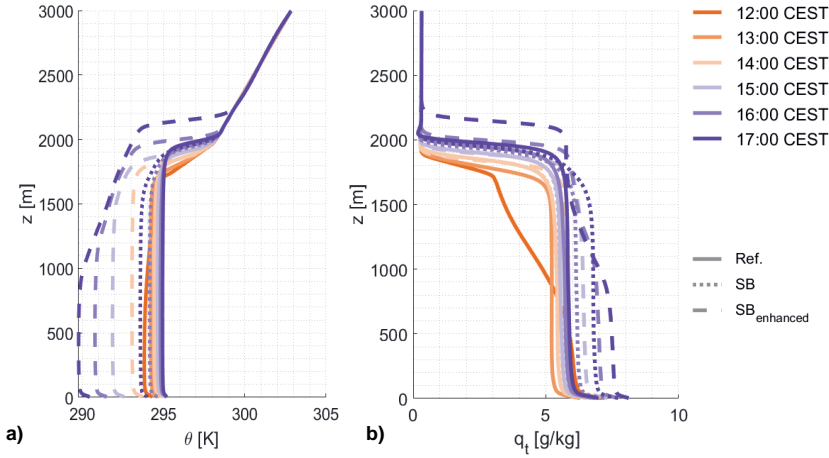
Figure 5.1: The vertical profiles at each hour from 12:00 to 17:00 CEST of the potential temperature, θ, (a) and the total water specific humidity, q_t, (b) for the reference experiment (Ref., solid), the sea breeze experiment (SB, dotted) and the extreme sea breeze experiment ($SB_{enhanced}$, dashed).

Table 5.1: The arrival time of the sea breeze, the forcing of the potential temperature (θ) and specific humidity (q_t), for both the sea breeze (SB) and the extreme sea breeze ($SB_{enhanced}$) experiment.

Experiment	Sea breeze arrival	$d\theta/dt$	dq_t/dt
SB	15:00 CEST	-0.75 K hour^{-1}	0.45 g kg^{-1} hour^{-1}
$SB_{enhanced}$	13:00 CEST	-1.50 K hour^{-1}	0.45 g kg^{-1} hour^{-1}

e.g. increasing by 1 K between 13:00 and 14:00 CEST for $SB_{enhanced}$, the boundary-layer inversion becomes less well defined. Starting at the top of the ABL, the profile of both θ and q_t changes and is no longer considered well-mixed, reminiscent of a ABL collapse at the end of the day. Again, this effect is more pronounced for $SB_{enhanced}$ experiment, as the well-mixed boundary layer only reaches up to about 1000 m at 17:00 CEST. With this change in the vertical profile, the capping inversion of both θ and q_t in Fig. 5.1 increases in height, rising from about 1800 m to over 2100 m for $SB_{enhanced}$. This height increase of the capping inversion corresponds to the increase in ABL height of $SB_{enhanced}$ shown in Fig. 5.2a. Here, the boundary-layer height is defined based on the height of the maximum gradient in potential temperature (Heus et al., 2010), which does not capture the decline of the well-mixed ABL height down to 1000 m shown Fig. 5.1.

The surface fluxes respond to the increase in humidity and cooling of the ABL, as seen in Fig. 5.2b. The latent heat flux (L_vE) decreases due to the increase in atmospheric
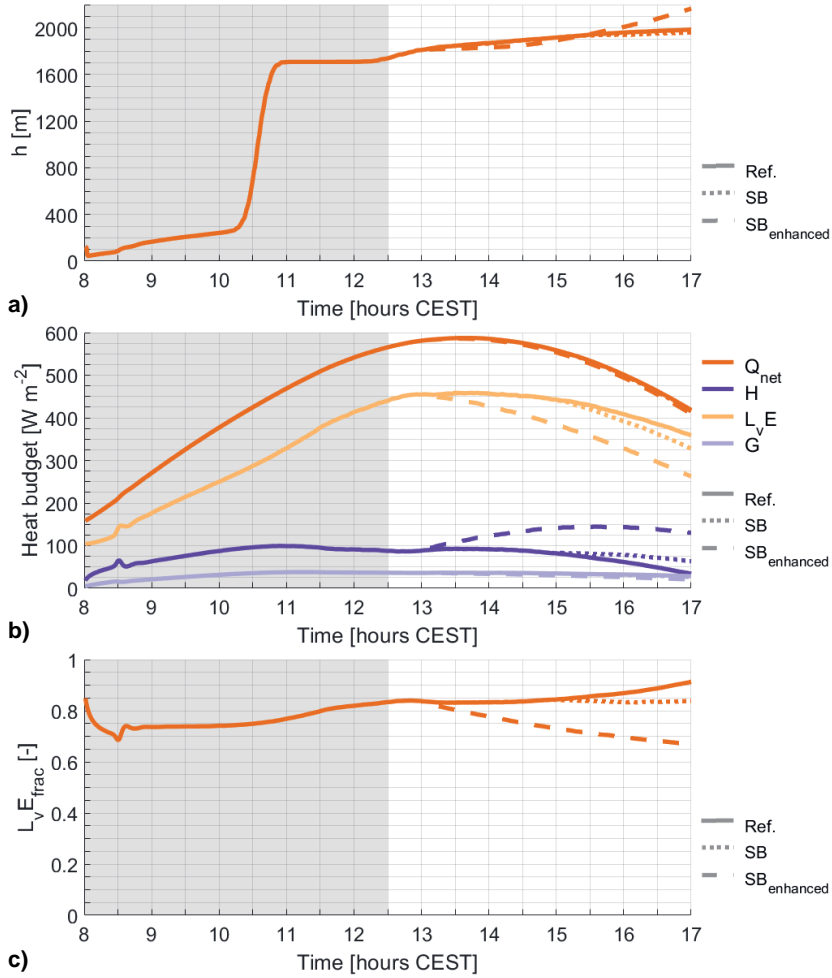
Figure 5.2: Time series of the domain average atmospheric boundary-layer height (a), the evaporation fraction (b) and the heat budget (c) for the reference experiment (solid), the sea breeze experiment (dotted) and the extreme sea breeze experiment (dashed). The grey area represents the meteorological spin-up phase of the experiment and is not considered in the sea-breeze experiment.
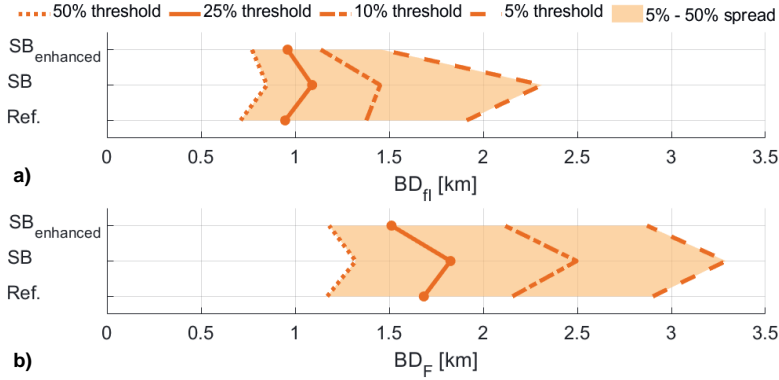
Figure 5.3: The blending distance based on the fluctuation intensity (a) and based on the NH_3 flux (b) for the reference experiment (Ref.), the sea breeze experiment (SB) and the extreme sea breeze experiment ($SB_{enhanced}$).

humidity with about 25 and 75 W m^{-2} for SB and $SB_{enhanced}$, respectively. In response, the sensible heat flux (H) increases by the same amount, as the forcing terms have little impact on the available energy, i.e. net radiation (Q_{net}) and soil heat flux (G). This is reflected in the evaporation fraction, shown in Fig. 5.2c, which shows that a smaller fraction of the available energy is used for evaporation in the late afternoon (16:30 CEST) for the SB (0.85) and $SB_{enhanced}$ (0.68) experiments when compared to the reference (0.9). These effects are amplified in the case of $SB_{enhanced}$, not only because the cooling term has doubled in strength, but also because the large-scale forcing starts 1.5 hours earlier compared to the SB experiment, at 13:00 CEST.

Focusing on our main interest, the impact of a large-scale disturbance in the turbulent characteristics of the ABL on blending distance, we find in Fig. 5.3 that the impact of the sea breeze is small. Both BD_{fl} and BD_F, slightly increase for the SB experiment, but not for the $SB_{enhanced}$ experiment. This could be attributed to the reduction of about 0.2 in the evaporation fraction between SB and $SB_{enhanced}$. The increased sensible heat flux for $SB_{enhanced}$ leads to stronger convection and more vertical mixing of the emission plume, which reduces the blending distance near the surface. Still, the effect of the sea breeze on the blending distance remains small for both experiments.

5.3 The diurnal variability of the blending distance

Similar to the sea-breeze numerical experiments, is the full-day experiment an adaptation of the reference experiment as presented in Chapter 4. This reference experiment was originally set up to allow for a sensitivity study where multiple meteorological and NH_3
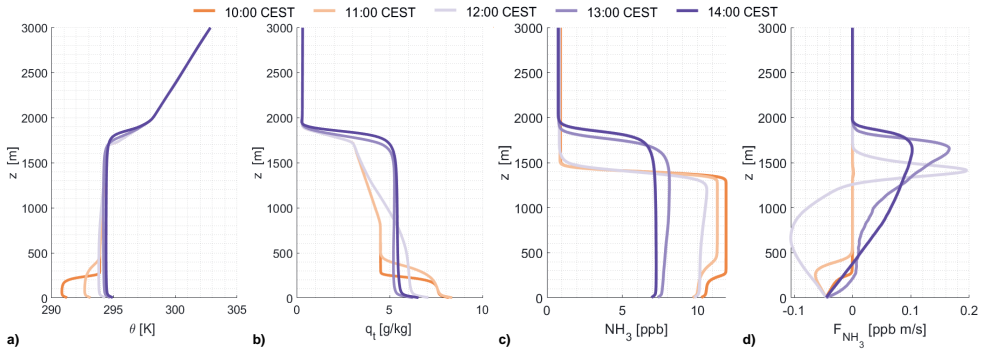
Figure 5.4: The domain average vertical profiles of the potential temperature (a), total water specific humidity (b), background NH$_3$ molar fraction (c) and background NH$_3$ flux (b) between 10:00 and 14:00 CEST.

pollution variables are varied individually, including varying the NH$_3$ background levels. Note that several variables included in this sensitivity study, such as the surface deposition, emission and the chemical conversion rate, affect the background NH$_3$ molar fraction. To minimize the impact of these variables on the background molar fraction in the sensitivity study, we used a fixed analysis phase in Chapter 4 from 14:00 to 17:00 CEST with surface deposition, emission and the chemical conversion rate being initialized at 12:30 CEST. In this full-day experiment, we initialize these processes at the start of the simulation (8:00 CEST). While we maintain the length of the analysis phase at three hours, we vary the starting time by 30 minutes from 8:30 to 14:00 CEST.

The growth of the ABL plays an important role in the diurnal variability of the NH$_3$ molar fraction. As the ABL grows, air masses with different NH$_3$ characteristics mix through entrainment of air from the residual layer or free troposphere, enhancing the fluctuations and changing the concentration of the background NH$_3$ (Schulte et al., 2021). The domain averaged vertical profile of θ in Fig. 5.4a shows that the 250 m shallow ABL at 10:00 grows rapidly as a result of a residual layer, becoming well mixed at 12:00 CEST. This matches the rapid increase of the ABL height shown in Fig. 5.2a, growing from 300 m to 1700 m in about 45 minutes, as the boundary-layer height is defined based on the largest θ gradient, as discussed in Section 5.2. The vertical profiles of q$_t$ and the background NH$_3$ molar fraction in Fig. 5.4b and 5.4c however, show a more gradual ABL growth between 10:00 and 13:00 CEST. Here, we see the 250 m shallow ABL mixing with the residual layer, gradually becoming well mixed around 13:00 CEST and reaching a height of about 1800 m.

Focusing on the background NH$_3$ molar fraction, Fig. 5.4c shows an ABL of about 250 m at 10:00 CEST. The NH$_3$ molar fraction of this shallow ABL is lower compared to the residual layer (250 - 1400 m), as a result of the prescribed surface deposition. Both the
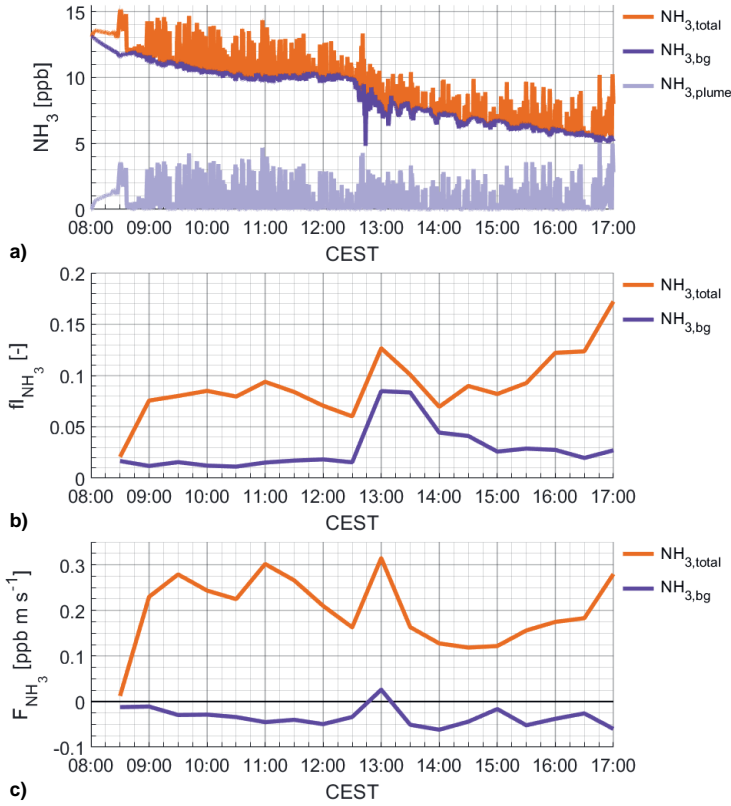
Figure 5.5: A time series of simulated NH_3 measurements of a single grid cell at a height of 37.5 m, 250 m distance downwind from the NH_3 emission source. The top panel (a) shows the time series $NH_{3,total}$ (orange), $NH_{3,bg}$ (purple) and $NH_{3,plume}$ (light purple) at 10 second temporal resolution. In the middle (b), the fluctuation intensity (fI) is shown for $NH_{3,total}$ and $NH_{3,bg}$, calculated every 30 minutes. The bottom panel (c) shows the 30 minute NH_3 flux (F_{NH_3} for $NH_{3,total}$ and $NH_{3,bg}$.

shallow ABL and the residual layer experience an additional uniform loss in the NH_3 molar fraction of 5% hour^{-1} representing chemical gas-aerosol transformations. The residual layer is gradually mixed with the ABL through entrainment, as the boundary-layer height increases between 10:00 and 12:00 CEST. Between 12:00 and 13:00 CEST, the ABL grows up to about its maximum height of 1800 m and entrainment of free tropospheric air ($NH_3 \approx 1$ ppb) reduces the NH_3 molar fraction in the ABL from 10 ppb to about 7.5 ppb.

This turbulent mixing of the ABL with the residual layer and free troposphere is clearly visible in the domain average vertical profile of the NH_3 flux in Fig. 5.4d. Here, a positive NH_3 flux corresponds to ammonia-rich air being transported upwards and ammonia-low

air being transported downwards (vice versa for a negative flux). At 12:00 CEST, the NH$_3$ molar fraction below 1300 m decreases as ammonia-low air from the surface is mixed with the air between 400 and 1300 m, resulting in a negative flux peaking at -0.1 ppb m s^{-1}. At the top of the ABL, in the entrainment zone, ammonia-low air of the free troposphere is entrained into the ABL and ammonia-rich air from the ABL is transported upwards. This is represented in Fig. 5.4d by a positive flux between 1300 and 1600 m that peaks at 0.2 ppb m s^{-1}. This positive entrainment flux is still found at 13:00 and 14:00 CEST, but weakens in strength as the ABL stops growing in height and entrainment weakens. Still, an entrainment flux of about 0.1 ppb m s^{-1} is shown at 14:00 CEST, which is over two time the prescribed surface flux of -0.045 ppb m s^{-1}.

The impact of entrainment of air with different NH$_3$ characteristics is clearly visible in the time series of the NH$_3$ molar fraction for a single grid cell of the simulation at 250 m distance from the emission source, shown in Fig. 5.5a. Between 10:00 and 12:00 CEST, when the ABL is mixing with the residual layer, NH$_{3,bg}$ slightly increases. Here, the loss of NH$_3$ by chemical transformations (5% hour^{-1}, or $\approx$ -0.5 ppb h^{-1}) and surface deposition (-0.045 ppb m s^{-1}) is offset by entrainment of air from the residual layer with a slightly higher NH$_3$ molar fraction. At about 12:30 CEST, entrainment of free-tropospheric air leads to a sudden decrease in NH$_{3,bg}$ of about 2.5 ppb, accompanied by large NH$_3$ fluctuations (up to 4 ppb), as shown in Fig. 5.5a and was visualized in the vertical cross-section in Figure 4.2b of Chapter 4.

The changes in the NH$_3$ molar fraction resulting from entrainment of free-tropospheric air also impact the fluctuation intensity (fI) and flux (F). Figure 5.5b shows that the fI of the background NH$_3$ (fI$_{bg}$) is low at about 0.01 until 12:30 CEST. The fI of the total NH$_3$ molar fraction (fI$_{total}$), is significantly higher at about 0.08 as the emission plume fluctuations (NH$_{3, plume}$) are now added to NH$_{3, bg}$. When free-tropospheric air is entrained at 12:30 CEST, we find that fI$_{bg}$ increases from 0.01 to about 0.85. The difference between fI$_{total}$ and fI$_{bg}$ decreases as the change in fI$_{total}$ appears to be dampened compared to the background.

Figure 5.5c shows simulated flux measurements of a single grid cell for NH$_{3, bg}$ (purple) and NH$_{3, total}$ at 250 m distance from the emission source. When only the background NH$_3$ is considered, F$_{bg}$ approaches the prescribed surface flux of -0.045 ppb m s^{-1}. By analyzing the flux for NH$_{3, total}$, we find that the emission plume increases the simulated flux measurements from deposition of about -0.045 ppb m s^{-1} to emissions ranging from 0.1 to 0.3 ppb m s^{-1}. At 12:30 CEST, entrainment of ammonia-low air from the free troposphere reaches the surface and changes F$_{bg}$ from deposition (negative) to emission (positive). For F$_{total}$, NH$_3$ entrainment leads to an increase in the simulated flux from 0.16 to 0.3 ppb m s^{-1}.

The blending distance is calculated over a three-hour analysis phase, following Eq. 5.1 and 5.2 where X can be substituted by fI or F, as presented in Chapter 4.

$$PC_X = |\frac{X_{total} - X_{bg}}{X_{bg}}| * 100\% \tag{5.1}$$

$$BD_X = max(\ dist(\ PC_X < threshold \ ) \ ) \tag{5.2}$$

To study the diurnal variability of the blending distance, BD_{fI} and BD_F are calculated at 30 minute intervals, between 8:30 and 17:00 CEST. The results for each three-hour window are shown in Fig. 5.6 for a range of thresholds (5% to 50%). To quantify the turbulent conditions of the ABL and relate it to the blending distance, we also show the explicitly resolved turbulent kinetic energy (TKE), integrated over the boundary layer height.

Fig. 5.6a shows that BD_{fI} is affected by the level of turbulent mixing, entrainment of free-tropospheric air and the change in the background molar fraction. In the morning, TKE increases as the ABL transitions from stable conditions to unstable conditions. BD_{fI} is high while there is little turbulent mixing of the emission plume, ranging from 1.5 to 6 km between 8:30 and 11:30 CEST. BD_{fI} rapidly decreases as the TKE increases and the emission plume is mixed with the background molar fraction

The fluctuations in the NH_3 molar fraction as a result of entrainment occur between 12:30 and 13:30 CEST. Here, not only fI_{bg} increases, but the difference between fI_{bg} and fI_{total} decreases as well. Following Eq. 5.1 and 5.2, BD_{fI} should therefore decrease as a result of entrainment. Figure 5.6a indeed shows that BD_{fI} reaches its lowest value, ranging from 0 to about 1 km, whenever entrainment (12:30 - 13:30 CEST) is included in the three-hour analysis phase.

In the afternoon, Fig. 5.5a shows that chemical transformations and surface deposition lead to a steady decrease of the background NH_3 molar fraction, without significantly affecting the fluctuations of the emission plume. Following the definition of the fluctuation intensity ($fI = \sigma_{NH_3}/\overline{NH_3}$), fI_{total} increases as the fluctuations of the emission plume gain in relative weight as $\overline{NH_3}$ is reduced by the decreasing $NH_{3, \, bg}$. This increase in fI_{total} leads to an increase BD_{fI} in the afternoon, as shown in Fig. 5.6a, because fI_{bg} is approximately constant.

Figure 5.6b shows that the blending distance of the simulated NH_3 flux (BD_F) is less sensitive to both changes in TKE or in $NH_{3, \, bg}$. We do find a strong sensitivity to entrainment, as BD_F increases by about 1.5 km whenever entrainment (12:30 - 13:30 CEST) is included in the three-hour analysis window. Entrainment transports air from the free troposphere downwards, mixing with the ABL. These downward plumes of ammonia-low air also reach the surface, which can locally result in a positive simulated flux, as shown in Fig. 5.5c. The change in the $NH_{3, \, bg}$ flux by entrainment reduces the absolute value of the flux. This results in an increase in PC_F, following Eq. 5.1, as the impact of the emission plume increases, relative to the background flux. With PC_F increasing, the
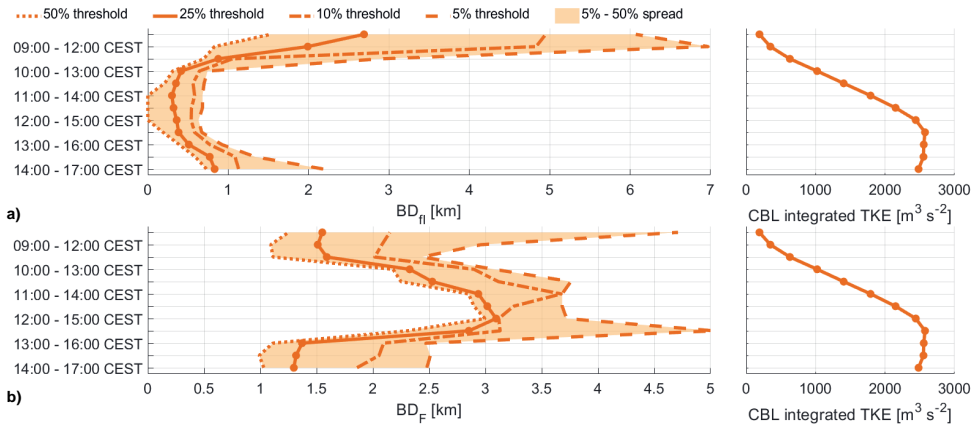
Figure 5.6: BD$_{fl}$ (a) and BD$_F$ (b) for each three-hour long analysis phase between 8:00 and 17:00 CEST, accompanied by the corresponding horizontal average TKE integrated over the boundary layer height in the panels on the right.

blending distance for flux measurements increases whenever entrainment is included in the analysis window.

The results in Fig. 5.6 show that the blending distance is only weakly sensitive to changes in the ABL turbulent characteristics. Atmospheric stability only plays an important role when transitioning from stable conditions to unstable conditions. For convective conditions, it is the change in the NH$_3$ characteristics in the ABL which drives the blending distance, like the mixing of air masses with different NH$_3$ characteristics. In this experiment, this mixing of air masses occurs when entrainment mixes ammonia-low air from the free troposphere in the ammonia-rich ABL. The mixing increases the turbulent NH$_3$ fluctuations and affects the flux of the background molar fraction, leading to a reduction of BD$_{fl}$ and an increase in BD$_F$ whenever entrainment is included in the analysis window. Even close to the surface, entrainment plays a key role in the diurnal variability of atmospheric ammonia and affects the relative impact of an emission source in close proximity to NH$_3$ observations.

5.4   The multi-process sensitivity of the blending distance

With the introduction of the concept of blending distance in Chapter 4, a sensitivity study was conducted to identify the driving variables and to obtain an first-order estimate of the range of the blending distance under different conditions. With this sensitivity study, only individual meteorological or NH$_3$ related variables were varied to analyze their individual impact on the blending distance. Here, we perform a multi-variable sensitivity analysis of the blending distance to determine the non-linearity of the processes.

Table 5.2: Variable names, symbols and their values for the reference experiment and the two multi-variable experiments (MVE#1 and MVE#2).

Variable		Reference experiment	MVE#1	MVE#2
NH$_3$ emission strength	E	45 ppb m s^{-1}	200 ppb m s^{-1}	45 ppb m s^{-1}
NH$_3$ deposition strength	D	-0.045 ppb m s^{-1}	0 ppb m s^{-1}	-0.045 ppb m s^{-1}
Geostrophic wind speed	u_g	8 m s^{-1}	8 m s^{-1}	4 m s^{-1}
Initial background NH$_3$	C_{bg}	10 ppb	10 ppb	25 ppb

To this end, we set up two new numerical experiments where we change two variables simultaneously. With the first experiment, multi-variable experiment number 1 (MVE#1), we focus on the combined impacts of surface heterogeneity, as we vary the strength of the emission source (E) and the surface deposition (D). Furthermore, both variables affect the turbulent NH$_3$ fluctuations. The deposition strength determines the strength of the near-surface NH$_3$ gradient, which leads to fluctuations in the background NH$_3$ through turbulent mixing. The emission strength directly affects the strength of the NH$_3$ plume fluctuations. In the second experiment, multi-variable experiment number 2 (MVE#2), we study the combined effect of the two non-local processes of the original sensitivity study by changing the geostrophic wind speed (u$_g$) and the background NH$_3$ molar fraction at the start of the analysis phase (C$_{bg}$). Changes in geostrophic wind speed are a result of pressure gradients at the synoptic scale and are one of the driving variables for the turbulent mixing in the ABL. The initial NH$_3$ background molar fraction is a measure of the regional level of NH$_3$ pollution and affects the magnitude of the turbulent fluctuations in the background NH$_3$.

The values of these four variables for the two multi-variable experiments, as well as the reference experiment, are listed in Table 5.2. With these two experiments, we aim to test the hypothesis stating that there is a linear relation between the results of the individual sensitivity study, i.e. the change in the blending distance of the multi-variable experiments is equal to the sum of the changes in blending distance of the individual experiments. To this end, we focus on the blending distance for molar fraction measurements (BD$_{fl}$) and define the change in blending distance as $\Delta BD = BD_{experiment} - BD_{reference}$.

In the first multi-variable experiment, we focus on enhancing the NH$_3$ heterogeneity by increasing the emission strength and decrease the surface-atmosphere exchange. The emission strength is increased from the 45 ppb m s^{-1} reference value, representative of a typical Dutch medium sized (80 cow) farm, to 200 ppb m s^{-1}. The surface deposition is decreased from -0.045 ppb m s^{-1} to 0 ppb m s^{-1}. Both individual scenarios result in a significant increase in BD$_{fl}$, following the results of the sensitivity study presented in Chapter 4. The left panel of Fig. 5.7 indeed shows a strong increase in BD$_{fl}$ for the
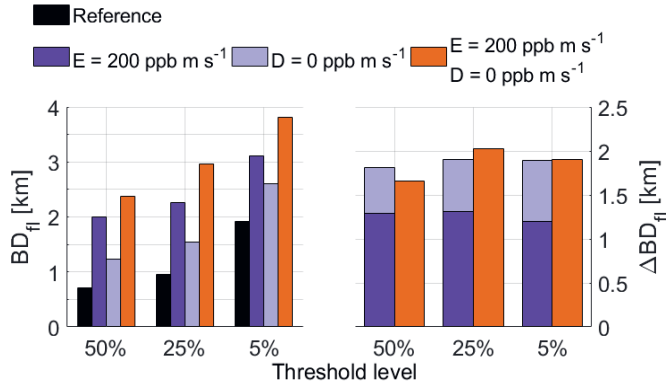
Figure 5.7: BD$_{fl}$ for the reference experiment (black), the individual scenarios (purple) and the multi-variable experiment #1 (orange) are shown on the left panel for three threshold levels. The right panel shows changes in blending distance with respect to the reference experiment (ΔBD$_{fl}$) for the sum of the individual scenarios (purple) and MVE#1 (orange)

MVE#1 (orange). The right panel shows the ΔBD$_{fl}$ for the sum of the individual scenarios in purple and the ΔBD$_{fl}$ of MVE#1 in orange. Here, we find that the sum of ΔBD$_{fl}$ for the individual scenarios is roughly equal to ΔBD$_{fl}$ of MVE#1, indicating that there is indeed a linear relation between the blending distance of these two scenarios.

In the second multi-variable experiment, we vary the background NH$_3$ molar fraction and geostrophic wind speed, variables which act on the regional and mesoscale. The background NH$_3$ molar fraction is increased to 25 ppb and the geostrophic wind speed is decreased to 4 m s^{-1}, which both result in a reduction of BD$_{fl}$. The left panel of Fig. 5.8 indeed shows that BD$_{fl}$ of MVE#2 is generally smaller than both the reference and the individual experiments. The only exception is the 50% threshold, where MVE#2 is slightly larger than the C$_{bg}$ = 25 ppb experiment. By analyzing ΔBD$_{fl}$ in the right panel, we find that the sum of the individual scenarios is consistently larger than the combination of the two scenarios. This indicates that there is a non-linear relation between the blending distance of these two scenarios and that, contrary to the results of MVE#1, the hypothesis is false for this numerical experiment.

The results of both MVE#1 and MVE#2 demonstrate that combining results from individual scenarios presented in the sensitivity study is not straightforward. It is therefore recommended to perform additional multi-variable experiments and systematically analyze the relationships between the variables and the change in the blending distance with respect to the reference experiment. Here, one could systematically repeat the multi-variable experiments presented in this section for all possible combinations of variables, focusing on the four variables with the largest impact on the blending distance: emission strength, deposition strength, background molar fraction and geostrophic wind speed.
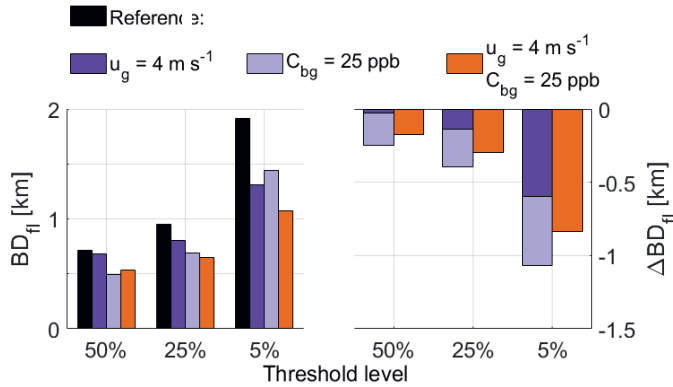
Figure 5.8: BD_{fl} for the reference experiment (black), the individual scenarios (purple) and the multi-variable experiment #2 (orange) are shown on the left panel for three threshold levels. The right panel shows changes in blending distance with respect to the reference experiment (ΔBD_{fl}) for the sum of the individual scenarios (purple) and MVE#2 (orange).

A more cost-effective approach would be to first perform a targeted subset of new experiments to identify what variables are causing the non-linear interactions, based on the new insights gained from the new experiments presented in this section. Here we find a linear relation when varying both the emission and deposition strength in MVE#1, two variables which directly affect the NH_3 fluctuations in the emission plume and background molar fraction and are related linearly through Eq. 5.1. Next would be to identify if either the change in C_{bg} or u_g is causing the non-linear relation found in MVE#2, or if the interaction is a specific to these two variables. This can be tested by performing two new multi-variable experiments where C_{bg} and u_g are combined with a different variable (e.g. the emission strength). With such targeted experiments, one should be able to identify non-linear relations without testing all possible combinations.

5.5   Conclusions

The concept of the blending distance integrates a wide range of processes that govern the evolution and distribution of atmospheric NH_3 in a single variable. With the introduction of the concept of the blending distance in Chapter 4, the strength of the emission source and the NH_3 deposition strength of the region, were identified as the main drivers of the blending distance, followed by the geostrophic wind speed and the background NH_3 levels (Schulte et al., 2022a). In this study, we expand on this original sensitivity study and find that changes in the turbulent characteristics of the convective boundary layer, e.g. the arrival of a sea-breeze front, do not significantly affect the blending distances for the NH_3 fluctuation intensity nor the NH_3 flux (changes < 500 m). Similar results were found when

analyzing the diurnal variability of the blending distance in Section 5.3. Here, we find that the blending distance is mainly driven by turbulent mixing of different NH$_3$ characteristics, i.e. entrainment of ammonia-low free-tropospheric air. Only in the morning, as the stable boundary layer transitions to convective conditions, does the atmospheric stability result in a large decrease in the blending distance. Furthermore, the results of multi-variable experiments, as presented in Section 5.4, indicate possible non-linear relations between individual variables of the sensitivity study presented in Chapter 4.

These new findings advance our understanding of the concept of the blending distance and provide valuable context for the interpretation of the original sensitivity study presented in Chapter 4. We find that the results of this sensitivity study are representative for the blending distance under convective conditions, as the blending distance is not sensitive to changes in the turbulent characteristics of the convective boundary layer. We do find the blending distance to be sensitive to entrainment of ammonia-low air from the free troposphere, affecting both the fluctuations in the background NH$_3$ molar fraction and simulated NH$_3$ flux near the surface. We therefore conclude that one should consider the impact of entrainment when selecting the analysis window used to estimate the blending distance. Furthermore, we find non-linear relations between the individual variables of the original blending distance sensitivity study for one of the two new multi-variable experiments. While the difference in the blending distances of this new multi-variable experiment and the original experiments is relatively small, a few hundred meters, the results indicate that combining scenarios presented in the sensitivity study is not straightforward and further research on different combinations is recommended. The scenarios and corresponding blending distance results presented here and in Chapter 4 do provide a valuable first-order estimate and understanding of the concept, which can already be used to assess the conditions at individual measurement sites.

The next step is to apply the simulation framework at individual measurement sites and account for the local surface and NH$_3$ characteristics, as well as meteorological conditions. The simulation framework allows for the analysis of more than one emission source and to study the effects of multiple nearby sources with different emission characteristics, furthering our understanding of the blending distance. A second point of interest is to go beyond estimations of the blending distance for convective stability conditions, as is done in this Chapter, and expand the analysis to a broader range of meteorological conditions, e.g. a neutral or cloud-topped boundary layer. A final point of interest is to continuously analyze the effect of future updates of the simulation framework on the blending distance, like a dynamic representation of the surface-atmosphere exchange or a thermodynamic chemistry module, representing dynamic gas-aerosol interactions. It is the strength of the concept of blending distance that this broad range of processes and interactions are integrated into one single intuitive variable.

Chapter 6

Conclusions and Outlook

In this Chapter, we summarize the main findings of the thesis. In Section 1.1, we organized our findings by providing an overarching research question, which was broken down into four sub-questions for each of the Chapters. In this Chapter, we provide an answer to these research (sub)questions in Section 6.1. We wrap up this thesis in Section 6.2, where we present our outlook for the future of atmospheric ammonia (NH_3) research, utilizing high-resolution ammonia observations and advanced simulation techniques.

6.1 Conclusions

6.1.1 Chapter 2

How do the individual processes governing the ammonia budget contribute to the diurnal variability of atmospheric ammonia?

Our analysis of the diurnal variability of atmospheric ammonia in Chapter 2 was centered around advanced observations of the atmospheric NH_3 concentration and flux (F_{NH_3}). By analyzing over 100 days of measurements and filtering for clear sky convective conditions, we designed a case study centered around a single representative day, supported by the averaged observed diurnal variability of over 20 unique days. Constrained by meteorological observations of this representative day, we modeled the meteorological conditions and NH_3 observations using a conceptual model that represents the evolution of a prototypical atmospheric boundary layer. With the model, we disentangled and quantified the contributions of the four main processes governing the ammonia budget: the NH_3 surface-atmosphere exchange, entrainment of air from the free troposphere, regional advection of NH_3 and chemical gas-aerosol transformations. Our analysis of the diurnal variability is based on two sets of experiments where we aimed to reproduce the observed NH_3 concentration with the model. In the first set of experiments, the surface-atmosphere exchange was prescribed to the model based on the observed F_{NH_3}, while this process was parameterized in the second set of experiments.

By prescribing the NH_3 surface flux, the modeled NH_3 concentration closely fitted the observed diurnal variability. The combined analysis of the mixed-layer model with observations allowed us to identify two distinct regimes in the diurnal variability of atmospheric NH_3, driven by boundary-layer dynamics. We found a clear distinction in the process contributions to the NH_3 budget between the morning and the afternoon. In the morning, the NH_3 concentrations decreased as a result of entrainment. In short, with the growth of the boundary-layer height, ammonia-low concentration air from the free troposphere was entrained and mixed with the ammonia-rich air of the boundary layer, reducing the NH_3 concentration. This process was partly offset by advection of NH_3 from regional emission sources, which acted as a significant source of NH_3. The remaining two processes, surface-atmosphere exchange and chemical transformations, were found to be less important to the morning variability of the NH_3 budget.

In the afternoon, the contribution of entrainment to the atmospheric NH_3 variability rapidly decreased, as the boundary-layer growth slows down. Here, the contribution of the surface-atmosphere exchange to the NH_3 budget increased significantly for the unfertilized grassland at Veenkampen, as high deposition was observed in the late afternoon. The loss of NH_3 through the local surface flux was counteracted by the aforementioned regional advection, resulting in a small net increase in the NH_3 concentration. As the contribution of chemical transformations was still negligible, the variability of the afternoon NH_3 budget was governed by the local surface-atmosphere exchange and regional advection of NH_3.

In the second set of numerical experiments, where the surface-atmosphere exchange was parameterized, we identified a mismatch between the observed and parameterized surface flux. A similarly close fit to the observed NH_3 observations was achieved in these experiments, but required an unrealistic representation of the processes governing the NH_3 budget, including high NH_3 concentrations in the free troposphere. While this second set of experiments was not used to answer the research questions, it did indicate towards potential improvements of the NH_3 surface-atmosphere parameterization. The results of both sets of experiments showed how our comprehensive approach, where we combined advanced observations with a conceptual land-atmosphere model including NH_3, supports the interpretation of the NH_3 observations and demonstrates that the diurnal variability of atmospheric ammonia is governed by processes acting on both local and non-local scales.

6.1.2 Chapter 3

What are the relationships between the observed NH_3 flux and the CO_2 uptake and transpiration by vegetation? Can this understanding help us to improve the NH_3 stomatal exchange parameterization?

In Chapter 3, we aimed to establish simple relations between the NH_3 surface-atmosphere exchange and photosynthesis, i.e. the stomatal exchange of CO_2 and water vapor (plant transpiration). The process of photosynthesis is well understood and such auxiliary observations can be used to further our understanding of NH_3 exchange through the individual exchange pathways, e.g. stomatal exchange. To this end, we analyzed daytime observations of F_{NH_3}, taken during the RITA-2021 campaign at the Ruisdael Observatory meteorological supersite at Cabauw. We focused on establishing relationships between the observed F_{NH_3}, the latent heat flux ($L_v E$), representing evapotranspiration, and gross primary production (GPP), representing CO_2 uptake by vegetation. The observations were organized following the main drivers of the dynamic vegetation response, based on temperature, radiation and moisture. Following this approach, we analyze the responses of the surface-atmosphere exchange fluxes to the atmospheric temperature, photosynthetically active radiation (PAR) and the water vapor pressure deficit (VPD).

In contrast to the unmanaged grassland at the Veenkampen site of Chapter 2, grassland near the Cabauw site is actively maintained and fertilized, with point sources of NH_3 emissions located in close proximity (< 2 km, connected with Chapter 4), e.g. farms, animal droppings or fertilization of nearby fields. As a result, the observed NH_3 flux is characterized by daytime emissions. Given the close proximity of potential NH_3 emission sources, we first aimed to link the observed emission to stomatal exchange. We did find high correlation between the observed daytime NH_3 emissions and L_vE (0.70) and PAR (0.72), as well as strong similarities in the diurnal variability of F_{NH_3} and GPP. These were strong indications towards stomatal NH_3 emissions and show that observations of L_vE and the GPP are appropriate variables to distinguish stomatal NH_3 exchange from non-stomatal exchange.

The complex NH_3 surface characteristics and varying meteorological conditions added additional layers of complexity to the analysis. The heterogeneous NH_3 characteristics of the area resulted in outlier observations from at least one fertilization event, with strong indications of other weaker fertilization events. Furthermore, only a small subset of the campaign measurements (9% or 102 hours) were suitable for analysis after filtering, with the largest loss of data resulting from filtering for wind directions where the airflow is obstructed. As a result the observed range in the measurements was dominated by the natural diurnal variability. Despite the unfavorable conditions, the results of the analysis did indicate towards a strong link between the NH_3 flux and plant transpiration. While the conditions at the Cabauw site were unsuitable to establish clear relationships between F_{NH_3} and the photosynthesis fluxes, the results presented in Chapter 3 did demonstrate that there is room to find patterns between the high-quality NH_3 observations and fluxes of CO_2 and water vapor.

6.1.3 Chapter 4

What is the impact of ammonia surface heterogeneity (e.g. a local emission source) on ammonia concentration and flux measurements?

Sparked by the heterogeneous NH_3 characteristics at the Cabauw site in Chapter 3, we designed a high-resolution simulation framework (20 x 20 x 5 m ^{3}, 10 s) for a 5 x 10 km^2 domain, including realistic representations of the processes governing the NH_3 budget. In Chapter 4, we simulated near-surface observations of the NH_3 concentration and flux in proximity of a single emission source, utilizing the large-eddy simulation technique which explicitly resolves nearly all (80 - 95%) turbulent energy. The simulation framework allows us to distinguish between the background NH_3 and the emission plume. Utilizing this turbulent resolved simulation framework, we introduced a new concept, called the blending distance, to assess the distance at which the emission plume is considered well-mixed with respect to the background NH_3 concentration.

The turbulent dispersion of the emission plume affected the simulated concentration measurements by increasing the fluctuation intensity (i.e. increased NH_3 fluctuations). The emission plume was found to affect concentration measurement at distances up to a couple of kilometers, as indicated by the blending distance ranging from 0.5 to 3.0 km. The numerical experiments further showed that flux measurements are more sensitive to the turbulent fluctuations of the emission plume, reflected by the blending distance ranging 0.75 up to 4.5 km.

The range presented in the blending distances for both concentration and flux measurements follows from a sensitivity analysis where we varied several meteorological and NH_3 related variables, as well as different values of an arbitrary threshold used to calculate the blending distance. This threshold determines the maximum acceptable percentage change induced by the emission plume with respect to the background NH_3, ranging from 5% to a 50% change. Decreasing this threshold from 50% to 5% resulted in an increase of the blending distance by over 1 km. Furthermore, we found the blending distance to be sensitive to several meteorological and NH_3 variables, with the distance increasing for increasing (geostrophic) wind speed and emission strength, while decreasing for increasing surface deposition.

The results presented in Chapter 4 showed that heterogeneity as a result of local emission sources has a significant impact on measurements of the both NH_3 concentration and flux over a distance of several kilometers. The simulation framework presented here can be applied to individual locations to study the representativity of existing or potential new measurement sites under local conditions by using the concept of blending distance.

6.1.4 Chapter 5

How do changes in the turbulent characteristics, driven by external factors, affect the impact of an emission plume on ammonia measurements?

In Chapter 5, we expanded upon the concept of blending distance by studying its sensitivity to changes in turbulent characteristics with three sets of new numerical experiments. First, we simulated the arrival of a mesoscale sea-breeze front, represented by adding large-scale forcing terms of cold and humid air. Next, the diurnal variability of the blending distance was studied. Finally, we performed two numerical experiments in which more than one meteorological and/or NH_3 processes was changed, studying potential non-linear interactions. Here, we calculated the blending distance when changing two variables and compared the results to the original sensitivity study, where only single variables were changed.

Based on these numerical experiments, we found the blending distance to be highly sensitive to NH_3 fluctuations and boundary layer stability. The diurnal variability experiment showed that the transition from a stable to an unstable boundary layer leads to a strong reduction

in the blending distance, from 7 km down to 1 km for the NH_3 concentration and from 4.5 to 2.5 km for the NH_3 flux. However, for an already unstable boundary layer, changes in the turbulent characteristics appeared to have little effect on the blending distance, as demonstrated with the sea-breeze experiments where the blending distance changes less than 0.5 km.

The diurnal variability experiment demonstrates that ammonia-low air is entrained from the free troposphere as the boundary layer grows, mixing with ammonia-rich air in the boundary layer and enhancing turbulent fluctuations in the background NH_3. This leads to a decrease in blending distance for concentration measurements, as the relative impact of the in-plume fluctuations is reduced with respect to the enhanced background NH_3 fluctuations. The opposite effect is found for the blending distance of the NH_3 flux, which increases as the downdraft of ammonia-low air affects the background NH_3 flux.

Finally, when varying both the turbulent characteristics by changing the geostrophic wind speed, as well as changing the background concentration, the change in the blending distance was about 75% compared to the results of the individual changes in blending distance in the original sensitivity study. This indicates towards potential non-linear relations between the individual variables when changing the turbulent characteristics of the boundary layer.

6.1.5   Concluding words

What processes and scales control the ammonia diurnal variability over Dutch grassland? Why are Cabauw and Veenkampen so different?

From the findings presented in this thesis we conclude that the diurnal variability of the atmospheric NH_3 concentration is governed by a wide range of processes, interacting and acting at different scales. The differences between the observed diurnal variability at the Veenkampen site and the Ruisdael Observatory at Cabauw stem from differences in both meteorological conditions and the NH_3 surface characteristics.

The analysis of the Veenkampen observations focused on clear-sky convective conditions, which generally correspond to high-pressure systems at the synoptic scale. For these conditions, a clear diurnal pattern is found in both the observed NH_3 concentration and flux. Here, the morning is governed by boundary-layer dynamics as entrainment of ammonia-low air from the free-troposphere decreases the NH_3 concentration as the boundary layer grows in height. This process is partially offset by regional advection of ammonia. As the role of boundary-layer dynamics decreases in the afternoon, regional advection and local surface-atmosphere exchange become the dominant processes. The advection of ammonia-rich air from the agriculturally active area results in high background levels of NH_3 (> 10 μg m^3) which, combined with the low nitrogen characteristics of the unfertilized grassland at the Veenkampen field, leads to high afternoon deposition of NH_3.

Finally, chemical transformations from gaseous NH_3 to aerosols was found to have little impact on the diurnal variability.

The conditions for the filtered observations at the Ruisdael Observatory at Cabauw differ from the unmanaged grassland at Veenkampen in multiple ways. During the measurement campaign, the meteorological conditions were characterized by low-pressure frontal passages. Furthermore, the grassland near the Cabauw site is actively managed and grazed upon, with NH_3 emission sources in close proximity (< 0.5 km), e.g. farms, grazing livestock and fertilized grassland. As a result, no clear diurnal pattern was found in the observed NH_3 concentration. Instead, large day-to-day differences are observed, with an average daytime concentration of about 5 μg m^3 and multiple days with concentrations over 10 μg m^3. Despite the variability in the NH_3 concentration, a clear diurnal pattern is found in the observed NH_3 flux, characterized by daytime emissions. These emissions are attributed to stomatal exchange, a process which occurs at micrometer level but affects the exchange at field scale.

The local advection of NH_3 from emissions near the Cabauw site increased the complexity of the analysis of the observations. The heterogeneity in the NH_3 surface characteristics and local emission sources affect both the concentration and flux measurements, with at least one fertilization event leading to outlier observations being identified. Based on the concept of blending distance, we found that local emission sources (< 5 km) can potentially have a significant impact on observations of both the NH_3 concentration and flux.

Our findings show that the diurnal variability is governed by processes at scales ranging from the synoptic scale, to heterogeneity of the NH_3 surface characteristics and the dynamic vegetation response at field scale. Integrating these scales and processes is essential to improve our understanding of the diurnal variability of atmospheric NH_3 and the surface-atmosphere exchange. The comprehensive approach presented in this thesis, where we combine advanced observations with both conceptual and turbulent-resolved models, paves the way for future ammonia research.

6.2   Outlook

When studying atmospheric ammonia, we are faced with a unique set of challenges. Gaseous ammonia is highly reactive, making observing the NH_3 concentration, and especially the NH_3 flux, a notoriously difficult endeavor, as the gas tends to "stick" to inlet surfaces. The reactive nature of NH_3 also results in a short atmospheric lifetime of about 1 day, due to the high deposition rate and the formation of aerosols. This short lifetime results in high spatial variability in both concentration and surface-atmosphere exchange, especially when combined with the large amount of emission (point) sources with heterogeneous spatial distribution and a wide range of emission rates. As a result, regions with high levels of agricultural activity are characterized by localized hot spots of high NH_3 concentration

and/or deposition. Additional complexity is added by the high level of heterogeneity in NH_3 surface characteristics at field level, due to differences in fertilization history. As a result, atmospheric ammonia is a system governed by both meteorological and heterogeneous surface processes, which requires an integrated approach at high spatio-temporal resolution for a detailed understanding. With the recent advances in both high-resolution measurements of the NH_3 concentration and flux, as well as the use of turbulent resolved models, this level of detail can now be achieved.

6.2.1 Towards a comprehensive simulation tool

The DALES simulation framework presented in this thesis, based on the large-eddy simulation technique, is well suited to tackle the challenges that come with research on atmospheric ammonia. In its current state, the simulation framework includes realistic representations of each of the processes governing the ammonia budget, while explicitly resolving 80 - 95% of the turbulent mixing of NH_3. While the simulation framework can already be applied to improve the interpretation of NH_3 measurements, we recommend to continue the development of this simulation framework.

Our main recommendation towards improving the simulation framework would be to further develop the representations of the surface-atmosphere exchange and the gas-aerosol transformations. First, we advocate for a dynamic representation of the surface-atmosphere exchange, following mechanistic models that reproduce the assimilation of CO_2 at leaf level coupled to the stomatal aperture, e.g. the A-g_s model (Ronda et al., 2001). These models depend on the meteorological variables (Chapter 3) and they are scaled from leaf to canopy. The output of these models is a representation of the stomatal variables in form of resistance. Such an approach is very suitable to integrate the NH_3 flux with the sensible heat, latent heat and CO_2 exchange fluxes.

By including such a dynamic representation of the stomatal exchange, the flux will be calculated based on the difference between the near-surface NH_3 concentration and the ammonia compensation points, i.e. internal NH_3 concentration at the surface. As a follow up, parameterization of the NH_3 compensation points should be added to the simulation framework, e.g. the DEPAC module (van Zanten et al., 2010; Wichink Kruit et al., 2010b). With these additions, it would be interesting to apply the approach of Chapter 2 to the measurements of NH_3 emissions during the RITA-2021 campaign presented in Chapter 3, using the turbulent resolved simulation framework.

With regards to the gas-aerosol transformation, we recommend coupling the simulation framework to a thermodynamic equilibrium model (e.g. ISORROPIA2). This would allow for a realistic and detailed representation of the transformation of NH_3 to aerosols, as the process will be resolved taking into account the local heterogeneity of trace gas concentrations, temperature and relative humidity. With these additions, the simulation framework is able to resolve both macromixing (meandering) and micromixing (in-plume
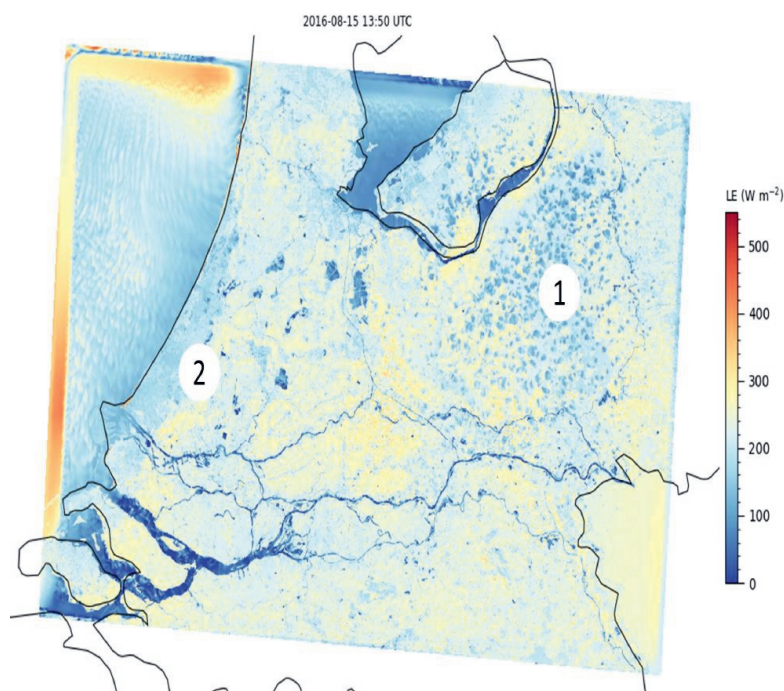
Figure 6.1: Fine-resolved simulation of evapotranspiration field in the Netherlands influenced by the presence of a shallow cumulus field (1) and the penetrations of a sea breeze front (2). The simulation is performed using the fine-scale Ruisdael TestBed (100 x 100 m2 resolution). These simulations have HARMONIE-AROME boundary conditions set at 2.5 km². The situation correspond to 15th August 2016 at 13.50 UTC. (Source: Vilà-Guerau de Arellano et al. (n.d.))

mixing) of the emission plume (Galmarini et al., 1995; Vilà-Guerau de Arellano et al., 1990). This allows for analysis of the role of non-linear effects of turbulent mixing on the chemical reaction rate within the plume and its impact on the local NH_3 concentration and surface-atmosphere exchange.

We strongly advocate that these developments on the representation of atmospheric NH_3 are incorporated in the high-resolution simulation efforts of the Ruisdael Project, the Ruisdael TestBed (in progress). The TestBed almost continuously combines observations and simulations of the meteorological conditions in the Netherlands. An example of the level of detail that can be achieved with the Ruisdael TestBed is shown in Fig. 6.1.

The efforts of the Ruisdael TestBed go beyond individual case studies and aim to test the performance and improve parameterizations under all sort of weather and atmospheric composition conditions. At the time of writing, the Ruisdael team is testing a realistic implementation of trace gas emission sources to the TestBed, based on the national emission

inventory for gasses like CO_2 and nitrogen compounds. Within this aim of more explicit treatment of the atmospheric flow to the spatial and temporal distribution of atmospheric compounds, we suggest to extend the Ruisdael TestBed to include atmospheric ammonia as well. This integration is done in a continuous manner that facilitates the comprehensive approach where turbulent resolved models are combined with observations.

At the current rate of increasing computational power and decreasing cost, the Ruisdael TestBed will be applied to complement, or potentially replace, operational models like OPS or LOTOS-EUROS within 5-10 years. Application of the TestBed for operational purposes will depend. For multi-year forecasting, the use of Large-Eddy simulation techniques will be too computationally expensive for quite some time. Here, the TestBed will likely be embedded in current operational models, providing high-resolution support in regions with high spatio-temporal variability at 100 m resolution. For other purposes, like monitoring the development of air pollution and nitrogen deposition in the Netherlands, the Ruisdael TestBed will likely be operational within a few years.

6.2.2 An integrated measurement approach

When establishing a measurement site, the local NH_3 surface characteristics and the orientation of the instruments require considerations. Ideally, the NH_3 characteristics are well-mixed, with (approximately) homogeneous NH_3 surface characteristics and negligible impact of emission sources within a few (1 - 3) kilometers distance. Such idealized conditions are rare in agriculturally active regions where understanding and mitigating the harmful effects of nitrogen deposition is most important. We therefore recommend to apply the simulation framework presented in this thesis (Chapter 4) beforehand, to assess the potential impact of the nearby (< 5 km) sources and avoid introducing a bias in the observations. While measuring, we also recommend to estimate the emissions based on the emission inventory or using inexpensive sensors (Melse et al., 2016) and collaborate with local farmers and other potential emitters of NH_3, in order to track manure applications and other potential emission events while NH_3 measurements are taken.

In addition to nearby emission sources, the orientation of the instruments requires considerable attention when designing a measurement site, in order to avoid introducing a bias in the long-term averages. Housing of the (NH_3) instruments, data storage and power supply will lead to an obstruction of the airflow and will require filtering for wind direction. As meteorological conditions have significant impact on both the NH_3 concentration and flux, we recommend to not only fixate on minimizing the loss of data, but to orient the measurement setup to capture a wide range of weather conditions. The importance was highlighted in Chapter 3, where the instrumental setup was designed anticipating prevailing winds from the south-west, resulting in the synoptic weather conditions, characterized frontal passages. As a result, very few measurement were taken for clear-sky conditions, while we found a strong relation between the stomatal exchange of NH_3 and radiation.

Figure 6.2: The miniDOAS NH$_3$ flux measurement setup at the Ruisdael Observatory at Cabauw during the RITA-2021 campaign. The light-path emitted by the miniDOAS instruments is clearly visible at night, with the miniDOAS instruments being housed in the container on the left and the retroreflectors at 22 m distance on the mast on the right. (Picture taken by Arnoud Apituley, September 2021)

Measurements for a broader range of meteorological conditions would have likely improved the analysis in Chapter 3.

A second consideration for the orientation of measurement instruments is the spatial variability of the NH$_3$ concentration. Filtering out specific wind directions can lead to an under- or overestimation of the observed NH$_3$. Depending on the upwind NH$_3$ characteristics, e.g. an agricultural area or a nature reserve, the airflow from a specific wind direction can be characterized by low or high upwind concentrations. These considerations should not only be taken into account with the measurement site preparations, but it also provides valuable context to the observations when analyzing the NH$_3$ measurements.

The newly developed miniDOAS flux measurement setup (Swart et al., 2023), shown in Fig. 6.2, is at the core of our observational approach. Typical inlet issues of conventional NH$_3$ observations are eliminated with the use of the differential optical absorption spectroscopy (DOAS) technique, measuring a line averaged concentration over a 22 m open-path. By applying the flux-gradient method on concentration measurements at two heights, the

miniDOAS setup sets a new standard for high-accuracy concentration and flux measurements at 30 minute resolution. Furthermore, the high up-time and low maintenance allows for long term (> 1 year) continuous NH_3 flux measurements. We recommend to support the miniDOAS flux measurements with occasional (e.g. biannual) intercomparison campaigns, using eddy-covariance flux measurements as presented by Swart et al. (2023). Using the miniDOAS system, we envision an integrated approach centered around long-term continuous NH_3 measurements (> 1 year), combining observations with both conceptual and turbulent-resolved models.

With the new miniDOAS setup, the contribution of the NH_3 surface-atmosphere exchange to the atmospheric ammonia budget is well constrained. We recommend the addition of auxiliary measurements, to better constrain the other processes governing the atmospheric NH_3 budget and further our understanding of the diurnal variability of atmospheric ammonia. To represent the process of gas-aerosol transformations, we recommend measurements of aerosol concentration and composition at the height of one of the miniDOAS instruments. When combined with measurements of temperature and relative humidity at both miniDOAS heights, one can estimate the equilibrium concentration of the aerosols at both miniDOAS heights using a thermodynamic equilibrium model. From this set of measurements, the role of the formation or evaporation of aerosols on the miniDOAS observed NH_3 gradient can be estimated, similar to Nemitz et al. (2004a).

The role of boundary-layer dynamics and entrainment can be represented in part by continuous measurements of the boundary-layer height, using ceilometers. Estimating the NH_3 concentration in the free troposphere or residual layer still remains a major challenge, which could be estimated based on high-tower (> 100 m) or airborne NH_3 measurements. Finally, advection can be estimated using turbulent-resolved or operational models, or by using the approach presented in Chapter 2 using a conceptual model.

Integrating these measurements with conceptual and turbulent-resolved models will further our understanding of the the atmospheric NH_3 budget. The results can be compared with operational models, to identify weaknesses in the representation of the diurnal variability of the NH_3 concentration, which is directly linked to the surface-atmosphere exchange.

6.2.3 Improving the parameterization of the NH_3 surface-atmosphere exchange

The results presented in this thesis indicate that exchange through the stomatal pathway is not yet fully understood and that the parameterization of the stomatal compensation point needs to be revisited to improve the performance at the subdaily scales. Long-term miniDOAS NH_3 observations provide a unique opportunity to systematically study the surface-atmosphere exchange parameterization, at both subdaily and seasonal timescales. We would recommend to start with estimating the NH_3 flux based on current parameterizations, parallel to the observed flux, to identify potential weaknesses in the parameterizations.

After this preliminary analysis, we recommend to follow up by combining the advanced NH_3 measurements with a comprehensive set of auxiliary measurements and a systematic suite of numerical experiments.

The miniDOAS setup infers the net NH_3 flux and cannot distinguish between stomatal and non-stomatal exchange. Generally, this distinction is made based on daytime (stomatal) and nighttime (non-stomatal) observations, as well as linking non-stomatal exchange to high relative humidity. We advocate to expand the efforts to distinguish between the pathways using auxiliary observations. The non-stomatal pathway mainly depends on the relative humidity and the water film on the leaf surface (dew). Adding auxiliary measurements of leaf wetness would therefore better constrain the analysis of non-stomatal exchange, especially after sunrise when the contribution of the stomatal pathway starts to increase.

To support the analysis of stomatal exchange, we recommend adding continuous flux measurements of water vapor and other trace gasses (e.g. CO_2, NO_2 and O_3), which each have a stomatal component, as well as the momentum flux, sensible heat flux and a wide range of meteorological variables (e.g. radiation and vapor pressure deficit). We recommend to expand these efforts with measurement campaigns including leaf-level observations (e.g. leaf temperature and stomatal aperture) and estimations of the stomatal compensation point based on bioassay measurements, similar to Loubet et al. (2002). Supported by these observations, relations can be inferred and the NH_3 compensation points can be estimated, which should be further analyzed and tested in numerical experiments.

In the future, the comprehensive approach described above should not be limited to a single site, but be applied to a comprehensive and representative measurement network. In that respect, the future Ruisdael TestBed provides a unique opportunity for the observations from this network to be integrated with advanced simulations. With the lessons learned in this thesis and the recent developments in both the use of advanced instrumental techniques and high spatio-temporal simulations, we are taking research on atmospheric ammonia to a higher level of quantification and detail. As such, we can further advance the understanding and representation of the diurnal variability of ammonia over grassland.

References

aan de Brugh, J. M. J., J. S. Henzing, M. Schaap, W. T. Morgan, C. C. van Heerwaarden, E. P. Weijers, H. Coe, and M. C. Krol (2012). "Modelling the partitioning of ammonium nitrate in the convective boundary layer". *Atmospheric Chemistry and Physics* 12.6, 3005–3023. DOI: `10.5194/acp-12-3005-2012`.

aan de Brugh, J. M. J., H. G. Ouwersloot, J. Vilà-Guerau de Arellano, and M. C. Krol (2013). "A large-eddy simulation of the phase transition of ammonium nitrate in a convective boundary layer". *J. Geophys. Res. Atmos.* 118.2, 826–836. DOI: `10.1002/jgrd.50161`.

Adams, P. J., J. H. Seinfeld, and D. M. Koch (1999). "Global concentrations of tropospheric sulfate, nitrate, and ammonium aerosol simulated in a general circulation model". *Journal of Geophysical Research: Atmospheres* 104.D11, 13791–13823. DOI: `10.1029/1999JD900083`.

Anys, M., B. Ullrich, M. Gager, and M. Pinterits (2020). *European Union emission inventory report 1990-2018: under the UNECE Convention on Long-range Transboundary Air Pollution*. Tech. rep. TH-AL-20-013-EN-N. Kongens Nytorv 6, 1050 Copenhagen K, Denmark: European Environment Agency.

Ardeshiri, H., M. Cassiani, S. Y. Park, A. Stohl, I. Pisso, and A. S. Dinger (2021). "On the Convergence and Capability of the Large-Eddy Simulation of Concentration Fluctuations in Passive Plumes for a Neutral Boundary Layer at Infinite Reynolds Number". *Boundary-Layer Meteorology* 176, 291–327. DOI: `10.1007/s10546-020-00537-6`.

Arnfield, A. J. (2003). "Two decades of urban climate research: a review of turbulence, exchanges of energy and water, and the urban heat island". *International Journal of Climatology: a Journal of the Royal Meteorological Society* 23.1, 1–26. DOI: `10.1002/joc.859`.

Arrillaga, J. A., J. Vilà-Guerau de Arellano, F. Bosveld, H. Klein Baltink, C. Yagüe, M. Sastre, and C. Román-Cascón (2018). "Impacts of afternoon and evening sea-breeze fronts on local turbulence, and on CO2 and radon-222 transport". *Quarterly Journal of the Royal Meteorological Society* 144.713, 990–1011. DOI: `10.1002/qj.3252`.

Asman, W. A. H. (1995). "Parameterization of below-cloud scavenging of highly soluble gases under convective conditions". *Atmospheric Environment* 29.12, 1359–1368. DOI: `10.1016/1352-2310(95)00065-7`.

Aubinet, M., C. Feigenwinter, B. Heinesch, C. Bernhofer, E. Canepa, A. Lindroth, L. Montagnani, C. Rebmann, P. Sedlak, and E. van Gorsel (2010). "Direct advection measurements do not help to solve the night-time CO_2 closure problem: Evidence from three different forests". *Agricultural and Forest Meteorology* 150, 655–664. DOI: `10.1016/j.agrformet.2010.01.016`.

Baldocchi, D., E. Falge, L. Gu, R. Olson, D. Hollinger, S. Running, P. Anthoni, C. Bernhofer, K. Davis, R. Evans, J. Fuentes, A. Allen Goldstein, G. Gabriel Katul, B. Law, X. Lee, Y. Malhi, M. Meyers, W. Munger, W. Oechel, K. T. Paw U, K. Pilegaard, H. P. Schmid, R. Valentini, S. Verma, T. Vesala, K. Wilson, and S. Wofsy (2001). "FLUXNET: A New Tool to Study the Temporal and Spatial Variability of Ecosystem-Scale Carbon Dioxide, Water Vapor, and Energy Flux Densities". *Bulletin of the American Meteorological Society* 82.11, 2415–2434. DOI: `10.1175/1520-0477(2001)082<2415:FANTTS>2.3.CO;2`.

Barad, M. L. (1958). *Project Prairie Grass, a field program in diffusion. Volume 1.* Tech. rep. No. 59, Vol I , Report AFCRC-TR-58-235(I). AIR FORCE CAMBRIDGE RESEARCH LABS.

Barbaro, E., M. C. Krol, and J. Vilà-Guerau de Arellano (2015). "Numerical simulation of the interaction between ammonium nitrate aerosol and convective boundary-layer dynamics". *Atmospheric Environment* 105, 202–211. DOI: `10.1016/j.atmosenv.2015.01.048`.

Barbaro, E., J. Vilà-Guerau de Arellano, H. G. Ouwersloot, J. S. Schröter, D. P. Donovan, and M. C. Krol (2014). "Aerosols in the convective boundary layer: Shortwave radiation effects on the coupled land-atmosphere system". *Journal of Geophysical Research: Atmospheres* 119.10, 5845–5863. DOI: `10.1002/2013JD021237`.

Behera, S. N., M. Sharma, V. P. Aneja, and R. Balasubramanian (2013). "Ammonia in the atmosphere: a review on emission sources, atmospheric chemistry and deposition on terrestrial bodies". *Environmental Science and Pollution Researc* 20.4, 8092–8131. DOI: `10.1007/s11356-013-2051-9`.

Beljaars, A. C. M. and A. A. M. Holtslag (1991). "Flux Parameterization over Land Surfaces for Atmospheric Models". *Journal of Applied Meteorology* 30.3, 327–341. DOI: `10.1175/1520-0450(1991)030<0327:FPOLSF>2.0.CO;2`.

Benner, W., B. Ogorevc, and T. Novakov (1992). "Oxidation of SO2 in thin water films containing NH3". *Atmospheric Environment. Part A. General Topics* 26.9, 1713–1723. DOI: `10.1016/0960-1686(92)90069-W`.

Berkhout, A. J. C., D. P. J. Swart, H. Volten, L. F. L. Gast, M. Haaima, H. Verboom, G. Stefess, T. Hafkenscheid, and R. Hoogerbrugge (2017). "Replacing the AMOR with the miniDOAS in the ammonia monitoring network in the Netherlands". *Atmospheric Measurement Techniques* 10.11, 4099–4120. DOI: `10.5194/amt-10-4099-2017`.

Bobbink, R., M. Hornung, and J. G. M. Roelofs (2003). "The effects of air-borne nitrogen pollutants on species diversity in natural and semi-natural European vegetation". *Journal of Ecology* 86, 717–738. DOI: 10.1046/j.1365-2745.1998.8650717.x.

Boermans, G. M. F. and J. W. Erisman (1990). *Meetstrategieontwikkeling voor het representativiteitsonderzoek als onderdeel van het additioneel meetprogramma ammoniak: fenomenologie van NH3 en meetritsimulaties.* Tech. rep. 222105001. Antonie van Leeuwenhoeklaan 9, 3721, MA Bilthoven, the Netherlands: National Institute for Public Health and the Environment (RIVM).

Boone, A., J. Bellvert, M. Best, J. Brooke, G. Canut-Rocafort, J. Cuxart, O. Hartogensis, P. Le Moigne, J. R. Miró, J. Polcher, J. Price, P. Quintana Seguí, and M. Wooster (2021). "Updates on the International Land Surface Interactions with the Atmophere over the Iberian Semi-Arid Environment (LIAISE) Field Campaign". *GEWEX News* 31.4, 17–21.

Bosveld, F. C., P. Baas, A. C. M. Beljaars, A. A. M. Holtslag, J. Vilà-Guerau de Arellano, and B. J. H. van de Wiel (2020). "Fifty Years of Atmospheric Boundary-Layer Research at Cabauw Serving Weather, Air Quality and Climate". *Boundary-Layer Meteorology* 177, 583–612. DOI: 10.1007/s10546-020-00541-w.

Bou-Zeid, E., W. Anderson, G. G. Katul, and L. Mahrt (2020). "The Persistent Challenge of Surface Heterogeneity in Boundary-Layer Meteorology: A Review". *Boundary-Layer Meteorol* 177.2, 227–245. DOI: 10.1007/s10546-020-00551-8. (Visited on 2020).

Brauer, C. C., P. J. J. F. Torfs, A. J. Teuling, and R. Uijlenhoet (2014). "The Wageningen Lowland Runoff Simulator (WALRUS): application to the Hupsel Brook catchment and the Cabauw polder". *Hydrology and Earth System Sciences* 18.10, 4007–4028. DOI: 10.5194/hess-18-4007-2014.

Brunekreef, B. and S. T. Holgate (2002). "Air pollution and health". *The Lancet* 360.9341, 1233–1242. DOI: 10.1016/S0140-6736(02)11274-8.

Buijsman, E., J. M. M. Aben, B. G. Van Elzakker, and M. G. Mennen (1998). "An automatic atmospheric ammonia network in the Netherlands set-up and results". *Atmospheric Environment* 32.3, 317–324. DOI: 10.1016/S1352-2310(97)00233-1.

Businger, J. A., J. C. Wyngaard, Y. Izumi, and E. F. Bradley (1971). "Flux-Profile Relationships in the Atmospheric Surface Layer". *Journal of the Atmospheric Sciences* 28.2, 181–189. DOI: 10.1175/1520-0469(1971)028<0181:FPRITA>2.0.CO;2.

Butterworth, B. J., A. R. Desai, P. A. Townsend, G. W. Petty, C. G. Andresen, T. H. Bertram, E. L. Kruger, J. K. Mineau, E. R. Olson, S. Paleri, R. A. Pertzborn, C. Pettersen, P. C. Stoy, J. E. Thom, M. P. Vermeuel, T. J. Wagner, D. B. Wright, T. Zheng, S. Metzger, M. D. Schwartz, T. J. Iglinski, M. Mauder, J. Speidel, H. Vogelmann, L. Wanner, T. J. Augustine, W. O. J. Brown, S. P. Oncley, M. Buban, T. R. Lee, P. Cleary, D. J. Durden, C. R. Florian, K. Lantz, L. D. Riihimaki, J. Sedlar, T. P. Meyers, D. M. Plummer, E. Ruiz Guzman, E. N. Smith, M. Sühring, D. D. Turner, Z. Wang,

L. D. White, and J. M. Wilczak (2021). "Connecting Land–Atmosphere Interactions to Surface Heterogeneity in CHEESEHEAD19". *Bulletin of the American Meteorological Society* 102.2, E421–E445. DOI: 10.1175/BAMS-D-19-0346.1.

Calders, K., T. Schenkels, H. Bartholomeus, J. Armston, J. Verbesselt, and M. Herold (2015). "Monitoring spring phenology with high temporal resolution terrestrial LiDAR measurements". *Agricultural and Forest Meteorology* 203, 158–168. DOI: 10.1016/j.agrformet.2015.01.009.

Cassiani, M., M. B. Bertagni, M. Marro, and P. Salizzoni (2020). "Concentration Fluctuations from Localized Atmospheric Releases". *Boundary-Layer Meteorology* 177, 461–510. DOI: 10.1007/s10546-020-00547-4.

Casso-Torralba, P., J. Vilà-Guerau de Arellano, F. Bosveld, M. R. Soler, A. Vermeulen, C. Werner, and E. Moors (2008). "Diurnal and vertical variability of the sensible heat and carbon dioxide budgets in the atmospheric surface layer". *Journal of Geophysical Research: Atmospheres* 113.D12. DOI: 10.1029/2007JD009583.

Cowan, I. R. and G. D. Farquhar (1977). "Stomatal function in relation to leaf metabolism and environment". *Camebridge: at the university press*, 471–505.

Cuxart, J., B. Wrenger, D. Martınez-Villagrasa, J. Reuder, M. O. Jonassen, M. A. Jiménez, M. Lothon, F. Lohou, O. Hartogensis, J. Dünnermann, L. Conangla, and A. Garai (2016). "Estimation of the advection effects induced by surface heterogeneities in the surface energy budget". *Atmospheric Chemistry and Physics* 16.14, 9489–9504. DOI: 10.5194/acp-16-9489-2016.

Dammers, E., M. Schaap, M. Haaima, M. Palm, R. J. Wichink Kruit, H. Volten, A. Hensen, D. Swart, and J. W. Erisman (2017). "Measuring atmospheric ammonia with remote sensing campaign: Part 1 – Characterisation of vertical ammonia concentration profile in the centre of The Netherlands". *Atmospheric Environment* 169, 97–112. DOI: 10.1016/j.atmosenv.2017.08.067.

Davis, K. J., D. H. Lenschow, and P. R. Zimmerman (1994). "Biogenic nonmethane hydrocarbon emissions estimated from tethered balloon observations". *Journal of Geophysical Research: Atmospheres* 99.D12, 25587–25598. DOI: 10.1029/94JD02009.

de Groot, G. E., J. Vilà-Guerau de Arellano, S. R. de Roode, A. M. J. Coenders-Gerrits, and B. J. H. van de Wiel (2019). "Evaporation Hysteresis over Vegetation: The Impact of Surface Processes and Boundary Layer Dynamics". MA thesis. the Netherlands: Delft University of Technology.

Dosio, A. and J. Vilà-Guerau de Arellano (2006). "Statistics of Absolute and Relative Dispersion in the Atmospheric Convective Boundary Layer: A Large-Eddy Simulation Study". *Journal of the Atmospheric Sciences* 63.4, 1253–1272. DOI: 10.1175/JAS3689.1.

Dosio, A., J. Vilà-Guerau de Arellano, A. A. M. Holtslag, and P. J. H. Builtjes (2003). "Dispersion of a Passive Tracer in Buoyancy- and Shear-Driven Boundary Layers".

Journal of Applied Meteorology 42.8, 1116–1130. DOI: 10.1175/1520-0450(2003)042<1116:DOAPTI>2.0.CO;2.

Duxbury, J. M. (1994). "The significance of agricultural sources of greenhouse gases". *Fertilizer research* 38, 151–163. DOI: 10.1007/BF00748775.

Dyer, A. J. (1974). "A review of flux-profile relationships". *Boundary-Layer Meteorology* 7.3, 363–372. DOI: 10.1007/BF00240838.

Dyer, A. J. and B. B. Hicks (1970). "Flux-gradient relationships in the constant flux layer". *Quarterly Journal of the Royal Meteorological Society* 96.410, 715–721. DOI: 10.1002/qj.49709641012.

EMEP/CCC (2001). *EMEP manual for sampling and chemical analysis*. Tech. rep. EMEP/CCC-Report 1/95, O-7726. Chemical Co-ordination Centre of EMEP (EMEP/CCC).

Erisman, J. and G. P. Wyers (1993). "Continuous measurements of surface exchange of SO2 and NH3; Implications for their possible interaction in the deposition process". *Atmospheric Environment. Part A. General Topics* 27.13, 1937–1949. DOI: 10.1016/0960-1686(93)90266-2.

Erisman, J. W., A. Bleeker, J. Galloway, and M. S. Sutton (2007). "Reduced nitrogen in ecology and the environment". *Environmental Pollution* 150.1, 140–149. DOI: 10.1016/j.envpol.2007.06.033.

Erisman, J. W., J. Galloway, S. Seitzinger, A. Bleeker, and K. Butterbach-Bahl (2011). "Reactive nitrogen in the environment and its effect on climate change". *Current Opinion in Environmental Sustainability* 3.5, 281–290. DOI: 10.1016/j.cosust.2011.08.012.

Erisman, J. W., J. N. Galloway, S. Seitzinger, A. Bleeker, N. B. Dise, A. M. R. Petrescu, A. M. Leach, and W. de Vries (2013). "Consequences of human modification of the global nitrogen cycle". *Philosophical Transactions of the Royal Society B: Biological Sciences* 368.1621, 20130116. DOI: 10.1098/rstb.2013.0116.

Erisman, J. W., P. Grennfelt, and M. Sutton (2003). "The European perspective on nitrogen emission and deposition". *Environment International* 29.2. Future Directions in Air Quality Research : Ecological,Atmospheric,Regulatory/Policy/Economic, and Educational Issues, 311–325. DOI: 10.1016/S0160-4120(02)00162-9.

Erisman, J. W. and M. Schaap (2004). "The need for ammonia abatement with respect to secondary PM reductions in Europe". *Environmental Pollution* 129.1, 159–163. DOI: 10.1016/j.envpol.2003.08.042.

Erisman, J. W., A. W. M. Vermetten, W. A. H. Asman, A. Waijers-Ijpelaan, and J. Slanina (1988). "Vertical distribution of gases and aerosols: The behaviour of ammonia and related components in the lower atmosphere". *Atmospheric Environment (1967)* 22.6, 1153–1160. DOI: 10.1016/0004-6981(88)90345-9.

Famulari, D., D. Fowler, K. Hargreaves, C. Milford, E. Nemitz, M. A. Sutton, and K. Weston (2005). "Measuring eddy covariance fluxes of ammonia using tunable diode laser absorption spectroscopy". *Water, Air, & Soil Pollution: Focus* 4.6, 151–158. DOI: `10.1007/s11267-005-3025-9`.

Famulari, D., D. Fowler, E. Nemitz, K. J. Hargreaves, R. L. Storeton-West, G. Rutherford, Y. S. Tang, M. A. Sutton, and K. J. Weston (2010). "Development of a low-cost system for measuring conditional time-averaged gradients of SO2 and NH3". *Environmental Monitoring and Assessment* 161.1, 11–27. DOI: `10.1007/s10661-008-0723-6`.

Farquhar, G. D., P. M. Firth, R. Wetselaar, and B. Weir (1980). "On the Gaseous Exchange of Ammonia between Leaves and the Environment: Determination of the Ammonia Compensation Point". *Plant Physiology* 66.4, 710–714. DOI: `10.1104/pp.66.4.710`.

Ferrara, R. M., P. Di Tommasi, D. Famulari, and G. Rana (2021). "Limitations of an Eddy-Covariance System in Measuring Low Ammonia Fluxes". *Boundary-Layer Meteorology* 180.1, 173–186. DOI: `10.1007/s10546-021-00612-6`.

Flechard, C. R., D. Fowler, M. A. Sutton, and J. N. Cape (1999). "A dynamic chemical model of bi-directional ammonia exchange between semi-natural vegetation and the atmosphere". *Quarterly Journal of the Royal Meteorological Society* 125.559, 2611–2641. DOI: `10.1002/qj.49712555914`.

Fountoukis, C. and A. Nenes (2007). "ISORROPIA II: a computationally efficient thermodynamic equilibrium model for K^+-Ca^{2+}-Mg^{2+}-NH_4^+-Na^+-SO_4^{2-}-NO_3^--Cl^--H_2O aerosols". *Atmos. Chem. Phys.* 7, 4639–4659. DOI: `10.5194/acp-7-4639-2007`.

Fowler, D., K. Pilegaard, M. A. Sutton, P. Ambus, M. Raivonen, J. Duyzer, D. Simpson, H. Fagerli, S. Fuzzi, J. K. Schjoerring, C. Granier, A. Neftel, I. S. A. Isaksen, P. Laj, M. Maione, P. S. Monks, J. Burkhardt, U. Daemmgen, J. Neirynck, E. Personne, R. Wichink-Kruit, K. Butterbach-Bahl, C. Flechard, J. P. Tuovinen, M. Coyle, G. Gerosa, B. Loubet, N. Altimir, L. Gruenhage, C. Ammann, S. Cieslik, E. Paoletti, T. N. Mikkelsen, H. Ro-Poulsen, P. Cellier, J. N. Cape, L. Horváth, F. Loreto, Ü. Niinemets, P. I. Palmer, J. Rinne, P. Misztal, E. Nemitz, D. Nilsson, S. Pryor, M. W. Gallagher, T. Vesala, U. Skiba, N. Brüggemann, S. Zechmeister-Boltenstern, J. Williams, C. O'Dowd, M. C. Facchini, G. de Leeuw, A. Flossman, N. Chaumerliac, and J. W. Erisman (2009). "Atmospheric composition change: Ecosystems–Atmosphere interactions". *Atmospheric Environment* 43.33. ACCENT Synthesis, 5193–5267. DOI: `10.1016/j.atmosenv.2009.07.068`.

Fowler, D., C. E. R. Pitcairn, M. A. Sutton, C. Flechard, B. Loubet, M. Coyle, and R. C. Munro (1998). "The mass budget of atmospheric ammonia in woodland within 1 km of livestock buildings". *Environmental Pollution* 102.1, Supplement 1, 343–348. DOI: `10.1016/S0269-7491(98)80053-5`.

Gailis, R. M., A. Hill, E. Yee, and T. Hilderman (2007). "Extension of a fluctuating plume model of tracer dispersion to a sheared boundary layer and to a large array of obstacles". *Boundary-Layer Meteorology* 122.3, 577–607. DOI: `10.1007/s10546-006-9118-9`.

Galloway, J. N., J. D. Aber, J. W. Erisman, S. P. Seitzinger, R. W. Howarth, E. B. Cowling, and B. J. Cosby (2003). "The Nitrogen Cascade". *BioScience* 53.4, 341–356. DOI: `10.1641/0006-3568(2003)053[0341:TNC]2.0.CO;2`.

Galmarini, S., J. Vilà-Guerau de Arellano, and P. G. Duynkerke (1995). "The effect of micro-scale turbulence on the reaction rate in a chemically reactive plume". *Atmospheric Environment* 29.1, 87–95. DOI: `10.1016/1352-2310(94)00224-9`.

Garratt, J. R. (1991). "The internal boundary layer — A review". *Boundary-Layer Meteorology* 50, 171–203. DOI: `10.1007/BF00120524`.

Gates, D. M. (1980). *Biophysical ecology.* Springer-Verlag.

Grant, A. L. M. (1991). "Surface drag and turbulence over an inhomogeneous land surface". *Boundary-Layer Meteorology* 56, 309–337. DOI: `10.1007/BF00119210`.

Guo, H., R. Otjes, P. Schlag, A. Kiendler-Scharr, A. Nenes, and R. J. Weber (2018). "Effectiveness of ammonia reduction on control of fine particle nitrate". *Atmospheric Chemistry and Physics* 18.16, 12241–12256. DOI: `10.5194/acp-18-12241-2018`.

Heinze, R., A. Dipankar, C. C. Henken, C. Moseley, O. Sourdeval, S. Trömel, X. Xie, P. Adamidis, F. Ament, H. Baars, C. Barthlott, A. Behrendt, U. Blahak, S. Bley, S. Brdar, M. Brueck, S. Crewell, H. Deneke, P. Di Girolamo, R. Evaristo, J. Fischer, C. Frank, P. Friederichs, T. Göcke, K. Gorges, L. Hande, M. Hanke, A. Hansen, H.-C. Hege, C. Hoose, T. Jahns, N. Kalthoff, D. Klocke, S. Kneifel, P. Knippertz, A. Kuhn, T. van Laar, A. Macke, V. Maurer, B. Mayer, C. I. Meyer, S. K. Muppa, R. A. J. Neggers, E. Orlandi, F. Pantillon, B. Pospichal, N. Röber, L. Scheck, A. Seifert, P. Seifert, F. Senf, P. Siligam, C. Simmer, S. Steinke, B. Stevens, K. Wapler, M. Weniger, V. Wulfmeyer, G. Zängl, D. Zhang, and J. Quaas (2017). "Large-eddy simulations over Germany using ICON: a comprehensive evaluation". *Quarterly Journal of the Royal Meteorological Society* 143.702, 69–100. DOI: `10.1002/qj.2947`.

Heus, T., C. C. van Heerwaarden, H. J. J. Jonker, A. Siebesma, S. Axelsen, K. van den Dries, O. Geoffroy, A. F. Moene, D. Pino, S. R. de Roode, and J. Vilà-Guerau de Arellano (2010). "Formulation of the Dutch Atmospheric Large-Eddy Simulation (DALES) and overview of its applications". *Geoscientific Model Development* 3.2, 415–444. DOI: `10.5194/gmd-3-415-2010`.

Heusinkveld, B. G., G. J. Steeneveld, L. W. A. Van Hove, C. M. J. Jacobs, and A. A. M. Holtslag (2014). "Spatial variability of the Rotterdam urban heat island as influenced by urban land use". *Journal of Geophysical Research: Atmospheres* 119.2, 677–692. DOI: `10.1002/2012JD019399`.

Holtslag, A. A. M., G. Svensson, S. Basu, B. Beare, F. C. Bosveld, and J. Cuxart (2012). "Overview of the GEWEX Atmospheric Boundary Layer Study (GABLS)". In: *Proceedings of the Workshop on Diurnal cycles and the stable boundary layer, 7-10 November 2011, Reading, UK*, 11–23.

Hoogerbrugge, R., G. P. Geilenkirchen, H. A. den Hollander, K. Siteur, W. Smeets, E. van der Swaluw, W. J. de Vries, and R. J. Wichink Kruit (2021). *Grootschalige concentratie- en depositiekaarten Nederland. Rapportage 2021.* Tech. rep. RIVM rapport 2021-0068. Rijksinstituut voor Volksgezondheid en Milieu RIVM. DOI: `10.21945/RIVM-2021-0068`.

Hsiao, T. C. (1973). "Plant responses to water stress". *Annu. Rev. Plant Physiol.* 24, 519–570.

Izett, J. G., B. J. H. van de Wiel, P. Baas, and F. C. Bosveld (2018). "Understanding and Reducing False Alarms in Observational Fog Prediction". *Boundary-Layer Meteorology* 169, 347–372. DOI: `10.1007/s10546-018-0374-2`.

Jacobs, C. M. J. (1994). "Direct impact of atmospheric CO2 enrichment on regional transpiration". PhD thesis. Wageningen University.

Jacobs, C. M. J. and H. A. R. de Bruin (1997). "Predicting Regional Transpiration at Elevated Atmospheric CO2: Influence of the PBL–Vegetation Interaction". *Journal of Applied Meteorology* 36.12, 1663–1675. DOI: `10.1175/1520-0450(1997)036<1663:PRTAEA>2.0.CO;2`.

Jacobs, C. M. J., A. F. G. Jacobs, F. C. Bosveld, D. M. D. Hendriks, A. Hensen, P. S. Kroon, E. J. Moors, L. Nol, A. Schrier-Uijl, and E. M. Veenendaal (2007). "Variability of annual CO_2 exchange from Dutch grasslands". *Biogeosciences* 4.5, 803–816. DOI: `10.5194/bg-4-803-2007`.

Jarvis, P. G., J. L. Monteith, and P. E. Weatherley (1976). "The interpretation of the variations in leaf water potential and stomatal conductance found in canopies in the field". *Philosophical Transactions of the Royal Society of London. B, Biological Sciences* 273.927, 593–610. DOI: `10.1098/rstb.1976.0035`.

Kljun, N., P. Calanca, M. W. Rotach, and H. P. Schmid (2015). "A simple two-dimensional parameterisation for Flux Footprint Prediction (FFP)". *Geoscientific Model Development* 8.11, 3695–3713. DOI: `10.5194/gmd-8-3695-2015`.

Kljun, N., R. Kormann, M. W. Rotach, and F. X. Meixer (2003). "Comparison of the lagrangian footprint model LPDM-B with an analytical footprint model". *Boundary-Layer Meteorology* 106.2, 349–355. DOI: `10.1023/A:1021141223386`.

Kulmala, M., A. Asmi, H. K. Lappalainen, U. Baltensperger, J. L. Brenguier, M. C. Facchini, H. C. Hansson, Ø. Hov, C. D. O'Dowd, U. Pöschl, A. Wiedensohler, R. Boers, O. Boucher, et al. (2011). "General overview: European Integrated project on Aerosol Cloud Climate and Air Quality interactions (EUCAARI) - integrating aerosol research from nano to global scales". *Atmospheric Chemistry and Physics* 11.24, 13061–13143. DOI: `10.5194/acp-11-13061-2011`.

Lolkema, D. E., H. Noordijk, A. P. Stolk, R. Hoogerbrugge, M. C. van Zanten, and W. A. J. van Pul (2015). "The Measuring Ammonia in Nature (MAN) network in the Netherlands". *Biogeosciences* 12.16, 5133–5142. DOI: `10.5194/bg-12-5133-2015`.

Loubet, B., P. Cellier, C. Milford, and M. A. Sutton (2006). "A coupled dispersion and exchange model for short-range dry deposition of atmospheric ammonia". *Quarterly Journal of the Royal Meteorological Society* 132.618, 1733–1763. DOI: 10.1256/qj.05.73.

Loubet, B., C. Decuq, E. Personne, R. S. Massad, C. Flechard, O. Fanucci, N. Mascher, J.-C. Gueudet, S. Masson, B. Durand, S. Genermont, Y. Fauvel, and P. Cellier (2012). "Investigating the stomatal, cuticular and soil ammonia fluxes over a growing tritical crop under high acidic loads". *Biogeosciences* 9.4, 1537–1552. DOI: 10.5194/bg-9-1537-2012.

Loubet, B., C. Milford, P. Hill, S. Tang, P. Cellier, and M. A. Sutton (2002). "Seasonal variability of apoplastic NH4$^+$ and pH in an intensively managed grassland". *Plant and Soil* 238, 97–110. DOI: 10.1023/A:1014208926195.

Manders, A. M. M., P. J. H. Builtjes, L. Curier, H. A. C. Denier van der Gon, C. Hendriks, S. Jonkers, R. Kranenburg, J. J. P. Kuenen, A. J. Segers, R. M. A. Timmermans, A. J. H. Visschedijk, R. J. Wichink Kruit, W. A. J. van Pul, F. J. Sauter, E. van der Swaluw, D. P. J. Swart, J. Douros, H. Eskes, E. van Meijgaard, B. van Ulft, P. van Velthoven, S. Banzhaf, A. C. Mues, R. Stern, G. Fu, S. Lu, A. Heemink, N. van Velzen, and M. Schaap (2017). "Curriculum vitae of the LOTOS-EUROS (v2.0) chemistry transport model". *Geoscientific Model Development* 10.11, 4145–4173. DOI: 10.5194/gmd-10-4145-2017.

Mangan, M. R., O. Hartogensis, A. Boone, O. Branch, G. Canut-Rocafort, J. Cuxart, H. de Boer, M. Le Page, D. Martinez-Villagrasa, M. Josep Ramon, J. Price, and J. Vilà-Guerau de Arellano (2023). "The surface-boundary layer connection across spatial scales of thermal heterogeneity". *Agricultural and Forest Meteorology*. (Under Review).

Marth, L. (1996). "The bulk aerodynamic formulation over heterogeneous surfaces". *Boundary-Layer Meteorology* 78, 87–119. DOI: 10.1007/BF00122488.

– (2000). "Surface Heterogeneity and Vertical Structure of the Boundary Layer". *Boundary-Layer Meteorology* 96, 33–62. DOI: 10.1023/A:1002482332477.

Martin, C., D. Fitzjarrald, M. Garstang, S. Greco, A. Oliveira, and E. Browell (1988). "Structure and growth of the mixing layer over the Amazon rain forest". *Journal of Geophysical Research Atmospheres* 93. DOI: 10.1029/JD093iD02p01361.

Massad, R. S., E. Nemitz, and M. A. Sutton (2010). "Review and parameterisation of bi-directional ammonia exchange between vegetation and the atmosphere". *Atmospheric Chemistry and Physics* 10.21, 10359–10386. DOI: 10.5194/acp-10-10359-2010.

Matthias, V., J. A. Arndt, A. Aulinger, J. Bieser, H. Denier van der Gon, R. Kranenburg, J. Kuenen, D. Neumann, G. Pouliot, and M. Quante (2018). "Modeling emissions for three-dimensional atmospheric chemistry transport models". *Journal of the Air & Waste Management Association* 68.8, 763–800. DOI: 10.1080/10962247.2018.1424057.

Mauder, M., R. L. Desjardins, E. Pattey, and D. Worth (2010). "An Attempt to Close the Daytime Surface Energy Balance Using Spatially-Averaged Flux Measurements". *Boundary-Layer Meteorology* 136.2, 175–191. DOI: 10.1007/s10546-010-9497-9.

Mauder, M., T. Foken, M. Aubinet, and A. Ibrom (2021). *Eddy-Covariance Measurements*. Springer International Publishing, 1473–1504.

McAllister, T. A., K. A. Beauchemin, S. M. McGinn, X. Hao, and P. H. Robinson (2011). "Greenhouse gases in animal agriculture—Finding a balance between food production and emissions". *Animal Feed Science and Technology* 166-167. Special Issue: Greenhouse Gases in Animal Agriculture - Finding a Balance between Food and Emissions, 1–6. DOI: 10.1016/j.anifeedsci.2011.04.057.

Meeder, J. P. and F. T. M. Nieuwstadt (2000). "Large-eddy simulation of the turbulent dispersion of a reactive plume from a point source into a neutral atmospheric boundary layer". *Atmospheric Environment* 34.21, 3563–3573. DOI: 10.1016/S1352-2310(00)00124-2.

Melse, R. W., J. P. M. Ploegaert, and N. W. M. Ogink (2016). *Laboratory test of Draeger Polytron 8000 with FL-6813260 sensor for NH3 measurement*. Tech. rep. BO-20-0004-049 /BO-20-004-093. Wageningen UR, Livestock Research. DOI: 10.18174/388326.

Meng, Z., X. Xu, W. Lin, B. Ge, Y. Xie, B. Song, S. Jia, R. Zhang, W. Peng, Y. Wang, H. Cheng, W. Yang, and H. Zhao (2018). "Role of ambient ammonia in particulate ammonium formation at a rural site in the North China Plain". *Atmospheric Chemistry and Physics* 18, 167–184. DOI: 10.5194/acp-18-167-2018.

Mensah, A. A., R. Holzinger, R. Otjes, A. Trimborn, T. F. Mentel, H. ten Brink, B. Henzing, and A. Kiendler-Scharr (2012). "Aerosol chemical composition at Cabauw, The Netherlands as observed in two intensive periods in May 2008 and March 2009". *Atmospheric Chemistry and Physics* 12.10, 4723–4742. DOI: 10.5194/acp-12-4723-2012.

Milford, C., K. J. Hargreaves, M. A. Sutton, B. Loubet, and P. Cellier (2001). "Fluxes of NH3 and CO2 over upland moorland in the vicinity of agricultural land". *Journal of Geophysical Research: Atmospheres* 106.D20, 24169–24181. DOI: 10.1029/2001JD900082.

Moene, A. F. and J. C. Van Dam (2014). *Transport in the Atmosphere-Vegetation-Soil Continuum*. Camebridge University Press.

Monin, A. S. and A. M. Obuhhov (1954). "Basic laws of turbulent mixing in the surface layer of the atmosphere". *Tr. Akad. Nauk SSSR Geophiz. Inst.* 24, 163–187.

Moravek, A., S. Singh, E. Pattey, L. Pelletier, and J. G. Murphy (2019). "Measurements and quality control of ammonia eddy covariance fluxes: a new strategy for high-frequency attenuation correction". *Atmospheric Measurement Techniques* 12.11, 6059–6078. DOI: 10.5194/amt-12-6059-2019.

Mozurkewich, M. (1993). "The dissociation constant of ammonium nitrate and its dependence on temperature, relative humidity and particle size". *Atmospheric Environment. Part A. General Topics* 27.2, 261–270. DOI: 10.1016/0960-1686(93)90356-4.

Mylne, K. R. and P. J. Mason (1991). "Concentration fluctuation measurements in a dispersing plume at a range of up to 1000 m". *Quarterly Journal of the Royal Meteorological Society* 117.497, 177–206. DOI: 10.1002/qj.49711749709.

Nemitz, E., C. Milford, and M. A. Sutton (2001). "A two-layer canopy compensation point model for describing bi-directional biosphere-atmosphere exchange of ammonia". *Quarterly Journal of the Royal Meteorological Society* 127.573, 815–833. DOI: 10.1002/qj.49712757306.

Nemitz, E., M. A. Sutton, J. K. Schjoerring, S. Husted, and G. P. Wyers (2000). "Resistance modelling of ammonia exchange over oilseed rape". *Agricultural and Forest Meteorology* 105.4, 405–425. DOI: 10.1016/S0168-1923(00)00206-9.

Nemitz, E., M. A. Sutton, G. P. Wyers, and P. A. C. Jongejan (2004a). "Gas-particle interactions above a Dutch heathland: I. Surface exchange fluxes of NH 3, SO 2, HNO 3 and HCl". *Atmospheric Chemistry and Physics* 4.4, 989–1005. DOI: 10.5194/acp-4-989-2004.

Nemitz, E., M. A. Sutton, G. P. Wyers, R. P. Otjes, M. G. Mennen, E. M. van Putten, and M. W. Gallagher (2004b). "Gas-particle interactions above a Dutch heathland: II. Concentrations and surface exchange fluxes of atmospheric particles". *Atmospheric Chemistry and Physics* 4.4, 1007–1024. DOI: 10.5194/acp-4-1007-2004.

Nieuwstadt, F. T. M. (1992). "A large-eddy simulation of a line source in a convective atmospheric boundary layer—I. Dispersion characteristics". *Atmospheric Environment. Part A. General Topics* 26.3, 485–495. DOI: 10.1016/0960-1686(92)90331-E.

Noordijk, H., M. Braam, S. Rutledge-Jonker, R. Hoogerbrugge, A. P. Stolk, and W. A. J. van Pul (2020). "Performance of the MAN ammonia monitoring network in the Netherlands". *Atmospheric Environment* 228, 117400. DOI: 10.1016/j.atmosenv.2020.117400.

Nowak, J. B., J. A. Neuman, R. Bahreini, C. A. Brock, A. M. Middlebrook, A. G. Wollny, J. S. Holloway, J. Peischl, T. B. Ryerson, and F. C. Fehsenfeld (2010). "Airborne observations of ammonia and ammonium nitrate formation over Houston, Texas". *Journal of Geophysical Research: Atmospheres* 115.D22304. DOI: 10.1029/2010JD014195.

Oke, T. R. (1982). "The energetic basis of the urban heat island". *Quarterly Journal of the Royal Meteorological Society* 108.455, 1–24. DOI: 10.1002/qj.49710845502.

Ouwersloot, H. G., A. F. Moene, J. J. Attema, and J. Vilà-Guerau de Arellano (2017a). "Large-Eddy Simulation Comparison of Neutral Flow Over a Canopy: Sensitivities to Physical and Numerical Conditions, and Similarity to Other Representations". *Boundary-Layer Meteorology* 162, 71–89. DOI: 10.1007/s10546-016-0182-5.

– (2017b). "Large-Eddy Simulation Comparison of Neutral Flow Over a Canopy: Sensitivities to Physical and Numerical Conditions, and Similarity to Other Representations". *Boundary-Layer Meteorology* 162, 71–89. DOI: 10.1007/s10546-016-0182-5.

Ouwersloot, H. G., J. Vilà-Guerau de Arellano, A. C. Nölscher, M. C. Krol, L. N. Ganzeveld, C. Breitenberger, I. Mammarella, J. Williams, and J. Lelieveld (2012). "Characterization of a boreal convective boundary layer and its impact on atmospheric chemistry during HUMPPA-COPEC-2010". *Atmospheric Chemistry and Physics* 12.19, 9335–9353. DOI: 10.5194/acp-12-9335-2012.

Ouwersloot, H. G., J. Vilà-Guerau de Arellano, C. C. van Heerwaarden, L. N. Ganzeveld, M. C. Krol, and J. Lelieveld (2011). "On the segregation of chemical species in a clear boundary layer over heterogeneous land surfaces". *Atmospheric Chemistry and Physics* 11.20, 10681–10704. DOI: 10.5194/acp-11-10681-2011.

Pagans, E., R. Barrena, X. Font, and A. Sánchez (2006). "Ammonia emissions from the composting of different organic wastes. Dependency on process temperature". *Chemosphere* 62.9, 1534–1542. DOI: 10.1016/j.chemosphere.2005.06.044.

Papaioannou, G., G. Nikolidakis, D. Asimakopoulos, and D. Retalis (1996). "Photosynthetically active radiation in Athens". *Agricultural and Forest Meteorology* 81.3, 287–298. DOI: 10.1016/0168-1923(95)02290-2.

Parrish, D. D. and F. C. Fehsenfeld (2000). "Methods for gas-phase measurements of ozone, ozone precursors and aerosol precursors". *Atmospheric Environment* 34.12, 1921–1957. DOI: 10.1016/S1352-2310(99)00454-9.

Paulson, C. A. (1970). "The Mathematical Representation of Wind Speed and Temperature Profiles in the Unstable Atmospheric Surface Layer". *Journal of Applied Meteorology* 9.6, 857–861. DOI: 10.1175/1520-0450(1970)009<0857:TMROWS>2.0.CO;2.

Pino, D., H. J. J. Jonker, J. Vilà-Guerau de Arellano, and A. Dosio (2006). "Role of Shear and the Inversion Strength During Sunset Turbulence Over Land: Characteristic Length Scales". *Boundary-Layer Meteorology* 121, 537–556. DOI: 10.1007/s10546-006-9080-6.

Pöschl, U. (2005). "Atmospheric Aerosols: Composition, Transformation, Climate and Health Effects". *Angewandte Chemie International Edition* 44.46, 7520–7540. DOI: 10.1002/anie.200501122.

Rannik, Ü., M. Aubinet, O. Kurbanmuradov, K. K. Sabelfeld, T. Markkanen, and T. Vesala (2000). "Footprint Analysis For Measurements Over A Heterogeneous Forest". *Boundary-Layer Meteorology* 97.1, 137–166. DOI: 10.1023/A:1002702810929.

Ražnjević, A., C. van Heerwaarden, B. van Stratum, A. Hensen, I. Velzeboer, P. van den Bulk, and M. Krol (2022). "Technical note: Interpretation of field observations of point-source methane plume using observation-driven large-eddy simulations". *Atmospheric Chemistry and Physics* 22.10, 6489–6505. DOI: 10.5194/acp-22-6489-2022.

Remmelink, G., J. van Middelkoop, W. Ouweltjes, and H. Wemmenhove (2020). *Handboek melkveehouderij 2020/21*. Dutch. Handboek / Wageningen Livestock Research 44. Over the year 2019/20. Wageningen Livestock Research. DOI: 10.18174/529557.

Research, W. U.

bibinitperiod (2021). *Dutch Farm Accountancy Data Network, agriculture.* last access: 21 June 2021.

RIVM (2021). *Landbouw, Emissiefactoren diercategorieën, Hoofdcategorie A: Rundvee.* `https://www.infomil.nl/onderwerpen/landbouw/emissiearme-stalsystemen/emissiefactoren-per/map-staltypen/hoofdcategorie/`. Accessed: 2021-01-28.

RIVM, CBS, PBL, and WUR (2019). *Nitrogen deposition, 1990-2018.* Available at `https://www.clo.nl/indicatoren/en018918`. (Indicator 0189, version 18 , 25 November 2019) RIVM National Institute for Public Health and the Environment, Bilthoven; Statistics Netherlands (CBS), The Hague; PBL Netherlands Environmental Assessment Agency, The Hague; and Wageningen University and Research, Wageningen. (Last access: 17 August 2022).

Ronda, R. J., H. A. R. de Bruin, and A. A. M. Holtslag (2001). "Representation of the Canopy Conductance in Modeling the Surface Energy Budget for Low Vegetation". *Journal of Applied Meteorology* 40.8, 1431–1444. DOI: `10.1175/1520-0450(2001)040<1431:ROTCCI>2.0.CO;2`.

Rumsey, I. C., K. A. Cowen, J. T. Walker, T. J. Kelly, E. A. Hanft, K. Mishoe, C. Rogers, R. Proost, G. M. Beachley, G. Lear, T. Frelink, and R. P. Otjes (2014). "An assessment of the performance of the Monitor for AeRosols and GAses in ambient air (MARGA): a semi-continuous method for soluble compounds". *Atmospheric Chemistry and Physics* 14.11, 5639–5658. DOI: `10.5194/acp-14-5639-2014`.

Russchenberg, H., A. Apituley, and R. Holzinger (2022). "The Ruisdael Observatory: advancing atmospheric science in the Netherlands". *EMS Annual Meeting 2022, Bonn, Germany.* EMS2022-200. DOI: `10.5194/ems2022-200`.

San José, J. J., R. Montes, and N. Nikonova-Crespo (1991). "Carbon Dioxide and Ammonia Exchange in the Trachypogon Savannas of the Orinoco Llanos". *Annals of Botany* 68.4, 321–328. DOI: `10.1093/oxfordjournals.aob.a088259`.

Sauter, F., M. van Zanten, E. van der Swaluw, J. Aben, F. de Leeuw, and H. van Jaarsveld (2018). *The OPS-model: Description of OPS 4.5.2.* Tech. rep. National Institute for Public Health and the Environment (RIVM.

Schaap, M., R. M. A. Timmermans, M. Roemer, G. A. C. Boersen, P. J. H. Builtjes, F. J. Sauter, G. J. M. Velders, and J. P. Beck (2008). "The LOTOS–EUROS model: description, validation and latest developments". *International Journal of Environment and Pollution* 32.2, 270–290. DOI: `10.1504/IJEP.2008.017106`.

Schalkwijk, J., H. J. J. Jonker, A. P. Siebesma, and E. Van Meijgaard (2015). "Weather Forecasting Using GPU-Based Large-Eddy Simulations". *Bulletin of the American Meteorological Society* 96.5, 715–723. DOI: `10.1175/BAMS-D-14-00114.1`.

Schaug, J. (1988). *Quality assurance plane for EMEP.* Tech. rep. EMEP/CCC-Report 1/88. Norwegian Institute for Air Research.

Schrader, F., C. Brüummer, C. R. Flechard, R. J. Wichink Kruit, M. C. van Zanten, U. Zöll, A. Hensen, and J. W. Erisman (2016). "Non-stomatal exchange in ammonia dry deposition models: comparison of two state-of-the-art approaches". *Atmospheric Chemistry and Physics* 16.21, 13417–13430. DOI: 10.5194/acp-16-13417-2016.

Schrader, F., J. W. Erisman, and C. Brümmer (2020). "Towards a coupled paradigm of NH3-CO2 biosphere–atmosphere exchange modelling". *Global Change Biology* 26.9, 4654–4663. DOI: 10.1111/gcb.15184.

Schrader, F., U. Schaap M. Zöll, R. Kranenburg, and C. Brümmer (2018). "The hidden cost of using low-resolution concentration data in the estimation of NH_3 dry deposition fluxes". *Scientific Reports* 8.969. DOI: 10.1038/s41598-017-18021-6.

Schulte, R. B., M. C. van Zanten, S. Rutledge-Jonker, D. P. J. Swart, R. J. Wichink Kruit, M. C. Krol, W. A. J. van Pul, and J. Vilà-Guerau de Arellano (2021). "Unraveling the diurnal atmospheric ammonia budget of a prototypical convective boundary layer". *Atmospheric Environment* 249, 118153. DOI: 10.1016/j.atmosenv.2020.118153.

Schulte, R. B., M. C. van Zanten, B. J. H. van Stratum, and J. Vilà-Guerau de Arellano (2022a). "Assessing the representativity of NH_3 measurements influenced by boundary-layer dynamics and the turbulent dispersion of a nearby emission source". *Atmospheric Chemistry and Physics* 22.12, 8241–8257. DOI: 10.5194/acp-22-8241-2022.

Schulte, R. B., M. C. van Zanten, B. J. H. van Stratum, and J. Vilà-Guerau de Arellano (2022b). "DALES v4.2 modified for ammonia plume dispersion and blending-distance estimations". *4TU.ResearchData [code]*. DOI: 10.4121/19869478.v1.

Seaton, A., D. Godden, W. MacNee, and K. Donaldson (1995). "Particulate air pollution and acute health effects". *The Lancet* 345.8943, 176–178. DOI: 10.1016/S0140-6736(95)90173-6.

Shah, A., J. R. Pitt, H. Ricketts, J. B. Leen, P. I. Williams, K. Kabbabe, M. W. Gallagher, and G. Allen (2020). "Testing the near-field Gaussian plume inversion flux quantification technique using unmanned aerial vehicle sampling". *Atmospheric Measurement Techniques* 13.3, 1467–1484. DOI: 10.5194/amt-13-1467-2020.

Shen, J., D. Chen, M. Bai, J. Sun, T. Coates, S. K. Lam, and Y. Li (2016). "Ammonia deposition in the neighbourhood of an intensive cattle feedlot in Victoria, Australia". *Sci Rep* 6.32793, 2045–2322. DOI: 10.1038/srep32793.

Simpson, D., A. Benedictow, H. Berge, R. Bergström, L. D. Emberson, H. Fagerli, C. R. Flechard, G. D. Hayman, M. Gauss, J. E. Jonson, M. E. Jenkin, A. Nyíri, C. Richter, V. S. Semeena, S. Tsyro, J. P. Tuovinen, Á. Valdebenito, and P. Wind (2012). "The EMEP MSC-W chemical transport model - technical description". *Atmospheric Chemistry and Physics* 12.16, 7825–7865. DOI: 10.5194/acp-12-7825-2012.

Sintermann, J., C. Spirig, A. Jordan, U. Kuhn, C. Ammann, and A. Neftel (2011). "Eddy covariance flux measurements of ammonia by high temperature chemical ionisation mass

spectrometry". *Atmospheric Measurement Techniques* 4.3, 599–616. DOI: `10.5194/amt-4-599-2011`.

Smit, L. A. M. and D. Heederik (2017). "Impacts of Intensive Livestock Production on Human Health in Densely Populated Regions". *GeoHealth* 1.7, 272–277. DOI: `10.1002/2017GH000103`.

Sommer, S. G., H. S. Østergård, P. Løfstrøm, H. V. Andersen, and L. Jensen (2009). "Validation of model calculation of ammonia deposition in the neighbourhood of a poultry farm using measured NH3 concentrations and N deposition". *Atmospheric Environment* 43, 915–920. DOI: `10.1016/j.atmosenv.2008.10.045`.

Stavi, I. and R. Lal (2013). "Agriculture and greenhouse gases, a common tragedy. A review". *Agronomy for Sustainable Development* 33, 275–289. DOI: `10.1007/s13593-012-0110-0`.

Steeneveld, G. J., S. Koopmans, B. G. Heusinkveld, L. W. A. Van Hove, and A. A. M. Holtslag (2011). "Quantifying urban heat island effects and human comfort for cities of variable size and urban morphology in the Netherlands". *Journal of Geophysical Research: Atmospheres* 116.D20. DOI: `10.1029/2011JD015988`.

Stelson, A. W. and J. H. Seinfeld (1982). "Relative humidity and temperature dependence of the ammonium nitrate dissociation constant". *Atmospheric Environment (1967)* 16.5, 983–992. DOI: `10.1016/0004-6981(82)90184-6`.

Stewart, J. B. (1988). "Modelling surface conductance of pine forest". *Agricultural and Forest Meteorology* 43.1, 19–35. DOI: `10.1016/0168-1923(88)90003-2`.

Stokstad, E. (2019). "Nitrogen crisis threatens Dutch environment- and economy". *Science* 366.6470, 1180–1181. DOI: `10.1126/science.366.6470.1180`.

Stolk, A. P., H. Noordijk, and M. C. van Zanten (2014). *Drogedepositiemetingen van ammoniak in Natura 2000-gebied Bargerveen*. Tech. rep. 680029001. Antonie van Leeuwenhoeklaan 9, 3721, MA Bilthoven, the Netherlands: National Institute for Public Health and the Environment (RIVM).

Stull, R. B. (1988). *An Introduction to Boundary Layer Meteorology*. Kluwer Academic Publishers.

Sutton, M. A. and A. Bleeker (2013). "The shape of nitrogen to come". *Nature* 494, 435–437. DOI: `10.1038/nature11954`.

Sutton, M. A., J. W. Erisman, F. Dentener, and D. Möller (2008). "Ammonia in the environment: From ancient times to the present". *Environmental Pollution* 156.3, 583–604. DOI: `10.1016/j.envpol.2008.03.013`.

Sutton, M. A. and D. Fowler (1993). "A model for inferring bi-directional fluxes of ammonia over plant canopies". In: *Proceedings of the WMO conference on the measurement and modelling of atmospheric composition changes including pollutant transport, World Meteorological Organization, Geneva*. WMO/GAW-91, 179–182.

Sutton, M. A., E. Nemitz, C. Milford, C. Campbell, J. Erisman, A. Hensen, P. Cellier, M. David, B. Loubet, E. Personne, J. K. Schjoerring, M. Mattsson, J. R. Dorsey, M. W. Gallagher, L. Horvath, T. Weidinger, R. Meszaros, U. Dämmgen, A. Neftel, B. Herrmann, B. E. Lehman, C. Flechard, and J. Burkhardt (2009). "Dynamics of ammonia exchange with cut grassland: synthesis of results and conclusions of the GRAMINAE Integrated Experiment". *Biogeosciences* 6.12, 2907–2934. DOI: `10.5194/bg-6-2907-2009`.

Sutton, M. A., J. K. Schjørring, G. P. Wyers, J. H. Duyzer, P. Ineson, D. S. Powlson, D. Fowler, D. S. Jenkinson, J. L. Monteith, and M. H. Unsworth (1995). "Plant—atmosphere exchange of ammonia". *Philosophical Transactions of the Royal Society of London. Series A: Physical and Engineering Sciences* 351.1696, 261–278. DOI: `10.1098/rsta.1995.0033`.

Swart, D., J. Zhang, S. van der Graaf, S. Rutledge-Jonker, A. Hensen, S. Berkhout, P. Wintjen, R. van der Hoff, M. Haaima, A. Frumau, P. van den Bulk, R. Schulte, M. van Zanten, and T. van Goethem (2023). "Field comparison of two novel open-path instruments that measure dry deposition and emission of ammonia using flux-gradient and eddy covariance methods". *Atmospheric Measurement Techniques* 16.2, 529–546. DOI: `10.5194/amt-16-529-2023`.

Takagi, K., T. Tsuboya, and H. Takahashi (1998). "Diurnal hystereses of stomatal and bulk surface conductances in relation to vapor pressure deficit in a cool-temperate wetland". *Agricultural and Forest Meteorology* 91.3, 177–191. DOI: `10.1016/S0168-1923(98)00078-1`.

Tang, I. N. (1996). "Chemical and size effects of hygroscopic aerosols on light scattering coefficients". *Journal of Geophysical Research: Atmospheres* 101.D14, 19245–19250. DOI: `10.1029/96JD03003`.

ten Brink, H., R. Otjes, P. Jongejan, and G. Kos (2009). "Monitoring of the ratio of nitrate to sulphate in size-segregated submicron aerosol in the Netherlands". *Atmospheric Research* 92.2, 270–276. DOI: `10.1016/j.atmosres.2008.12.003`.

Tennekes, H. and A. G. M. Driedonks (1981). "Basic entrainment equations for the atmospheric boundary layer". *Boundary-Layer Meteorology* 20.4, 515–531. DOI: `10.1007/BF00122299`.

Tevlin, A. G., Y. Li, J. L. Collett, E. E. McDuffie, E. V. Fischer, and J. G. Murphy (2017). "Tall Tower Vertical Profiles and Diurnal Trends of Ammonia in the Colorado Front Range". *Journal of Geophysical Research: Atmospheres* 122.22, 12, 468–12, 487. DOI: `10.1002/2017JD026534`.

Theobald, M. R., P. Løfstrøm, J. Walker, H. V. Andersen, P. Pedersen, A. Vallejo, and M. A. Sutton (2012). "An intercomparison of models used to simulate the short-range atmospheric dispersion of agricultural ammonia emissions". *Environmental Modelling & Software* 37, 90–102. DOI: `10.1016/j.envsoft.2012.03.005`.

Thomas, R. M., I. Trebs, R. Otjes, P. A. C. Jongejan, H. ten Brink, G. Phillips, M. Kortner, F. X. Meixner, and E. Nemitz (2009). "An Automated Analyzer to Measure Surface-Atmosphere Exchange Fluxes of Water Soluble Inorganic Aerosol Compounds and Reactive Trace Gases". *Environmental Science & Technology* 43.5, 1412–1418. DOI: 10.1021/es8019403.

van Bruggen, C., A. Bannink, C. M. Groenestein, J. F. M. Huijsmans, L. A. Lagerwerf, H. H. Luesink, M. B. H. Ros, G. L. Velthof, J. Vonk, and T. van der Zee (2021). *Emissies naar lucht uit de landbouw berekend met NEMA voor 1990-2019*. Dutch. WOt-technical report 203. Project number WOT-04-008-031.01 and WOT-04-008-025.02. Wettelijke Onderzoekstaken Natuur & Milieu. DOI: 10.18174/544296.

van der Hoek, K. W. (1998). "Estimating ammonia emission factors in Europe: Summary of the work of the UNECE ammonia expert panel". *Atmospheric Environment* 32.3, 315–316. DOI: 10.1016/S1352-2310(97)00168-4.

van der Maas, C. W. M., P. H. A. J. Jones, P. W. Westerhoff, S. B. Hazelhorst, and D. G. C. Roest (2021). *Bijdrage aan de stikstofdepositie in de natuur vanuit de industrie, het verkeer en de consumenten*. Tech. rep. RIVM rapport 2021-0200. Rijksinstituut voor Volksgezondheid en Milieu RIVM. DOI: 10.21945/RIVM-2021-0200.

van der Peet, G., F. Leenstra, I. Vermeij, N. Bondt, L. Puister, and J. van Os (2018). *Feiten en cijfers over de Nederlandse veehouderijsectoren 2018*. Dutch. Wageningen Livestock Research rapport 1134. Wageningen Livestock Research. DOI: 10.18174/464128.

van der Swaluw, E., W. de Vries, F. Sauter, J. Aben, G. Velders, and A. van Pul (2017). "High-resolution modelling of air pollution and deposition over the Netherlands with plume, grid and hybrid modelling". *Atmospheric Environment* 155, 140–153. DOI: 10.1016/j.atmosenv.2017.02.009.

van Heerwaarden, C. C., J. P. Mellado, and A. De Lozar (2014). "Scaling Laws for the Heterogeneously Heated Free Convective Boundary Layer". *Journal of the Atmospheric Sciences* 71.11, 3975–4000. DOI: 10.1175/JAS-D-13-0383.1.

Van Heerwaarden, C. C. and J. Vilà-Guerau de Arellano (2008). "Relative Humidity as an Indicator for Cloud Formation over Heterogeneous Land Surfaces". *Journal of the Atmospheric Sciences* 65.10, 3263–3277. DOI: 10.1175/2008JAS2591.1.

van Heerwaarden, C. C., J. Vilà-Guerau de Arellano, A. F. Moene, and A. A. M. Holtslag (2009). "Interactions between dry-air entrainment, surface evaporation and convective boundary-layer development". *Quarterly Journal of the Royal Meteorological Society* 135.642, 1277–1291. DOI: 10.1002/qj.431.

Van Hove, L. W. A. and E. H. Adema (1996). "The effective thickness of water films on leaves". *Atmospheric Environment* 30.16. 6th EURASAP International Workshop on Wind and Water Tunnel Modelling of Atmospheric Flow and Dispersion, 2933–2936. DOI: 10.1016/1352-2310(96)00012-X.

Van Hove, L. W. A., E. H. Adema, W. J. Vredenberg, and G. A. Pieters (1989). "A study of the adsorption of NH3 and SO2 on leaf surfaces". *Atmospheric Environment (1967)* 23.7, 1479–1486. DOI: 10.1016/0004-6981(89)90407-1.

van Jaarsveld, J. A., A. Bleeker, and N. J. P. Hoogervorst (2000). *Evaluatie ammoniak emissiereduktes met behulp van metingen en modelberekeningen.* Tech. rep. 722108025. National Institute for Public Health and the Environment (RIVM).

van Jaarsveld, J. A. and F. A. A. M. de Leeuw (1993). "OPS: An operational atmospheric transport model for priority substances". *Environmental Software* 8.2, 91–100. DOI: 10.1016/0266-9838(93)90019-E.

van Jaarsveld, J. (2004). *The Operational Priority Substances model: Description and validation of OPS-Pro 4.1.* Tech. rep. 500045001. Antonie van Leeuwenhoeklaan 9, 3721, MA Bilthoven, the Netherlands: National Institute for Public Health and the Environment (RIVM).

Van Oss, R., J. Duyzer, and P. Wyers (1998). "The influence of gas-to-particle conversion on measurements of ammonia exchange over forest". *Atmospheric Environment* 32.3, 465–471. DOI: 10.1016/S1352-2310(97)00280-X.

van Pul, A., H. van Jaarsveld, T. van der Meulen, and G. Velders (2004). "Ammonia concentrations in the Netherlands: spatially detailed measurements and model calculations". *Atmospheric Environment* 38.24. Includes Special Issue Section on Results from the Austrian Project on Health Effects of Particulates (AUPHEP), 4045–4055. DOI: 10.1016/j.atmosenv.2004.03.051.

van Stratum, B. J. H. (2022). personal communication.

van Tiggelen, M., S. R. de Roode, A. P. Siebesma, and B. J. H. van de Wiel (2018). "Towards improving the land-surface-atmosphere coupling in the Dutch Amospheric Large-Eddy Simulation model (DALES)". MA thesis. the Netherlands: Delft University of Technology.

van Zanten, M. C., F. J. Sauter, R. J. Wichink Kruit, J. A. van Jaarsveld, and W. A. J. van Pul (2010). *Description of the DEPAC module: Dry deposition modelling with DEPAC-GCN2010.* Tech. rep. 680180001. National Institute for Public Health and the Environment (RIVM).

van Zanten, M. C., R. J. Wichink Kruit, R. Hoogerbrugge, E. Van der Swaluw, and W. A. J. van Pul (2017). "Trends in ammonia measurements in the Netherlands over the period 1993–2014". *Atmospheric Environment* 148, 352–360. DOI: 10.1016/j.atmosenv.2016.11.007.

Velders, G. J. M., J. M. M. Aben, G. P. Geilenkirchen, H. A. den Hollander, H. Noordijk, W. J. de Vries, J. Wesseling, and M. C. van Zanten (2014). *Grootschalige concentratie- en depositiekaarten Nederland. Rapportage 2014.* Tech. rep. 680363002. National Institute for Public Health and the Environment (RIVM).

Vermeulen, A. T., A. Hensen, M. E. Popa, W. C. M. Bulk, and P. A. C. Jongejan (2011). "Greenhouse gas observations from Cabauw Tall Tower (1992-2010)". *Atmospheric Measurement Techniques* 4.3, 617. DOI: 10.5194/amt-4-617-2011.

Verzijlbergh, R. A., H. J. J. Jonker, T. Heus, and J. Vilà-Guerau de Arellano (2009). "Turbulent dispersion in cloud-topped boundary layers". *Atmospheric Chemistry and Physics* 9.4, 1289–1302. DOI: 10.5194/acp-9-1289-2009.

Vesala, T., N. Kljun, Ü. Rannik, J. Rinne, A. Sogachev, T. Markkanen, K. Sabelfeld, T. Foken, and M. Y. Leclerc (2008). "Flux and concentration footprint modelling: State of the art". *Environmental Pollution* 152.3, 653–666. DOI: 0.1016/j.envpol.2007.06.070.

Vilà-Guerau de Arellano, J., A. Dosio, J. F. Vinuesa, A. A. M. Holtslag, and S. Galmarini (2004a). "The dispersion of chemically reactive species in the atmospheric boundary layer". *Meteorology and Atmospheric Physics* 87.1, 23–38. DOI: 10.1007/s00703-003-0059-2.

Vilà-Guerau de Arellano, J., P. G. Duynkerke, and P. J. H. Builtjes (1993). "The divergence of the turbulent diffusion flux due to chemical reactions in the surface layer: NO-O_3-NO_2 system". *Tellus B* 45, 23–33. DOI: 10.1034/j.1600-0889.1993.00002.x.

Vilà-Guerau de Arellano, J., B. Gioli, F. Miglietta, H. J. J. Jonker, H. Klein Baltink, R. W. A. Hutjes, and A. A. M. Holtslag (2004b). "Entrainment process of carbon dioxide in the atmospheric boundary layer". *Journal of Geophysical Research: Atmospheres* 109.D18110. DOI: 10.1029/2004JD004725.

Vilà-Guerau de Arellano, J., O. Hartogensis, I. Benedict, H. de Boer, P. J. M. Bosman, S. Botía, M. A. Cecchini, K. A. P. Faassen, R. González-Armas, K. van Diepen, B. G. Heusinkveld, M. Janssens, F. Lobos-Roco, I. T. Luijkx, L. A. T. Machado, M. R. Mangan, A. F. Moene, W. B. Mol, M. van der Molen, R. Moonen, H. G. Ouwersloot, S. Park, X. Pedruzo-Bagazgoitia, T. Röckmann, G. A. Adnew, R. Ronda, M. Sikma, R. B. Schulte, B. J. H. van Stratum, M. A. Veerman, M. C. van Zanten, and C. C. van Heerwaarden (n.d.). "Advancing understanding of land–atmosphere interactions by breaking discipline and scale barriers". *Annals of the New York Academy of Sciences* n/a.n/a (), 1–25. DOI: doi.org/10.1111/nyas.14956.

Vilà-Guerau de Arellano, J., P. Ney, O. Hartogensis, H. de Boer, K. van Diepen, D. Emin, G. de Groot, A. Klosterhalfen, M. Langensiepen, M. Matveeva, G. Miranda-Garcıa, A. F. Moene, U. Rascher, T. Röckmann, G. Adnew, N. Brüggemann, Y. Rothfuss, and A. Graf (2020). "CloudRoots: integration of advanced instrumental techniques and process modelling of sub-hourly and sub-kilometre land–atmosphere interactions". *Biogeosciences* 17.17, 4375–4404. DOI: 10.5194/bg-17-4375-2020.

Vilà-Guerau de Arellano, J., E. G. Patton, T. Karl, K. van den Dries, M. C. Barth, and J. J. Orlando (2011). "The role of boundary layer dynamics on the diurnal evolution of isoprene and the hydroxyl radical over tropical forests". *Journal of Geophysical Research: Atmospheres* 116.D7. DOI: 10.1029/2010JD014857.

Vilà-Guerau de Arellano, J., A. M. Talmon, and P. J. H. Builtjes (1990). "A chemically reactive plume model for the NO-NO2-O3 system". *Atmospheric Environment. Part A. General Topics* 24.8, 2237–2246. DOI: 10.1016/0960-1686(90)90255-L.

Vilà-Guerau de Arellano, J., C. C. van Heerwaarden, B. J. H. van Stratum, and K. van den Dries (2015). *Atmospheric Boundary Layer: Integrating Air Chemistry and Land Interactions.* Cambridge: Cambridge University Press. DOI: 10.1017/CBO9781316117422.

Visser, A. J., L. N. Ganzeveld, I. Goded, M. C. Krol, I. Mammarella, G. Manca, and K. F. Boersma (2021). "Ozone deposition impact assessments for forest canopies require accurate ozone flux partitioning on diurnal timescales". *Atmospheric Chemistry and Physics* 21.24, 18393–18411. DOI: 10.5194/acp-21-18393-2021.

Volten, H., J. B. Bergwerff, M. Haaima, D. E. Lolkema, A. J. C. Berkhout, G. R. van der Hoff, C. J. M. Potma, R. J. Wichink Kruit, W. A. J. van Pul, and D. P. J. Swart (2012a). "Two instruments based on differential optical absorption spectroscopy (DOAS) to measure accurate ammonia concentrations in the atmosphere". *Atmospheric Measurement Techniques* 5.2, 413–427. DOI: 10.5194/amt-5-413-2012.

Volten, H., M. Haaima, D. P. J. Swart, M. C. van Zanten, and W. A. J. van Pul (2012b). *Ammonia exchange measured over a corn field in 2010.* Tech. rep. 680180003. National Institute for Public Health and the Environment (RIVM).

von Bobrutzki, K., C. F. Braban, D. Famulari, S. K. Jones, T. Blackall, T. E. L. Smith, M. Blom, H. Coe, M. Gallagher, M. Ghalaieny, M. R. McGillen, C. J. Percival, J. D. Whitehead, R. Ellis, J. Murphy, A. Mohacsi, A. Pogany, H. Junninen, S. Rantanen, M. A. Sutton, and E. Nemitz (2010). "Field inter-comparison of eleven atmospheric ammonia measurement techniques". *Atmospheric Measurement Techniques* 3.1, 91–112. DOI: 10.5194/amt-3-91-2010.

Vonk, J., E. J. M. M. Arets, A. Bannink, C. van Bruggen, C. M. Groenestein, J. F. M. Huijsmans, L. A. Lagerwerf, H. H. Luesink, M. B. H. Ros, M. J. Schelhaas, T. van der Zee, and G. L. Velthof (2020). *Referentieraming van emissies naar de lucht uit landbouw en landgebruik tot 2030, met doorkijk naar 2035: Achtergronddocument bij de Klimaat- en Energieverkenning 2020.* Dutch. Rapport / Wageningen Livestock Research 1278. Wageningen Livestock Research. DOI: 10.18174/533503.

Vrieling, A. J. and F. T. M. Nieuwstadt (2003). "Turbulent dispersion from nearby point sources—interference of the concentration statistics". *Atmospheric Environment* 37.32, 4493–4506. DOI: 10.1016/S1352-2310(03)00576-4.

Wang, K., P. Kang, Y. Lu, X. Zheng, M. Liu, T. Lin, K. Butterbach-Bahl, and Y. Wang (2021). "An open-path ammonia analyzer for eddy covariance flux measurement". *Agricultural and Forest Meteorology* 308-309, 108570. DOI: 10.1016/j.agrformet.2021.108570.

Wentworth, G. R., J. G. Murphy, K. B. Benedict, E. J. Bangs, and J. L. Collett Jr. (2016). "The role of dew as a night-time reservoir and morning source for atmospheric ammonia".

Atmospheric Chemistry and Physics 16.11, 7435–7449. DOI: `10.5194/acp-16-7435-2016`.

Whitehead, J. D., M. Twigg, D. Famulari, E. Nemitz, M. A. Sutton, M. W. Gallagher, and D. Fowler (2008). "Evaluation of Laser Absorption Spectroscopic Techniques for Eddy Covariance Flux Measurements of Ammonia". *Environmental Science and Technology* 42.6, 2041–2046. DOI: `10.1021/es071596u`.

Wichink Kruit, R., A. Bleeker, M. Braam, T. van Goethem, R. Hoogerbrugge, S. Rutledge-Jonker, G. Stefess, A. Stolk, E. van der Swaluw, M. Voogt, and A. van Pul (2021). *Op weg naar een optimale meetstrategie voor stikstof*. Tech. rep. RIVM rapport 2021-0118. Rijksinstituut voor Volksgezondheid en Milieu RIVM. DOI: `10.21945/RIVM-2021-0118`.

Wichink Kruit, R., M. Braam, R. Hoogerbrugge, and A. van Pul (2020). *Implementation of a data fusion approach to assess the concentration and dry deposition of ammonia in the Netherlands*. Tech. rep. RIVM rapport 2020-0076. Rijksinstituut voor Volksgezondheid en Milieu RIVM. DOI: `10.21945/RIVM-2020-0076`.

Wichink Kruit, R. J., J. Aben, W. de Vries, F. Sauter, E. van der Swaluw, M. C. van Zanten, and W. A. J. van Pul (2017). "Modelling trends in ammonia in the Netherlands over the period 1990–2014". *Atmospheric Environment* 154, 20–30. DOI: `10.1016/j.atmosenv.2017.01.031`.

Wichink Kruit, R. J., M. Haaima, D. P. J. Swart, M. C. van Zanten, and W. A. J. van Pul (2010a). *Ammonia exchange measurements over a corn field in Lelystad, the Netherlands in 2009*. Tech. rep. 680180002. National Institute for Public Health and the Environment (RIVM).

Wichink Kruit, R. J., M. Schaap, F. J. Sauter, M. C. van Zanten, and W. A. J. van Pul (2012). "Modeling the distribution of ammonia across Europe including bi-directional surface–atmosphere exchange". *Biogeosciences* 9.12, 5261–5277. DOI: `10.5194/bg-9-5261-2012`.

Wichink Kruit, R. J. and W. A. J. van Pul (2018). *Ontwikkelingen in de stikstofdepositie*. Briefrapport 2018-0117. National Institute for Public Health and the Environment (RIVM). DOI: `10.21945/RIVM-2018-0117`.

Wichink Kruit, R. J., W. A. J. van Pul, R. P. Otjes, P. Hofschreuder, A. F. G. Jacobs, and A. A. M. Holtslag (2007). "Ammonia fluxes and derived canopy compensation points over non-fertilized agricultural grassland in The Netherlands using the new GRadient Ammonia - High Accuracy - Monitoring (GRAHAM)". *Atmospheric Environment* 41.6, 1275–1287. DOI: `10.1016/j.atmosenv.2006.09.039`.

Wichink Kruit, R. J., W. A. J. van Pul, F. J. Sauter, M. van den Broek, N. E., M. A. Sutton, M. Krol, and A. A. M. Holtslag (2010b). "Modeling the surface–atmosphere exchange of ammonia". *Atmospheric Environment* 44.7, 945–957. DOI: `10.1016/j.atmosenv.2009.11.049`.

Wyers, G. P., R. P. Otjes, and J. Slanina (1993). "A continuous-flow denuder for the measurement of ambient concentrations and surface-exchange fluxes of ammonia". *Atmospheric Environment. Part A. General Topics* 27.13, 2085–2090. DOI: 10.1016/0960-1686(93)90280-C.

Zhang, L., L. P. Wright, and W. A. H. Asman (2010). "Bi-directional air-surface exchange of atmospheric ammonia: A review of measurements and a development of a big-leaf model for applications in regional-scale air-quality models". *Journal of Geophysical Research: Atmospheres* 115.D20. DOI: 10.1029/2009JD013589.

Zhang, Q., S. Manzoni, G. Katul, A. Porporato, and D. Yang (2014). "The hysteretic evapotranspiration — Vapor pressure deficit relation". *Journal of Geophysical Research: Biogeosciences* 119.2, 125–140. DOI: 10.1002/2013JG002484.

Acknowledgements

During a PhD project, young aspiring scientists aim to prove themselves as independent scientists. While this is mostly an individual journey, nobody truly travels alone. PhD candidates are guided along the way, have the opportunity to meet a lot of new people and are accompanied by other PhD candidates, who travel in similar directions. Looking back at the past five years, it is safe to say that I would not be where I am now, without all the people who are directly, or indirectly, involved with the project. In particular, I would like to thank the following people.

Jordi, our weekly meetings, discussing science with you, are some of the moments I enjoyed the most throughout the project. The project has not been an easy one, spanning both a national and international crisis. I particularly remember your efforts in safeguarding the scientific discussion around the first paper, in the midst of the nitrogen crisis. During the next crisis, the COVID pandemic, you managed the situation at MAQ very well. I truly admire how you always put the (mental) health of the group first, while still making sure that people stayed connected. Whenever my motivation started to falter, you always found time in your busy schedule to give me a confidence boost or to highlight the value of our work. I would also like to thank you for the opportunity to visit the LIAISE campaign in Spain, especially since our plans to visit international conferences failed due to the COVID crisis. I still sometimes tell myself that "I worry too much", in a poor imitation of your voice. Thank you for your unwavering support and guidance throughout the project. I can now truly say that I am proud of what we achieved during the project.

Margreet, ook jou wil ik uitgebreid bedanken voor je steun en begeleiding gedurende het project. Jij en Jordi vormen samen een sterk team, waarbij jullie elkaar zowel inhoudelijk, als op persoonlijk vlak goed aanvullen. In de afrondingsfase van het eerste paper zat je nog wel eens tussen twee vuren, maar je wist altijd knap de balans te bewaren. Tijdens de COVID crisis konden we elkaar, naar mijn idee, steeds beter vinden. Het was altijd interressant om inhoudelijk met je te sparren. Het meest dankbaar ben ik voor het feit dat ik altijd bij je terecht kon voor een luisterend oor wanneer ik dat nodig had. Met je praktische aanpak lukte het ons ook telkens weer om samen de beren op de weg in perspectief te plaatsen, om vervolgens weer vooruit te kijken en verder te gaan. Onze

(digitale) koffie sessies hebben mij er meer dan eens doorheen gesleept. Voor dit alles wil ik je bedanken. Ik kon me geen betere begeleiders wensen.

The group of **MAQ** has been a very nice environment to work on a PhD project. To me, one of the most important aspects of a job is the environment you work in. The open and inspiring atmosphere at the group is something to be proud of. Thank you all very much and keep up the good work!

Special thanks to **Sjoerd**, **Mary Rose**, **Kim**, **Christoph**, **Arjan** and **Aris**, with who I shared an office. I feel like you build a special connection when you share an office and work together on a regular basis. It's an environment where you really get to know each other, learn from each other and have both serious and silly discussions. It was always a pleasure to work with you all! Thank you.

Anja, I very much enjoyed having a sparring partner on plume dispersion using LES models. Our irregular coffee walks and digital check-ins during lockdown were really nice breaks from writing and work in general. Thank you for sharing your struggles with writing, the COVID crisis and the general hardships of finishing a PhD project, as well as being there when I needed to vent or just needed a relaxing little break from work.

Als laatste MAQer wil ik natuurlijk **Auke** bedanken. Ik ben heel blij dat je ja zei toen ik je vroeg om paranimf te zijn. Het was een plezier om de afgelopen jaren een kantoor met je te delen, zowel op zakelijk als persoonlijk vlak. De overeenkomsten tussen onze projecten, ook jij onderzocht stomatale- en niet-stomatale gasuitwisseling, leidden tot meerdere sparringsessies, waarbij ook het whiteboard goed werd gebruikt. Jouw goede ideeën en enthousiasme in deze discussies gaven me altijd weer nieuwe energie en hielpen me meer dan eens een barrière te doorbreken. Ik ben ook dankbaar voor onze regelmatige koffiemomenten tijdens de lockdowns, digitaal of buiten op 1.5 m afstand. Dit persoonlijk contact heeft me absoluut door deze lastige tijd heen gesleept. Het was een plezier om met je samen te werken en ik ben dankbaar voor je steun tijdens de verdediging!

Naast mijn Wageningse collega's wil ik natuurlijk ook mijn collega's bij het **RIVM** bedanken. **Susanna**, **Daan**, **Addo**, **Roy**, **Thomas**, **Miranda**, **Margreet** en de rest van het **ammoniak team** ben ik dankbaar dat ik direct werd opgenomen binnen het team. Ik heb veel van jullie geleerd, zeker tijdens tweewekelijkse NH_3-overleggen. Ik bewonder de integriteit en gedrevenheid toen we in het oog zaten van de storm genaamd "de stikstofcrisis". Ook vond ik het leuk om het ammoniak team te zien groeien en ontwikkelen in de afgelopen vijf jaar. Ik hoop dat ik hier een bescheiden bijdrage aan heb kunnen leveren.

Twee mensen op het RIVM wil ik er in het bijzonder uitlichten. **Susanna**, ik kijk fijn terug op onze samenwerking. Je nam me vanaf het begin mee met de DOAS metingen op de Veenkampen en was altijd beschikbaar voor een inhoudelijke discussie of een ontspannen kop koffie. **Daan**, ook jou wil ik speciaal bedanken voor de samenwerking. Ik heb

altijd met veel plezier met je gespard over de DOAS metingen en veel van je geleerd. Ik heb bewondering voor je geduldige, grondige en ook praktische aanpak in je werk en interactie met collega's. Ik ben blij dat ik met je samen heb kunnen werken. Geniet van je welverdiende pensioen in Zeeland.

Het project had nooit kunnen slagen zonder het (mini)DOAS team van het RIVM. Bij dezen wil ik **Daan**, **Stijn**, **René**, **Marty** en de andere betrokkenen bedanken voor hun harde werk en het delen van de ammoniak metingen. Ook **Susanna**, **Miranda**, **Shelley** en **Kim** ben ik dankbaar voor het verwerken van de metingen en voor de discussies over de verschillende datasets. Jullie stonden altijd open voor mijn vragen en opmerkingen.

I would also like to thank **Arjan**, **Jun**, **Arnoud** and the others at **TNO** for the interesting and sometimes humorous discussions, centred around the miniDOAS and Healthy Photon measurements at Cabauw and the Veenkampen. I very much enjoyed participating in the bi-weekly TNO-RIVM meetings, lead by Thomas. I am glad that I had the chance to play a small role in the collaboration between TNO and RIVM. I hope the collaboration will have a long and bright future!

Mijn nieuwe collega's bij OZHZ, **Leonie**, **Agaath**, **Linda**, **Jelle** en **Jan**, wil ik ook bedanken voor hun geduld en steun tijdens de laatste loodjes. Ik heb gemerkt dat het afronden van een PhD niet altijd eenvoudig is, zeker niet wanneer je al aan een nieuwe baan bent begonnen. Ik ben dan ook dankbaar voor jullie geduld en steun.

Mariska, wat leuk dat we na onze tijd in Delft beiden een PhD zijn gaan doen, zij het bij andere universiteiten. We konden altijd bij elkaar terecht om ervaringen te delen, of om een lekker speciaalbiertje open te trekken. Ik ben heel blij met jou als mijn paranimf!

Vervolgens wil ik mijn **familie** en **vrienden** bedanken voor de steun gedurende alle fases van het project. Ik kon altijd bij jullie terecht met mijn verhalen over de hoogte- en dieptepunten van het PhD traject. **Pap** en **mam**, jullie wil ik in het bijzonder bedanken voor jullie vertrouwen, steun en oprechte interesse in mijn werk. **Lisanne** en **Martijn**, **Joran** en **Eline**, bedankt dat ik ook bij jullie altijd terecht kon met mijn enthousiaste verhalen en steun in lastigere tijden. Ook Erwin en Anouk ben ik dankbaar. Niet alleen voor de steun in moeilijke tijden, maar zeker ook voor de gezelligheid samen! Ik weet dat ik altijd op jullie allemaal kan rekenen en daar ben ik dankbaar voor.

Tot slot wil ik natuurlijk ook mijn vriendin **Selma** bedanken. Het PhD traject kent vele pieken en dalen en ik ben blij dat ik ze met jou heb kunnen delen. Je stond altijd open voor mijn enthousiaste verhalen, met je oprechte interesse. Tijdens de COVID lockdowns was je zelfs, of je het nu wilde of niet, sparringspartner en klankbord wanneer ik weer eens vast liep. Je bleef altijd geduldig en deed het geweldig! Ik ben dankbaar dat ik jou altijd naast me heb staan en dat je mij de ruimte gaf om dit traject te volgen. Samen sluiten we deze reis af bij de defence, kijken we terug op de mooie momenten en kijken we vooruit naar nog vele jaren samen. Dank je wel lieverd!

About the author

Ruben Schulte was born on 2 January 1991 in Zwijndrecht, the Netherlands. It was in Zwijndrecht, where he stayed throughout his youth, growing up together with his older sister, Lisanne, and younger brother, Joran.

His interest for nature and the atmosphere started at a young age. Perhaps it all started during long car trips. Ruben would often spent his time looking through the window at the clouds, possibly because he got carsick when doing anything else. Clouds, (thunder)storms and the weather phenomena would keep fascinating him throughout his life. In elementary school, his interests developed towards learning about natural disasters, as tornadoes, hurricanes and volcanoes were among his favourite topics when writing reports or giving presentations.

At high school, his curiosity in the atmosphere took a back seat. Ruben followed his natural skill in mathematics and physics, choosing advanced mathematics, physics and chemistry as his elective courses. In his fifth year in high-school, Ruben joined the extracurricular **CanSat** project, organized by Delft University of Technology (TU Delft). In this project, high school students from all across the country competed by designing and building the most advanced satellite the size of the can of coke. The top 10 entries having their satellite launched with a rocket to an altitude of 1 km. This project planted the seeds for his future academic career in technology at TU Delft.

Studying **Mechanical Engineering** at **TU Delft** was a logical next step for Ruben. The track covered a wide range of topics, ranging from courses on mathematics and dynamics, to fluid dynamics and thermodynamics. The latter set of courses would come in handy during his future academic career. In 2012 and 2013, Ruben joined the **Human Power Team** as a one-year (nearly full-time) extracurricular project. The Human Power Team

aimed to build the fastest human powered vehicle: an aerodynamic recumbent bicycle. In September 2013, Ruben and the team traveled to United States of America to compete in the "World Human Powered Speed Challenge" in Battle Mountain, Nevada. The team broke the **Guinness world record** on 14 September 2013, as their aerodynamic recumbent bike, the VeloX3 reached a speed of 133.78 km/hour (83.13 mph). Ruben finished his Bachelors one year later, in 2014.

After a short detour at the Space Flight MSc track, Ruben realized that technology was not the right path for him. He finally felt at home at the MSc track **Geoscience and Remote Sensing** at **TU Delft**, returning to his childhood fascination for the atmosphere and understanding system Earth. At this small MSc track, with about 25 students per year, students explored system Earth through remote sensing techniques and modeling. This turned out to be the right decision and Ruben even became **President** of the study association **Snellius Dispuut**, representing the MSc students and PhD candidates at the chair group. It was here, where he specialized in research of the atmosphere, particularly the atmospheric boundary layer. This resulted in a Master thesis, supervised by Bas van de Wiel and his PhD candidates, exploring measurements of short-lived turbulence in the nocturnal boundary layer.

After graduating Cum Laude from the Geoscience and Remote Sensing MSc track, the opportunity presented itself to continue researching the atmospheric boundary layer. This time, not at his familiar TU Delft, but as a PhD candidate at **Wageningen University** and at the **Dutch Institute of Public Health and the Environment (RIVM)**. The project very much appealed to Ruben, thanks to its exploratory nature and high societal relevance. Exploring state-of-the-art ammonia deposition measurements and the potential of advanced atmospheric models is what drew Ruben in, as well as the collaboration with RIVM. The results can be found in this PhD thesis you are now reading.

Peer-reviewed Journal Publications

de Graaf, M., **R. B. Schulte**, F. Peers, F. Waquet, L. G. Tilstra, and P. Stammes (2020). "Comparison of south-east Atlantic aerosol direct radiative effect over clouds from SCIAMACHY, POLDER and OMI–MODIS". *Atmospheric Chemistry and Physics* 20.11, 6707–6723. DOI: `10.5194/acp-20-6707-2020`.

Izett, J. G., B. J. H. van de Wiel, P. Baas, J. A. van Hooft, and **R. B. Schulte** (2019). "Dutch fog: On the observed spatio-temporal variability of fog in the Netherlands". *Quarterly Journal of the Royal Meteorological Society* 145.723, 2817–2834. DOI: `https://doi.org/10.1002/qj.3597`.

Schulte, **R. B.**, M. C. van Zanten, S. Rutledge-Jonker, D. P. J. Swart, R. J. Wichink Kruit, M. C. Krol, W. A. J. van Pul, and J. Vilà-Guerau de Arellano (2021). "Unraveling

the diurnal atmospheric ammonia budget of a prototypical convective boundary layer". *Atmospheric Environment* 249, 118153. DOI: `10.1016/j.atmosenv.2020.118153`.

Schulte, **R. B.**, M. C. van Zanten, B. J. H. van Stratum, and J. Vilà-Guerau de Arellano (2022). "Assessing the representativity of NH₃ measurements influenced by boundary-layer dynamics and the turbulent dispersion of a nearby emission source". *Atmospheric Chemistry and Physics* 22.12, 8241–8257. DOI: `10.5194/acp-22-8241-2022`.

Swart, D., J. Zhang, S. van der Graaf, S. Rutledge-Jonker, A. Hensen, S. Berkhout, P. Wintjen, R. van der Hoff, M. Haaima, A. Frumau, P. van den Bulk, **R. B. Schulte**, M. C. van Zanten, and T. van Goethem (2022). "Field comparison of two novel open-path instruments that measure dry deposition and emission of ammonia using flux-gradient and eddy covariance methods". *Atmospheric Measurement Techniques Discussions*, 1–32. DOI: `10.5194/amt-2022-171`.

Vilà-Guerau de Arellano, J., O. Hartogensis, I. Benedict, H. de Boer, P. J. M. Bosman, S. Botía, M. A. Cecchini, K. A. P. Faassen, R. González-Armas, K. van Diepen, B. G. Heusinkveld, M. Janssens, F. Lobos-Roco, I. T. Luijkx, L. A. T. Machado, M. R. Mangan, A. F. Moene, W. B. Mol, M. van der Molen, R. Moonen, H. G. Ouwersloot, S. Park, X. Pedruzo-Bagazgoitia, T. Röckmann, G. A. Adnew, R. Ronda, M. Sikma, **R. B. Schulte**, B. J. H. van Stratum, M. A. Veerman, M. C. van Zanten, and C. C. van Heerwaarden (n.d.). "Advancing understanding of land–atmosphere interactions by breaking discipline and scale barriers". *Annals of the New York Academy of Sciences* n/a.n/a (), 1–25. DOI: `doi.org/10.1111/nyas.14956`.

Netherlands Research School for the
Socio-Economic and Natural Sciences of the Environment

D I P L O M A

for specialised PhD training

The Netherlands research school for the
Socio-Economic and Natural Sciences of the Environment
(SENSE) declares that

Ruben Bastiaan Schulte

born on 2 January 1991 in Zwijndrecht, the Netherlands

has successfully fulfilled all requirements of the
educational PhD programme of SENSE.

Wageningen, 24 March 2023

Chair of the SENSE board

Prof. dr. Martin Wassen

The SENSE Director

Prof. Philipp Pattberg

The SENSE Research School has been accredited by the Royal Netherlands Academy of Arts and Sciences (KNAW)

K O N I N K L I J K E   N E D E R L A N D S E
A K A D E M I E   V A N   W E T E N S C H A P P E N

The SENSE Research School declares that **Ruben Bastiaan Schulte** has successfully fulfilled all requirements of the educational PhD programme of SENSE with a work load of 35.5EC, including the following activities:

SENSE PhD Courses

- o   Environmental research in context (2018)
- o   Research in context activity: 'Researching atmospheric ammonia in the context of the Dutch nitrogen crisis at the RIVM' (2018-2022)

Other PhD and Advanced MSc Courses

- o   Atmospheric boundary layer: Integrating chemistry and land interactions. applications of the CLASS model, Wageningen University (2018)
- o   Brain-friendly Working & Writing, Wageningen Graduate Schools (2018)
- o   Brain Training, Wageningen Graduate Schools (2019)
- o   Communication with the Media and the General Public, Wageningen Graduate Schools (2019)
- o   Career Perspectives Wageningen Graduate Schools (2020)
- o   GEWEX 2nd evapotranspiration workshop: Novel insights through models and observations, Global Energy and Water Exchanges (2021)

Management and Didactic Skills Training

- o   LIAISE international measurement campaign (Spain), assistance board meetings and field work (2021)
- o   Co-organizer RITA-2021 and Veenkampen ammonia measurement campaigns and publications (2021-2022)
- o   Teaching in the BSc course 'Introduction Atmosphere' (2018-2020)

Selection of Oral Presentations

- o   *Interpreting ammonia concentration and flux observations using a conceptual convective boundary layer model*. BBOS Autumn Symposium, 23-25 October 2019, Den Bosch, The Netherlands
- o   *Unravelling the diurnal atmospheric ammonia budget*. BBOS Boundary Layer and Turbulence, 31-January 2020, Utrecht, The Netherlands
- o   *Towards a virtual NH3 testbed with explicitly resolved turbulence*. RITA-2021 data workshop, 2 November 2021, Online
- o   *Towards a virtual NH3 testbed with explicitly resolved turbulence*, Ammoniak-Workshop, Staatliches Gewerbeaufsichtsamt Hildesheim, 3-4 November 2021, Online

SENSE coordinator PhD education

Dr. ir. Peter Vermeulen